Centre for Astrophysics and Supercomputing

Massive stars and gravitational waves: Bridging the gap with a new method for rapid stellar evolution

Poojan Agrawal

Presented in fulfillment of the requirements
of the degree of Doctor of Philosophy

Jan 2022

School of Science, Computing and Engineering Technologies
Swinburne University of Technology

Abstract

Observations of Galactic globular clusters in the last two decades and the more recent detection of gravitational waves from compact binary mergers have prompted us to examine the role of stellar evolution, especially that of stars more massive than $9\,\mathrm{M}_{\odot}$, in stellar populations. While numerical simulations have shown that massive stars, particularly those in binaries, can dramatically impact the evolution of star clusters and vice-versa, their evolution remains highly approximated in most population synthesis codes.

Therefore, in this thesis, we develop a new framework for modelling the evolution of stars in population synthesis codes. The METhod of Interpolation for Single Star Evolution (METISSE) uses interpolation within a grid of pre-computed single stellar tracks to calculate stellar parameters. It is an improvement over the existing approach of the Single Star Evolution (SSE; Hurley et al., 2000) fitting formulae, as the use of interpolation allows the user to easily use different sets of stellar evolution tracks, computed with different input parameters.

We focus on the role of massive stars in regulating the properties of their populations, especially binaries. Due to their apparent rarity and short lives, the evolution of massive stars remains poorly constrained by observations. These gaps in our knowledge of massive stars force stellar evolution codes to make certain assumptions while modelling their evolution. The result is a variety of stellar models in the literature which can differ significantly from one another, especially for very massive stars.

We examine the differences in the predictions of massive star models from five projects: BPASS, BOOST, GENEVA, MIST and PARSEC. We find that besides the differences in the physical approximations such as chemical composition, mass-loss rates, and convective boundaries, various methods used in the treatment of numerical instabilities in one-dimensional codes can also contribute to differences found in the massive stellar models. Moreover, the interplay of these methods with other physical inputs can also lead to potential bias in constraining the latter.

To quantify the differences arising due to the numerical treatments related to density inversions in massive stars, we perform a systematic study of the impact of these methods

within the stellar evolution code MESA using a single set of assumptions. Even when using the minimum enhancements needed to overcome numerical instabilities, we find that the differences between the methods can be non-trivial.

While the ultimate solution of these numerical treatments might lie in a three-dimensional modelling approach, in combination with future observations dedicated to constraining the physical processes operating in massive stars, it is important to test the results of populations synthesis using different models of massive stars. We demonstrate the usefulness of METISSE in achieving this purpose, by using it with stellar models computed not just with different input parameters but also from different stellar evolution codes: MESA and the Bonn code. We find that the uncertainties in modelling the evolution of massive stars, such as their radiation dominated envelopes, can impact their properties such as the maximum radial expansion and mass of the remnants obtained through their interpolation. We thus establish the suitability of METISSE in systematic studies dedicated to exploring the impact of uncertain parameters in stellar evolution on the properties of binary populations and dynamical systems of stars.

We update METISSE to include the impact of mass changes, such as through binary interaction. We compare stellar tracks computed by SSE and METISSE using the same set of input models from Pols et al. (1998) while adding mass loss on top. We find that with the current set of assumptions for modelling additional mass loss in METISSE, it can reproduce the results from SSE for low-mass-loss rates. However, for high-mass-loss rates we find differences in the behaviour of stellar radii, indicating the need for a re-evaluation of our assumptions for extra mass loss. We find similar results when comparing METISSE with detailed models computed by MESA using the same mass-loss rates, confirming the source of discrepancy.

We integrate this updated version of METISSE with the Binary Stellar Evolution (BSE; Hurley et al., 2002) code. Preliminary results from the evolution of an initially wide massive binary system, computed using METISSE and SSE respectively with BSE, presents an example of the impact the variance in radius can have on the behaviour of binaries. While the discrepancy in the behaviour of radius signifies the need for immediate future work in improving METISSE, the success of METISSE in reproducing results of other evolutionary parameters and its seamless integration with BSE is encouraging.

This thesis provides the necessary groundwork for exploring the impact of massive stars in stellar multiples and star clusters. It paves the way forward to obtaining new insights into the interaction within binaries and dense cluster systems. With minor modifications, METISSE will help us answer the questions pertaining to recent observations, such as the origin and evolution of compact binary systems as the source of gravitational wave emissions.

Acknowledgements

A PhD is not a race, it is a marathon, and an unusually long marathon in times of a global pandemic. Pursuing it to completion would not have been possible without all the help and guidance I have received in the past four years. There is a long list of people who made this journey easier for me.

First and foremost, a huge thanks to my supervisors, Jarrod, Simon, and Dorottya (Dori), for your constant support and guidance. Jarrod – you have been an amazing supervisor, mentor and guide. You always made sure that everything else has been taken care of, so I can focus on my PhD, including always keeping meetings in the afternoons to accommodate my late night work schedule. I regard myself as incredibly lucky to have the opportunity to improve upon the work that you started for your own PhD. I hope I have been able to do justice to it. Simon – it has been great working with you, with all the ideas and discussions. Despite your packed schedule, you have always been prompt whenever I needed help. It was great being able to reach out to you for all the big and small things. Dori – you are always generous with your motivating words and comments. From discussions on massive stars to pieces of advice on improving job applications and write-ups, I have learned so much from you.

A little help and support can go a long way. Jade, Darren, Sarah Maddison, and Chris Flynn – thanks for all the help, support, and words of advice that greatly improved my academic life. Michelle – You have been more than a mentor to me. I cannot thank you enough for going above and beyond to ensure my well-being, for your advice on life, academia, everything.

Special thanks to OzGrav for providing financial support and extra-curricular opportunities. A big thanks to the OzGrav outreach team, especially Jackie, for helping me become better at communicating my science to others. Lisa – thank you for all the cakes, cookies, advice, and all the 'minions'. Carl, Mark, Erin, Luana – I will miss our little random lunchtime/tea-time conversations. I am also thankful to Team COMPAS (Ilya, Alejandro, Coen, Serena, Floor, Jeff, Ryo, ...) for all the awesome science discussions.

Thanks to fellow marathoners and friends: Alexey Bobrick, Daniel Berke, Adam, Bronwyn, Renne, Marcus, Hao, Jielai, Cherie, Vivek (VG), Ayushi, Debatri, Mohsen, Guri and former marathoners Shivani, Vivek (Anna), Chandra, Wael for all the help, advice and support. Rahul and Praveer – thank you for being friends I can always count on and for all the coffee and lunchtime jibber-jabbers. I will miss being the DJ at our late evening work sessions at AMDC. Nandini – thanks for all the festivals and trips, for patiently bearing my rants, for looking out for me, and for cheering me up with good food.

Vikram, Abhilasha, Katyayani, Shailendra, Vijay and Nitesh – thanks for always believing in me, for all the laughter and those happy little moments to keep me going. Alex – thanks for being my pillar of support. It is, because of you that not only have I been able to survive finishing a PhD, but thrive in it.

Finally, thanks to my favourite people in the world, my parents, my bossy sister, and my cool brother-in-law. Whatever I am today, whatever I have been able to achieve in life, it is because of your constant love and support. There are not enough words to express my gratitude for you. Baba and dadi – I wish you were here to witness this moment. Love you.

Declaration

The work presented in this thesis has been carried out in the Centre for Astrophysics & Supercomputing at Swinburne University of Technology between 2017 and 2021. This thesis contains no material that has been accepted for the award of any other degree or diploma. To the best of my knowledge, this thesis contains no material previously published or written by another author, except where due reference is made in the text of the thesis. The content of the chapters listed below has appeared in refereed journals. Minor alterations have been made to the published papers in order to maintain argument continuity and consistency of spelling and style.

- Chapter 2 is soon to be submitted for publication in a peer-reviewed journal as **"Examining the differences in massive star models from various simulations"** authored by Poojan Agrawal, Dorottya Szécsi, Simon Stevenson and Jarrod Hurley.

  Data Analysis and drafting of this chapter was done jointly by Dorottya Szécsi and myself. I have also made all the figures and tables accounting for 70 percent of the total work. Jarrod Hurley and Simon Stevenson contributed by providing helpful feedback on the manuscript.

- Chapter 3 is soon to be submitted for publication in a peer-reviewed journal as **"A systematic study of super-Eddington envelopes in massive stars"** authored by Poojan Agrawal, Simon Stevenson, Dorottya Szécsi and Jarrod Hurley.

  For this chapter, I ran the simulations with MESA, wrote the software for analyzing the data and creating the figures, and drafted the paper. My contribution amounts to 85 percent of the total work. I was helped in this task by Simon Stevenson, Jarrod Hurley and Dorottya Szécsi through useful help and suggestions.

- Chapter 4 has been published as **"The fates of massive stars: exploring uncertainties in stellar evolution with METISSE"**, authored by Poojan Agrawal, Jarrod Hurley, Simon Stevenson, Dorottya Szécsi and Chris Flynn, 2020 MNRAS, 497, 4549.

- Chapter 5 will be published as **"The role of stellar evolution in mass transferring binaries and gravitational wave progenitors"**, authored by Poojan Agrawal, Jarrod Hurley, Simon Stevenson and Dorottya Szécsi.

  For these two chapters, I have written METISSE and the associated software. I have also drafted these chapters, and made all the figures and tables in them, contributing towards 85 percent of the work. My supervisors, Jarrod Hurley, Simon Stevenson and Dorottya Szécsi provided guidance and feedback on both the code and the manuscript. Chris Flynn helped with the software/Fortran issues related to METISSE and also provided feedback on Chapter 4.

Figures for this thesis have been made using Python libraries mainly Matplotlib (Hunter, 2007), NumPy (Harris et al., 2020) and Pandas (pandas development team, 2020). Some of the figures in Chapter 1 have been sourced from Misra et al. (2020), European Space Agency/Hubble Space Telescope and LIGO image library. I also acknowledge Aaron Dotter for the code ISO (Dotter, 2016) on which the initial version of METISSE was based.

Poojan Agrawal
Melbourne, Victoria, Australia
2022

Dedicated to all the women whose determination paved the path that I now tread so freely.

Contents

List of Figures

List of Tables

1

Introduction

Since the dawn of astronomy, our view of the cosmos has changed a lot. As our telescopes improved, so did our understanding of the Universe. A good example is globular clusters (GCs), which were first spotted by Abraham Ihle in 1665 (Halley, 1715) as a fuzzy patch of light. By 1764, telescopes were able to resolve individual stars in the clusters (Messier, 1774). For the nearly two centuries that followed they were considered to be a relatively simple, static system of stars. It was only in the mid-twentieth century that the role of dynamical interactions between the member stars in GCs was established (Meylan & Heggie, 1997). By the end of the twentieth century they had gained a central position in astronomy as a test-bed for theories of stellar and galactic evolution (Heggie & Hut, 2003).

In the last few decades, high-resolution data from both ground- and space-based telescopes have enabled us to observe unprecedented details in these stellar systems. Recent photometric and spectroscopic images of GCs have revealed that the chemical makeup of their member stars is much more complicated than previously thought. Galactic GCs have been found to contain not just one but multiple populations (MPs) of stars, with each population showing peculiar abundance variations (Bastian & Lardo, 2018; Milone, 2020). The origin of these abundance variations largely remains unsolved, and is an active area of research.

Advancements in our capabilities to observe the Universe in the electromagnetic wavelengths have been further complemented by the detections of neutrinos, cosmic rays, and gravitational waves (GWs) resulting from various astrophysical processes, starting a new era of multi-messenger astrophysics (Mészáros et al., 2019). Among the most useful non-electromagnetic signals are the GWs that are emitted following the merger of compact binary systems of neutron stars and black holes (Abbott et al., 2016). Such mergers can happen either through dynamical interactions in dense stellar systems such as globular clusters and galactic nuclei, or through certain evolutionary processes in isolated binary systems. The GW signals from these mergers can be detected by current ground-based detectors and can help reveal unforeseen details about the Universe that are otherwise invisible in the electromagnetic regime.

As observatories improve in terms of better detectors both in the electromagnetic and gravitational wave regimes, it is required that the models generated by our codes mimic the observational results closely. Hence the need for realistic models of multiple-star systems such as stellar binaries and star clusters. To create such models, one needs to simulate the evolution of a large number of stars (a population) while taking into account the different interactions between them through a technique known as *population synthesis*. Population synthesis codes help us simulate the complicated physical processes operating in stellar systems in a fast, computationally robust manner. This permits the evolution of millions of stars, allowing us to simulate large stellar systems like star clusters as well as identify the evolutionary pathways that can lead to phenomena of interest such as GW mergers.

Both the phenomena of MPs in GCs and the emission of GWs through compact binary mergers require comprehending the contribution of massive stars in both binary and star cluster environments. However, stellar evolution remains highly approximated in most population synthesis codes. While in the past, this may have been sufficient to reproduce observations of stellar systems, current and upcoming observations require an improved and up-to-date treatment of stellar evolution, especially for stars more massive than around $9\,M_\odot$. These massive stars are the precursors of many vivid and energetic phenomena in the Universe, however their evolution remains shrouded with uncertainties. Massive stars are born less often compared to lower mass stars and are short lived, thus it is hard to get observational constraints on their lives. Dedicated telescopic surveys of massive stars in nearby galaxies (Evans et al., 2011; Kaper et al., 2011; van Gelder et al., 2020) have significantly improved our understanding of them in the recent years. It is, therefore, a great time to reconsider the way we model them in binary populations and star clusters and test them with the present-day observations.

The aim of this thesis is to combine our most up-to-date understanding of massive stars with population synthesis studies to explore the lives of massive stars and their role in modifying the properties of stellar multiples and star clusters. In the following sections, we provide a summary of massive star evolution, binary evolution and globular cluster evolution and the different ways they can be modelled with various codes. We then give an overview of the problem of MPs and GWs, followed by possible solutions in the form of populations synthesis. We conclude with an outline of the rest of this thesis.

1.1 Modelling stellar evolution

The life of a star can, in theory, be modelled by using the set of differential equations governing the structure and evolution of the star. These are mainly the equations of stellar structure together with the equations for energy generation and transport inside the star. Since stars are three-dimensional (3D) objects, the ideal way to solve these equations would be using 3D codes. However, modelling the complete evolution of stars with 3D codes is currently infeasible. Therefore, the evolution of stars is usually modelled using one-dimensional (1D) codes.

In the Lagrangian formulation of these equations, a star of total mass M, can be divided into cells of mass m, such that $r = r(m, t)$ denotes the radius of the star containing the mass cell m at time t, $\varrho = \varrho(m, t)$ denotes the density while P is pressure and T is temperature at the edge of the cell. Assuming the star is spherically symmetric, in hydrostatic and thermal equilibrium, then its structure and evolution can be given by the following equations (cf. Kippenhahn et al., 2012).

Equation for the conservation of mass:

$$\frac{\partial r}{\partial m} = \frac{1}{4\pi r^2 \varrho} \quad . \tag{1.1}$$

Equation for the conservation of momentum:

$$\frac{1}{4\pi r^2}\frac{\partial^2 r}{\partial t^2} = -\frac{\partial P}{\partial m} - \frac{Gm}{4\pi r^4} \quad , \tag{1.2}$$

where G represents the gravitational constant.

At hydrostatic equilibrium, the acceleration term on the left hand side vanishes and the equation reduces to,

$$\frac{\partial P}{\partial m} = -\frac{Gm}{4\pi r^4} \quad . \tag{1.3}$$

Equation for the conservation of energy: If l is the luminosity (rate of energy flowing outward through a sphere of radius r), ε_{n} is the energy generated by nuclear reactions, ε_v is the energy lost in the form of neutrinos, c_P is the specific heat capacity at constant pressure, then conservation of energy gives,

$$\frac{\partial l}{\partial m} = \varepsilon_{\mathrm{n}} - \varepsilon_v - c_P \frac{\partial T}{\partial t} + \frac{\delta}{\varrho}\frac{\partial P}{\partial t} \quad , \tag{1.4}$$

$$\text{where, } \delta = \left(\frac{\partial \ln \varrho}{\partial \ln T}\right)_P \quad .$$

Equation for chemical changes: If X_i denotes mass fractions of the nuclei of elements $i = 1, \ldots, I$ having masses m_i, and r_{ij} is the reaction rate (number of reactions per unit time per unit volume transforming nuclei from type i to type j) then,

$$\frac{\partial X_i}{\partial t} = \frac{m_i}{\varrho}\left(\sum_j r_{ji} - \sum_k r_{ik}\right) \quad . \tag{1.5}$$

Equation for the thermal stratification:

$$\frac{\partial T}{\partial m} = -\frac{GmT}{4\pi r^4 P}\nabla \quad , \tag{1.6}$$

$$\text{where, } \nabla = \left(\frac{d \ln T}{d \ln P}\right) \quad .$$

This equation describes the transport of energy in the star. If the energy is transported through radiation then,

$$\nabla = \nabla_{rad} = \frac{3}{16\pi acG}\frac{\kappa l P}{mT^4} \quad .$$

In the above equation, κ denotes the mean opacity, c is the velocity of light and $a = 7.57\times\ 10^{-15}\ \mathrm{erg\,cm^{-3}\,K^{-4}}$ is the radiation density constant. If, however, the energy is carried by convection, then the value of ∇ is given by the 1D approximation for convection process in stars; the mixing length theory (MLT; Böhm-Vitense, 1958; Böhm, 1963). It is further supplemented by additional mixing process such as convective overshoot, semiconvection and diffusion (Kippenhahn et al., 2012).

Solving these non-linear and coupled partial differential equations requires various inputs such as the equation of state (to describe the thermodynamic properties of the stellar matter), nuclear physics (to provide energy generation mechanisms and their rates) and opacity tables (to determine energy transport mechanism inside stars) along with other boundary conditions.

One dimensional stellar structure and evolution codes work by dividing a star into smaller regions based on either radius or mass. Then, they solve the above set of equations while applying appropriate boundary conditions at the center and the surface to give a *model* of the stellar structure at any instant. A time sequence of these stellar models gives what is commonly known as a *stellar track*, depicting the evolutionary path followed by the star. The final output is in the form of an evolutionary track with a large set of properties for each point in the model at any given instant.

Depending on the mass, the metallicity and the evolutionary phase of a star, mass loss through stellar winds can be computed using a combination of observations and computational models. However, the above equations do not include a mechanism for stellar mass loss. Hence, mass loss is calculated explicitly from parameterized prescriptions (e.g., Reimers, 1975; Vink et al., 2000) at each time step before solving these equations.

Similar to convection, the impact of rotation on the evolution of stars is implemented using a 1D approximation, such as the 'shellular approximation' (Kippenhahn & Thomas, 1970; Meynet & Maeder, 1997) while magnetic fields are implemented, for example, through the Spruit–Tayler dynamo (Spruit, 2002).

In the last few decades, 1D stellar evolution codes (also known as 'detailed' codes) have progressed a lot. The development of sophisticated numerical methods for simulating physical processes and newer input data in the form of opacity tables and nuclear reaction rates has led to the development of modern and improved stellar structure and evolution codes (Langer, 2012; Ekström et al., 2020). Examples include the Cambridge STARS code (Eggleton, 1971), the Bonn code (Brott et al., 2011a), the Geneva code (Eggenberger et al., 2008), PARSEC (Bressan et al., 2012), FRANEC (Degl'Innocenti et al., 2008), MESA (Paxton et al., 2019), BPASS (Eldridge et al., 2017), STAREVOL (Decressin et al., 2009) and KEPLER (Weaver et al., 1978).

Detailed codes are the current best way of modelling stellar evolution, although modelling a population of stars with them can be computationally very expensive. Thus rapid stellar evolution codes, that approximate the evolution of stars using evolutionary tracks from 1D stellar evolution codes, are used for the purpose of population synthesis (see Section 1.8 for details).

1.2 MESA

In this thesis we use Module for Experiments in Stellar Astrophysics (MESA: Paxton et al., 2011, 2013, 2015, 2019) for computing detailed models of massive stars. MESA is an advanced one dimensional stellar structure and evolution code. It has been developed as an improvement over the EZ stellar evolution code (Eggleton, 1971; Paxton, 2004), and is capable of solving the coupled differential equations of the stellar structure simultaneously for all mass cells from the center to the surface and their evolution with time.

It can evolve stars for a wide range of masses and metallicities. Different prescriptions exist in MESA for computing mass-loss rates within the various evolutionary phases of stars. For dust-driven winds of cool stars, the mass-loss schemes of Reimers (1975), Bloecker (1995), de Jager et al. (1988), Nieuwenhuijzen & de Jager (1990), and van Loon et al. (2005) are available. For radiation-driven winds of hot stars Kudritzki et al. (1989), or Vink et al. (2000, 2001), or Gräfener & Hamann (2008) can be used. For massive stars, mass loss can also be modelled using a collective 'Dutch' scheme (Glebbeek et al., 2009). The scheme follows Vink et al. (2000, 2001) for hot winds, de Jager et al. (1988) for cool winds and Nugis & Lamers (2000) for Wolf-Rayet winds.

Convection and the associated mixing processes such as overshooting, semiconvection, and thermohaline mixing are modelled using the MLT. In addition to the original version by Böhm-Vitense (1958), other modified versions of MLT from Cox & Giuli (1968), Bohm & Cassinelli (1971), Mihalas (1978) and Kurucz (1979), and Henyey et al. (1965) are also included in MESA. Including the effect of diffusion and gravitational settling is also an option. For other input data, MESA makes use of up-to-date surface boundary conditions, equation of states, opacity tables, nuclear reaction network and reaction rates for both thermonuclear and weak reactions.

While the effect of stellar rotation on chemical and angular momentum transport is implemented using the shellular approximation (Meynet & Maeder, 1997), that of magnetic fields is incorporated using the Spruit-Tayler dynamo (Spruit, 2002; Heger et al., 2005). The effect on mass loss owing to rotation is also included from Heger et al. (2000). Additional capabilities include the effect of oscillations through GYRE (Townsend & Teitler, 2013; Townsend et al., 2018), astroseismology through ADIPLS (Christensen-Dalsgaard, 2008) and radial stellar pulsations through RSP (Smolec & Moskalik, 2008).

Apart from the vast number of input options that MESA provides for modelling various physical process, customized prescriptions can also be added through the 'other' routine of MESA. The code is open source and parallelizable via thread-safe modules. It has an active user community and is continuously being updated to include newer physics and input data.

1.3 Massive stars and their evolution

Stars that are massive enough to undergo core collapse at the end of their lives are termed massive stars. The minimum initial mass at which this happens is uncertain and depends on various factors such as the properties of convective overshoot or the chemical composition of the star. At solar metallicity, the minimum initial mass of massive stars can be between 8–12 $M_\odot$ (Poelarends et al., 2008). In general, stars above 9 $M_\odot$ are considered massive stars.

Massive stars are born, like any other star in the Universe, out of molecular clouds of dust and (primarily) hydrogen, albeit less often than their low-mass counterparts (Salpeter, 1955; Kroupa, 2001). Even at birth, they are much more luminous ($>10^4\,L_\odot$) and hotter ($>25\,000$ K) than low-mass stars. Due to their high luminosity they emit copious amounts of ionizing radiation (Strömgren, 1939; Spitzer, 1978), regulating star formation and the evolution of galaxies (Gatto et al., 2017; Kennicutt & Evans, 2012). Their high luminosity combined with their large radius also leads to rapid mass loss from the surface in the form of stellar winds. These winds further enrich the interstellar medium with nuclear processed material (Lamers, 2008) and drive shocks into the surrounding medium, producing X-rays and providing yet another source of ionisation and heating of the interstellar medium (Weaver et al., 1977).

To support themselves against gravitational collapse, massive stars undergo nuclear burning rapidly, lasting only for a few million to a few tens of million years before they run out of fuel. Depending on the properties of the core towards the end of their lives, they either undergo a supernova explosion or silently implode to form neutron stars and black holes. In some cases, e.g. in the case of a pair-instability supernova, the explosion completely disrupts the star and does not leaves any stellar remnant. Supernova explosions again release high energy radiation and are a primary source of heavy elements in nature (e.g., Maund et al., 2017).

The birth properties of neutron stars and black holes can be determined by the parameters of the stellar core at the time of collapse, along with other parameters such as the total mass and the binding energy of the star. These compact remnants are further responsible for several observed transient processes, such as gamma-ray bursts (e.g. Yoon et al., 2006; Szecsi, 2017), X-ray binaries (Verbunt, 1993) and gravitational-wave events (e.g. Stevenson et al., 2019; Mapelli et al., 2020).

Throughout their lives, massive stars play an important role in shaping their surroundings, yet how exactly they undertake their journey from birth to death remains unsettled (e.g., see Langer, 2012). Uncertainties in the physical inputs for these stars such as the mass-loss rates (Smith, 2014; Renzo et al., 2017), nuclear reaction rates (Heger et al., 2002; Fields et al., 2018), impact of rotation (Heger et al., 2000; Maeder, 2009) and the magnetic field (Walder et al., 2012; Keszthelyi et al., 2019) hinder determining their exact evolutionary path. Moreover, most massive stars are predicted to occur in binaries, complicating their evolution even further.

A common evolutionary pathway for massive single stars is given by the Conti scenario (Conti, 1975; Maeder, 2009), depicted in Figure 1.1. In this scenario (Lamers & Levesque, 2017), massive stars spend most of their lives as OB type main-sequence stars. Those with initial masses in the range of 9–30 $M_\odot$ evolve to become red supergiants (RSGs) while burning helium in the core. They spend the rest of their nuclear burning lives as a

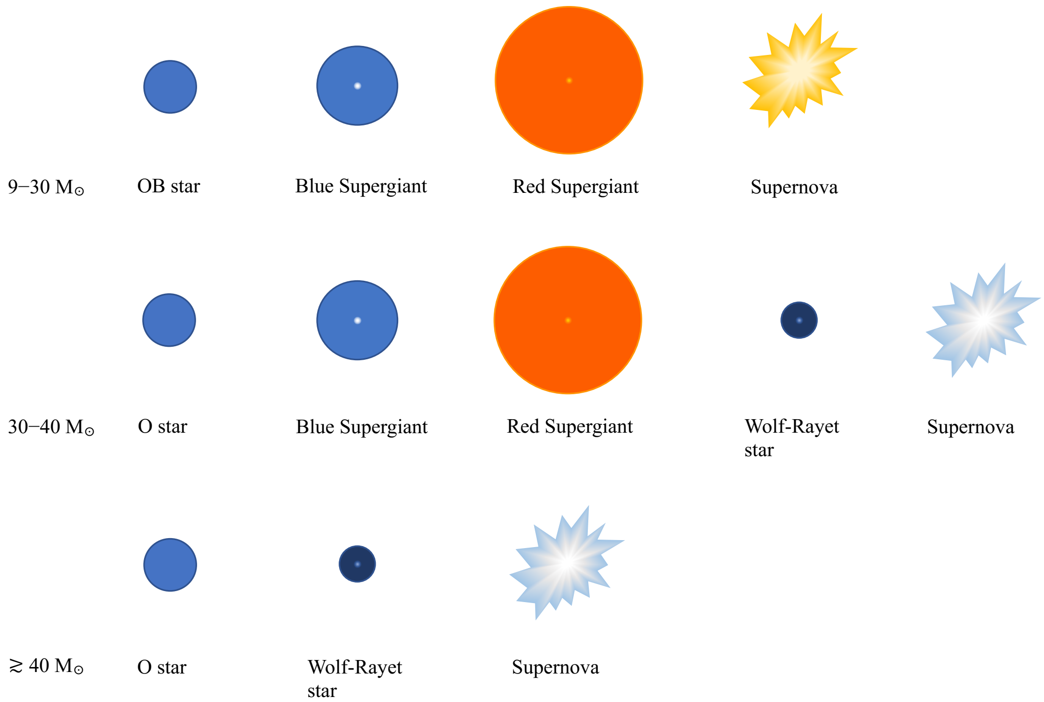

Figure 1.1 Schematic representation of the Conti scenario for the evolution of non-rotating, massive single stars at solar metallicity.

RSG before exploding in a Type II supernova. Stars with initial mass between 30–40 $\mathrm{M}_{\odot}$ may also go through the RSG phase. However, owing to their high luminosity, rapid mass loss strips-off their hydrogen-rich envelope and these stars end their lives in a stripped envelope supernovae (Type IIb or Type Ib/c). Stars more massive than 40 $\mathrm{M}_{\odot}$, experience high mass-loss rates while still burning hydrogen in their core, and evolve directly to a naked helium star phase. However, this scenario is not a definite one as uncertainties in massive stellar evolution can easily complicate this simple picture.

The evolution of stars more massive than 40 $\mathrm{M}_{\odot}$ is also complicated by the presence of sub-surface elemental opacity bumps (Cantiello et al., 2009; Gräfener et al., 2012). The already high luminosity of these stars, in combination with the presence of these opacity bumps, can exceed the Eddington luminosity: the maximum luminosity required to balance inward gravitation pressure and outward radiation pressure (Eddington, 1926). Proximity to the Eddington luminosity has been attributed as the cause of several observed effects, including inflation of massive star envelopes (Sanyal et al., 2015) and enhanced mass-loss rates in the form of luminous blue variables (LBVs; Bestenlehner et al., 2014; Gräfener, 2021). From a computational perspective, if the luminosity carried through radiation exceeds the local Eddington luminosity in the low-density envelopes of massive stars, it can result in numerical difficulties, inhibiting further computation of stellar models beyond that point (Maeder, 1987; Paxton et al., 2013). This problem is exacerbated by the fact that very few massive stars are observed beyond the Humphreys-Davidson limit (Humphreys & Davidson, 1979), the same region in the Hertzsprung–Russell (HR) diagram where the aforementioned numerical issues relating to the Eddington luminosity occur in stellar models. Thus 1D stellar evolution codes have to use certain fixes to evolve massive stars through this computationally difficult phase. While these fixes help with computing the evolution of massive stars until core collapse, their interplay with other physical parameters of massive stars adds yet another element of uncertainty in massive star models.

The challenges in computing the evolution of massive stars are significant, but so is their importance in a wide range of astrophysical fields. With the rise in our observing capabilities, as well as improvements in our computing abilities, it is a great time to test different models of massive stars with population synthesis codes.

1.4 Binary stellar evolution

Two stars gravitationally bound to each other are said to form a binary system. These binary systems can be born in such a state (binary by birth) or can be formed through dynamical interactions in dense stellar systems.

In a reference frame co-rotating with the orbit of a binary system, different equipotential surfaces can be defined around the component stars, where the potential is determined by the gravitational pull of the two stars and their motion around each other. A critical equipotential surface, known as the Roche surface, consists of two teardrop shaped potential surfaces (called Roche lobes) around each star which meet at the inner Lagrangian point (L_1, see Figure 1.2). The effective radius of a Roche lobe can be defined as the radius of a sphere containing the same volume as the true Roche lobe.

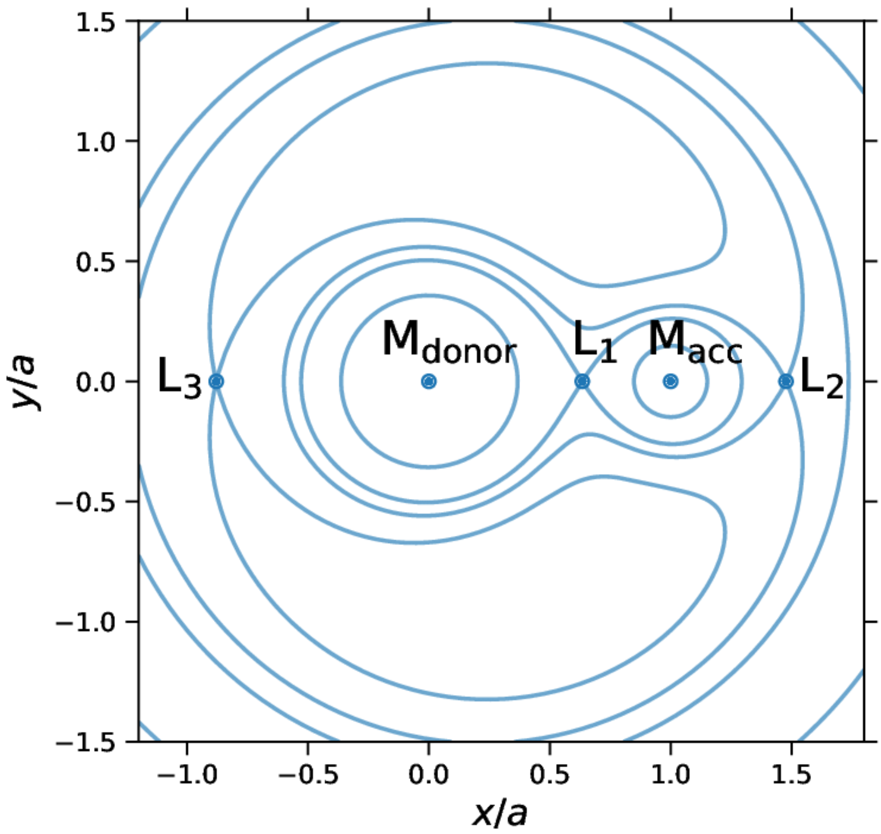

Figure 1.2 Equipotential surfaces for a binary system of stars. The critical equipotential surface passing through the inner Lagrangian point L_1 is known as the Roche surface or Roche lobes (Image sourced from Misra et al., 2020).

As a star evolves to become a giant and or a supergiant, its stellar radius can exceed its effective Roche lobe radius and the star is said to be filling its Roche lobe. Even when both stars in the binary are within their respective Roche lobes, they can still interact through wind accretion and tides (Tout et al., 1997; Hurley et al., 2002). These interactions can change the orbital separation between the stars and can therefore alter their Roche geometry. Once either star is able to fill its Roche lobe, the process of mass transfer through Roche-lobe overflow can be initiated. When material from one of the stars in the binary system expands beyond L_1, it becomes (gravitationally) dominated by the pull of the second star. Depending on the energy and momentum of the material, the outer layers of this star can be accreted by the companion star. This can change the mass, angular momentum and the surface composition of both stars.

If this expansion occurs beyond the outer Lagrangian point of the system L_2, then the outer layer of the star can escape the pull of both stars and form a common envelope around them (Paczynski, 1976; Ivanova et al., 2013). The common envelope is a temporary phase in the life of a binary system of stars. The motion of the stellar cores inside this envelope occurs at the expense of their orbital energy and causes subsequent decay of the orbit and the ejection of the envelope. If this decay does not lead to a stellar merger before the envelope is ejected, it can leave behind two tightly orbiting cores.

Binary interactions – particularly episodes of mass transfer – can lead to completely different evolutionary pathways compared to single stellar evolution, producing objects such as Algols (van Rensbergen et al., 2011), X-ray binaries (Verbunt, 1993) and millisecond pulsars (Phinney & Kulkarni, 1994), as well as phenomenon such as novae (Kraft, 1964), gamma-ray bursts (Izzard et al., 2004), and stellar mergers (de Mink et al., 2014). Binary interactions are also important for the chemical enrichment of the galaxy (De Donder & Vanbeveren, 2004; Eldridge & Stanway, 2020) and may have served a pivotal role in the reionization of the early Universe (Stanway et al., 2016; Götberg et al., 2020).

For massive stars the impact of binary interactions is even more important. The binary fraction for massive stars is almost one hundred percent compared to only fifty percent for Sun-like stars (Moe & Di Stefano, 2017). The high occurrence of massive stars in binaries can lead to mass-transfer episodes in about seventy percent of the stars, leading to mergers in every third binary system thus formed (Sana et al., 2012). If at the time of merger both stars were compact objects – neutron stars and black holes – the gravitational waves generated during the merger can be detected by the GW detectors here on Earth. The parameters measured from GW signals, such as the spins and masses of the binary components, can be used in constraining the evolution of massive stars and interaction with their neighbours (e.g., Stevenson et al., 2015, 2017).

Similar to stellar evolution, the evolution of binaries can be modelled with detailed stellar evolution codes. The PNS code (De Donder & Vanbeveren, 2004), the Twin code (Glebbeek et al., 2008), the Bonn code (Yoon et al., 2010), BinStar (Siess et al., 2013), BPASS (Eldridge et al., 2017), and MESA (Paxton et al., 2015) are a few examples of the detailed codes that can compute the evolution of a binary system of stars and the different interactions between them. However, owing to their large computational costs these codes are not suited for the purposes of population synthesis.

Therefore, binary populations synthesis codes, such as IBIS (Tutukov & Yungelson, 1996), BSE (Hurley et al., 2002), STARTRACK (Belczynski et al., 2002, 2008), binary_c (Izzard et al., 2004; Claeys et al., 2014), SEBA (Toonen & Nelemans, 2013), COMPAS (Stevenson et al., 2017; Vigna-Gómez et al., 2018), MOBSE (Giacobbo et al., 2018) and COSMIC (Breivik et al., 2020), are used for computing the evolution of a population of binary stars. These codes employ approximate methods for isolated binary evolution, and can take into account the impact of supernovae and necessary binary physics such as the effect of tidal interactions, mass transfer and common envelope evolution. Some of them also include tools for the statistical analysis of GWs (e.g., Barrett et al., 2018) and other binary processes such as novae (Kemp et al., 2021) and certain supernovae (Ruiter et al., 2014; Stevance et al., 2020).

1.5 Star cluster evolution

Typically found in the halos and bulges of galaxies, GCs are gravitationally bound collections of a large number of stars. For decades they have been useful not only for the study of galaxy properties in general but, within our Galaxy, they have served as an ideal test bed for the theories of stellar evolution (Heggie & Hut, 2003). They are the oldest and the most massive of the star cluster populations. They are also incredibly dense and dynamic. The gravitational interactions between their member stars can lead to the formation of binary or multiple stellar systems which in turn can form objects such as millisecond pulsars (Verbunt et al., 1987; Ransom, 2008), blue stragglers (Sandage, 1953; Piotto et al., 2004) and fast radio bursts (Kirsten et al., 2021; Kremer et al., 2021). Open clusters are an avenue of interest as well. Although they are smaller and comparatively less dense than GCs, the dynamical interactions between stars in an open cluster can still lead to the formation of objects such as blue stragglers (Johnson & Sandage, 1955; Ahumada & Lapasset, 2007). Therefore, it is necessary to consider the contribution from stellar dynamics while answering any questions related to star clusters.

The current state of computing and technology enables direct modelling of these systems. The orbits of N objects in a cluster constitute the classical N-body problem, the generalisation of Newton's Law of gravitation for a system of N interacting bodies. For a system of N bodies of mass m_i $(i = 1, \ldots, N)$ at position r_i, the equation of motion due to gravitational interaction is given by

$$m_i \frac{d^2\mathbf{r}_i}{dt^2} = \sum_{j \neq i, j=1}^{n} \frac{G m_i m_j \left(\mathbf{r}_j - \mathbf{r}_i\right)}{\left\|\mathbf{r}_j - \mathbf{r}_i\right\|^3} \quad . \tag{1.7}$$

For more than three bodies, there exist no analytical solutions to this equation, so it is solved through numerical integration. Also, while collisions can safely be ignored for galaxy scale N-body dynamics, they should be taken into account for accurately modelling star clusters as stellar interactions play an important role in their dynamical evolution. GCs can be modelled by approximate statistical methods using the Fokker-Planck Model (Drukier, 1993; Dull et al., 1997) and Monte Carlo Models (Giersz & Heggie, 2003; Rodriguez et al., 2021) or by direct integration using N-body models (Aarseth, 2003). In the direct integration method, the equation of motion is solved for each star and hence is the most precise method. This preciseness, however, comes at the cost of computational resource and time, so relevant simplifications are made to reduce the run-time.

The dynamical environment of a cluster can directly influence its member stars which in turn can affect the evolution of the cluster itself (Heggie & Hut, 2003). For example, as stars evolve their mass can change owing to winds or mass transfer in a binary. This can lead to a change in the gravitational force experienced by the stars, thereby changing their dynamics. Conversely, the dynamical motion of stars can alter their interaction with the companion and so their evolution. Hence, realistic modelling of globular clusters requires including the contribution from the evolution of individual stars. As described in Section 1.8, this is achieved by using rapid stellar evolution algorithms. Use of these algorithms makes it possible to include effects such as mass-loss due to stellar winds and follow binary evolution in detail for the GC evolution (Hurley et al., 2001).

1.6 Multiple stellar populations in globular clusters

It was long assumed that all stars in a given GC were formed almost at the same time and out of the same material, hence constituting a simple stellar population varying only in mass. It was possible to fit a color-magnitude diagram of stars in a GC by just one

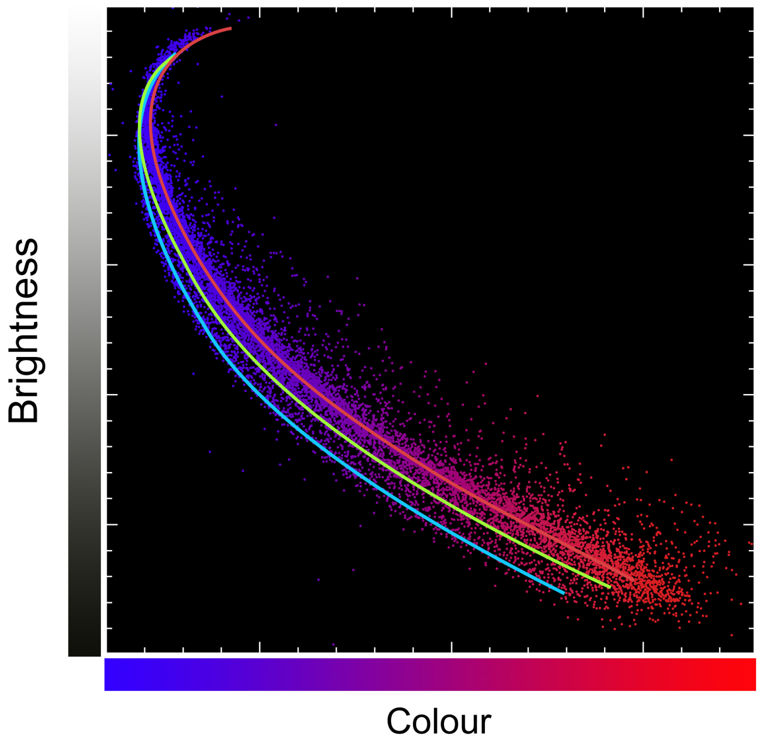

Figure 1.3 Color-magnitude diagram showing multiple populations of stars in the globular cluster NGC 2808. Image by M. Kornmesser, L. L. Christensen (ESA/Hubble).

isochrone and study the concepts of stellar evolution with it. This simple image of GCs first came into question when Osborn (1971) noted the nitrogen enhancement in the Red Giant Branch (RGB) stars of the same magnitude in M10 and M5. This was followed by the detection of cyanogen (CH, CN and NH) anomalies in other RGB stars (Norris, 1987). Correlations and anti-correlation in light elements like sodium and oxygen were soon established for various stars in different GCs (e.g. Sneden et al., 1992). An extreme mixing scheme was proposed (e.g. Denisenkov & Denisenkova, 1990) to explain the CN relation in RGB stars but it was unable to explain the observations of stars near the main-sequence turnoff (e.g. Cannon et al., 1998).

A strong blow to the simple stellar population theory came when three distinct main sequence bands were observed in the photometric observations of NGC 2808 (Piotto et al., 2007) through the Advanced Camera for Surveys on the Hubble Space Telescope. This split indicated three generations of stars formed discretely at three separate epochs with different helium content (see Figure 1.3). Bragaglia et al. (2010) extended this work by studying the chemical composition of two main-sequence stars in the same cluster, one each from the two extreme main sequences. The first star, taken from the reddest main sequence had a composition similar to that normally found in field stars, while the second star from the bluest MS showed depletion of carbon and magnesium and enhancement of nitrogen, sodium and aluminium, a pattern indicative of the second population of stars. Similar results were later obtained for other clusters and the theory of multiple stellar populations in GCs was established, demolishing the long-lived picture of simple stellar populations.

1.6.1 Key observations

Galactic globular clusters as young as 2 Gyr show a split in their stellar populations. This split has been observed not just in bright RGB stars but stars at all evolutionary phases (Gratton et al., 2019). There seems to be at least two distinct populations present in the GCs, one comprised of stars with a composition similar to those of field stars of the same metallicity (primordial branch) and others showing a spread in the chemical abundance of its stars (enriched branch or branches). The enriched populations in all GCs have been observed to exhibit all or most of the following relations: correlation in the abundances of elements like lithium & oxygen (Li-O), sodium & nitrogen (Na-N) and an anti-correlation of nitrogen with carbon (N-C), sodium with oxygen (Na-O), magnesium with aluminium (Mg-Al) and nitrogen (N) & sodium (Na) with helium (He).

Despite the variation in these light elements, the composition of heavier elements [Fe/H] and the sum of C+N+O have been observed to be fairly constant between the populations for most GCs (known as Type I clusters; Milone et al., 2017). These relations are characteristic of high-temperature hydrogen burning operating via Mg-Al, Ne-Na chains or the CNO cycle (Langer et al., 1993; Prantzos et al., 2007), further supported by the variation in the helium content obtained by the photometric observations of these stars. A small number of clusters, known as Type II clusters also show variation in iron and s-process elements (Marino et al., 2015).

Apart from the variations in chemical abundances, MPs also exhibit differences in their dynamical properties (D'Ercole et al., 2008). For example, the enriched population in most of the clusters seems to be concentrated towards the centre (Lardo et al., 2011) and has low velocity dispersion (e.g. Bellazzini et al., 2012) relative to the primordial population.

Multiple populations have also been observed for GCs outside the Milky Way, e.g. in Large Magellanic Cloud (LMC, Mucciarelli et al., 2009) and Small Magellanic Cloud (SMC, Dalessandro et al., 2016). Although the extent of the correlation and substructure of stellar populations differs from cluster to cluster, it does exhibit a dependence on the total mass of the cluster, indicating the role of GC properties (Milone, 2020). The phenomenon of MPs is not shown by stars in open clusters (Bragaglia et al., 2012; Vallenari, 2014) or the galactic field (Carretta et al., 2010), again suggesting a phenomenon unique to GCs.

1.6.2 Proposed explanations

Several scenarios have been proposed as a possible explanation for the observed chemical abundances in the stellar populations in GCs. A key element to this problem are the proton capture reactions that operate at high-temperatures of around 75 million Kelvin (MK: Langer et al., 1993). These temperatures can not be achieved by the low mass stars that are observed in GCs today but could have been attained inside the more massive stars that died out long ago. The following have been proposed as possible sources of enrichment in GC stars.

1. Intermediate mass stars ($\sim$ 5–8 $M_\odot$) on the asymptotic giant branch:

   The outer layers of intermediate-mass stars can reach very high temperatures (up to 100 MK) during the asymptotic giant branch phase of the evolution due to interaction of the envelope with the hydrogen burning shell (dredge-up). This can cause high-temperature hydrogen burning or hot bottom burning at the base of these envelopes. Products of this reaction can be transported via convection from the base of the envelope to the surface of the star and then expelled in stellar winds (Karakas & Lattanzio, 2014; D'Antona et al., 2016).

2. Fast rotating massive stars ($\geq$ 15 $M_\odot$):

   Massive stars can sustain hydrogen burning reactions at high temperatures ($\gtrsim$75 MK) in their cores during the main-sequence phase of evolution. If such stars are rotating at sufficiently high speeds (close to the limit of breakup) then the processed material can be transported to the surface through rotational mixing and centrifugally expelled to enrich the cluster medium (Prantzos & Charbonnel, 2006; Decressin et al., 2007b,a).

3. Interacting binaries:

   The formation and disruption of binaries due to dynamical interaction is quite common in GCs. Mass transfer in a binary system from a massive donor star can directly pollute a main-sequence or pre-main-sequence accretor star with processed material (Bastian et al., 2013; Jiang et al., 2014). Further, non-conservative mass transfer and stellar mergers in a massive binary system can shed large amounts of the enriched outer layers of the constituent stars into the surroundings. Assuming all massive stars in GCs were once part of a binary system, substantial amounts of enriched matter can be lost to the cluster, and then subsequently used to form multiple generations of stars (de Mink et al., 2009b; Wang et al., 2020).

4. Massive red supergiants ($\geq 80\,\mathrm{M}_\odot$):

   Massive stars at the end of their main sequence can become RSGs if they do not lose their envelope completely due to wind mass loss. Stellar models show that at sufficiently low metallicity ($Z = 0.02\,\mathrm{Z}_\odot$, [Fe/H] = -1.7; Szécsi et al. 2015), even stars with initial mass $\geq 80\,\mathrm{M}_\odot$ can become RSGs while burning hydrogen in their core as they undergo envelope inflation near the Eddington limit (Sanyal et al., 2015). Their deeply convective envelope can transport products of hydrogen burning to the surface where it can be lost in the stellar winds (Szécsi et al., 2018; Szécsi & Wünsch, 2019).

In the classical self-enrichment scenario, material lost by the first generation stars through one (or a combination) of the above factors gets trapped in the cluster potential. This material can then either pollute the second generation stars or the second population stars can form out of it (Gratton et al., 2012; Bastian & Lardo, 2018). With sufficient dilution from non-enriched material, this can explain most of the observed abundance anomalies but it does not explain how clusters like Ruprecht 106 (Villanova et al., 2013) can lack MPs. Also, enriched stars make up 50–70 percent of the present day GC population (Carretta et al., 2009), imposing a mass budget required to form these stars.

Other theories, such as disc accretion by low-mass stars (Bastian et al., 2013), fragmentation from very massive stars ($\sim 10^4\,\mathrm{M}_\odot$; Denissenkov & Hartwick, 2014), or the primordial branch stars forming out of the enriched stars (reverse order for formation, Marcolini et al., 2009), have been proposed to explain the origin of MPs. Due to the importance of dynamical interactions in the evolution of globular clusters, simulations based on the dynamics of gas (D'Ercole et al., 2008; McKenzie & Bekki, 2021) and stars in GCs (Vesperini et al., 2013, 2021) have also been developed. Although, so far none of them has been successful in explaining the observations completely (Bastian & Lardo, 2018; Mastrobuono-Battisti & Perets, 2021).

The problem of multiple stellar populations has challenged our conventional notions of star clusters. It requires unravelling the early evolution of GCs when massive stars would have lived and explaining the complex formation history of these clusters. Therefore, alternate models for GCs are needed that can take into account the impact of updated models of massive stars on the long-term dynamical evolution of clusters.

1.7 Gravitational waves

GWs are ripples in spacetime generated by the time variations of the mass quadrupole moment of the source. They were predicted by Albert Einstein in 1916 in his general theory of relativity (Einstein, 1916). On 14 September 2015, the advanced Laser Interferometer Gravitational-Wave Observatory (aLIGO) detected a GW signal from the merger of two black holes (GW150914; Abbott et al., 2016). This event marked the first direct detection of GWs. Since then, there have been more than 50 such detections from the merger of binary systems of black holes (BHs), binary systems of neutron stars (NSs), and binary systems containing a BH and a NS (Abbott et al., 2019, 2021a,b). A schematic diagram showing the masses of the compact remnants obtained with GW observations is presented in Figure 1.4.

This list contains the special event GW170817 which originated due to the merger of two NSs along with a kilonova explosion (Abbott et al., 2017b,c). It was observed in both the GW and electromagnetic regimes and helped make progress towards answering questions behind various mechanisms such as gamma-ray bursts (Abbott et al., 2017a), the origin of r-process elements (Kasen et al., 2017), the NS equation of state (Abbott et al., 2018a) and even constraining the physics of general relativity (The LIGO Scientific

Collaboration et al., 2018). At the same time, along with other GW detections, it raised new questions like how massive BHs and NSs form, what is their number and size in the Universe, and what is the role of environment on the evolution of binaries (Ricci, 2019). It hence became necessary to reconsider the origin and evolution of compact binary systems as the source of GW emissions.

1.7.1 Mechanisms for the formation of compact binary systems

Three main channels for the formation of compact binary systems have been proposed.

1. Dynamical formation in the dense stellar environments:

   Gravitational interactions in dense stellar systems can not only affect stellar evolution but can also lead to the formation of binary stellar systems (Heggie & Hut, 2003).

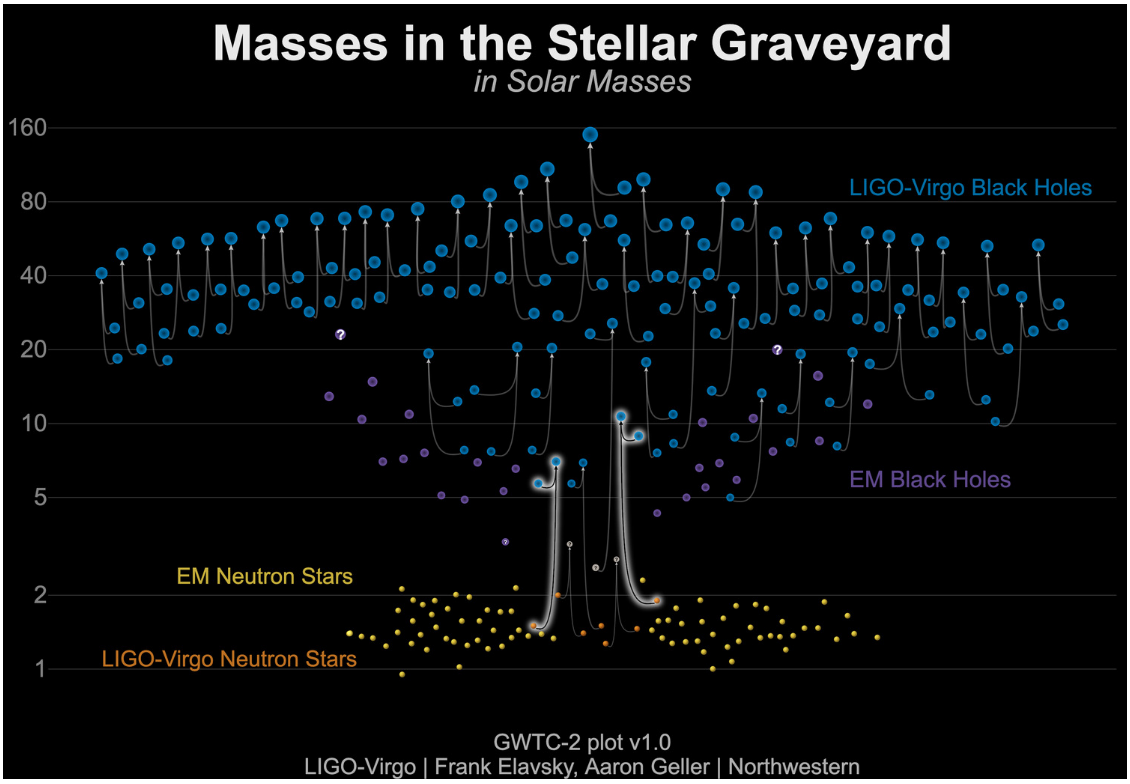

Figure 1.4 Mass of neutron stars, black holes and their merger products obtained through gravitational wave signals and electromagnetic observations. The two highlights in the centre represent the recently announced black hole-neutron star mergers detected through GWs (Abbott et al., 2021b). Image by Frank Elavsky and Aaron Geller, Northwestern University, LIGO-Virgo

Simulations have shown that the three-body dynamics inside globular clusters (Hurley et al., 2016; Rodriguez et al., 2016; Antonini & Gieles, 2020), young stellar clusters (Mapelli, 2016; Banerjee, 2017), and nuclear star clusters (Antonini & Rasio, 2016; Arca Sedda, 2020) can not only cause binary systems of neutron stars and black holes to form but also tighten and merge in the Hubble time to produce gravitational waves detectable by current detectors.

2. Tightening of isolated binaries through mass transfer and common envelope evolution:

   Binary interactions alter the orbital properties of the system, and may even tighten a binary sufficiently to merge within the age of the Universe. This can happen via stable mass transfer within late phases of evolution (van den Heuvel et al., 2017; Neijssel et al., 2019; Gallegos-Garcia et al., 2021) or via common envelope evolution (Eldridge & Stanway, 2016; Stevenson et al., 2017; Giacobbo & Mapelli, 2018). As explained in Section 1.4, these phenomenon can lead to a tight binary system which, if the stars are massive enough, can later evolve into a compact binary and merge to give rise to the observed GW signals.

3. Chemically homogeneous evolution in very close tidally locked binaries:

   If a single star is rotating rapidly, then mixing due to rotation can cause even the outer layers of stars to be transported to the center and participate in nuclear burning. Because of their homogeneous structure, these stars evolve compactly on the main sequence to form a massive helium star and eventually end their lives as massive compact remnants. In close binary systems, changes in angular momentum due to the effect of tides, mass transfer, and merger processes can also induce high rotation-rates and thus chemically homogeneous evolution in stars. At the end of their lives, such stars in binary systems can develop into a tight system of a compact binary which can merge in 4–11 Gyr after formation to produce GWs (Mandel & de Mink, 2016; Marchant et al., 2016; Riley et al., 2021).

In addition to the above three channels, low-metallicity Population III stars, primordial black holes, Kozai-Lidov oscillations (Lidov, 1962; Kozai, 1962) induced through interaction in higher order stellar multiples or by the central BH in galactic nuclei on the binary system have also been proposed as sources of binary BH mergers (Inayoshi et al., 2017; Kimpson et al., 2016; Liu & Lai, 2021). Attempts to constrain fractional mix between the field and binary channels indicate that a combination of channels might be responsible for the current population of GW signals (Zevin et al., 2017, 2021).

Given that the evolution of stars in dense stellar systems is different from that in a galactic field (Heggie & Hut, 2003), it is important to explore different formation channels of compact binary mergers. This need is further amplified by the detection of the most massive binary black hole merger event to date, GW190521 (Abbott et al., 2020; Abbott et al., 2020), where the mass of the merger product, $142\,\mathrm{M}_{\odot}$, corresponds to that of an intermediate-mass BH while the masses of the component BHs, $66\,\mathrm{M}_{\odot}$ and $85\,\mathrm{M}_{\odot}$, lie in the pair-instability mass gap.

Pair instability results from the production of electron-positron pairs in the core during the late evolutionary phases of a massive star. For stars with a carbon-oxygen core mass in the range of 30–60 $\mathrm{M}_{\odot}$, it results in enhanced mass loss in the form of pulsations while for stars with a carbon-oxygen core mass in the range of 60–120 $\mathrm{M}_{\odot}$, it can lead to the total destruction of the star (Fowler & Hoyle, 1964; Fraley, 1968; Woosley, 2017), leaving behind no remnant. Thus, the occurrence of pair instability predicts an absence of BHs in a mass range of 55–130 $\mathrm{M}_{\odot}$, known as the pair-instability mass gap. However, the exact value of this gap is uncertain and depends on the uncertainties in the evolution of massive stars and physics of pair-instability supernovae (Stevenson et al., 2019; Farmer et al., 2019; Renzo et al., 2020; Mapelli et al., 2020). While such massive black holes can also form through multiple mergers in star clusters (Anagnostou et al., 2020; Dall'Amico et al., 2021; Mapelli et al., 2021; Kimball et al., 2021), formation through isolated binary evolution cannot be ruled out (Belczynski, 2020) owing to large uncertainties in massive stellar evolution (Costa et al., 2021; Farrell et al., 2021b; Vink et al., 2021).

Understanding how compact binaries form not only presents a unique opportunity to test the existing massive stellar evolution models, it also allows us to develop new theories to better understand the evolution of these stars. The knowledge acquired through GWs can be further used to constrain uncertain parameters in massive single star evolution (Stevenson et al., 2015), such as the nuclear reaction rates, (Farmer et al., 2020) and binary evolution such as the efficiency of mass transfer (Bouffanais et al., 2021) and common envelope evolution (Wong et al., 2021).

1.8 Integrating stellar evolution with population synthesis codes: an overview

The need to integrate a method of stellar evolution with binary population synthesis and stellar dynamics codes was first realized in the late nineties when space-based telescopes such as Hubble and Chandra started showing intricate details in different stellar systems. In order to explain these observations, it became important to account for the role of stellar evolution on the different stellar interactions, through dedicated stellar recipes. The high computational costs of detailed stellar evolution codes prohibited their direct use in population synthesis codes. Therefore, rapid stellar evolution codes were developed to address the problem (see e.g., Hut et al., 2003, for an overview of the topic).

These codes exploited the similarities between the stellar tracks produced by the detailed codes, and the underlying physics, to condense the tracks into a handful of fitting formulae. Instead of generating a detailed stellar track every time one could just use these fitting formulae to generate new tracks (Eggleton, 1996). The use of these fitting formulae in populations synthesis successfully explained the behaviour of many stellar systems at that time (e.g. Hurley & Shara, 2003). However, recent observations of various stellar systems, such as the phenomenon of MPs and the GWs as outlined in Section 1.6 and Section 1.7, require updating these algorithms with the latest results from stellar modelling. Moreover, uncertainties in massive stellar evolution further add the requirement of testing different models of massive stars in population synthesis codes. Ideally, the underlying stellar evolution method employed in population modelling should fulfill the following criteria:

- it should not require an intensive amount of computing resources, i.e., it should be computationally cheap;
- it should be fast and robust so as to not impede the progress of the overlying population synthesis code;
- it should be able to communicate efficiently with the overlying code;

- it should allow easy swapping of different stellar tracks, so that different models of massive stars can be tested;
- it should be able to provide information about stellar properties and structure, such as the chemical composition of the stellar surface, or the binding energy of the stellar envelope, that can be used to compare with observations.

Based on the above requirements, the existing methods of modelling stellar evolution in population synthesis codes can be evaluated as follows.

1.8.1 Detailed stellar evolution codes

One-dimensional stellar evolution codes are the current best way of modelling stellar evolution. The advent of high-performance computers and parallel programming methods has made it possible to use them directly for population synthesis purposes e.g. Church et al. (2009), BPASS (Eldridge et al., 2017), and the Astrophysical Multipurpose Software Environment (AMUSE; Portegies Zwart et al., 2009, 2013; Pelupessy et al., 2013).

The use of detailed codes provides the flexibility of using a range of input parameters in the stellar models. In terms of output, parameters related to both the structure and the evolution of the stars can be easily extracted at any time-step. Nevertheless, simulating a population of stars with a detailed code is computationally expensive. It can take a few minutes to a few hours to evolve a single star. These codes are also liable to break down at times owing to numerical difficulties and can impede the progress of population synthesis codes. Even though the models produced by the detailed codes best describe the evolution processes in the star, for testing different parameters related to population synthesis, these grids will have to be computed over and over again that can lead to a large accumulated computational cost. These computational costs are usually mitigated by using low spatial and temporal resolution in the simulations or simplifying the input physics such as using a small nuclear reaction network or a simplistic equation of state. However, physical processes such as convection and rotation become important in massive stars and require sophisticated modelling methods with higher temporal and spatial resolution, increasing the computational cost and the potential for numerical issues to develop. User intervention and expertise is often required to push detailed codes past failure points. The data from these simulations also needs to be manually checked for any non-physical results which would arise from erroneous numerical evolution of a model star. Thus, despite their obvious advantages, detailed codes are not the best method for current population synthesis requirements.

1.8.2 Defining fitting formulae for the stellar tracks

The method of using fitting formulae for stellar tracks relies on defining polynomial fits for each part of a stellar track (obtained from a detailed code) and then using those formulae to generate new tracks. The resulting codes are computationally cheap, fast and robust, and are hence well suited to the requirements of population synthesis.

The earliest attempts to achieve this were by Wielen (1968) and Chernoff & Weinberg (1990). These works employed simple schemes for stellar lifetimes and mass loss to form white dwarfs or undergo supernovae. A more accurate method was developed by Eggleton et al. (1989), where the authors devised sophisticated formulae for calculating the luminosity, radius and core mass as function of the mass and the age of the star. This work was later improved by Portegies Zwart & Verbunt (1996) and Tout et al. (1997), who also extended the formulae to include the impact of binary interactions.

Hurley et al. (2000) further expanded the work of Tout et al. (1997) to include the impact of metallicity and developed a full set of formuale, fitted to the set of stellar tracks computed by Pols et al. (1998) using an updated version of the Cambridge STARS code Eggleton (1971). The evolution formulae were incorporated into a rapid stellar evolution algorithm to form the Single Star Evolution (SSE; Hurley et al., 2000) code. Using SSE, stars in the mass range 0.1–100 $M_\odot$ and metallicity range $Z = 10^{-4}$ to 0.03 can be evolved starting from the Zero Age Main Sequence (ZAMS; Tout et al., 1996) up to and including their respective remnant phases. An extension of SSE for binary stars is given through the Binary-Star Evolution (BSE) algorithm (Hurley et al., 2002).

With the latest developments in stellar astrophysics, especially those related to massive stars, the SSE formulae are now outdated and there is a pressing need to update them. Since these fitting formulae were calculated using a particular set of tracks, they need to be redefined to use a different, more recent set of stellar tracks. This task has been undertaken by Tanikawa et al. (2019), who updated the SSE formulae for metal-poor massive stars. Even with the updated fitting formulae, this only covers a particular subset of the parameter space and the user is still limited to results from a single set of evolutionary tracks.

Determining the impact of varying input parameters to stellar evolution modelling (such as overshooting or nuclear reaction networks) on a population requires several different sets of tracks, and it is an arduous task to define a new set of formulae for each set of tracks (Church et al., 2009). Hence, there is a need for a more flexible method as an alternative.

1.8.3 Interpolating between a set of stellar tracks

Interpolation is the method of estimating an intermediate value of a quantity that is known only at a discrete set of points and can be used to estimate the properties of a star using that of neighbouring mass stars with similar properties (Schaller et al., 1992). It employs grids of tabulated data, generated from the output of detailed stellar evolution codes for a discrete set of tracks.

In this method, the stellar parameters interpolated from a given set of detailed tracks are calculated in real time. Therefore, codes produced using this method are not only fast, accurate and robust but can also make use of different stellar evolutionary grids, evolved with different parameters. To achieve this, one simply needs to change the input stellar tracks to generate a new set of stellar parameters. This method can also be used over a much wider variety of stellar parameters beyond the usual quantities (e.g., the total mass of the star, luminosity, temperature and radius) with hardly any additional effort.

To ensure the accuracy of the output, the grid of stellar models used should be dense enough, thus requiring a certain amount of computer memory ($\sim$GigaBytes) for storing and loading tracks. Thus, despite a being a popular choice for constructing stellar isochrones (e.g. Schaller et al., 1992; Bergbusch & VandenBerg, 2001), memory requirements made it difficult to use interpolation in population synthesis codes involving stellar interactions in the past.

With modern computing facilities with gigantic data storage capabilities, this approach is becoming more popular due to its increased feasibility. In the past few years, codes exploiting the method of interpolation such as SEVN (Spera et al., 2015; Spera & Mapelli,

2017) and ComBinE (Kruckow et al., 2018) have been developed to study the formation channels of GW progenitors. These codes are offering new insights into the impact of changing physical inputs on GW formations channels, by using a range of stellar models calculated with detailed codes as input.

However, uncertainties in stellar evolution are not limited to physical inputs and the numerical techniques employed by different stellar evolution codes can also have a non-negligible impact in determining the evolutionary pathway of a star. Thus it is equally important to quantify the effect of numerical uncertainties in modelling the evolutionary pathways of different stars and compare the tracks computed with different codes.

1.9 Thesis outline

The goal of this thesis is to shed light on the role of massive stars in modifying the behaviour of stellar populations, and to determine if they can help in explaining some otherwise perplexing recent observations.

To achieve this, we have developed a new code for modelling stellar evolution in population synthesis codes: METhod of Interpolation for Single Star Evolution or METISSE uses interpolation to rapidly compute stellar evolution parameters and can easily switch between using input stellar tracks evolved using different physical inputs, and even with different stellar evolution codes. It has been designed to serve as an alternative to the commonly used SSE fitting formulae in population synthesis codes and can be easily incorporated in any code which uses SSE as its single star evolution mechanism.

The work in this thesis can be categorised in two major parts. The first part (comprised of Chapters 2 and 3) examines the differences in the predictions from several different sets of massive star models. The second part (Chapter 4 and 5) describes the capabilities of METISSE in the context of single and binary stellar evolution, and evaluates its usefulness by utilising a few different sets of stellar models.

In Chapter 2, we explore five commonly used sets of models of massive stars, computed with different 1D stellar evolution codes, with an aim of finding a reliable set of models to use in METISSE. We compare the models in terms of their physical inputs as well as the numerical techniques that were used in computing them.

In Chapter 3, we investigate numerical issues in the modelling of massive stars related to the proximity of their extremely luminous envelopes to the Eddington-limit. We perform a systematic study of the solutions employed by different stellar evolution codes to facilitate the evolution of stellar models beyond these issues and the impact they can have in predicting the evolutionary pathways of massive stars.

Chapter 4 describes the methodology of METISSE and its capabilities as a standalone single stellar evolution code. We also use METISSE to demonstrate that uncertainties in modelling the evolution of massive stars, such as their radiation dominated envelopes, can impact their evolutionary outcome, including remnant masses and maximal radial expansion. These differences in the predictions of different stellar models can have important implications in accounting for the recent observations of the stellar populations.

In Chapter 5, we update METISSE to include the impact of additional mass changes and compare the results to those obtained with SSE fitting formulae using the same set input data. We also test the validity of the mass-loss implementation in METISSE using detailed models computed with MESA. Finally, we present preliminary results from integrating METISSE with the binary population synthesis code, BSE. We show how variations in the predictions of stellar parameters such as the radius of the star can affect mass transfer in binary systems, and thus can have a major impact on predictions for the populations of compact binaries that will go on to merge and be observed in gravitational waves.

The final Chapter 6, concludes the work while highlighting the importance of this thesis and the science that METISSE will enable in the future.

2

Examining the differences in massive star models from various simulations

All models are wrong, but some are useful.

—George Box

2.1 Introduction

Stellar evolutionary model sequences serve as input for a broad range of astrophysical applications; from star-formation (e.g. Gatto et al., 2017) to galaxy evolution (e.g. Weinberger et al., 2020), from cluster dynamics (e.g. Heggie & Hut, 2003) to gravitational-wave studies (e.g. Vigna-Gómez et al., 2018). These sequences provide an easy and powerful way to account for both individual stars (e.g. Schneider et al., 2014) and stellar populations (e.g. Brott et al., 2011b) in a given astrophysical environment.

One dimensional (1D) model sequences (from now on: *stellar models*) can be computed from first principles (Kippenhahn & Weigert, 1990) and have become a household tool in astrophysical research. But when it comes to stars more massive than $\sim 9\,\mathrm{M}_{\odot}$ – those that, despite being rare, provide the bulk of the radiation, chemical pollution and the most exotic death throes in the Universe (Woosley et al., 2002) – stellar models are still riddled with large uncertainties.

High-mass stars are born less often than their low-mass counterparts (Salpeter, 1955) and have comparatively shorter lives (Crowther, 2012). Consequently, observational constraints on their evolution are more difficult to obtain. The situation is further complicated by many massive stars being observed to be fast rotators (Ramírez-Agudelo et al., 2013), which breaks down perfect symmetry, and to have a close-by companion star (Sana et al., 2012), breaking the assumption of perfect isolation. Even for isolated, non-rotating single stars, the physical conditions both inside (Heger et al., 2000) and around (Lamers & Cassinelli, 1999) the star are so peculiar and complex that developing appropriate numerical simulations becomes highly challenging. This is why the evolution of massive stars remains an actively studied field to this day.

Much progress has been made in the last few decades concerning massive stars and their evolution. Mass loss in the form of high-velocity winds from massive stars is being intensively studied and accounted for in the models (Smith, 2014; Sander & Vink, 2020). Observations of massive stars from the Large and Small Magellanic Clouds are being used to constrain the efficiency of interior mixing processes (Brott et al., 2011a; Schootemeijer et al., 2019a). 1D stellar models have also been updated to account for the effects of rotation (Maeder, 2009; Costa et al., 2019) and magnetic fields (Maeder & Meynet, 2005; Takahashi & Langer, 2021) which can significantly change their evolutionary paths (Walder et al., 2012; Petit et al., 2017; Groh et al., 2020).

Despite the progress, there are still many open questions surrounding the lives of massive ($\gtrsim 9\,\mathrm{M}_\odot$) and 'very' massive (here designated as $\gtrsim 40\,\mathrm{M}_\odot$) stars, and in the absence of well-defined answers, stellar evolution codes make use of different assumptions. Earlier studies comparing models of massive stars from different codes (e.g. Martins & Palacios, 2013; Jones et al., 2015) have already established that the differences in the physical parameters such as mixing and mass-loss rates adopted by various stellar evolution codes can affect the evolutionary outcome of these stars.

Here we highlight another major uncertainty arising due to the numerical treatment of low-density envelopes of very massive stars. These stars have luminosity close to the Eddington-limit and changes in the elemental opacities during their evolution can lead to the formation of density and pressure inversions in the stellar envelope (Langer, 1997). The presence of these density inversions can cause numerical instabilities for 1D stellar evolution codes. To deal with these instabilities, the codes use different pragmatic solutions whose interplay with mixing and mass loss can further vary the evolution of massive stars.

The role of the Eddington limit and the associated density inversions in massive stars is well known within the stellar evolution community but remains relatively unknown outside the field. With the surge in the use of massive star models, for example, in gravitational-wave event rate predictions and supernova studies, it has become important to be aware of this issue. Our goal is to present the broader community with a concise overview, including how it affects the evolutionary properties such as the radial expansion and the remnant mass of very massive stars. To this end, we compare models of massive and very massive stars from five published sets created with different evolutionary codes: *(i)* models from the PAdova and TRieste Stellar Evolution Code (PARSEC; Bressan et al., 2012; Chen et al., 2015); *(ii)* the MESA Isochrones and Stellar Tracks (MIST; Choi et al., 2016) from the Modules for Experiments in Stellar Astrophysics (MESA; Paxton et al., 2011); *(iii)* models (Ekström et al., 2012) from the Geneva code (Eggenberger et al., 2008); *(iv)* models from the Binary Population and Spectral Synthesis (BPASS; Eldridge et al., 2017) project; and *(v)* the Bonn Optimized Stellar Tracks (BoOST; Szécsi et al., 2020) from the 'Bonn' Code.

We describe the major physical ingredients used in computing each set of models in Section 2.2 and Section 2.3. In Section 2.4, we compare the predictions from each set of models in the Hertzsprung-Russell diagram, as well as the predictions for the maximum radial expansion of stars, and their remnant masses. Finally we draw conclusions in Section 2.5.

2.2 Physical inputs

2.2.1 Chemical composition

The chemical composition of the Sun is often used as a yardstick in computing the metal content of other stars. However, the exact value remains inconclusive and has undergone several revisions since 2004 (see Basu, 2009; Asplund et al., 2021, for an overview). Therefore, different stellar models often make use of different abundance scales.

The BPASS, PARSEC, Geneva and MIST models base their chemical compositions on the Sun, while the BoOST models use a mixture tailored to the sample of massive stars from the FLAMES survey (Evans et al., 2005) with $Z_{Gal} = 0.0088$. For stellar winds and opacity calculations, BoOST models use $Z = 0.017$ from Grevesse et al. (1996) as the reference solar metallicity. The BPASS models use solar abundances from Grevesse & Noels (1993) with $Z_{\odot} = 0.02$. The PARSEC models follow Grevesse & Sauval (1998) with revisions from Caffau et al. (2011) and $Z_{\odot} = 0.01524$. Geneva models use Asplund et al. (2005) abundances with Ne abundance from Cunha et al. (2006) and $Z_{\odot} = 0.014$ while, finally, the MIST models base their abundance on Asplund et al. (2009a) with $Z_{\odot} = 0.01428$.

For the purpose of comparison here, we use $Z = 0.014$ models for each set except for BoOST where we use the Galactic composition, $Z = 0.0088$ as the closest match. Iron is an important contributor to metallicity, as numerous iron transition lines dominate both opacity and mass-loss rates, therefore directly affecting the structure of massive stars (e.g., Puls et al., 2000). The stellar models compared here have similar iron content, with the normalised number density ($A_{\rm Fe} = \log(\rm N_{Fe}/N_H) + 12.0$) ranging from 7.40 (for BoOST models) to 7.54 (for MIST models).

2.2.2 Mass-loss rates

Stellar mass is a key determinant of a star's life and evolutionary outcome. It can, however, change as stars lose their outer layers in the form of stellar winds, and through interactions with a binary companion. Consequently, mass loss can affect not only the structure and chemical composition of the star, but is also important in determining its final state (Renzo et al., 2017).

For massive stars, the effects of mass loss are even more pronounced. The mass loss experienced by hot massive stars (O type stars and Wolf–Rayet stars) is known to be line-driven (Lamers & Cassinelli, 1999) while that of cool massive stars (red supergiants, Levesque, 2017) is suggested to be dust-driven. Both types of mass loss are an intensively studied subject. However, the complexity of the problem of atomic and molecular transitions in the wind together with the rarity of stars at these high masses means that the model assumptions are usually based either on a few observations (a small sample of stars) or on what we know about the wind properties of low-mass stars.

All models in this study follow Vink et al. (2000, 2001) for hot wind-driven mass-loss. The PARSEC, Geneva, BPASS and MIST models follow de Jager et al. (1988) for cool dust-driven mass-loss and Nugis & Lamers (2000) for mass loss in the naked helium star phase. The Geneva models further switch to Crowther (2000) for hydrogen-rich stars with $\log T_{\rm eff}/{\rm K} \leq 3.7$. The BoOST models follow Nieuwenhuijzen & de Jager (1990) for cool winds and Hamann et al. (1995, reduced by a factor of 10) for stars with surface helium mass fraction > 0.7. For computing mass-loss rates of stars with surface helium mass fraction between 0.4 and 0.7, BoOST models linearly interpolate between the mass-loss rates of Vink et al. (2001) and Hamann et al. (1995, reduced by a factor of 10).

To account for the dependence of the mass-loss rates on the chemical composition, BoOST, MIST and BPASS models scale the mass-loss rates by a factor of $Z^{0.85}$ (Vink et al., 2001) [1]. Geneva and PARSEC models also use additional mass-loss as described in Section 2.3.

2.2.3 Convection and overshooting

Internal mixing processes such as convection and overshooting play an important role in determining both the structure and evolution of massive stars (e.g., see Sukhbold & Woosley, 2014). Similar to mass loss, these processes represent another major source of uncertainty in massive stellar evolution (Schootemeijer et al., 2019a; Kaiser et al., 2020). In 1D stellar evolution codes convection is modelled using the Mixing-Length Theory (Böhm-Vitense, 1958, MLT) in terms of the mixing length parameter $\alpha_{\rm MLT}$. However, 3D simulations suggest that convection in massive stars might be more sophisticated and turbulent than described by MLT (Jiang et al., 2015).

The BoOST, Geneva, PARSEC and BPASS models used here follow standard MLT (Cox & Giuli, 1968) for convective mixing with mixing length parameter $\alpha_{\rm MLT} = (1.5, 1.6, 1.74, 2.0)$ respectively. MIST follows a modified version of MLT given by Henyey et al. (1965) with $\alpha_{\rm MLT} = 1.82$. Convective boundaries in PARSEC, Geneva and BPASS models are determined using the Schwarzschild criterion (Schwarzschild, 1958). BoOST and MIST use the Ledoux criterion (Ledoux, 1947) for determining convective boundaries with semiconvective mixing parameters of 1.0 and 0.1, respectively. For determining convective core overshoot, Geneva and BoOST use step overshooting with overshoot parame-

[1] Note that for some models the factor $Z^{0.69}$ is quoted, depending on whether the dependence of the terminal velocity on Z is explicitly considered or not.

ter $\alpha_{ov} = (0.1, 0.335)$. MIST uses exponential overshooting following Herwig (2000) with $\alpha_{ov} = 0.016$. PARSEC uses overshoot from Bressan et al. (1981) with $\alpha_{ov} = 0.5$. BPASS uses the overshoot prescription from Pols et al. (1998) with $\alpha_{ov} = 0.12$. For comparison, the rough equivalent in the step overshooting formalism would be 0.2, 0.25 and 0.4 for the MIST, PARSEC and BPASS models respectively (See Choi et al., 2016; Pols et al., 1998; Bressan et al., 2012, for details of each method).

MIST and PARSEC also include small amounts of overshoot associated with convective regions in the envelope. However, apart from modifying surface abundances, envelope overshoot has a negligible effect on the evolution of the star (Bressan et al., 2012). Rotational mixing also plays an important role in the evolution of massive stars, however, for simplicity we only compare non-rotating models for PARSEC, MIST, Geneva and BPASS. For BoOST, although we do use slowly rotating ($100\,\mathrm{km\,s^{-1}}$) models, this small difference in the initial rotation rate is again not relevant from the point of view of the overall evolutionary behaviour (Brott et al., 2011a).

Major input parameters used in each set of models are summarized in Table 2.1.

Table 2.1 Summary of input parameters used in the computation of the models of massive stars from different codes. See Section 2.2 for details.

Stellar Model	$\mathbf{Z_\odot}$	**Hot Wind**	**Cool Wind**	**Wolf-Rayet Wind**	**Convective boundary**	$\alpha_{\rm MLT}$	**Overshoot type**	$\alpha_{\rm ovs}$	$\alpha_{\rm semi}$
BPASS	0.020	Vink et al. (2000, 2001)	de Jager et al. (1988)	Nugis & Lamers (2000)	Schwarzschild (1958)	2.0	Pols et al. (1998)	0.12[e]	–
BOOST	0.008[a]	Vink et al. (2000, 2001)	Nieuwenhuijzen & de Jager (1990)	Hamann et al. (1995)[b]	Ledoux (1947)	1.5	step	0.335	1.0
GENEVA	0.014	Vink et al. (2000, 2001)	de Jager et al. (1988)[c]	Nugis & Lamers (2000)	Schwarzschild (1958)	1.6[d]	step	0.1	–
MIST	0.014	Vink et al. (2000, 2001)	de Jager et al. (1988)	Nugis & Lamers (2000)	Ledoux (1947)	1.82	Herwig (2000)	0.016[e]	0.1
PARSEC	0.015	Vink et al. (2000, 2001)	de Jager et al. (1988)	Nugis & Lamers (2000)	Schwarzschild (1958)	1.74	Bressan et al. (1981)	0.5[e]	–

Notes. [a] For calculating mass-loss rates and opacities, $Z_\odot = 0.017$ is used.
[b] Reduced by a factor of 10.
[c] For $\log T_{\rm eff}/K \leq 3.7$, mass-loss rates from Crowther (2000) are used.
[d] For stars with initial mass $\geq 40\,M_\odot$, $\alpha_{\rm MLT} = 1.0$ is used but with a different scale height (see Section 2.3).
[e] The rough equivalent in the step overshooting formalism is 0.2, 0.25 and 0.4 for the MIST, PARSEC and BPASS models respectively.

2.3 Eddington luminosity and the numerical treatment of density inversions

The Eddington luminosity is the maximum luminosity that can be transported by radiation while maintaining hydrostatic equilibrium (Eddington, 1926). In the low-density envelopes of massive stars changes in the elemental opacities during the evolution of stars can cause the local radiative luminosity to exceed the Eddington luminosity (Langer, 1997; Sanyal et al., 2015). To maintain hydrostatic equilibrium, density and pressure inversion regions form in the stellar envelope. In the absence of efficient convection (which is also typical for the low-density envelopes, Grassitelli et al. 2016), this can lead to convergence problems for 1D stellar evolution codes (Paxton et al., 2013). Owing to numerical difficulties, the time-steps become exceedingly small, preventing further evolution of the star. While less massive stars are only affected by this process in their late evolutionary phases (Harpaz, 1984; Lau et al., 2012), very massive stars can exceed the Eddington-limit already during the core-hydrogen-burning phase (Gräfener et al., 2012; Sanyal et al., 2015) and inhibit computation of their evolution. Therefore, 1D stellar evolution codes have to employ various solutions to compute further evolution of very massive stars.

In PARSEC models, density inversions and the consequent numerical difficulties are avoided by limiting the temperature gradient such that the density gradient never becomes negative (see Sec. 2.4 of Chen et al., 2015; Alongi et al., 1993). Limiting the temperature gradient prevents inefficient convection and the evolution of the stars proceeds uninterrupted. Also, the models include a mass-loss enhancement following Vink (2011) whenever the total luminosity of the star approaches the Eddington-luminosity.

MIST models suppress density inversions through the MLT++ formalism (Paxton et al., 2013) of MESA. In this method, the actual temperature gradient is artificially reduced to make it closer to the adiabatic temperature gradient whenever radiative luminosity exceeds the Eddington luminosity above a pre-defined threshold. This approach again increases convective efficiency, helping stars to overcome density inversions. Additionally, radiative pressure at the surface of the star is also enhanced in the MIST models to help with convergence (Choi et al., 2016).

In the extended envelopes of massive stars, the density scale height is much larger compared to the pressure scale height (which is typically used for computing the mixing length). Therefore, setting the mixing length to be comparable with the density scale height helps avoid density inversion (Nishida & Schindler, 1967; Maeder, 1987). The Geneva models include this treatment when computing models with initial masses greater than $40\,\mathrm{M}_\odot$ with $\alpha_{\mathrm{MLT}} = 1.0$ (see Sec. 2.3 of Ekström et al., 2012). Additionally, the mass-loss rates for the models are increased by a factor of three whenever the local luminosity in any of the layers of the envelope is higher than five times the local Eddington luminosity.

BoOST models do not include any artificial treatment to prevent massive stars from encountering density inversions. Instead, their models undergo envelope inflation when massive stars reach the Eddington limit (Sanyal et al., 2015). On encountering the density inversions in their envelopes, the computation of very massive stars becomes numerically difficult. Further evolution of such stars is then computed through post-processing. It involves removing layers from the surface of the star (which would anyway happen due to regular mass loss) while correcting for surface properties such as effective temperature and luminosity (Szécsi et al., 2020).

BPASS models also allow density inversions to develop in the envelope of massive stars. However, these models are able to continue the evolution without numerical difficulties, most likely due to the use of a non-Lagrangian mesh (see Stancliffe, 2006, for an overview) and the resolution factors being lower than in other models (J.J. Eldridge, private communication, also see Eggleton, 1973).

2.4 Comparing the models

2.4.1 Differences between models in the Hertzsprung–Russell diagram

The evolution of stars can be easily represented through tracks on the Hertzsprung-Russell (HR) diagram, depicting the evolutionary paths followed by a series of stars. Figure 2.1 presents the HR diagram of stars of various initial masses from the five simulation approaches. The observational analogue to the Eddington-limit is the Humphreys–Davidson limit or HD-limit (Humphreys & Davidson, 1979). Since the luminosity of a star depends on its mass, more massive stars also are more luminous. This means they can easily exceed the Eddington-limit, develop density inversions and require the use of numerical solutions

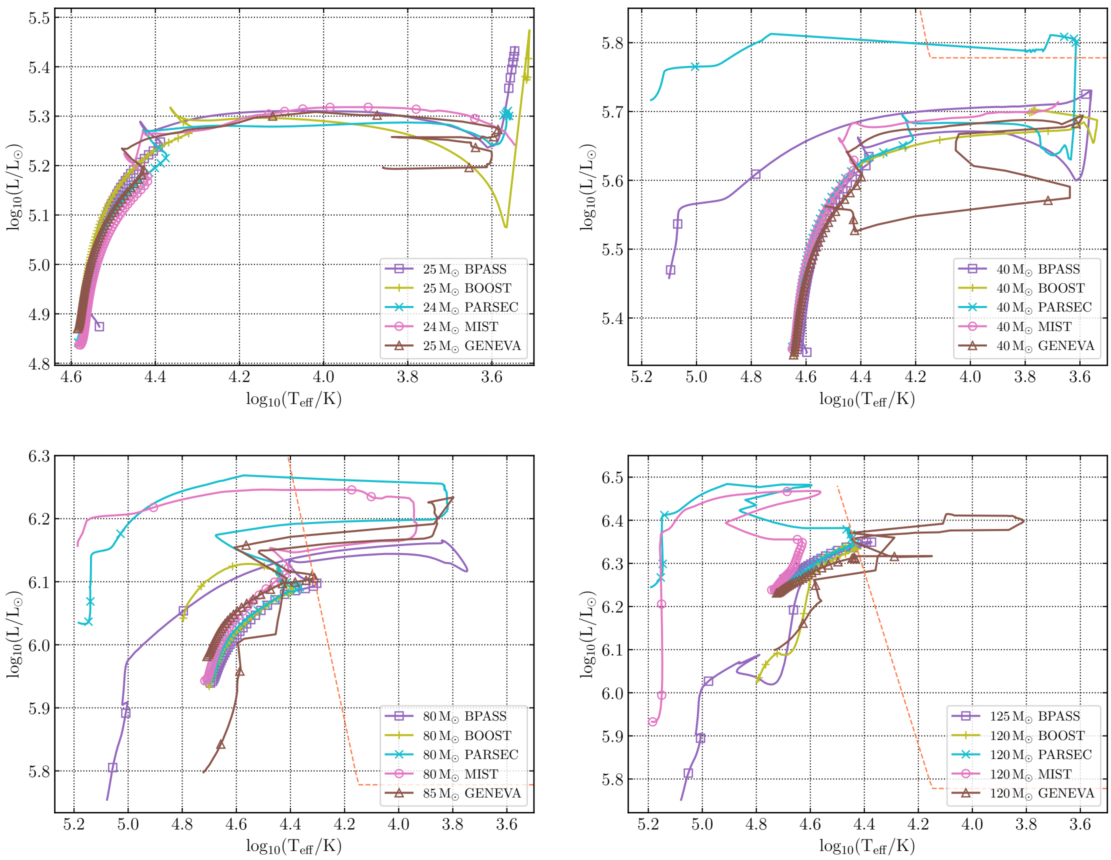

Figure 2.1 Hertzsprung–Russell diagrams of the massive single star models analysed in this work. All models have near solar composition. Symbols mark every 10^5 years of evolution. Only the core-hydrogen- and core-helium-burning phases are plotted. The dashed red line marks the observational Humphreys–Davidson limit (Humphreys & Davidson, 1979) where relevant. The tracks become more varied with increasing initial mass. This is because the codes apply various treatments for the numerical instabilities associated with the Eddington-limit proximity, cf. Section 2.3.

as discussed in Section 2.3.

From Figure 2.1 we see that the tracks of the $25\,M_\odot$ (or $24\,M_\odot$ in some cases) stars agree well during most of the evolution. This is because stars of this mass do not exceed the Eddington limit and are thus not affected by the related numerical treatments. The minor differences in their tracks are due to the difference in physical inputs (Section 2.2) between the simulations. For example, the differences in the position of the main-sequence (MS) hook feature in the HR diagram arise due to the varied extent of convective overshoot used in each set of models.

A $40\,M_\odot$ star is clearly affected by the numerical treatment employed during the post-main sequence phase of its evolution, as evidenced by the difference in the tracks in the HR diagram shown in Figure 2.1. More massive stars, i.e, those with initial masses $80/85\,M_\odot$ and $120/125\ M_\odot$, can exceed the Eddington-limit in their envelopes while on the MS and therefore their simulations differ significantly from each other. At these masses, the mass-loss rates can be as high as $10^{-3} - 10^{-4}\,M_\odot\,yr^{-1}$, completely dominating over every other physical ingredient in determining the evolutionary path. While all tracks have been computed with similar prescriptions for wind mass loss (cf. Section 2.2), the actual rates can be strongly modified by the numerical methods adopted by each code in response to numerical instabilities (Section 2.3), resulting in vast differences in the tracks.

2.4.2 Predictions of maximum stellar radii

The radial expansion of a star plays a significant role in determining the nature of binary interaction as it can lead to episodes of mass transfer in close interacting binaries. Recent studies indicate that most of the massive stars occur in binaries (Sana et al., 2012; Moe & Di Stefano, 2017). Therefore, predictions of stellar radii become even more important for determining the binary properties of massive stars.

Figure 2.2 shows the maximum radial expansion achieved by massive stars from each simulation. For stars with initial mass up to $30\,M_\odot$, all simulations predict the formation of a red supergiant. The maximum difference in the radius predictions here is $\lesssim 1000\,R_\odot$. For higher initial masses, the predictions for maximum stellar radii become more divergent as proximity to the Eddington-limit increases and numerical treatments adopted by each code modify the mass-loss rates.

The greatest difference in the maximum radius predictions ($\gtrsim 1000\,R_\odot$) occurs for stars with initial masses between 40 and $100\,M_\odot$. Above $\sim 100\,M_\odot$, stars have even higher mass-loss rates which can completely strip a star of its envelope before it can become a red-supergiant. Such stars evolve directly towards the naked helium star phase and have much smaller radii. Therefore, for stars with initial masses more than $100\,M_\odot$, the difference between the maximum radius predictions by each simulation reduces to $\lesssim 100\,R_\odot$. The predictions in this mass range seem to further converge into two groups: PARSEC and MIST represent one group predicting smaller radii compared to the second group which consists of BoOST and BPASS models. Since the maximum initial mass of a star in the Geneva set is 120 $M_\odot$, we cannot comment on the behaviour of their models outside of this range.

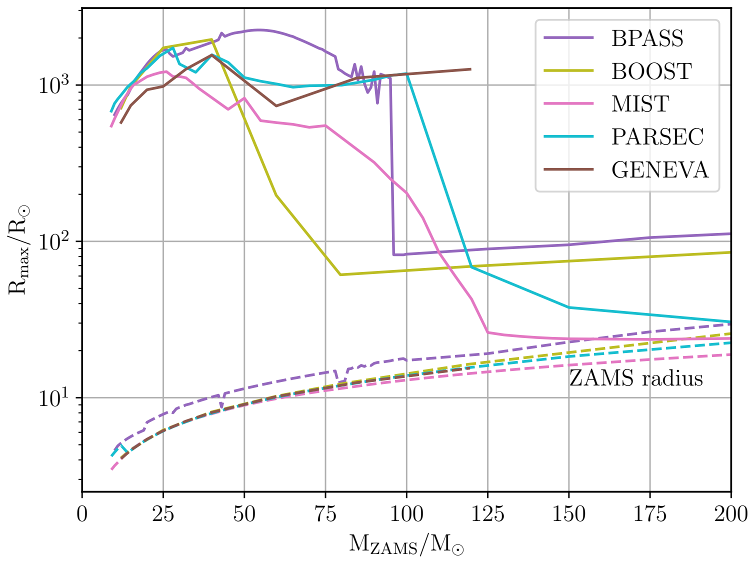

Figure 2.2 Maximum stellar radii as a function of the initial mass of the star. Similar to Figure 2.1, differences in the physical inputs and the numerical methods adopted by each code can lead to a difference of more than 1 000 $R_\odot$ in predictions in terms of the maximum radial expansion achieved by the stars.

2.4.3 Remnant mass predictions

Stellar evolutionary models provide an easy way of estimating the properties of stellar remnants such as black holes and neutron stars, which are needed in many fields including supernova studies (e.g. Aguilera-Dena et al., 2018; Raithel et al., 2018), gamma-ray bursts progenitors (e.g. Yoon et al., 2006; Szecsi, 2017), and gravitational-wave event rate predictions (e.g. Stevenson et al., 2019; Mapelli et al., 2020).

Following Belczynski et al. (2010) we show in Figure 2.3 how the uncertainties in the models we compare here also pose a challenge for the predictions of remnant properties. Remnant masses have been calculated from the carbon-oxygen core mass and the total mass of the star at the end of the core helium-burning phase using the prescription of Belczynski et al. (2008) (same as the StarTrack prescription in Fryer et al., 2012).

The remnant masses are heavily influenced by the modelling assumptions (cf. Section 2.2) and the numerical methods (cf. Section 2.3) especially above $M_{ini} = 40\,M_\odot$ where the most massive black holes are predicted. We find that the mass of the black holes predicted by the different sets of models can differ by $\sim 20\,M_\odot$. The maximum black hole mass varies from about $20\,M_\odot$ for BPASS models to about $38\,M_\odot$ for MIST and PARSEC models and $35\,M_\odot$ for the BoOST models. Since all the models we study have near-solar metallicity and therefore rather high mass-loss rates, none of them stays massive enough at the end of their lives to undergo pair-instability.

Similar variability is found in the core mass and the final total mass of the star (from which the remnant masses have been calculated). BPASS models consistently predict the lowest values of final core mass and the total mass for most of the massive stars while BoOST predictions are the highest. MIST and PARSEC models predict values in between. The Geneva models do not provide information on core masses, hence we omit them from the analysis of the core mass and the remnant mass. However, we do show their predictions for the final total mass which, for stars up to $100\,M_\odot$, are similar to the predictions of BPASS models.

Similar to the predictions of maximum stellar radii in Figure 2.2, the predictions of final masses for stars with initial mass $\gtrsim 100\,M_\odot$ separate into two groups, although the groups are slightly different this time, BPASS and MIST represent one group predicting smaller final masses compared to the second group consisting of BoOST and PARSEC models.

2.5 Conclusions

We compare 1D evolutionary models of massive and very massive stars from five independent simulations. Focusing on near-solar composition, we find that the predictions from different codes can differ from each other by more than $1000\,R_\odot$ in terms of maximum radial expansion achieved by the stars and about $20\,M_\odot$ in terms of the stellar remnant mass. The differences in the evolution of massive stars can arise due to physical inputs like chemical abundances, mass-loss rates, and internal mixing properties. However, very massive stars, that is stars with initial masses $40\,M_\odot$ or more, show a larger difference in

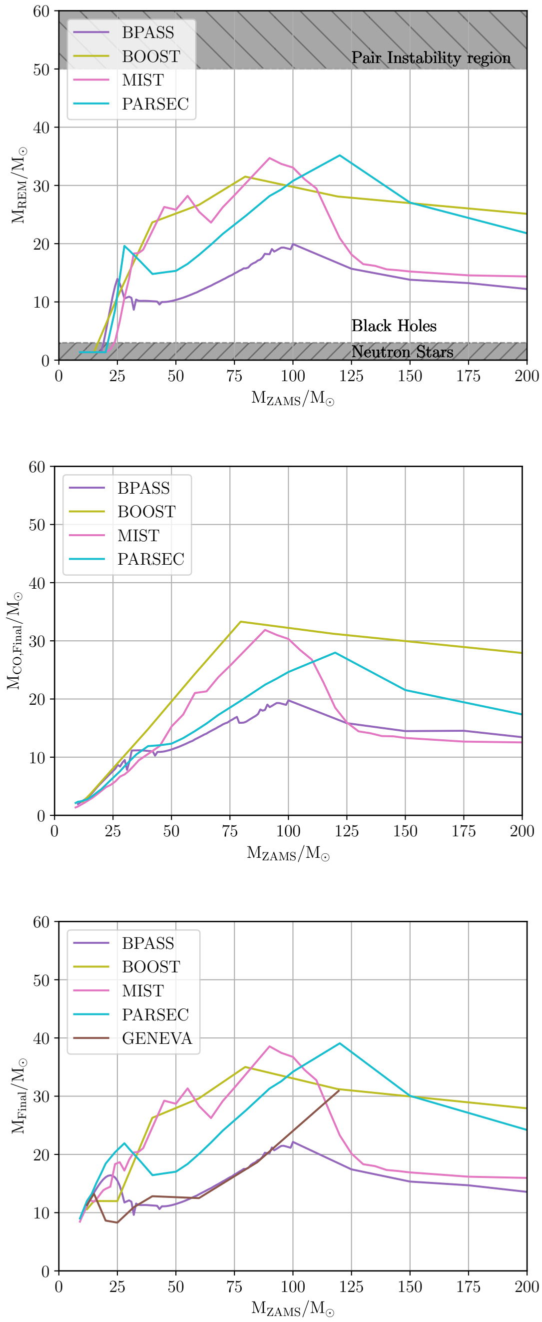

Figure 2.3 Final masses of stars as a function of their initial mass, M_{ZAMS}. The top panel shows the mass of stellar remnants as predicted by the BPASS, BoOST, MIST and PARSEC models. The middle panel shows the carbon-oxygen core mass and the bottom panel shows the total mass of the star at the end of the core helium-burning phase, as used in the calculation of the remnant masses. Differences in the evolutionary parameters for massive stars can cause variations of about $20\,M_{\odot}$ in the remnant masses between the stellar models from various simulations.

evolutionary properties compared to lower mass stars. For these stars, the differences in the evolution can be largely attributed to the numerical treatment of the models when the Eddington-limit is exceeded in their low-density envelopes.

The different methods used by 1D codes to compute the evolution of massive stars beyond density inversions (or to avoid the inversions) can modify the radius and temperature of the star, and can therefore affect the mass-loss rates. A phenomenological justification for the mass loss enhancement comes from the fact that there are stars observed with extremely high, episodical mass loss, i.e. luminous blue variables (Bestenlehner et al., 2014; Sarkisyan et al., 2020). However, other studies, such as the recent measurement of a approximately $20\,M_{\odot}$ black hole in the Galactic black hole high-mass X-ray binary Cyg X-1 (Miller-Jones et al., 2021), suggest that the mass-loss rates for massive stars at near-solar metallicity may be lower than usually assumed in the 1D stellar models (Neijssel et al., 2021). The exact nature of wind mass loss for very massive stars remains disputed (Smith & Tombleson, 2015). Moreover, variation in remnants masses in Figure 2.3 shows other uncertainties in massive star evolution can lead to differences at least as large as variations in mass-loss rates, which could also easily explain the formation of a $20\,M_{\odot}$ black hole in Cyg X-1 in the Galaxy.

None of the solutions that the BoOST, Geneva, MIST and PARSEC models employ can currently be established as better than the others. In each case they have been designed to address numerical issues in 1D stellar evolution. However, the interplay of these solutions with mass-loss rates and convection further adds to the uncertainties in massive stellar evolution. Therefore, a systematic study to untangle the effect of the treatment of the Eddington-limit from other physical assumptions will be conducted in the near future (Chapter 3).

In the case of BPASS the stellar models evolve without requiring any numerical enhancement. Whether this is a result of using a non-Lagrangian mesh (the 'Eggletonian' mesh, which is more adaptive to changes in stellar structure) or if this is an artifact of bigger time steps (that helps stars skip problematic short-lived phases of evolution) is currently not known. A separate study to explore the effect of the 'Lagrangian' versus the 'Eggletonian' mesh structure for massive stars (similar to Stancliffe et al. 2004 study for low and intermediate mass stars) is highly desirable.

In conclusion, it is crucial to be aware of the uncertainties resulting from numerical methods whenever the evolutionary model sequences of massive stars are applied in any scientific project, such as gravitational-wave event rate predictions or star-formation and feedback studies.

We only focus on massive stars as isolated single stars in this work. However, there is mounting evidence that massive stars are formed as binaries or triples, thus treating them as single stars might not be correct (e.g. Klencki et al., 2020; Laplace et al., 2021). Several studies have shown that binarity can heavily influence the lives of massive stars through mass and angular momentum transfer (de Mink et al., 2009a; Marchant et al., 2016) and can therefore help in avoiding density and pressure inversion regions in stellar envelopes (Shenar et al., 2020).

We also limit our study to massive stars at near-solar metallicity, where due to high opacity, the numerical instabilities related to the proximity to the Eddington-limit are maximum. Since opacity decreases with metallicity, opacity peaks become less prominent at lower metallicity. Nevertheless, stars with low-metal content also reach the Eddington-limit, although at higher initial masses (Sanyal et al., 2015, 2017). While progenitors of currently detectable gravitational-wave (GW) sources may have been born in the early Universe where the metal content is sub-solar (cf. Santoliquido et al., 2021), high star-formation rates at near solar metallicities offer a fertile ground for the formation of more GW sources, although less massive compared to sub-solar metallicity (Neijssel et al., 2019). As such, there is good motivation for studying the behaviour and reliability of massive star models across a wide range of metallicities. We explore the effect of the Eddington-limit at sub-solar metallicities in Chapter 3 and Chapter 5.

Collecting observational data as well as improvements in 3D and hydrodynamical modelling will help us better constrain the models of massive stars in the future. Until then, however, we urge the broader community to treat any set of stellar models with caution. Ideally, one would implement all available simulations as input into any given astrophysical study, and test the outcome also in terms of stellar evolution related uncertainties. With tools such as METISSE (Agrawal et al., 2020) and SEVN (Spera et al., 2019), this task is becoming feasible.

Data Availability

All the stellar models used in this work are publicly available: PARSEC, MIST, Geneva BPASS, BoOST.

Acknowledgements

DSz has been supported by the Alexander von Humboldt Foundation. PA acknowledges the support from the Australian Research Council Centre of Excellence for Gravitational Wave Discovery (OzGrav). We also thank Stefanie Walch-Gassner, Debashis Sanyal, Ross Church and Jan Eldridge for useful comments and discussions.

3

A systematic study of super-Eddington envelopes in massive stars

Stars must have a luminosity inferior to the Eddington limit, otherwise "... the radiation observed to be emitted ...would blow up the star"

—Eddington (1926)

3.1 Introduction

Stars more massive than about $9\,\mathrm{M}_\odot$ are key to several astrophysical processes. During their lives, they enrich their surroundings with ionising flux and nuclear processed material while altering the dynamics of their host systems. At the end of their lives, these massive stars again expel copious amount of radiation and metal-rich matter in the form of supernovae, leaving behind compact remnants: neutron stars and black holes. Furthermore, mergers of these compact remnants result in gravitational wave (Abbott et al., 2016, 2017b) emission and can also lead to the formation of rare elements (Kasen et al., 2017). Therefore, a better understanding of how these stars evolve is crucial in comprehending their contribution to the evolution of star clusters and galaxies.

The evolution of massive stars is typically modelled using one-dimensional (1D) stellar evolution codes. In the last few decades, these stellar evolution codes have progressed a lot and so has our understanding of massive stars. Together with the advances in our observing capabilities (Evans et al., 2011; Simón-Díaz et al., 2015; Wade et al., 2014;

Abbott et al., 2016), the development of sophisticated numerical methods for simulating physical processes and newer input data in the form of opacity tables and nuclear reaction rates has led to the development of modern and improved stellar structure and evolution codes (Langer, 2012; Ekström et al., 2020).

Even with these new capabilities, 1D modeling of massive stars is limited by a number of approximations. Several evolutionary properties of massive stars such as the mass-loss rates (Smith, 2014; Renzo et al., 2017), nuclear reaction rates (Heger et al., 2002; Fields et al., 2018) and rotation (Heger et al., 2000; Maeder, 2009) remain uncertain. The high mass of these stars makes it feasible for sophisticated physical process to operate in these stars but their short lives makes it difficult to obtain observational constraints.

One such process is the treatment of convective transport of energy through the Mixing Length Theory (MLT; Böhm-Vitense, 1958). In this theory, energy is transported through fluid elements supported by buoyancy forces. These elements travel over a radial distance known as the mixing length after which they dissolve in their surroundings. MLT assumes hydrostatic equilibrium in stars, meaning no acceleration of particles and depends only on local conditions (i.e., local values of pressure, density etc.), without taking into account other parts of the star. Time-dependency and non-local treatments are included through ad-hoc methods such as convective overshoot, semiconvection and diffusion (e.g., Renzini, 1987; Kippenhahn et al., 2012).

The simplicity of MLT makes it a popular choice for many stellar evolution codes. However, in the low-density envelopes of massive stars, convection as given by MLT is inefficient. Changes in the elemental opacity as the star evolves can cause the radiative luminosity to exceed the Eddington-luminosity and lead to the formation of density and gas pressure inversions in the sub-surface layers. The presence of density inversions has been attributed as the source of several instabilities such as the dynamical instability (Stothers & Chin, 1993), the convective instability (Langer, 1997), and the strange-mode instability (Saio et al., 1998, 2013) in massive stars. Observationally, these have been linked to stellar variability phenomena such as stochastic low-frequency photometric variability (Pedersen et al., 2019; Bowman, 2020), spectroscopic macroturbulence (Simón-Díaz & Herrero, 2014; Simón-Díaz et al., 2017) and episodic mass ejection behaviour in luminous blue variables (LBVs: Bestenlehner et al., 2014; Gräfener, 2021).

From a numerical perspective, the presence of density inversions in the inflated envelopes of supergiant stars requires 1D stellar evolution codes to take prohibitively short time-steps (of the order of hours and minutes) leading to convergence issues (Maeder, 1987; Alongi et al., 1993; Paxton et al., 2013). Evolving stars past these numerical difficulties in the supergiant phase has been a long standing challenge for the 1D stellar evolution approach. As shown in Chapter 2, stellar evolution codes often resort to numerous pragmatic methods to evolve stars such as enhancing the convective efficiency (e.g. Ekström et al., 2012) or limiting temperature gradients such that the density gradient is always positive (e.g. Chen et al., 2015). While these methods help evolve stars through numerically difficult phases of evolution, they can also modify their surface behaviour, such as the radius evolution and mass-loss rates.

The different methods used by 1D codes and their interplay with other physical parameters of massive stars can alter the dynamics of stellar evolution, thereby adding a potential bias to any study aiming to determine the properties of these input parameters from the evolution of a star. While other uncertainties in the evolution of massive stars have received considerable attention in a number of studies, the role of density inversions has not been explored to the same extent.

In Chapter 2, the comparison of stellar models from five different codes revealed large differences in the evolutionary behavior of stars more massive than $40\,\mathrm{M}_\odot$ around solar metallicity (at $Z = 0.014$). The maximum radial expansion predicted by different stellar models varied by more than $1000\,\mathrm{R}_\odot$ and the predictions of remnant mass varied by $20\,\mathrm{M}_\odot$. However, the stellar models also had different physical inputs beside the treatment of density inversions arising due to the Eddington luminosity, making it difficult to untangle the impact of this process from other inputs. There is therefore a need for a systematic study of the impact of these methods within a single code and single set of assumptions.

In this work, we perform a study of the impact of density inversions on the evolution of massive stars up to $110\,\mathrm{M}_\odot$ using consistent input parameters. Since Chapter 2 focused only on solar metallicity stars, we choose a metallicity ten times lower than solar here to demonstrate the impact of density inversions at a metallicity relevant to the progenitors of current gravitational wave observations (e.g. Stevenson et al., 2017). As we show here, the different methods used by 1D codes can have a non-negligible impact on the evolutionary properties of massive stars. These differences are important, as they can help us explain the formation of gravitational wave progenitors and other observations of stellar populations.

The paper is organised as follows. We provide an overview of the physics related to density inversions in Section 3.2. In Section 3.3, we describe our standard or default set of models with MESA and discuss the effect of density inversions on their completeness. We recompute the models that fail to reach the end of evolution, using three different numerical methods in Section 3.4 and compare the impact of these methods in predicting the different evolutionary properties of massive stars in Section 3.5. In Section 3.6, we compare the stellar models from Section 3.4 with the observations of massive stars and conclude our study in Section 3.7.

3.2 Physics of density inversions in massive stars

In this section, we describe the conditions for the formation of density and gas pressure inversions in stellar envelopes and their impact on modelling the evolution of massive stars.

For a spherically symmetric star containing mass $m(r)$ inside radius r and with radiative opacity $\kappa(r)$ and density $\rho(r)$, the luminosity that can be carried by radiative transport of energy is given by

$$L_{\rm rad}(r) = -\frac{4\pi r^2 c}{\rho(r)\kappa(r)}\frac{dP_{\rm rad}}{dr}\,, \tag{3.1}$$

where $P_{\rm rad}$ denotes the radiation pressure and c is the speed of light.

The Eddington luminosity gives the maximum value of luminosity that can be transported by radiation while maintaining hydrostatic equilibrium (Eddington, 1926). The expression for the Eddington luminosity is given by

$$L_{\rm Edd}(r) = \frac{4\pi c G m(r)}{\kappa(r)}\,, \tag{3.2}$$

where G represents the gravitational constant. The total pressure P in the star is the sum of the radiation pressure, $P_{\rm rad}$ and the gas pressure $P_{\rm gas}$. Using equations 3.1 and 3.2 and the equation of hydrostatic equilibrium $dP/dr = -Gm(r)\kappa(r)/r^2$, the ratio of radiative luminosity to the Eddington luminosity can be defined as

$$\frac{L_{\mathrm{rad}}}{L_{\mathrm{Edd}}} = \frac{dP_{\mathrm{rad}}}{dP} = \left[1 + \frac{dP_{\mathrm{gas}}}{dP_{\mathrm{rad}}}\right]. \tag{3.3}$$

Normally, the luminosity transported by radiation (L_{rad}) is less than the Eddington-luminosity (L_{Edd}) inside a star, and the density and gas pressure of stellar material decrease with the stellar radius ($d\rho/dr < 0, dP_{\mathrm{gas}}/dr < 0$). However, during the evolution of the star, changes in the elemental ionisation states can lead to an increase in the opacity $\kappa(r)$. In the low density ($\rho \ll 1\,\mathrm{g\,cm^{-3}}$) radiation pressure dominated ($P_{\mathrm{rad}}/P \approx 1$) envelopes of massive stars, an increase in opacity can reduce the Eddington luminosity below the radiative luminosity ($\frac{L_{\mathrm{rad}}}{L_{\mathrm{Edd}}} > 1$). Since dP_{rad}/dr is always less than 0, when $\frac{L_{\mathrm{rad}}}{L_{\mathrm{Edd}}} > 1$ Equation 3.3 implies $dP_{\mathrm{gas}}/dr > 0$ i.e., a gas pressure inversion.

From the ideal gas equation of state, P_{gas} can be expressed as a function of ρ and P_{rad}. Using Equation 3.3, the condition for density inversion ($d\rho/dr > 0$) can therefore be written as

$$\frac{L_{\mathrm{rad}}}{L_{\mathrm{Edd}}} > \left[1 + \left(\frac{\partial P_{\mathrm{gas}}}{\partial P_{\mathrm{rad}}}\right)_{\rho}\right]^{-1} \tag{3.4}$$

(Joss et al., 1973; Paxton et al., 2013).

The effect of density inversions on the evolution of massive stars is complex and remains an active field of research (Mihalas, 1969; Érgma, 1971; Langer, 1997; Owocki et al., 2004; Cantiello et al., 2009; Sanyal et al., 2015). Gräfener et al. (2012) found that an increase in the radiative luminosity near the opacity peak due to the iron-group elements (at $\sim 2 \times 10^5$ K) leads to the formation of an 'inflated envelope' containing density inversions (also see Ishii et al., 1999; Petrovic et al., 2006). In this state, the star has an extended radiative envelope with a relatively small convective core. As pointed out by Sanyal et al. (2015), these inflated stars are different to classical red supergiants, as envelope inflation does not require hydrogen shell burning and can even occur while the star is on the main sequence.

For hydrogen-rich stars, the formation of the inflated envelope reduces the opacity and therefore the radiative luminosity, driving down $L_{\mathrm{rad}}/L_{\mathrm{Edd}}$. However, as the envelope expands, its outer layers become sufficiently cool to encounter opacity bumps due to helium ionization (at $\sim 2 \times 10^4$ K) and hydrogen recombination (at $\sim 10^4$ K) and further expansion no longer reduces $L_{\mathrm{rad}}/L_{\mathrm{Edd}}$.

The presence of density inversions in the inflated envelopes makes it difficult to match solutions of stellar structure equations in the envelope (Maeder, 1987, 1992). The combination of low gas pressure and the high entropy at the base of the inflated envelope leads to numerical difficulties if time-steps are large (Paxton et al., 2013). To avoid these difficulties, stellar evolution codes are forced to adopt exceedingly small time-steps and struggle to complete the evolution of these stars.

3.3 Stellar Models: the standard set

Module for Experiments in Stellar Astrophysics (MESA: Paxton et al., 2011, 2013, 2015, 2018, 2019) is an advanced one dimensional stellar structure and evolution code. MESA solves the coupled differential equations of stellar structure simultaneously with the energy transport equation for all mass cells from the surface to the center. In this work, we make use of version 11701 of MESA.

Convection is treated as a diffusive process with convective boundaries determined by the Ledoux criterion. To account for convection due to varying opacity in layers, we use the Henyey et al. (1965) treatment of MLT with mixing length parameter, $\alpha_{\mathrm{MLT}} = 1.82$. Semiconvection is implemented using Langer et al. (1985) with $\alpha_{\mathrm{semiconvection}} = 1.0$ while a small amount of Thermohaline mixing is used ($\alpha_{\mathrm{th}} = 2.0$) following Kippenhahn et al. (1980). For convective overshooting we follow the calibration adopted by Brott et al. (2011a): step overshoot with f = 0.335 and f0 = 0.05. We only apply overshooting in the core and not in the convective envelope.

Mass loss is modelled using the commonly used MESA 'Dutch' scheme (Glebbeek et al., 2009) with the mass loss scaling factor, $\eta_{\mathrm{Dutch}} = 1.0$. The scheme follows Vink et al. (2000, 2001) for hot winds, de Jager et al. (1988) for cool winds and Nugis & Lamers (2000) for Wolf-Rayet winds.

Opacities are calculated using OPAL (Iglesias & Rogers, 1993, 1996) Type I and Type II (at the end of hydrogen burning) using Asplund et al. (2009b) photospheric abundances. Electron screening is included for both the weak and strong regimes using the 'extended' option in MESA, which computes the screening factors by extending the classic Graboske et al. (1973) method with that of Alastuey & Jancovici (1978), and adopting plasma parameters from Itoh et al. (1979) for strong screening. Boundary conditions at the surface of the star are calculated using the `'Eddington_grey'` option of MESA, which uses the Eddington T-tau integration (Eddington, 1926) to obtain temperature and pressure in the outer layer of the stars.

Nuclear reaction networks can have a non-trivial effect on the evolution of massive stars (Farmer et al., 2016), especially the inclusion of elements like iron and nickel (Nabi et al., 2019). Hence, we make use of an extensive grid of isotopes for the nuclear reaction network in our models to closely follow the evolution of massive stars. The network has been chosen to match globular cluster observations and has 72 elements, including Mg, Li and Fe. The reaction rates are determined using the Jina Reaclib database (Cyburt et al., 2010).

We use high spatial resolution with `mesh_delta_coeff` $= 0.5$ and the maximum relative cell size `max_dq` $= 5 \times 10^{-4}$. Model to model structure variation is kept modest with `varcontrol` between 7×10^{-4} and 10^{-3}, and additional constraints are used to limit time steps where necessary.

We compute the evolution of stars in the mass range of 10–110 $\mathrm{M}_{\odot}$ at metallcity, $Z = 0.00142$ ([Fe/H] = -1). All stars start from the pre-main-sequence (PMS) with uniform composition and the goal is to evolve each model until the point of carbon depletion in the core ($X_c \leq 10^{-2}$). Following Choi et al. (2016), we adopt solar scaled abundances from Asplund et al. (2009b), with Solar metallicity $Z_{\odot} = Z_{\odot,\mathrm{protosolar}} = 0.0142$. The primordial helium abundance Y_p is taken to be 0.249 while the protosolar helium abundance $Y_{\odot,\mathrm{protosolar}} = 0.2703$. Initial hydrogen (X) and helium abundances (Y) for PMS models are calculated using the following formula

$$Y = Y_p + \left(\frac{Y_{\odot,\mathrm{protosolar}} - Y_{\mathrm{p}}}{Z_{\odot,\mathrm{protosolar}}} \right) Z, \tag{3.5}$$

$$X = 1 - Y - Z.$$

Models are evolved without mass loss from the PMS until the zero-age main sequence (ZAMS), defined as when the central hydrogen abundance reduces by 1 percent of the initial value. Evolution is then restarted (including mass loss) using the stellar model saved at ZAMS, and continues until either the termination condition is reached ($X_c \leq 10^{-2}$) or the end of 96 CPU-hrs (running parallel on 4 cores for 24 hrs).

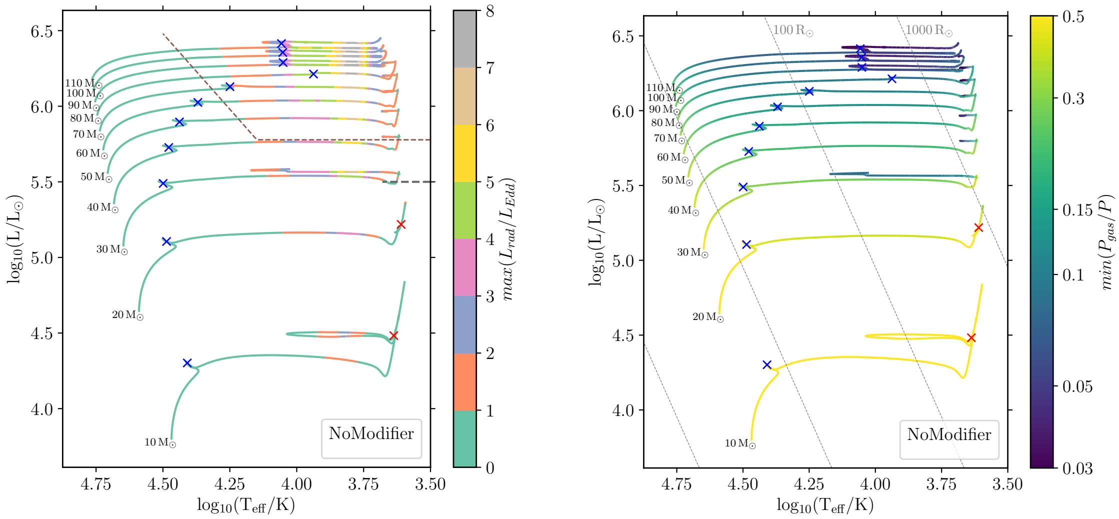

Figure 3.1 Hertzsprung-Russell (HR) diagram showing stellar models from the standard set coloured by the maximum of $L_{\rm rad}/L_{\rm Edd}$ (left panel) and the minimum of $P_{\rm gas}/P_{\rm total}$ (right panel). The blue cross marks the end of core hydrogen burning and the red cross marks the end of core helium burning (where applicable). The brown dashed line in the left panel denotes the position of the observational Humphreys & Davidson (1979) limit beyond which few stars are observed, while the grey dashed line signifies the luminosities of the brightest red supergiants as inferred by Davies et al. (2018). Density inversions in the envelopes of stars with initial masses 30 $\mathrm{M}_\odot$ and above causes the evolution of these stars to become halted at $\log\mathrm{T}_{\rm eff}/\mathrm{K} \approx 3.7$, and their models fail to finish core carbon burning.

3.3.1 Results

The set of models evolved using the physical inputs described above fail to reach the end of carbon burning in the core within the allocated time (24 hrs) for stars more massive than 20 $\mathrm{M}_\odot$. Hereafter, we refer to this set as the 'standard set' and label it as 'NoModifier' in the figures, since the models were computed without any modifications to facilitate their evolution. The results for the standard set are unaffected by the increase in temporal and spatial resolution.

Figure 3.1 presents the stellar tracks in the Hertzsprung-Russell (HR) diagram for our standard set of models. In the left panel, the tracks are coloured by the maximum of $L_{\rm rad}/L_{\rm Edd}$, while the right panel shows the minimum of $P_{\rm gas}/P_{\rm total}$ for each stellar model. We see that in these models $L_{\rm rad}$ can become close to $L_{\rm Edd}$ and even exceed it by factors of a few during the evolution as the stars encounter opacity bumps in their envelopes. These opacity bumps are due to the partial ionisation states of iron and helium, as well as the recombination of hydrogen. However, for 10 and 20 $\mathrm{M}_{\odot}$ stars, $P_{\mathrm{gas}}/P_{\mathrm{total}}$ remains high enough (>0.5) for their evolution to proceed uninterrupted (see Section 3.2).

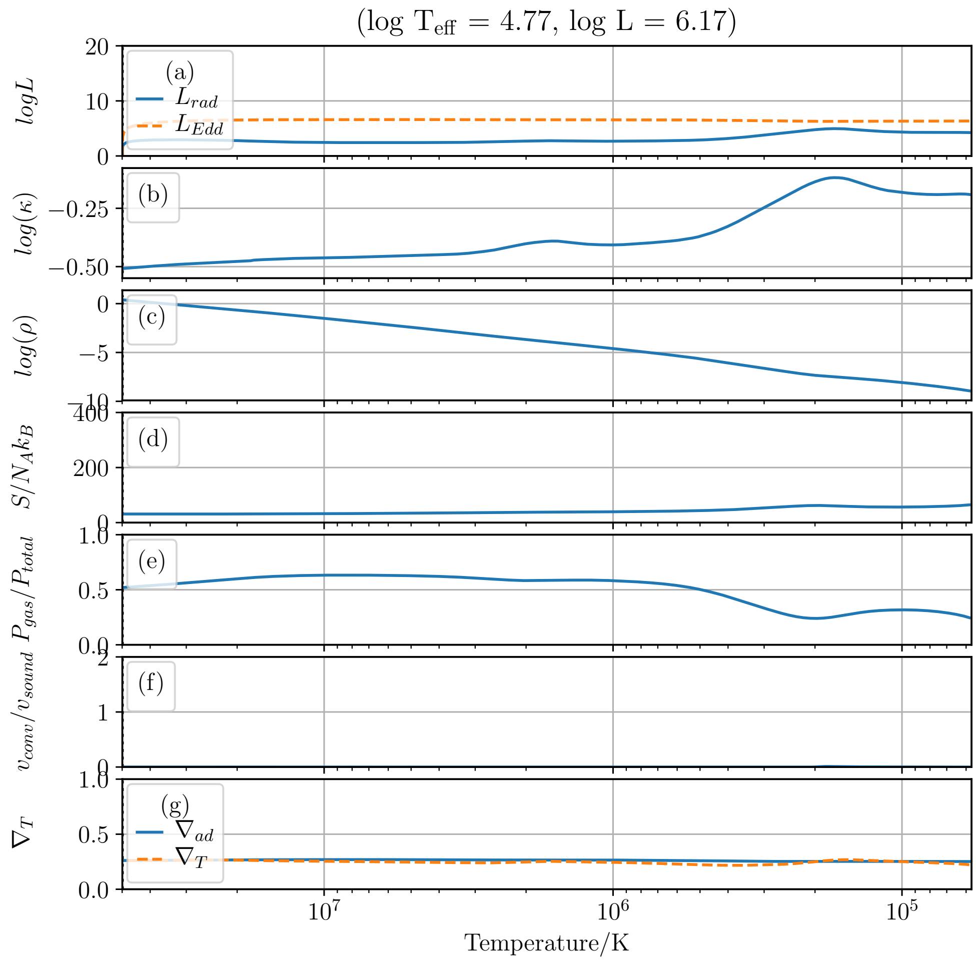

Figure 3.2 Temperature profile of a 110 $\mathrm{M}_{\odot}$ star at the ZAMS evolved using the standard set. Opacity peaks due to partial ionisation states of iron are present at 1.5×10^6 and 1.8×10^5 K. However, L_{rad} is less than L_{Edd} throughout the star and the evolution of the star proceeds smoothly. See Section 3.3.1 for details of each panel.

Models with initial masses between 30 and 110 $\mathrm{M}_{\odot}$ fail during core helium burning at similar effective temperatures, $\log\mathrm{T_{eff}}/\mathrm{K} \approx 3.7$. In these models, the stellar envelope inflates in response to the iron-opacity peak, thereby preventing density inversion. However, as the star expands and cools, the minima in gas pressure fraction at the opacity peak decreases as highlighted in the right panel of Figure 3.1. The evolution of these models progresses smoothly until stars encounter the opacity peak due to hydrogen and helium in

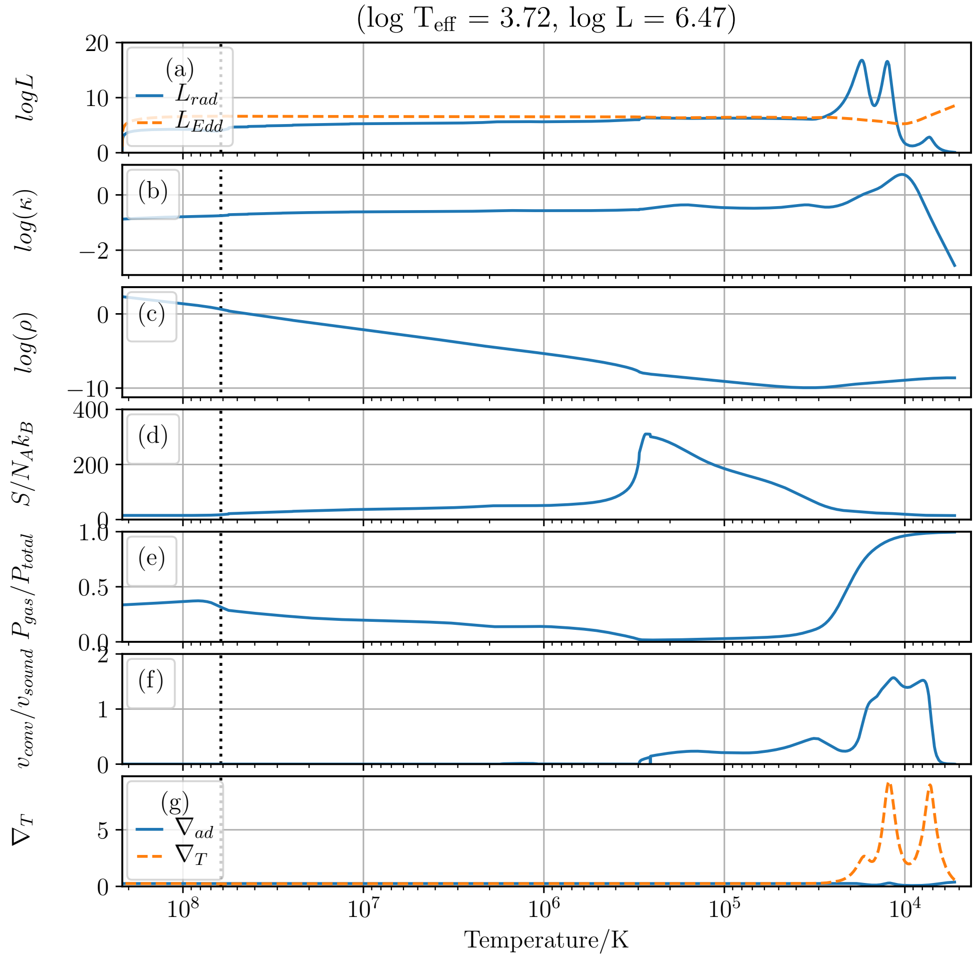

Figure 3.3 Temperature profile of a $110\,\mathrm{M}_\odot$ star at the end of the simulation, evolved using the standard set. Vertical black dotted line marks the boundary of the helium core. The high luminosity of the star combined with the peak in opacity due to hydrogen and helium ionisation around 10^4 K causes $L_{\rm rad}$ to exceed $L_{\rm Edd}$. This causes density and gas pressure inversions at 3×10^4 K. However, the low-density of the environment renders convection inefficient and the star struggles to evolve despite reaching supersonic convective velocities.

their sub-surface layers at $\log T_{\rm eff}/\mathrm{K} \approx 4.0$. The envelope inflation there is not sufficient to prevent the radiative luminosity from exceeding the Eddington luminosity, which leads to the density inversions.

To elaborate on the conditions in the stellar interior, the temperature profiles for a $110\,\mathrm{M}_\odot$ star at the ZAMS (at $\log T_{\rm eff}/\mathrm{K} = 4.77$), and at the end of the track (at $\log T_{\rm eff}/\mathrm{K} = 3.72$, corresponding to the final model reached after 24 hrs of computation), are shown in Figure 3.2 and Figure 3.3.

In panel (a) of Figure 3.2, L_{rad} shows a small increase corresponding to the opacity peaks due to partial ionisation of iron at 1.5×10^6 and 1.8×10^5 K (panel b). In response to the increase in L_{rad}, gas pressure dips a little (visible as a minimum in $P_{\mathrm{gas}}/P_{\mathrm{total}}$) in panel e), although, density consistently decreases outwards (shown in panel c). The bottom panel (g) shows the variation of the actual temperature gradient and the adiabatic temperature gradient inside the star. Their difference, $\nabla_{\mathrm{T}} - \nabla_{\mathrm{ad}}$, is known as superadiabaticity (see Section 3.4.3 for details). Al the location of the opacity peak, superadiabaticity is positive but small and the convective velocity (v_{conv}) is less than the sound velocity (v_{sound}) (panel f), signifying efficient convection. The specific entropy ($S/N_A k_B$) in panel (d) at the base of the convective region is small and the evolution of the star proceeds smoothly.

In panel (b) of Figure 3.3, in addition to the iron opacity peak, opacity peaks corresponding to partial ionisation of helium and hydrogen recombination can be seen at 3.5×10^4 and 10^4 K. In contrast to Figure 3.2, the increase in opacity due to hydrogen and helium ionisation increases L_{rad} such that it exceeds L_{Edd} by more than a factor of two, causing density and gas pressure inversion that can be seen in the other panels. However, the high value of superadiabaticity ($\nabla_{\mathrm{T}} - \nabla_{\mathrm{ad}} \approx 10$) renders convection inefficient and prone to radiative losses. The convective velocity increases to increase the amount of flux convection can carry, becoming more than the local sound speed. However, the high value of specific entropy ($S/N_A k_B \geq 300$) at the base of the convective envelope causes time-steps to be small, of the order of days.

The evolution of the star is essentially halted until it is able to get rid of the density inversion as mass loss slowly chips away the outer convective layers. However, evolving the star this way requires a lot of computational time (e.g., it takes ≈ 200 CPU-hrs for a $40\,\mathrm{M}_\odot$ star) which might not be feasible.

3.4 Stellar models: the model variations

In the absence of efficient convection, the radiation dominated envelopes of massive stars in 1D modelling are prone to numerical difficulties (Stothers & Chin, 1979; Maeder, 1987). Therefore, stellar evolution codes adopt various techniques to compute the evolution of massive stars beyond these numerically difficult points (Alongi et al., 1993; Ekström et al.,

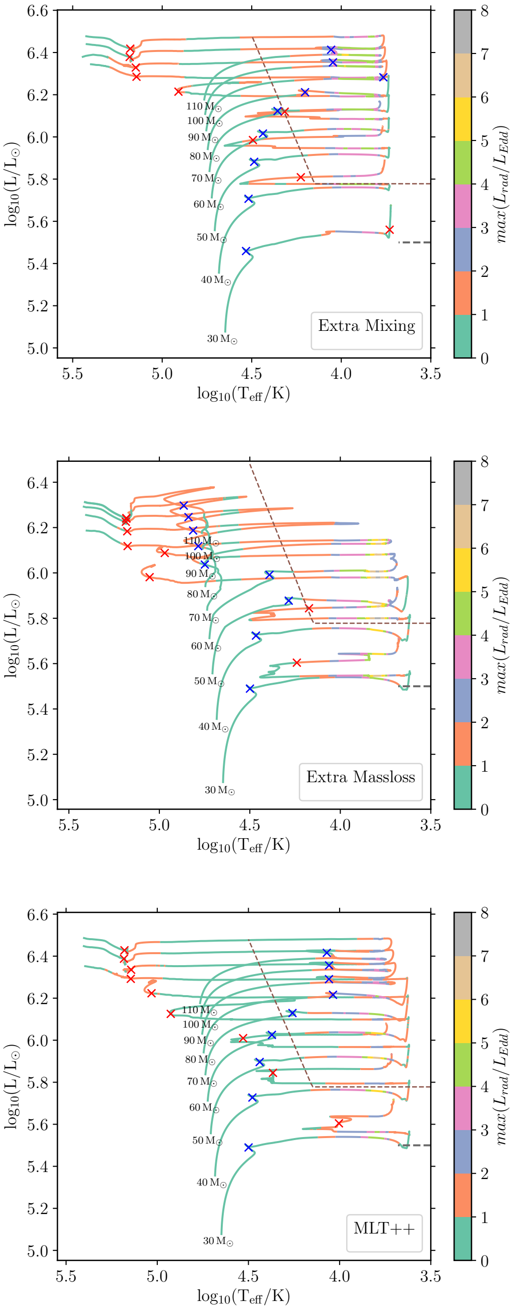

Figure 3.4 HR diagrams showing the evolutionary tracks graded with the maximum of $L_{\rm rad}/L_{\rm Edd}$ for stars in the mass range 30–110 $\rm M_{\odot}$, computed with the model variations described in Section 3.4. The top panel shows the tracks computed with enhanced mixing ($\alpha_{\rm MLT} = 5.46$), the middle panel shows tracks with enhanced mass loss ($\eta_{\rm Dutch} = 8.0$ whenever L exceeds $\rm L_{Edd}$) and the bottom panel shows tracks computed with MLT++. Similar to Figure 3.1, blue and red crosses mark the end of core hydrogen burning and core helium burning while the brown and grey dashed lines signify the Humphreys & Davidson (1979) limit and the Davies et al. (2018) limit respectively.

2012; Paxton et al., 2013). The exact technique differs from code to code, however, they can be summed up into the three main categories: using higher mixing length to increase the efficiency of the mixing process, using higher mass-loss rates to remove layers with numerical instabilities, or suppressing the numerical instability by limiting the temperature gradient and thereby suppressing density inversions. We explore each of them in details in the following subsections.

3.4.1 Enhancing internal mixing

In the convective transport of energy by MLT, the mixing length, l travelled by a fluid element before dissolving in the surroundings is given in terms of the local pressure scale height H_p and mixing length parameter $\alpha_{\rm MLT}$ such that $l = H_p \times \alpha_{\rm MLT}$. For a given H_p, a higher value of $\alpha_{\rm MLT}$ implies a higher l and therefore better convective efficiency. $\alpha_{\rm MLT}$ is a free parameter with a value that is often calibrated from the observations of the sun and eclipsing binaries. For example, in the standard set of models in this work the value of $\alpha_{\rm MLT}$ has been calculated using solar data (see Choi et al., 2016, for details). There is increasing evidence that the value of $\alpha_{\rm MLT}$ is not universal and varies with the evolutionary phase, mass and metallicity of the stars (Joyce & Chaboyer, 2018; Johnston, 2021).

While MLT gives fairly good results in the deep interiors of stars where density is high and convection is nearly adiabatic (with negligible radiative losses), its limitations start becoming apparent in low-density environments where the convection is highly superadiabatic and prone to radiative losses (Maeder, 2009). In the presence of density inversions, convective velocity becomes supersonic and convection is time-dependent. In such situations both standard and non-adiabatic theories of MLT are out of their domain of applicability.

While testing the models with a different theory of convective energy transport is beyond the scope of this work, we do test the role of increased efficiency of convection on the convergence properties of the models from the standard set that fail to reach the end of carbon burning. Beginning with $\alpha_{\rm MLT} = 1.82$ (used in the standard set), we compute a series of stellar models with $\alpha_{\rm MLT} = 3.0, 3.64, 4.0, 5.0, 5.46, 7.28, 8.0$ for stars with initial mass $30\,{\rm M}_\odot$ and above. We find that for $\alpha_{\rm MLT} \geq 5.46$, which is three times the value used in the standard set, the models are able to evolve without any numerical instabilities until carbon depletion in the core.

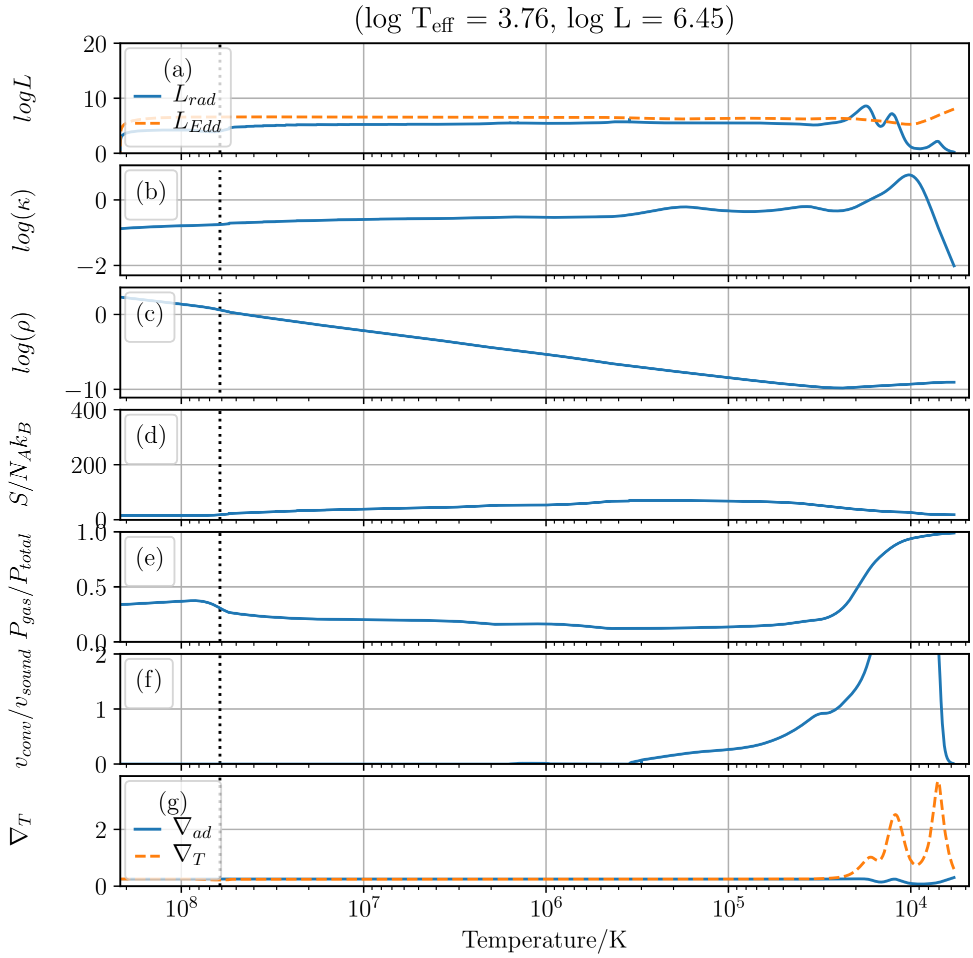

Figure 3.5 Temperature profile of a 110 $M_\odot$ star computed with the mixing length parameter, $\alpha_{\rm MLT}$ = 5.46. Similar to Figure 3.3, a density inversion can be seen in panel (c). However, higher convective velocity (panel f) and smaller superadiabaticity (panel g) resulting from the higher value of $\alpha_{\rm MLT}$ helps to keep the specific entropy small (panel d) and time-steps large enough to evolve the model without numerical instabilities.

The top panel of Figure 3.4 shows the evolutionary tracks evolved with $\alpha_{\rm MLT}$ = 5.46. From the figure we see that $L_{\rm rad}$ still exceeds $L_{\rm Edd}$ in the stellar envelope, however, this does not limit the time-steps of the computation of the stellar models. The reason for this can be understood from Figure 3.5, where we show the temperature profile of 110 $M_\odot$ star at a similar location in the HR diagram where the computation for the 110 $M_\odot$ star from the standard set became stuck. Similar to Figure 3.3, the stellar profile contains opacity peaks due to ionisation of iron, helium and hydrogen (panel b), resulting in excess $L_{\rm rad}$ (panel a) and the density and gas pressure inversions (panel c and e). However, higher convective velocities resulting from higher $\alpha_{\rm MLT}$ imply that the convective fluid element travels faster and transports more energy before it leaks out due to radiative losses. The superadiabaticity in the outer layers is also smaller compared to the standard case ($\nabla_{\rm T} - \nabla_{\rm ad} \approx 2$), meaning radiative losses are also smaller. The overall convective flux is, therefore, higher than the standard case. The specific entropy remains small ($S/N_A k_B < 100$) and time-steps large enough to efficiently compute the evolution of the star until the end of carbon burning.

Increasing convective efficiency in this way helps compute the evolution of stars until core carbon burning. However, it also changes the effective temperature of these stars and makes them appear bluer in the HR diagram (Maeder, 1987; Kippenhahn et al., 2012). Comparing the tracks with extra mixing (top panel of Figure 3.4), with the standard set (left panel of Figure 3.1), we find that stellar models with extra mixing are indeed limited to $\log{\rm T_{eff}}/{\rm K} \approx 3.73$ in the HR diagram which is greater than the minimum $\log{\rm T_{eff}}/{\rm K} \approx 3.63$ reached by models in the standard set. We discuss this further in Section 3.5.

3.4.2 Enhancing mass loss

Winds of hot massive main-sequence stars are optically thin line-driven winds. Due to their high luminosity, massive stars can generate a high number of photons which can be scattered via ions, transferring momentum with them which then accelerates material outwards that can escape the gravitational potential of the star. As the star evolves to the cool red supergiant phase, these winds transition to being dust-driven where they are generated by the interaction of photons with dust grains instead of ions. Massive stars can lose a substantial amount of mass through stellar winds, even their entire hydrogen envelope to become naked helium stars. The mass loss in naked helium stars is again driven by radiation pressure and can be higher by a factor of ten or more than their hydrogen-rich counterparts (Smith & Tombleson, 2015)

The mass-loss rates for massive stars are highly uncertain (Renzo et al., 2017) and can be affected by instabilities and processes other than described above. For example, Gräfener & Hamann (2008) and Vink (2011) have shown the contribution of optically thick (clumped) winds in the presence of sub-surface opacity bumps in massive stars. Moreover, massive stars exceeding the classical Eddington limit can also experience episodes of much stronger mass-loss rates (up to $10^{-3}\,\mathrm{M}_\odot\,\mathrm{yr}^{-1}$), known as LBV eruptions or super-Eddington winds (Lamers & Fitzpatrick, 1988; Humphreys & Davidson, 1994; Smith et al., 2004). Despite being the stronger contributor to mass-loss rates for massive stars, the exact rates and the mechanism behind the LBV eruptions remains disputed (Puls et al., 2008; Smith, 2014; Owocki, 2015) and most stellar evolution models often exclude their contributions in the mass-loss rates.

Apart from the uncertainties in the mass-loss rates of massive stars, the differential equations of stellar structure and evolution do not include stellar mass loss. In stellar evolution codes, the mass change at each time step is computed from parameterized algorithms as time-averaged mass loss, before solving the equations of stellar structure. The stellar variables are then adjusted accordingly to account for the mass change. High mass-loss rates can therefore help remove outer layers in the stellar model containing the density inversion, helping the stellar model avoid numerical instabilities (Petrovic et al., 2006; Cantiello et al., 2009).

To determine the impact of enhanced wind mass-loss on the convergence properties of models that fail to evolve in the standard set, we recomputed these models with increased wind mass-loss rates for different evolutionary phases until the models are able to evolve without numerical difficulties. We find that setting the mass loss scaling factor to $\eta_{\mathrm{Dutch}} \geq 8.0$, i.e., at least eight times the mass loss used in the standard set, whenever the stellar luminosity exceeds the Eddington luminosity, leads to smooth evolution of the stellar models with initial mass greater than or equal to $30\,\mathrm{M}_\odot$.

We also find that this mass-loss enhancement is only required for stars with a hydrogen-rich envelope ($\mathrm{X}_{\mathrm{surf}} \geq 0.4$). Although naked helium stars can also exceed the Eddington-limit and can develop density inversions in their envelopes, their evolution proceeds uninterrupted for our models without any numerical instabilities.

The models with extra mass loss as described above, with $\eta_{\mathrm{Dutch}} = 8.0$, are shown in the middle panel of Figure 3.4. A $110\,\mathrm{M}_\odot$ star with extra mass loss is able to evolve to the end of carbon burning, while the maximum of $L_{\mathrm{rad}}/L_{\mathrm{Edd}}$ remains close to unity

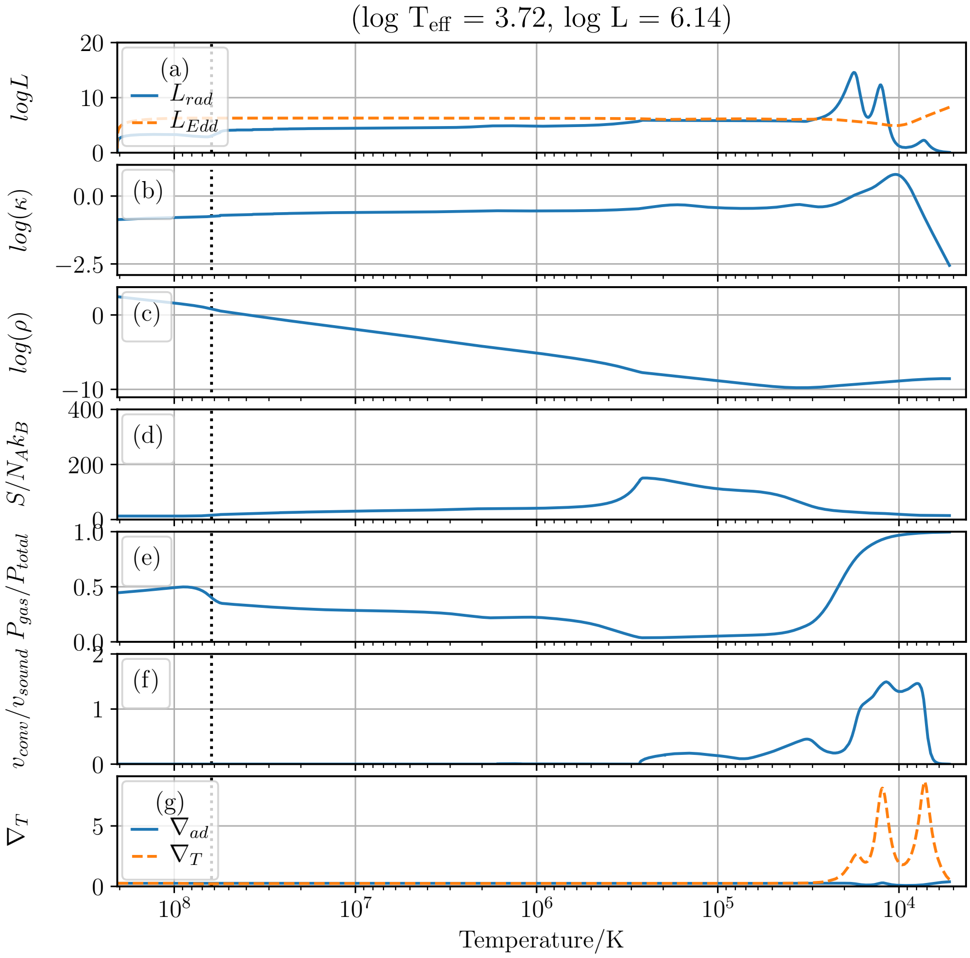

Figure 3.6 Temperature profile of a $70\,\mathrm{M}_{\odot}$ star computed with extra mass loss, as described in Section 3.4.2. Opacity-peaks due to the ionisation states of hydrogen, helium and iron and associated density inversions can be seen in panel (b) and panel (c) respectively. However, high mass-loss rates remove the layers containing the density inversion, moderating the specific entropy at the base of the convective envelope and the model is able to evolve until completion with reasonably large time-steps.

throughout the evolution. However, for models less massive than $70\,\mathrm{M}_{\odot}$, the maximum of $L_{\mathrm{rad}}/L_{\mathrm{Edd}}$ can be up to 8, similar to models in the standard set. These values of $L_{\mathrm{rad}}/L_{\mathrm{Edd}}$ do lead to the formation of density inversions, as shown in the temperature profile of the $70\,\mathrm{M}_{\odot}$ star in Figure 3.6, but enhanced mass-loss rates ($\sim 10^{-4}\,\mathrm{M}_{\odot}\,\mathrm{yr}^{-1}$ at this point) help remove the outer layers containing density inversions before specific entropy at the base of the envelope becomes large or time-steps become too small. Thus, all models are able to evolve smoothly to completion without any numerical instability.

Extra mass loss helps compute the evolution of massive stars all the way through to carbon depletion in their core. However, it also influences the structure and evolutionary properties of the stars as explained in Section 3.5.

3.4.3 Suppressing density inversions

According to the MLT, convection sets in when the temperature gradient of the surrounding material is greater than the gradient interior to the moving element: $\nabla_{\rm T} > \nabla_{\rm element}$. For convection to transport the maximum possible energy, the element should move adiabatically, i.e. without dissipating energy in the surroundings or $\nabla_{\rm T} \sim \nabla_{\rm ad}$.

The difference between $\nabla_{\rm T}$ and $\nabla_{\rm ad}$ is termed the superadiabaticity and is a measure of the efficiency of convection (Maeder, 2009; Kippenhahn et al., 2012). For efficient convection, superadiabaticity is positive but close to 0. It means that the element loses hardly any energy as it traverses the mixing length. However, a higher value of superadiabaticity ($\gtrsim 10^{-2}$) implies that the element suffers energy-losses as it travels, and by the time it reaches the end of the mixing length it is left with hardly any energy, thereby, rendering the convective transport of energy quite inefficient.

In the envelopes of massive stars superadiabaticity is the order of unity and the convective transport of energy given by MLT is inefficient, providing fertile ground for density inversions to form and be sustained. Some authors even consider density inversions to be non-physical, possibly an artifact of the MLT and 1D stellar evolution (Ekström et al., 2012) while others consider the possible presence of some unknown mixing mechanism that helps stars get rid of density inversions in nature (Paxton et al., 2013). Either way, since these density inversions are associated with numerical instabilities in the models of massive stars, many stellar evolution codes suppress them either by limiting $\nabla_{\rm T}$ or by reducing $\nabla_{\rm T}$ to make it closer to $\nabla_{\rm ad}$. This reduces the superadiabaticity, thereby making convection efficient and helping stellar models overcome numerical instabilities.

MESA uses the latter approach of reducing $\nabla_{\rm T}$ in the stellar envelope through a method known as MLT++. In this method, whenever the superadiabaticity exceeds a predefined threshold `gradT_excess_f1`, MESA decreases $\nabla_{\rm T}$ to make it closer to $\nabla_{\rm ad}$. The amount of decrease is given by the combination of the parameter `gradT_excess_f2` which can be defined by the user, and the parameter `gradT_excess_alpha` which is calculated based on the the maximum of $L_{\rm rad}/L_{\rm Edd}$ and the minimum of $P_{\rm gas}/P_{\rm total}$ (see Appendix C for details). In general, a smaller `gradT_excess_f2` implies a larger reduction in the superadiabaticity and more efficient convective transport of energy.

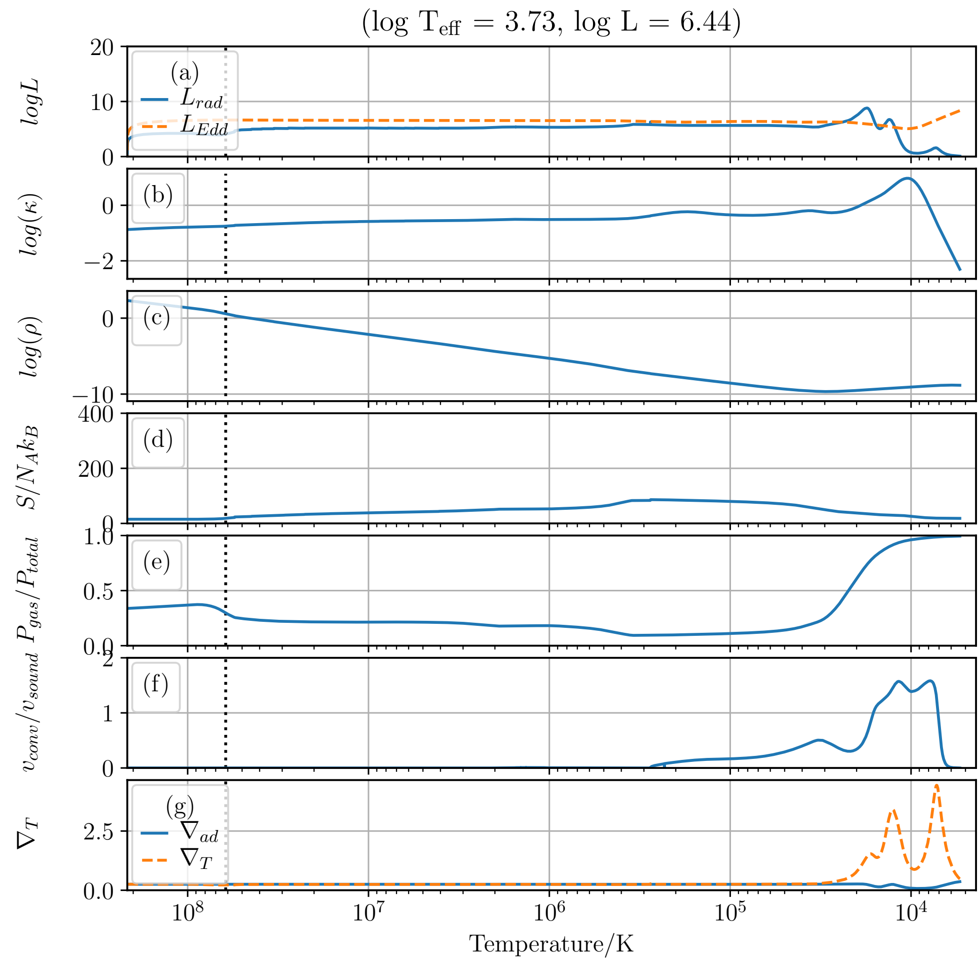

Figure 3.7 Temperature profile of a $110\,\mathrm{M}_\odot$ star computed with the MLT++ method of MESA. The method artificially reduces the difference between $\nabla_{\rm T}$ and $\nabla_{\rm ad}$ in the stellar envelope, acting as an source of additional envelope mixing (see Section 3.4.3 for details). The small envelope mixing used here is not enough to suppress density inversions completely (panel c) but it does help to keep the specific entropy small (panel d), and therefore time steps reasonable.

We find that using the default values of the MLT++ parameters completely suppresses density inversions but it also gives unrealistic values of luminosity for the most massive stars in our set. Therefore, we test the models in the standard set with different combinations of parameters in MLT++, as described in Appendix C. Compared to the default values of the MLT++ parameters, we find that using a smaller value of gradT_excess_f2=10^{-1}, therefore a smaller reduction in the superadiabaticity but occurring more frequently inside the star (with $\lambda_1 = 0.6$ and $\beta_1 = 0.05$) is sufficient for the smooth evolution of the models without any numerical instabilities or inaccuracies.

The stellar models evolved using MLT++ are shown in the bottom panel of Figure 3.4. The evolutionary paths of models computed with MLT++ are quite similar to models evolved with extra mixing. Although, unlike the models with extra mixing, models with MLT++ are not limited to $\log T_{\rm eff}/K \approx 3.73$ and evolve to lower effective temperatures. The temperature profile of a $110\,M_\odot$ star evolved with MLT++ (Figure 3.7) again shows a similar behaviour compared to the temperature profile of the $110\,M_\odot$ star evolved with extra mixing (Figure 3.5), at similar logL and $\log T_{\rm eff}$. However, MLT++ artificially reduces ∇_T, such that the superadiabaticity and the specific entropy at the base of the convective envelope remain small despite having smaller convective velocity compared to the $110\,M_\odot$ model with extra mixing.

3.5 Implications

Each of the three methods described in Section 3.4 help compute the evolution of massive stellar models in the standard set until the end of carbon burning. However, in the process they also modify the evolutionary pathway of the stars and impact their evolutionary outcome. In this section, we compare the set of stellar models obtained with the minimum numerical enhancement from each method and determine the impact of these methods on the structure and evolution of the massive stellar models.

3.5.1 Structure of the star

Figure 3.8 shows the Kippenhahn plot of a $110\,M_\odot$ star—depicting regions within the star by mass as a function of time in the period leading up to the end of the run—for each of the models computed with the numerical fixes described in Section 3.4. The evolution of the $110\,M_\odot$ model evolved using MLT++ is similar to the model with extra mixing but quite different to the evolution of the model computed with extra mass loss.

All three models start with a $90\,M_\odot$ convective core, (shown by the green hatching)

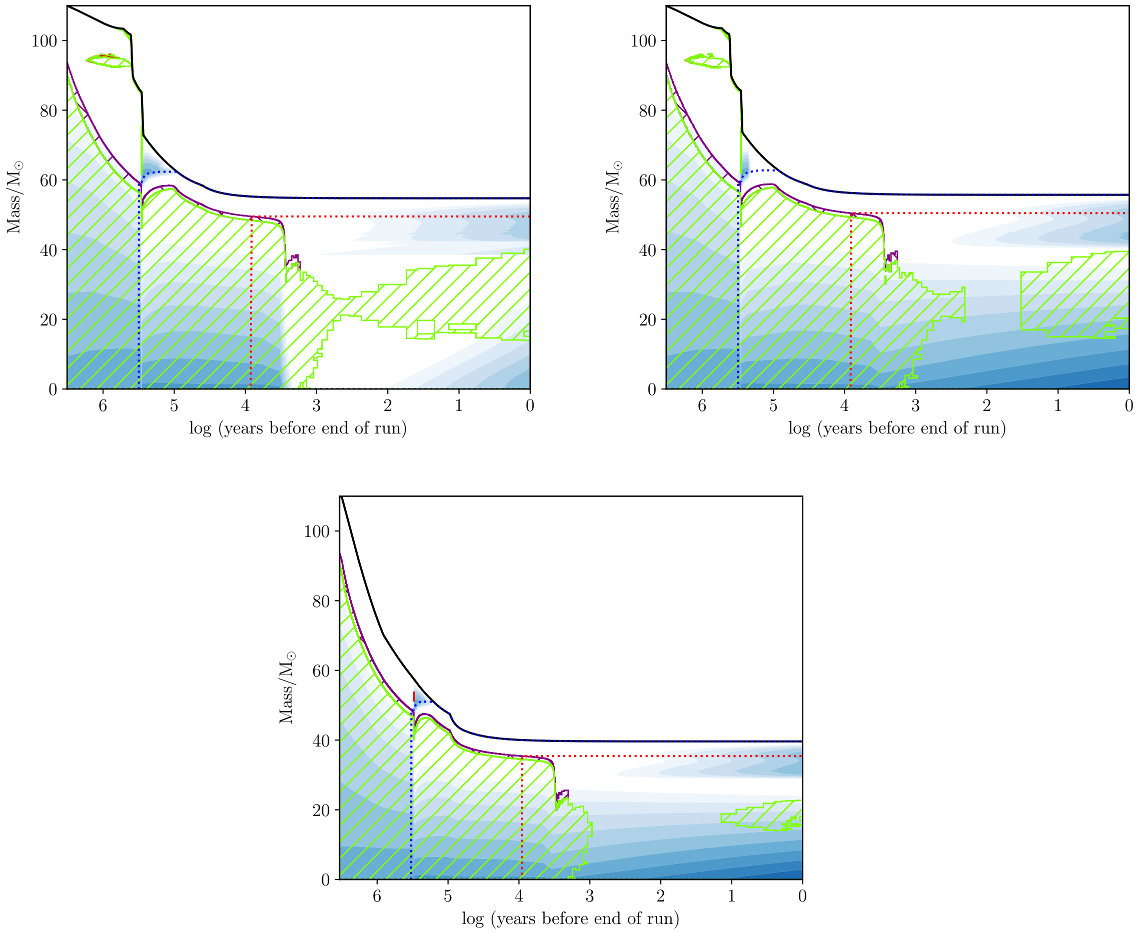

Figure 3.8 Kippenhahn diagrams showing the structure of a $110\,\mathrm{M}_\odot$ star evolved with enhanced mixing (top-left), with MLT++ (top-right) and with enhanced mass loss (bottom). The Y-axis represents the mass co-ordinate inside the star while the X-axis represents the time remaining in the life of the star before end of the run is reached. Green, purple and red hatching mark the regions with convection, overshooting and semiconvective mixing, respectively. In all three panels, the helium core boundary is the outermost location where the hydrogen mass fraction is less than 0.01, while the helium mass fraction is ≥ 0.01, and is represented by the blue dashed line. Similarly, the carbon core boundary is defined as the outermost location where the hydrogen and helium mass fraction are less than 0.01 while the carbon mass fraction is ≥ 0.01. It is represented as the red dashed line.

accompanied by a $3\,\mathrm{M}_\odot$ overshoot region outside the core, (shown by the purple hatching). The convective core decreases in size as the star evolves through the main-sequence.

In models computed with extra mixing and MLT++, thin strips of convection, two close to the surface and the third at about $90\,\mathrm{M}_\odot$, are formed as the star encounters the hydrogen, helium and iron opacity bumps in the final 10^6 years of its evolution. The envelope inflation due to the iron opacity bump causes the star to become a red supergiant before core hydrogen burning can finish. The star suffers higher mass-loss rates as a red supergiant that can be – seen as a rapid decline in the total mass of the star (black solid line) – until a $60\,\mathrm{M}_\odot$ helium core is formed – depicted by a blue dotted line in the figure. The star continues to lose mass, as the core helium burning and the hydrogen shell burning ensues, although at a comparatively lower rate. It ultimately loses its envelope to form a naked helium star in the final 10^5 years of its evolution, before finally forming a roughly $50\,\mathrm{M}_\odot$ carbon core in the end.

In the model computed with enhanced mass loss, mass-loss rates are quite high ($> 10^{-5}\ \mathrm{M}_\odot\,\mathrm{yr}^{-1}$) during the main-sequence evolution. The convective core shrinks rapidly in response to high mass-loss rates. The star loses its outer layers before any sub-surface convection region can form, becoming a naked helium star shortly after a $50\,\mathrm{M}_\odot$ helium core is formed. The final product is a $40\,\mathrm{M}_\odot$ naked helium star with a $35\,\mathrm{M}_\odot$ carbon core.

The similarities in the evolution of the models using MLT++ and enhanced mixing can be understood as follows. In models with enhanced mixing, convection is already efficient in the core, owing to its high density and increasing α_{MLT} (and therefore the mixing length) hardly makes any difference. However, the density in the subsurface of layers of the star can be $\approx 10^{-10}\,\mathrm{g\,cm^{-3}}$ and convection is highly inefficient, therefore increasing α_{MLT} leads to more efficient convective transport of energy in the stellar envelope.

For models using MLT++ to suppress density inversions, the story is similar. Reducing the temperature gradient (superadiabaticity) prevents radiative losses from the convective cells, making them more efficient at transporting energy. However, near the centre convection is nearly adiabatic and the value of superadiabaticity is small ($<10^{-4}$), therefore MLT++ is not applicable there. Thus models with high α_{MLT} and MLT++ produce similar core structure.

For models with extra mass-loss the evolution is quite different from the first two cases as the star loses quite a lot of mass even on the main sequence. This same trend continues for the post-main sequence evolution. Therefore, it has the least of both the helium and carbon core masses. Similar to the other two methods, the $110\,\mathrm{M}_\odot$ model again loses all its envelope and ends up as a naked helium star during the core helium burning phase.

Interestingly, the maximum mass-loss rate encountered by the $110\,\mathrm{M}_\odot$ star with extra mass loss is lower than the models with enhanced mixing and with MLT++, as shown in Figure 3.9. However, models with extra mass loss by construction have higher mass-loss rates during most of the main sequence, therefore they become a naked helium star without ever undergoing the red supergiant phase where the peak in mass-loss rates usually occurs (due to the large radius of the star). Models with enhanced mixing and MLT++ lose their envelope later in the evolution as they encounter high mass-loss rates as a red-supergiant and therefore end up with higher total mass compared to the model with extra mass loss.

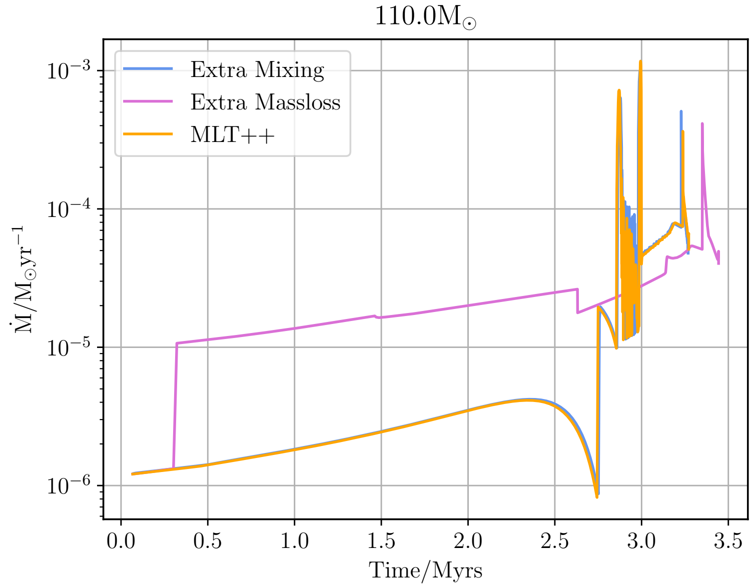

Figure 3.9 Variation in mass-loss rates with time for a $110\,M_\odot$ star evolved with extra mixing (blue line), extra mass loss (pink line) and with MLT++ (orange line). While the maximum mass-loss rate encountered by the $110\,M_\odot$ model with extra mass loss is less than the maximum mass-loss rate encountered by the models evolved with the other two methods, it still ends up being the least massive of all in the end. See Section 3.5.1 for an explanation.

3.5.2 Final mass and remnant properties

Massive stars are expected to end their lives in supernovae, leaving behind compact remnants (neutron stars and black holes) in a core-collapse or a pulsational-pair instability supernova or undergoing complete disruption in a pair-instability supernova. Their demise as a supernova explosion is also important for modifying the chemical and energy makeup of their surroundings, paving way for the formation of new generations of stars. Further-

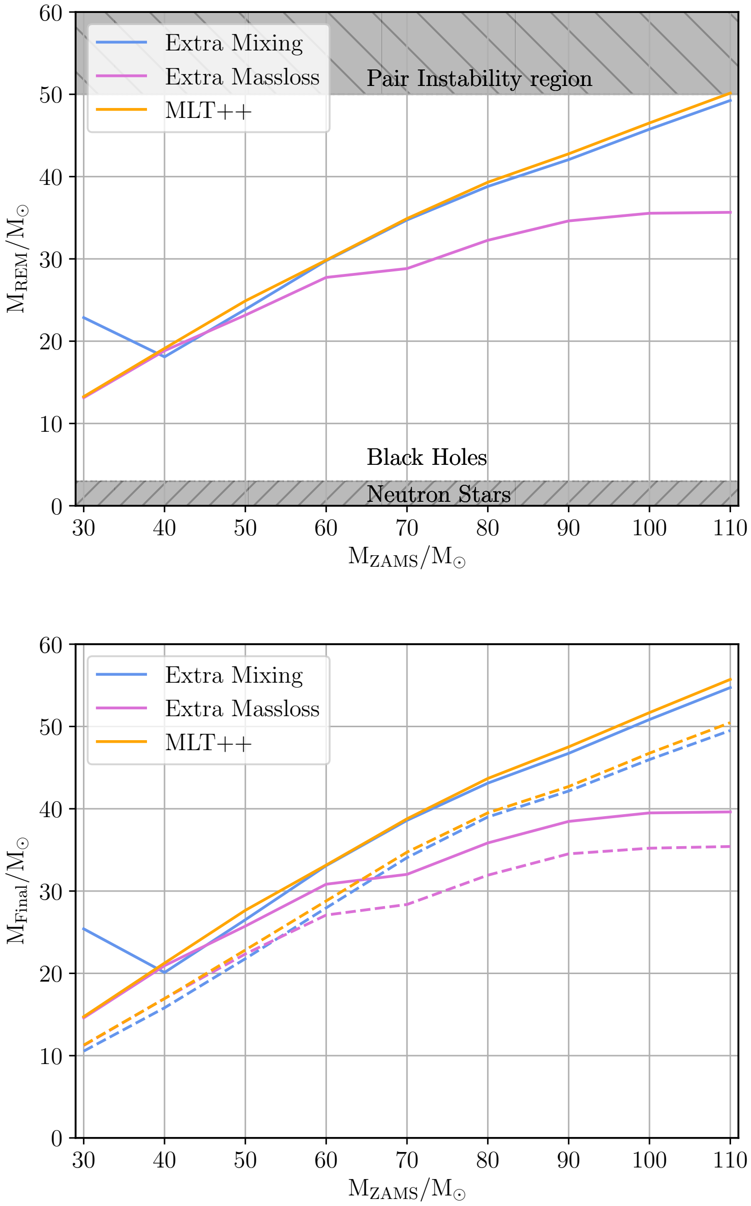

Figure 3.10 The top panel shows the mass of stellar remnants as a function of their initial mass, as predicted by sets of models with different numerical enhancements using the Belczynski et al. (2008) prescription. The bottom panel shows the final total mass (solid line) and the carbon-oxygen core mass (dashed line) that were used in calculating the remnant mass. For stars more massive than 60 $M_\odot$ the differences in the remnant mass can be up to 14 $M_\odot$.

more, stellar remnants are important for studies across a wide spectrum. They are the progenitors of X-ray binaries, gamma rays bursts, and compact binary mergers that lead to gravitational waves. Hence, it is important to quantify the differences between the properties of the remnants formed by the massive star models.

There are many prescriptions available in the literature that relate the final properties of the star with the mass of the remnant it would form (e.g., Eldridge & Tout, 2004; O'Connor & Ott, 2011; Fryer et al., 2012; Ertl et al., 2016). Here we use the Belczynski et al. (2008) prescription, which is the same as the StarTrack prescription in Fryer et al. (2012), to calculate the mass of the stellar remnants for each set of models. The method uses the total mass and the core mass of the star at the end of carbon burning to calculate the mass of the remnant (we refer the interested reader to Section 6.1 of Agrawal et al., 2020, for further details of the method).

Following Belczynski et al. (2010), we plot the remnant mass of the stars as a function of their initial mass as given by the three sets with numerical enhancements in Figure 3.10. The top panel of the figure shows the remnant mass of the stars while the bottom panel shows the final total mass of the star and mass of the carbon-oxygen core.

For all the sets of models, the Belczynski et al. (2008) prescription predicts the formation of black holes with masses in the range of 13–50 $\mathrm{M}_\odot$. The difference in the mass of black holes as predicted by each set is less than 2 $\mathrm{M}_\odot$ for stars with initial masses up to 60 $\mathrm{M}_\odot$, with the exception of the 30 $\mathrm{M}_\odot$ star where the model with extra mixing predicts a significantly higher remnant mass (22 $\mathrm{M}_\odot$ black hole) compared to other two sets (13 $\mathrm{M}_\odot$ black hole). For stars more massive than 60 $\mathrm{M}_\odot$ the curve diverges rapidly, and the difference between the remnant masses can be up to 14 $\mathrm{M}_\odot$. A similar trend can be seen in the total mass and core masses for each set. For the 30 $\mathrm{M}_\odot$ star, the model with extra mixing predicts a higher final total mass but lower carbon-oxygen core mass compared to the other two sets. This is because a larger mixing length in the model leads to a more compact star with lesser mass loss. Thus, the 30 $\mathrm{M}_\odot$ model is able to retain most of its envelope and ends up with the final total mass of 26 $\mathrm{M}_\odot$. Similarly, the origin of differences in the black hole mass predictions can be traced back to the mass-loss rates experienced by each model which themselves are dependent on the surface properties of the star.

3.5.3 The maximum radial expansion

Figure 3.11 shows the maximum radial expansion achieved by the stars during their evolution, computed with the three different numerical fixes. The maximum difference in the maximum radial expansion is ~2000 $R_\odot$ which occurs between models with extra mass loss and models with MLT++, for the most massive 110 $M_\odot$ star in the set. For models with extra mixing and MLT++ which appear to undergo similar evolutionary paths and final fates, the difference in maximum radial expansion can still be up to 1000 $R_\odot$, especially for stars in the mass range 30–80 $M_\odot$. Even for the 110 $M_\odot$ star, where the difference between models with extra mixing and MLT++ appears to be the least, the maximum radius can differ by 500 $R_\odot$. This has important implications for the binary evolution of the star, as radial proximity determines the episodes of mass transfer in close binary systems.

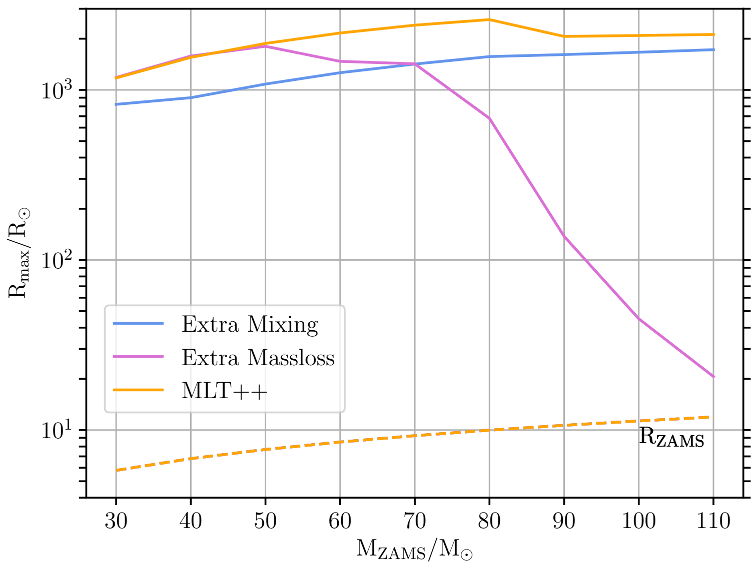

Figure 3.11 Maximum radial expansion achieved by a star during its lifetime as a function of its initial mass, as predicted by the three sets of stellar models with numerical enhancements. The difference in predictions of the maximum radial expansion by each models varies between 500–2000 $R_\odot$, and can have important implications if the star is in a binary system.

These differences in the stellar radii are again the result of the numerical enhancements used in each set. For models with initial masses greater than 60 $M_\odot$ and computed with extra mass loss, high mass-loss rates strip the envelope of the stars before they can become a red supergiant. Thus these stars evolve directly towards the naked helium star phase and show the least radial expansion. For stars with extra mixing, a higher mixing length means the fluid element is more efficient at transporting energy through convection. This decreases the size of the convective cells in the envelope and the model remains more compact and at higher effective temperatures than the models from the other two sets.

An interesting case is presented by models with MLT++ where reducing the temperature gradient can have the same effect as excess envelope mixing (Sabhahit et al., 2021). For stars up to $50\,M_\odot$, models using MLT++ closely mimic the behaviour of models with extra mass loss, although beyond $50\,M_\odot$, the excess envelope mixing in models with MLT++ makes them resemble more closely the models with enhanced mixing.

3.6 Clues from observations: the Humphreys-Davidson limit

It is well established that the evolution of massive stars is highly uncertain. It is riddled with many physical and numerical problems. Therefore the need for numerical fixes arises. To make matters worse, it is difficult to say which method is closer to reality as there is an apparent scarcity of massive stars in the region of the HR diagram where numerical issues with density inversions occur.

First characterised by Humphreys & Davidson (1979), the Humphreys-Davidson (HD) limit defines the region in the HR diagram above $\log L/L_\odot = 5.8$ where very few massive stars in the Galaxy have been observed to date. Using recent observations of red supergiants in the Large Magellanic Cloud (LMC) and the Small Magellanic Cloud (SMC), Davies et al. (2018) found the limiting luminosity of the brightest red supergiants to be $\log L/L_\odot = 5.5$ in both galaxies, slightly lower than previous studies. The LMC and SMC are lower metallicity environments than the Milky Way, closer to the metallicity used in this work. The findings of Davies et al. (2018) also suggest that the maximum red supergiant luminosity does not vary strongly with metallicity.

While the absence of massive stars as red-supergiants beyond the HD limit may not help trace the exact evolutionary path of massive stars, it does provide an important clue that stars more massive than about $40\,M_\odot$ do not spend much time in the HD region. In recent years, several studies (e.g., Castro et al., 2018; Kaiser et al., 2020; Vink et al., 2021) have tried to constrain the different mixing mechanisms (such as semiconvection, overshooting), mass-loss rates and binary properties of massive stars by using stellar models evolved with different physical inputs to reproduce the HD limit. However, they also employ numerical fixes for instabilities due to density inversions to compute the complete evolution of the stellar track. Using these numerical fixes interferes with other physical inputs and adds an implicit bias in the computation of models. As these numerical fixes can be different across different stellar evolution codes, results obtained with them might not reflect the true value of the physical parameter being constrained for the massive stars.

Studies that do not employ any numerical fixes (e.g. Klencki et al., 2018) are usually limited to stars less massive than $30\,\mathrm{M}_\odot$ or to the evolutionary phases before numerical instabilities arise in more massive stars. While this helps avoid bias due to numerical methods, it also inhibits exploring the late stage evolution of massive stars, such as the end of core helium burning and beyond. Thereby, affecting the potential studies involving stellar remnants and transients.

Some studies also show that the HD limit can also be reproduced by stellar models by just using these numerical fixes. For example, using just MLT++ as the source of excess envelope mixing in massive stars up to $50\,\mathrm{M}_\odot$, Sabhahit et al. (2021) were able to reproduce the lack of massive stellar models beyond the HD limit and the Davies limit at Galactic ($Z = 0.017$), LMC ($Z = 0.008$) and SMC ($Z = 0.004$) metallicity.

Recently, Gilkis et al. (2021) showed that using significantly enhanced mixing parameters in stellar models can reduce the time spent by stars beyond the HD limit. Following Gilkis et al. (2021), in Figure 3.12 we show the amount of time stars spend beyond the HD limit as a function of initial mass for each of our sets of models. We see that the models computed with extra mass loss spend the least time (except for a $40\,\mathrm{M}_\odot$ stellar model) while most of the massive stars computed with enhanced mixing and MLT++ can spend between 2×10^5 and 4×10^5 years in the HD region. Therefore, models with extra mass loss may appear to be closest to observations (or lack of observations) of massive stars. This, however, has serious implications for gravitational wave observations, as the maximum black hole mass predicted by this set of the model is just $35\,\mathrm{M}_\odot$ (see Figure 3.10).

To unravel this problem, we plot the evolutionary tracks, colored according to the mass-loss rates, from the set computed with the extra mass loss in Figure 3.13. Despite the enhancement near the Eddington-limit, the maximum mass-loss rates for models with enhanced mass loss seem to be consistent with the typical mass-loss rates for massive stars (Smith, 2014). The maximum mass-loss rate of $1.8 \times 10^{-3}\,\mathrm{M_\odot\,yr^{-1}}$ is experienced by stars in the 40–60 $\mathrm{M_\odot}$ mass range during the red supergiant phase of their evolution. However, these rates only last for a maximum of 7×10^3 yrs. For stars more massive than $60\,\mathrm{M_\odot}$, the maximum mass-loss rates are an order of magnitude lower, about $3 \times 10^{-4}\,\mathrm{M_\odot\,yr^{-1}}$, and last between 3×10^2–2×10^4 yrs. The lower mass-loss rates encountered by more massive stars are a consequence of the enhanced mass loss during their main-sequence evolution. These stars experience mass-loss rates of about $10^{-5}\,\mathrm{M_\odot\,yr^{-1}}$ for more than 3×10^5 years. Therefore, they lose a significant portion of their envelope while on the main-sequence and do not undergo the red-supergiant phase of evolution.

Whether massive stars can retain these high mass-loss rates for prolonged periods of time is currently questionable. Moreover, several authors have recently argued that mass-loss rates for massive stars should be lower, rather than higher, than what is commonly used in computing massive single star models (e.g., Beasor et al., 2020; Vink & Sander, 2021). Interaction with a companion in a binary system can lead to higher mass-loss

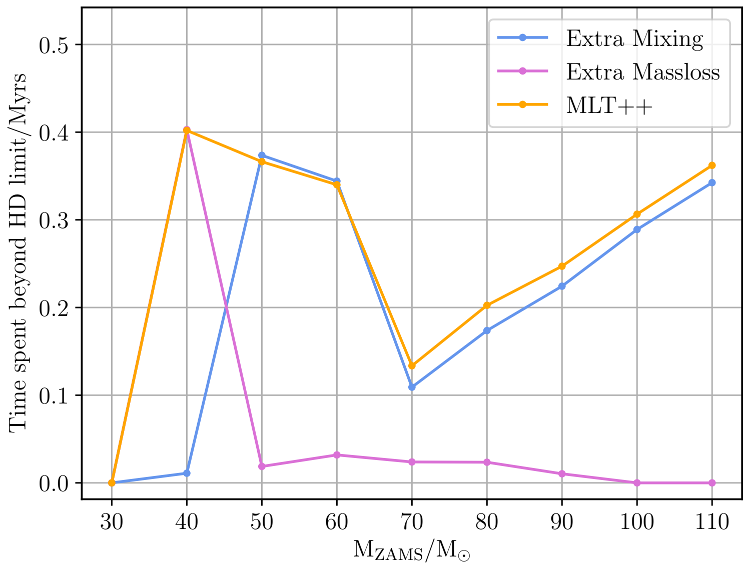

Figure 3.12 Time spent beyond the Humphreys-Davidson limit as a function of the initial mass of the star as given by each set of stellar models with numerical enhancements.

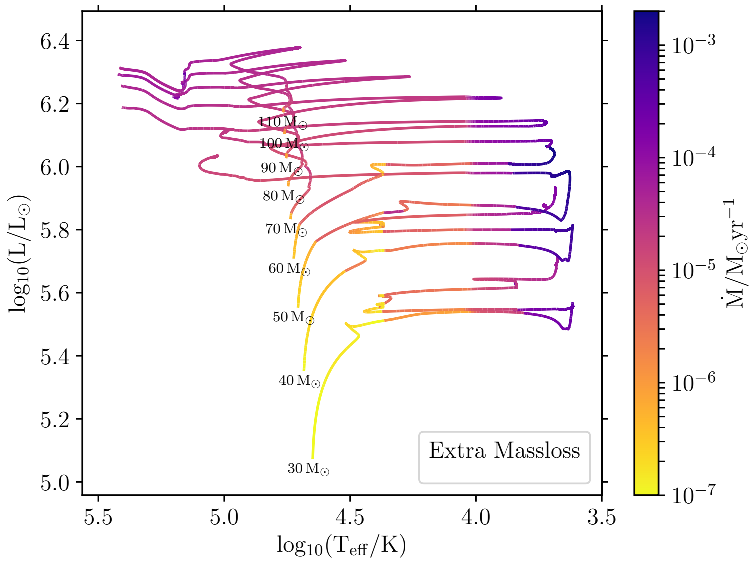

Figure 3.13 HR diagram showing the mass-loss rates for stars in the mass range 30–110 $M_\odot$, computed with the extra mass loss described in Section 3.4.2.

rates, but again the smaller radii predicted by these models (Figure 3.11) makes binary interactions less likely. Therefore, the validity of mass-loss rates in models computed with extra mass-loss, or in general any of numerical fixes used by the codes cannot be ascertained at present.

Mixing process such as rotation, semiconvection and overshooting have also been shown to have large impact on the red supergiant phase of evolution for massive stars and on the reproducibility of the HD limit (Schootemeijer et al., 2019a; Higgins & Vink, 2020; Gilkis et al., 2021; Sabhahit et al., 2021). Further, many studies suggest that magnetic fields can have a significant effect on the sub-surface convection regions of the stars and hence on the density inversions. For example, Jiang et al. (2018) have shown that the turbulent velocity fields around the iron opacity peak can be escalated in the presence of magnetic fields. We have not explored the role of semiconvection, rotation, magnetic fields and binarity in this work, each of which we acknowledge can have a significant impact on the evolution of massive stars. Evolving massive stellar models with these properties is important and will be a part of future work.

3.7 Conclusion

In this work, we performed a systematic study of the impact of the Eddington limit and the subsequent density inversions on computing the evolution of massive stars with the 1D stellar evolution code MESA. Using commonly used input parameters for massive stellar models, we compute the non-rotating evolutionary tracks of 10-110 $\mathrm{M}_{\odot}$ stars for $Z = 0.00142$. Models with initial masses between 30 and 110 $\mathrm{M}_{\odot}$ in this standard set fail to reach the end of core carbon depletion ($X_c \leq 10^{-2}$) as the time-steps become too small (of the order of days) as models encounter density inversions in the sub-surface layers. We find that this is due to large specific entropy ($S/N_A k_B \geq 300$) at the base of the convective envelope.

We recompute the models for 30–110 $\mathrm{M}_{\odot}$ stars using three numerical fixes: enhancing the mixing length parameter, enhancing mass-loss rates and suppressing density inversions through adopting MLT++. These three are a general form of the methods used by different stellar evolution codes to resolve numerical instabilities associated with density inversions in models of massive stars. With each method, we are able to compute the evolution of massive stars up to carbon depletion in the core.

To determine the least impact each method can have on the evolution of the star, we pick the sets with the minimum enhancement for each method. With these, we find that density inversion regions can still form in these models, but the specific entropy stays small and the evolution of models proceeds smoothly, i.e, without time-steps becoming too short.

We compare the stellar models evolved using each method. Even with sets of models with minimum numerical enhancement from each method, the remnant mass of the stars can vary by up to 14 $\mathrm{M}_{\odot}$ while the maximum radial expansion achieved by stars can vary by up to 2000 $\mathrm{R}_{\odot}$ between the sets. These differences are important for comparing stellar models with observations and the possible feedback on the evolution of massive stars. For example, the above differences can have huge implications for studies involving binary interactions of stars and stellar remnants.

We also find that the differences in the various evolutionary properties predicted by the set of models computed with extra mixing and those using MLT++ are quite small.

However, these models show a difference of 1000 K in the minimum effective temperatures achieved by the star as a red supergiant (cf. Section 3.4.3). The effective temperature is critical for determining the spectral properties and surface abundances of the stars (Davies et al., 2013). Thus, this discrepancy in the effective temperature can be significant for studies involving abundance properties of massive stars, such as galactic chemical composition studies.

In commonly used 1D stellar evolution models, a combination of these methods is used and not necessarily limited to their minimum value. Thus, the differences in the evolutionary properties of massive stars can he higher than what we get here, as shown in Chapter 2.

Here we considered an intermediate value of metallicity ($Z = 1.42 \times 10^{-3}$), as this is the metallicity where progenitors of current gravitational wave observations are more likely to form. Due to the dependence of opacity on chemical composition and the diminishing effect of opacity peaks at lower metallicities (Sanyal et al., 2017), numerical issues related to the proximity to the Eddington limit become less prominent at lower metallicities. For example, using the same set of input parameters as the standard set (Section 3.3), we find that stellar models fail to evolve for initial masses beyond $20\,\mathrm{M}_\odot$ at higher (solar) metallicity ($Z = 1.42 \times 10^{-2}$) but evolve smoothly for initial masses up to $100\,\mathrm{M}_\odot$ at lower metallicity ($Z = 1.42 \times 10^{-4}$).

Multi-dimensional stellar models suggest that convection can be more turbulent and non-localised than assumed by MLT (Kupka, 2009). 3D modelling of the density inversion regions in massive stars by Jiang et al. (2015, 2018) showed a complex interplay of convective and radiative transport dependent on the ratio of the photon diffusion time to the dynamical time and a smaller convective flux compared to 1D codes. There are ongoing efforts to improve the treatment of mixing 1D codes using results from 3D simulations (Arnett et al., 2019; Schultz et al., 2020).

As observations of massive stars become more accessible, and our ability to compute 3D models of massive stars improves, the problem of density inversions might be resolved in future. Meanwhile, it is important to be aware of and acknowledge the impact different numerical methods can have on the evolutionary model sequences of massive stars.

Acknowledgements

We thank Ross Church, Jan Eldridge and, Debashis Sanyal for useful comments and discussions. We thank Pablo Marchant for the script to make Kippenhahn diagrams. DSz has been supported by the Alexander von Humboldt Foundation. PA, JH and SS acknowledge the support by the Australian Research Council Centre of Excellence for Gravitational Wave Discovery (OzGrav), through project number CE170100004. This work made use of the OzSTAR high performance computer at Swinburne University of Technology. OzSTAR is funded by Swinburne University of Technology and the National Collaborative Research Infrastructure Strategy (NCRIS).

4

METhod of Interpolation for Single Star Evolution

One decade's supercomputer is the next decade's desktop.

—Hansen, Kawaler & Trimble in Stellar interiors

4.1 Introduction

Modelling the integrated properties of stellar systems such as galaxies or star clusters requires the use of population synthesis codes which can simulate a large number of stars (a population) and the myriad interactions between them. In order to produce realistic models of such systems which can be compared to modern observations (e.g. Mackey, 2008), it is important to include an up to date treatment of stellar evolution.

Stellar evolution is typically modelled using a one-dimensional (1D) stellar structure and evolution code, which we refer to as a 'detailed stellar evolution code'. Such codes solve the differential equations of stellar structure (namely for mass, momentum and energy conservation, energy generation and transport) within the star, at different points in time to compute a sequence of stellar structure models. Detailed evolution codes are a recommended way to evaluate both the structure and the evolution of stars but running them for a population of stars can be computationally expensive and time consuming.

With the advent of high-performance computers and parallel programming methods, detailed evolution codes are being used in combination with stellar dynamics and population synthesis codes e.g. Church, Tout, & Hurley (2009) and Astrophysical Multipurpose Software Environment (AMUSE; Portegies Zwart et al., 2009, 2013; Pelupessy et al., 2013).

However, detailed stellar evolution codes can break down at times owing to numerical difficulties which can impede the progress of the overlying simulation (Aarseth, Tout, & Mardling, 2008). Physical processes such as convection and rotation become important in massive stars and require sophisticated modelling methods with higher temporal and spatial resolution, increasing the computational cost and the potential for numerical issues to develop. User intervention and expertise is often required to push detailed codes past failure points. The data from these simulations also need to be manually checked for any non-physical results which would arise from erroneous numerical evolution of a model star.

While there are considerable differences in the evolutionary tracks for stars of various masses and metallicities, if the step in mass and metallicity is small, the changes are usually smooth enough to parameterize. Furthermore, for most population synthesis requirements only the global parameters of the stars such as mass, radius, and luminosity are needed. Similarities between the stellar tracks can be exploited and the output of a detailed code for a few stars can be parameterized in the form of formulae (Eggleton, 1996). These formulae can then be used to calculate evolution properties for a large number of stars.

The earliest attempts to include the effects of stellar evolution in the study of star clusters were made by Wielen (1970), Terlevich (1987) and Chernoff & Weinberg (1990). The authors employed simple schemes for stellar lifetimes and only accounted for the mass lost in the form of planetary nebulae or during supernovae events. A more accurate method was developed by Hurley, Pols, & Tout (2000) in the form of the Single Star Evolution (SSE) package obtained using polynomial fits to the set of stellar tracks by Pols et al. (1998). It was an expansion of the work by Eggleton, Fitchett, & Tout (1989) along the lines of Tout et al. (1997). The SSE package employs fitting formulae and analytical expressions for the underlying physics to describe quantities such as the radius and luminosity of a star given its mass, metallicity and age. Fitting formulae have been a popular choice for population synthesis codes because the resulting algorithms are computationally inexpensive, fast and robust.

Two decades later, ground-based telescopes such as the Very Large Telescope (Schilling, 1998; Moorwood, 2009) and Keck (Kassis et al., 2018) have been observing fainter and rarer stars while the Hubble Space Telescope (Paresce, 1991; Stockman, 1994), Chandra X-ray Observatory (Wilkes, 2019) and Gaia (de Bruijne, 2012; Eyer et al., 2019) have monitored complex stellar phenomena from space. Furthermore, interferometers such as the Very Large Array and the Atacama Large Millimeter Array have helped us probe the formation and afterlives of stars through radio observations (Matthews, 2019). Advances in multi-messenger astronomy have also provided us with unprecedented data with which we can better understand the universe. The IceCube Neutrino Observatory (Williams & IceCube Collaboration, 2020) is detecting high energy neutrinos from stellar outbursts, while the Advanced Laser Interferometer Gravitational-wave Observatory (aLIGO; Aasi et al., 2015) and Advanced Virgo (Acernese et al., 2015) detectors continue to report gravitational-wave observations from the merging of compact binaries (Abbott et al., 2016, 2017b, 2019; The LIGO Scientific Collaboration & the Virgo Collaboration, 2020).

Together with the advances in our observing capabilities the development of sophisticated numerical techniques in programming and newer input data in the form of opacity tables and nuclear reaction rates has led to the development of modern and improved stellar structure and evolution codes with updated physics (Paxton et al., 2019). Thus, there is a pressing need to update the fitting formulae used in SSE using the data from up-to-date stellar evolution tracks.

Re-calculating the fitting formulae from a new set of stellar tracks is a non-trivial task (Church et al., 2009). Tanikawa et al. (2019) recently performed an update of the SSE formulae for metal-poor massive stars. However, even with the updated fitting formulae, this only covers a particular subset of the parameter space and the user is still limited to results from a single set of evolutionary tracks. There is thus a need for a more flexible method which is also fast, robust and can easily make use of different stellar evolution tracks.

Interpolation between a set of pre-calculated evolutionary tracks provides a promising alternative. This method employs tabulated data from 1D stellar evolution codes to estimate stellar parameters for a desired star. Unlike fitting formulae, stellar parameters from the given set of detailed tracks are calculated in real time with this method. Hence, one just needs to change the input stellar tracks to generate a new set of stellar parameters.

Although interpolation between stellar tracks has been extensively used to construct stellar isochrones (e.g. Schaller et al., 1992; Bergbusch & VandenBerg, 2001), the memory requirement for storing and loading the tracks made it difficult for computationally expensive codes involving stellar dynamics to make use of interpolation in the past. With modern computers, computer memory is readily available and recently, the codes SEVN (Spera, Mapelli, & Bressan, 2015; Spera & Mapelli, 2017) and ComBinE (Kruckow et al., 2018) have employed the method of interpolation over a range of stellar parameters to study the properties of gravitational wave progenitors. Presently, interpolation offers the most viable option for an efficient, robust and flexible approach.

In this paper, we present results from our newly developed synthetic stellar evolution code METhod of Interpolation for Single Star Evolution (METISSE). It uses interpolation to approximate the properties of a star of given mass and metallicity at any age. It is a modern Fortran code and can serve as an alternative to SSE fitting formulae in stellar dynamics and population synthesis codes. It relies on the concept of Equivalent Evolutionary Phases (EEPs) and can make use of stellar tracks from a variety of stellar evolution codes. In this work, we have used sets of stellar tracks computed using the Cambridge STARS code, Modules for Experiments in Stellar Astrophysics (MESA) and the Bonn Evolutionary Code (BEC) as input to METISSE. Using the MESA and BEC tracks in METISSE, we predict stellar parameters such as the maximal extent of the radius or the remnant mass for massive stars and compare the results in terms of their physical ingredients. We thus demonstrate the usefulness of METISSE in systematic studies dedicated to exploring how uncertain parameters in stellar evolution effect the properties of binary populations and dynamical systems of stars.

This paper is organized as follows. We provide an overview of evolutionary tracks for different stars and the concept of EEPs in Section 4.2. We describe the construction of METISSE as a standalone stellar evolution code in Section 4.3. In Section 4.4 we introduce the three sets of stellar models that we have used to show METISSE's capabilities. We validate results obtained with METISSE by comparing to SSE in Section 4.5. In Section 4.6, we present results from METISSE using stellar tracks computed with MESA and BEC as input. We mention the key differences between these tracks and their implications in Section 4.7. We discuss caveats and potential future work in Section 4.8 and conclude the paper in Section 4.9.

4.2 Stellar life and EEPs

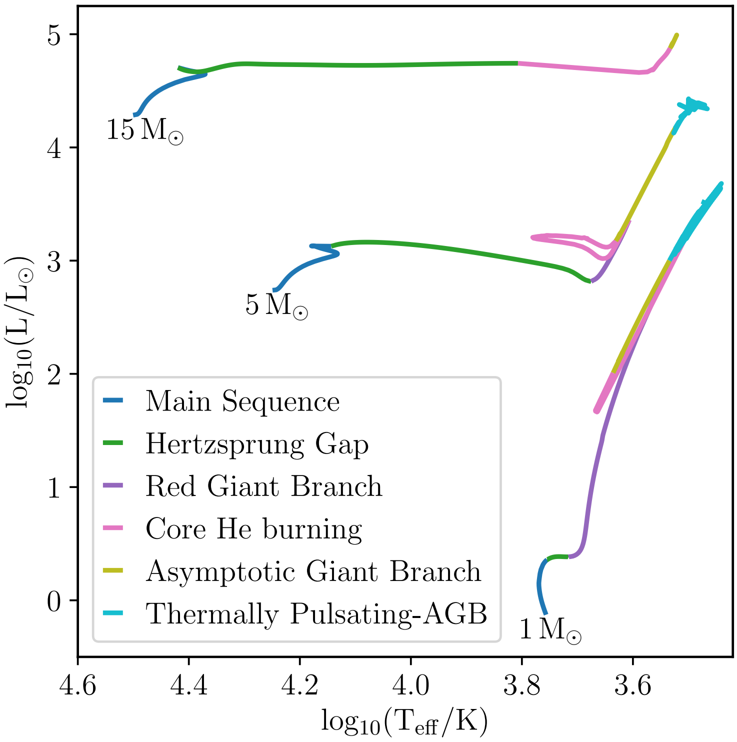

Figure 4.1 Hertzsprung–Russell (HR) diagram showing evolutionary tracks for stars of mass 1, 5 and 15 $M_{\odot}$ at a metallicity of $Z = 0.0142$. Different evolutionary phases are highlighted along each track. The post-asymptotic giant branch phase has not been plotted for clarity.

Stars have varied lives depending on their mass and chemical composition. Owing to the differences in their evolution, stars experience different evolutionary phases and trace different paths on a Hertzsprung–Russell (HR) diagram (see, e.g., Cox & Giuli, 1968; Kippenhahn & Weigert, 1990, for an in-depth discussion of the evolution of stars). Stellar tracks highlighting different evolutionary phases are shown in Fig. 4.1.

A low-mass star like our Sun (1 $M_{\odot}$) burns hydrogen (H) via the proton-proton chains in a radiative core. This causes the surface temperature and the luminosity to increase moderately while the star is on the main sequence (MS). At the end of MS, the core is not hot enough to ignite helium (He) and contracts, becoming degenerate at some point on the Hertzsprung Gap (HG). The envelope, however, cools and expands as the star ascends the Red Giant Branch (RGB). The H burning in the shell surrounding the core adds to the core mass until it becomes hot and massive enough to ignite He off-center in a thermonuclear run-away (He flash). The star descends the giant branch as the core expands due to a decrease in the hydrostatic pressure and burns He in the core while on the horizontal branch. It ascends the Asymptotic Giant Branch (AGB) at the end of core He burning, and then transitions to the Thermally Pulsating-AGB (TPAGB) where it eventually loses its envelope to become a white dwarf (WD).

An intermediate-mass (e.g. $5\,M_{\odot}$) star, on the other hand, burns H via the Carbon-Nitrogen-Oxygen cycle in a convective core. The effective temperature of the star decreases during the main-sequence evolution, making it move redwards on the HR diagram. Mixing by convection causes the sudden depletion of H in the region surrounding the core. In the absence of nuclear energy generation in the core, the star contracts on a thermal timescale, producing the hook-like feature on the HR diagram seen at the end of the MS. H-shell burning ensues as the star ascends the giant branch. He ignition happens at the tip of the RGB, in semi-degenerate conditions without a flash, and the star burns He in a blue loop, ascending the AGB at the end of He burning and ending life most likely as a carbon-oxygen white dwarf.

Massive stars (e.g. $15\,M_{\odot}$) behave similarly to intermediate-mass stars during the main-sequence phase. Their core becomes hot enough to ignite He on the HG, close to the end of the MS so these stars do not become red giants as low and intermediate-mass stars do. Instead, they continue fusing elements in the core while rapid shell burning adds to the core mass and causes the envelope to slowly expand, thereby making the star a red supergiant (RSG). Finally, with the formation of an iron core, the star runs out of fuel and ends its life in a supernova (SN) explosion.

Modelling stars through different evolutionary phases using detailed evolution codes typically requires numerous and unequal steps in time. Using the output of a detailed code directly to create an interpolated new track can thus be inefficient and even inaccurate. A track obtained by sequentially interpolating between the same numbered lines in neighbouring mass tracks, might not represent the actual evolution of the star (the evolution we would obtain by simulating the star through detailed codes). Using time as a parameter for interpolation would also not serve the purpose as the associated timescales can again be different for different mass stars. For example, it takes about 10 billion years for a $1\,M_\odot$ star to complete H burning in its core while a $15\,M_\odot$ star can complete all the fusion reactions and form a remnant in just a few million years.

Utilizing evolutionary features such as the depletion of the central hydrogen mass fraction to a certain value along stellar tracks (similar to Simpson et al., 1970) provides more accurate ground for comparison. These features mark the boundary of evolutionary phases in a stellar track and divide the track into what are known as Equivalent Evolutionary Phases (EEPs; Prather, 1976; Bergbusch & VandenBerg, 2001). For different stellar tracks, EEPs are readily identifiable by a set of physical conditions. The portion of an evolutionary track between each EEP is further subdivided into an equally spaced set of points. The final product is an EEP-track containing stellar parameters at a fixed number of points. Depending on how many phases a particular track has, the total number of points on an EEP-track can vary. A new track can be generated by interpolating between corresponding points of the neighboring mass tracks.

In the remainder of the paper we use the term 'stellar model' to mean the same as the sequence of stellar models or a stellar track while the term 'set of stellar models' or 'set of stellar tracks' means evolutionary tracks of stars with different initial masses but the same metallicity.

4.3 METISSE

METhod of Interpolation for Single Star Evolution (METISSE) is a synthetic stellar evolution code which uses interpolation to compute evolutionary tracks for many stars using tracks for a finite set of stars. The tracks for input are evolved using detailed stellar evolution codes and should be converted to EEP form for use in METISSE. The EEPs can be identified with programs like ISO (e.g. Dotter, 2016) or by direct inspection (e.g. Szécsi et al., 2020). Given a set of EEP-tracks, a schematic of how METISSE calculates the properties of a star within the input mass range is described next.

4.3.1 Interpolation scheme

The mass interpolation routine used in this work is adapted from the ISO code (Dotter, 2016). For a particular value of metallicity, first the corresponding EEP-tracks are read by METISSE. Next, the tracks with initial masses that immediately envelop the input mass are located from the given set. A new track is interpolated by the method of monotonic interpolation with a piece-wise cubic function (Steffen, 1990). No interpolation occurs at this stage if the track for the mass in question is already present in the set (up to some tolerance defined by the user).

Depending on the metallicity, stars greater than a certain mass do not undergo some evolutionary phases (e.g. the red-giant branch). Interpolation between tracks where some undergo a certain phase and others do not, can result in an incorrect new track. To handle this we identify certain critical mass tracks in the set of EEP tracks for a given metallicity. Both the search and the interpolation method change if the input mass falls near a critical mass, such as the mass above (or below) which stars do (or do not) ignite He on the HG. In this case, the track is either linearly interpolated or extrapolated if necessary. In Section A.1 and Section B.1, we provide details on how these critical masses are identified.

The mass interpolated track, however, contains stellar parameters for a set of ages. These generally differ from the age at which evolution parameters are required by a population synthesis code. So another interpolation is performed in age within the newly interpolated track to return stellar parameters at any given time. Section B.2 details the step by step interpolation process in METISSE.

4.3.2 Stellar phases

From an input set of models, METISSE determines the location of certain major EEPs to assign stellar evolution phases similarly to SSE (Hurley et al., 2000) to the interpolated tracks. The key EEP names and the corresponding SSE phases are listed in Table 4.1. As an example, the EEP points corresponding to the location of primary EEPs from Choi et al. (2016), which are also the default EEP values in METISSE, are listed in the last column of the table. For different sets of stellar models, where primary EEPs might be located at different EEP points, the value of these EEPs can be redefined by the user.

Table 4.1 SSE phases with the EEP name used by METISSE to identify the start of each phase and the corresponding EEP number.

No.	Stellar Phase	EEP name	EEP value[a]
0	Main Sequence (MS) M <= 0.7 $M_\odot$	Zero-Age Main Sequence (ZAMS)	202
1	Main Sequence (MS) M > 0.7 $M_\odot$	Zero-Age Main Sequence (ZAMS)	202
2	Hertzsprung Gap (HG)	Terminal-Age Main Sequence (TAMS)	454
3	First Giant Branch (GB)	Base of Giant Branch (BGB)	[a]
4	Core Helium Burning (cHeB)	core He Ignition (cHeI)	605
5	Early Asymptotic Giant Branch (EAGB)	Terminal-Age core He Burning (TAcHeB)	707
6	Thermally Pulsating AGB (TPAGB)	TPAGB	808
7	Naked Helium Star MS (HeMS)	None	–
8	Naked Helium Star HG (HeHG)	None	–
9	Naked Helium Star Giant Branch (HeGB)	None	–
10	Helium White Dwarf (HeWD)	None	–
11	Carbon-Oxygen White Dwarf (COWD)	None	–
12	Oxygen-Neon White Dwarf (ONeWD)	None	–
13	Neutron Star (NS)	None	–
14	Black Hole (BH)	None	–
15	Massless remnant	None	–

Notes. [a] The EEP values here denote the default in METISSE and correspond to the location of primary EEPs from Choi et al. (2016), except for the BGB EEP which is identified separately for each track. For different stellar models, the value of these EEPs (including the BGB EEP) can be redefined by the user.
For phases 7-15, see section 4.3.2 for how these are calculated.

To ensure that the interpolation occurs between equivalent evolutionary phases for each star, each stellar phase should occur at the same EEP value and hence at the same line number across the input stellar tracks. For evolutionary phases that do not occur in all evolutionary tracks, the EEP value is treated as a continuation of the preceding phase. For example, the base of the giant branch (BGB) may be missing for massive stars, so the BGB EEP there is treated as a part of the HG. This ensures that the successive phases, such as the core Helium burning phase start at the same EEP for all stars.

As outlined in Section 4.2, low and intermediate-mass stars enter a remnant phase after losing their envelope on the AGB while high-mass stars fuse elements all the way until iron in their core before becoming a remnant. However, modelling the evolutionary phases beyond carbon burning is numerically difficult and the phases themselves are short lived, hardly contributing to the overall evolution of the stars. Hence, we assume that the star has reached the end of its life when it either reaches the end of the detailed track during the AGB phase or when the carbon-oxygen core mass exceeds the maximum allowed core mass (c.f. equation 75 of Hurley et al., 2000):

$$M_{\rm c,SN} = \max\left(M_{\rm ch}, 0.773 M_{\rm c,BAGB} - 0.35\right), \tag{4.1}$$

where $M_{\rm ch}$ denotes the Chandrasekhar mass and $M_{\rm c,BAGB}$ is the core mass at the start of the AGB phase of the star. The stellar parameters at this stage are used to determine the type and the properties of the remnant that the star would form. Corresponding parameters are calculated using the methods described in Section A.2.

At each step, we also check if the star has lost its hydrogen envelope. For massive single stars, this can occur during late evolutionary stages. For low-mass stars this can only occur in binary systems where mass transfer prematurely removes the envelope of the donor star. The evolution of such stripped (naked helium) stars is different compared to other stars and helium star models are needed to follow their subsequent evolution (Pols & Dewi, 2002; Woosley, 2019; Laplace et al., 2020). Currently in METISSE we revert to using the fitting formulae outlined by Hurley et al. (2000) for evolving stars after they lose their envelope. In the future, we will make use of helium star model data in METISSE to treat the evolution of naked helium star phases by interpolating in a set of helium star models in METISSE (as in Spera et al., 2019).

4.4 Stellar models

In order to interpolate a stellar track of a given mass and metallicity, METISSE requires a set of EEP-tracks of the same metallicity. These are calculated with detailed evolutionary codes. In this paper, we make use of stellar models calculated using three different detailed stellar evolution codes. Below we describe these models and how they are converted to EEP form for application in METISSE. Additional details about these models are discussed in Section 4.7.

4.4.1 POLS98 models

The POLS98 models were used for computing the original SSE fitting formulae by Hurley et al. (2000) and were evolved by Pols et al. (1998) using an updated version of the stellar evolution code STARS (Eggleton, 1971). The stellar models cover metallicities between $Z = 0.0001$ and $Z = 0.03$. There are about 25 tracks between 0.5 and $50\,\mathrm{M}_\odot$ for each metallicity. Depending on their initial mass, these tracks have been computed from the ZAMS to different end points. The evolution of massive stars was computed until central carbon ignition. For stars with initial mass less than $1\,\mathrm{M}_\odot$, tracks are complete up to the occurrence of the degenerate helium flash while for intermediate-mass stars the evolution ends at the start of the first thermal pulse on the asymptotic giant branch.

In this paper, we use the sets of tracks labelled as the OVS tracks by Pols et al. (1998). The tracks were computed with enhanced mixing (described in Section 4.7.3) and assume no mass loss due to stellar winds. For application in METISSE, the tracks are converted into the EEP-format by use of critical turning points defined in Table 2 of Pols et al. (1998) and a weighted metric function from Dotter (2016).

4.4.2 MESA models

Modules for Experiments in Stellar Astrophysics (MESA; Paxton et al., 2019) is a modern, open-source stellar evolution code. In order to test METISSE, we have used MESA version 11701 to compute a set of stellar tracks for metallicity $Z = 0.00142$. The set consists of 25 tracks of non-rotating single stars between 9 and $200\,\mathrm{M}_\odot$. The tracks have been computed from the pre-main sequence until carbon depletion ($X_c \leq 10^{-4}$) in the core, although for the purposes of testing METISSE, only the phases after the ZAMS are relevant.

When computing these tracks, we have used the physical inputs described in Chapter 3 except for the mass-loss rates, overshooting parameters, and the use of MLT++, which are described separately in Section 4.7 of this paper. Output tracks from MESA have been converted into EEP-format with ISO (Dotter, 2016).

4.4.3 BEC models

The Bonn Code, which we refer to as 'BEC' in this paper, is a detailed stellar evolution code which has been used in the last decades in various science projects (see e.g. Heger, Langer, & Woosley, 2000, Petrovic et al., 2005, Yoon, Langer, & Norman, 2006 and references therein). Here we apply a set of models computed with this code and published in the BoOST project (Szécsi et al., 2020). These models are slowly rotating (at about $100\,\mathrm{km\ s^{-1}}$) and have been computed from the ZAMS until the end of core helium burning.

The BoOST project published stellar models as well as interpolated tracks between these models. Here we have made use of only the former. We use their dwarfA set of models which have a metallicity $Z = 0.00105$. The tracks are optimized for astrophysical applications such as population synthesis and the format of the published models does already fulfil the requirements of the EEP-tracks.

4.5 Testing METISSE with POLS models

The main requirement of a synthetic stellar evolution code such as METISSE is for the interpolated tracks to replicate the underlying detailed evolutionary tracks as closely as possible. In this section we check the accuracy of METISSE by comparing its output with the detailed models and we also compare the results obtained by METISSE with those by SSE (Hurley et al., 2000). To make a direct comparison with SSE, the stellar tracks generated with METISSE use the set of detailed tracks by Pols et al. (1998) as input. Because the input models do not include mass loss in stellar winds, all the results shown in this section, with both SSE and METISSE, do not have mass loss enabled either, except during the formation of the remnant (in the form of planetary nebula or supernova ejecta, cf. Sections A.2 and 4.3.2).

4.5.1 Accuracy of interpolated tracks

To test the quality of tracks computed with METISSE, we interpolated evolutionary tracks for certain initial masses present in the Pols et al. (1998) set of detailed models. Usually, if an EEP-track is already present in the set of input tracks, METISSE would simply return that track and would not perform an interpolation in mass. Hence, we sequentially removed the detailed track for each input mass from the set before interpolating a new track. The interpolated tracks and the corresponding detailed tracks from Pols et al. (1998) are shown in Fig. 4.2.

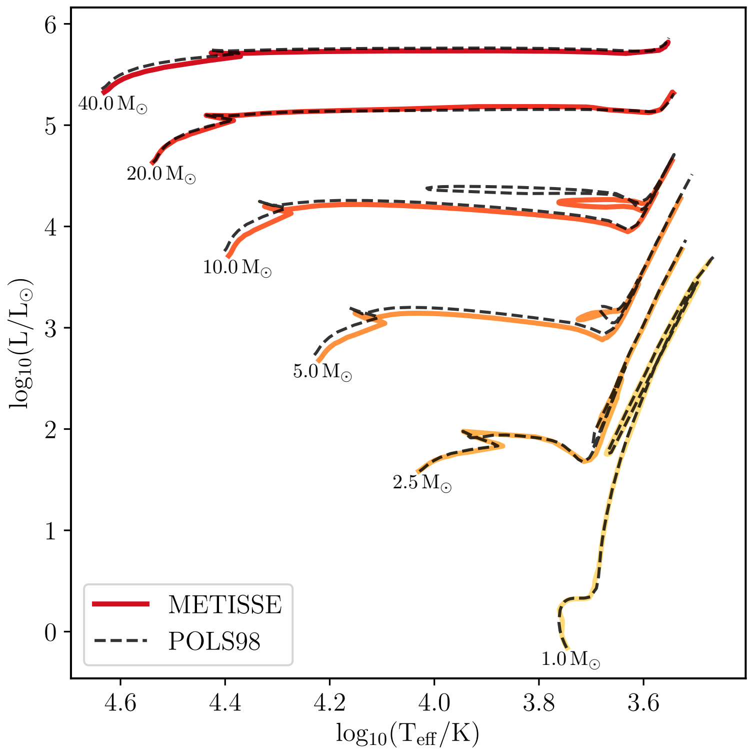

Figure 4.2 HR diagram showing tracks interpolated by METISSE (solid lines) with detailed tracks by Pols et al. (1998) and the detailed tracks themselves (dashed lines) for a metallicity of $Z = 0.02$. For each mass, the detailed track was removed from the set before performing interpolation.

We find that the tracks interpolated by METISSE are in good agreement with the detailed tracks. To quantify this agreement we calculate the relative difference in luminosity (L) and surface temperature ($T_{\rm eff}$) between detailed and mass interpolated EEP tracks. For most evolutionary phases, the average difference between the track interpolated with the Steffen (1990) scheme and the detailed track is less than 3 per cent for both quantities. For the core helium burning (blue loop) phase the variation in L can be up to 10 per cent. The greatest dissimilarity occurs if the input mass is close to a critical mass (cf. Section A.1). In Fig. 4.2, the $5\,\mathrm{M}_\odot$ track falls near the critical mass above which C ignition can occur non-degenerately in the core while the $10\,\mathrm{M}_\odot$ track falls near the critical mass above which He ignition occurs on the HG. Unlike the other tracks, where third order interpolation has been used, these two tracks have been linearly interpolated from their neighbouring tracks and in this case the average difference can be as high as 21 per cent in L and 13 per cent in $T_{\rm eff}$ during the core helium burning phase.

We note that the quality of interpolation also depends on the density and the completeness of the input tracks (cf. Section 4.8). For a denser grid of stellar models, tracks interpolated by METISSE mimic detailed tracks even more closely.

4.5.2 Comparison with SSE

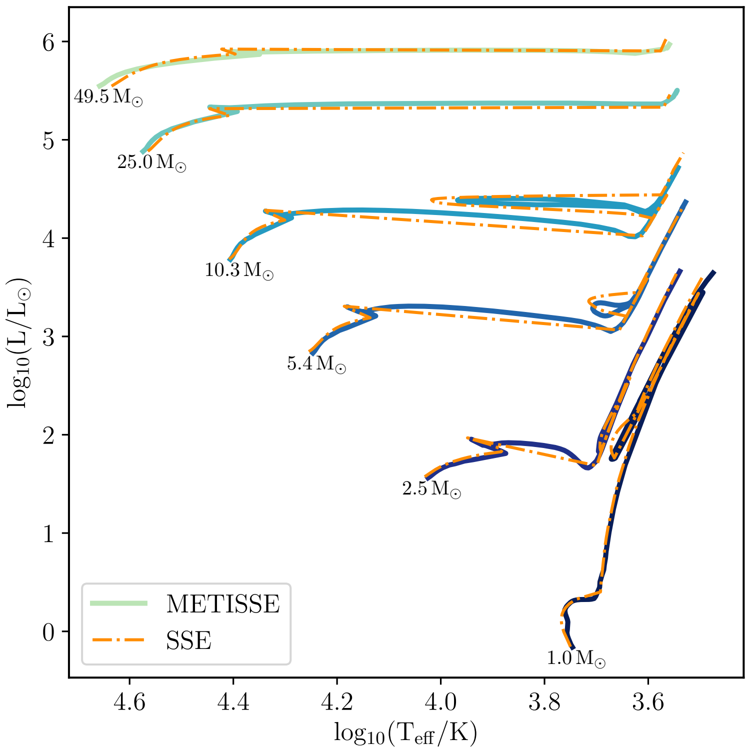

Figure 4.3 HR diagram comparing tracks interpolated by METISSE (solid lines) with tracks computed by the fitting formulae of SSE (dashed lines) for metallicity $Z = 0.02$. Both methods use detailed tracks by Pols et al. (1998) as input and assume no mass loss in stellar winds.

Any two methods of synthetic stellar evolution using the same input data should be able to produce matching output. Hence in Fig. 4.3, we compare the tracks interpolated by METISSE using Pols et al. (1998) models and tracks generated by SSE for the same

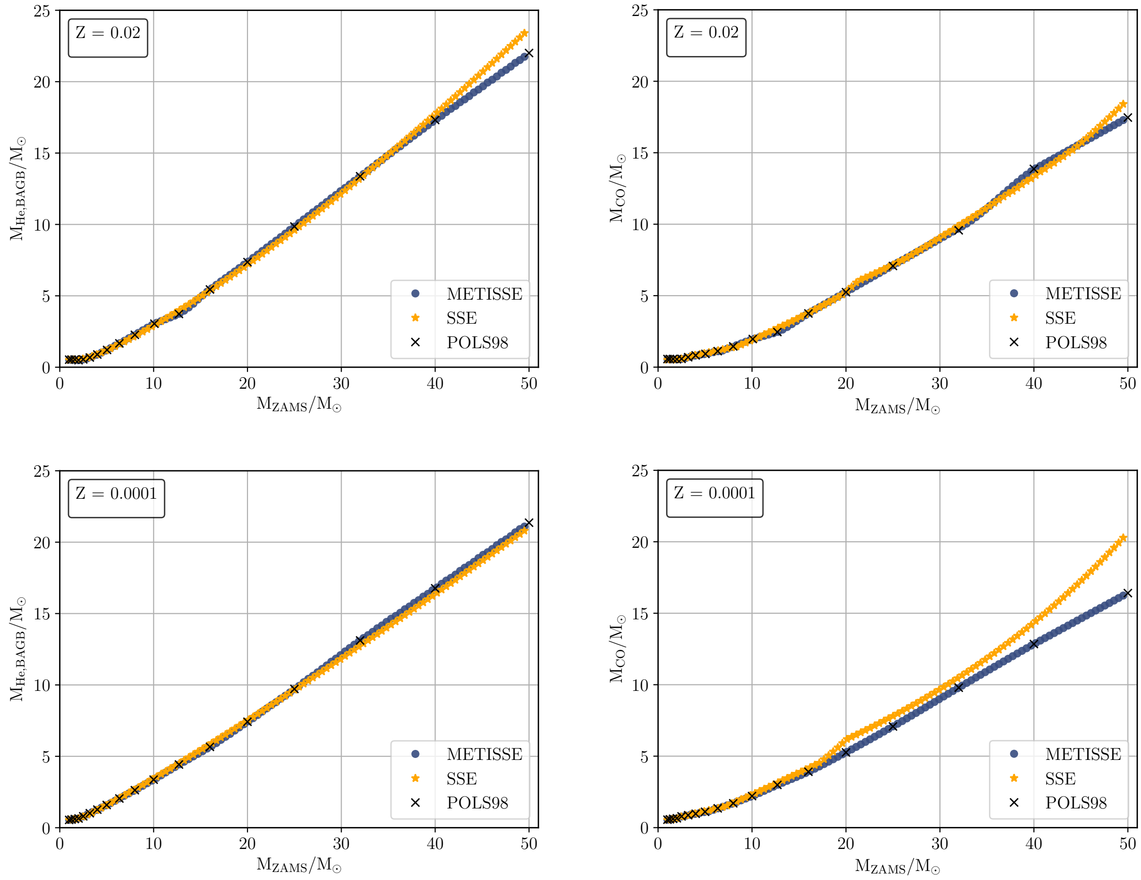

Figure 4.4 He-core mass at the base of the AGB ($M_{\mathrm{He,BAGB}}$: left panels) and CO-core mass at the end of AGB (M_{CO}: right panels) as a function of the ZAMS mass (M_{ZAMS}) of the star for different metallicities (Z, as indicated in each panel). Star symbols show the values predicted by SSE while circles denote the values predicted by METISSE for a uniform distribution of stars of initial mass between 1 and 50 $\mathrm{M}_\odot$, assuming no mass loss due to stellar winds. Corresponding values from Pols et al. (1998) are marked as a cross.

input mass and metallicity ($Z = 0.02$). Because the set of stellar models used by the two codes is the same, the difference in the tracks simply reflects the difference between the use of fitting formulae and that of using interpolation. As is evident from the figure, METISSE is able to better preserve the finer details in the tracks, for example those during the Hertzsprung Gap.

These seemingly tiny details in the tracks can lead to non-trivial dissimilarities in predicting other stellar properties. To show this, in Fig. 4.4, we plot the He core mass of stars at the base of the AGB (corresponding to the TAcHeB EEP) and the CO core mass at the end of AGB (corresponding to the TPAGB EEP for low and intermediate-mass stars, and C ignition for massive stars) as predicted by METISSE and by SSE for stars in the mass range 1 to $50\,\mathrm{M}_{\odot}$ with metallicities $Z = 0.02$ and $Z = 0.0001$. For $Z = 0.02$ the core masses predicted by METISSE agree well with SSE. There are some discrepancies in the prediction of CO core mass for stars with initial mass greater than about $40\,\mathrm{M}_{\odot}$. The differences are larger for lower metallicity ($Z = 0.0001$) and extend down to $20\,\mathrm{M}_{\odot}$ stars.

These differences are a result of how the evolution of the CO core is treated in each code. On the AGB, the CO core of a star grows in size owing to He-shell burning. If the star is massive enough, the core at some point can reach sufficient conditions to ignite carbon and the mass of the CO core can decrease. In SSE, the evolution of the CO core of a star has been simplified, allowing the CO core mass to grow until it reaches $M_{\mathrm{c,SN}}$ (Equation 4.1). On the other hand, METISSE makes no prior assumptions and relies on the input set of detailed models to provide information about the CO core mass of the interpolated track. It can, therefore, more accurately relay the behaviour of the CO core that has been computed in the detailed input stellar models. This illustrates the reliability of stellar parameters computed with METISSE.

4.5.3 Timing and performance

In METISSE, input tracks from the chosen detailed evolution code need to be read and loaded in the computer memory before any interpolation can be performed. Depending on the density of the input set of models, the memory requirement can be of the order of Megabytes to Gigabytes. The memory required depends not only on the number of tracks but also on the amount of data read for each track.

The number of data columns from the input tracks can be easily controlled by the user in METISSE. By selecting fewer columns, one can speed up the runs and reduce memory usage. This is useful for simulating systems with millions of stars (e.g. globular clusters in N-body simulations). If more surface abundances are needed, for example, to trace the evolution of different elements in stellar populations, the columns can be included from the detailed stellar models with only a modest increase in the memory usage and computing time.

To compare the performance of METISSE with SSE, we computed 10 to 10^5 stellar

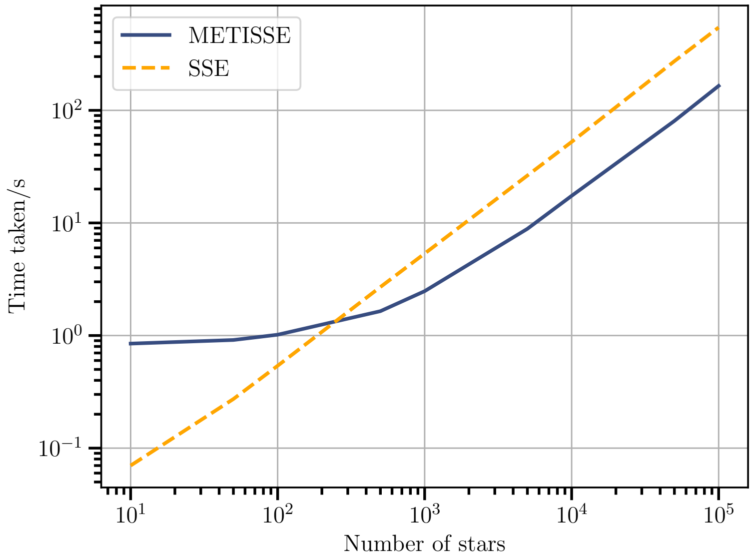

Figure 4.5 Timing METISSE: solid line represents the time taken by METISSE while the dashed line is the time taken by SSE as a function of number of stars evolved. The timing is for a single 2.3 GHz Intel i5 core.

tracks between 1 and 50 $M_\odot$, evolving each star up to 12 Gyr for each method. For a fair comparison, the input set of tracks and data columns used by METISSE were kept the same as in SSE. In Fig. 4.5, we show the average time taken by METISSE compared to that by SSE to evolve different numbers of stars. For SSE the increase in run-time with the number of stars is linear. METISSE requires more time (0.8 s here) in the beginning to process the set of input tracks, independent of the number of stars evolved. Hence, for fewer stars, METISSE takes longer than SSE to complete the run. For larger populations however, the time taken to process the input tracks becomes a negligible fraction of the total run time and METISSE becomes almost three times faster than SSE.

It is necessary to emphasize here that like memory, the time taken by METISSE does increase depending on the number of input stellar tracks. Overall, it can be safely concluded that at the very least METISSE is comparable to SSE in terms of performance.

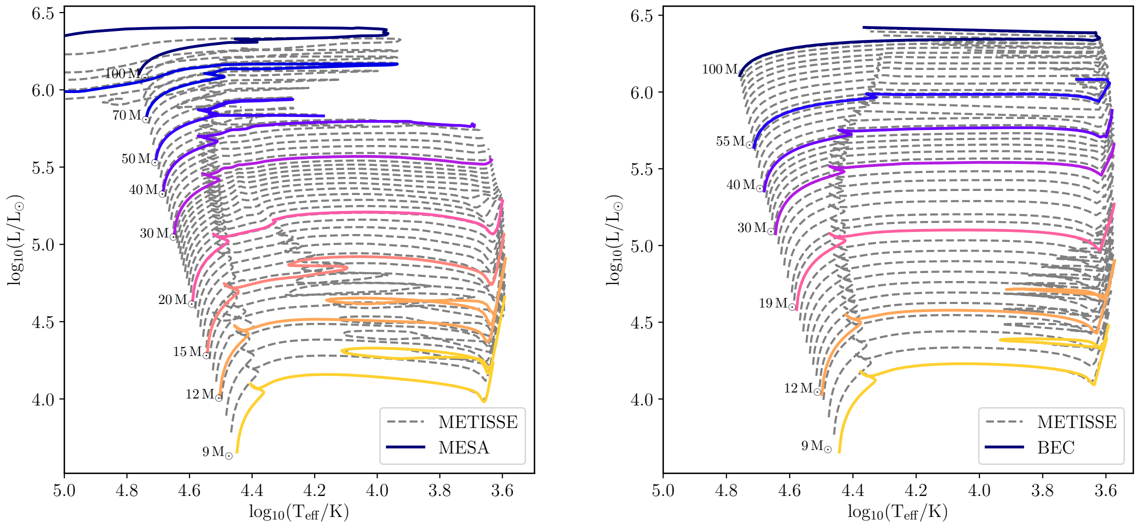

Figure 4.6 HR diagram showing tracks in the mass range 9 to 100 $M_\odot$ interpolated with METISSE with detailed tracks from MESA (for $Z = 0.00142$, left panel) and tracks from BEC (for $Z = 0.00105$, right panel) as input. For clarity, only selected tracks from each set are shown.

4.6 METISSE with MESA and BEC: Predicting properties of massive stars

Massive stars are responsible for the chemical enrichment of their surroundings. They are precursors of astrophysical transient phenomena including supernovae and gamma-ray bursts, progenitors of compact objects. As these stars are rare in nature, their evolutionary parameters, such as mass-loss rates, mixing processes and nuclear reaction rates, are not very well constrained (see, for example, Farmer et al., 2016; Renzo et al., 2017; Fields et al., 2018). Therefore stellar evolution codes make certain assumptions about the interior and physics of these stars which can lead to different evolutionary outcomes. In order to check the validity of these assumptions, it is necessary to compare their predictions with observations of massive stellar populations. For this one needs to be able to apply different stellar evolution models in population synthesis codes.

Built exactly for this purpose, METISSE can read different sets of evolutionary tracks, including those generated by different stellar evolution codes. The only requirement is that the input tracks should be in the EEP format. In this section, we demonstrate the capability of METISSE to use sets of evolutionary tracks evolved using BEC and MESA. We apply the sets of stellar models introduced in Sections 4.4.2 and 4.4.3 respectively, as an input to METISSE and interpolate 100 stars uniformly distributed in mass between 9 and 100 $M_\odot$ at metallicity $Z = 0.00142$ for MESA tracks and $Z = 0.00105$ for BEC tracks. The HR diagram for a subset of both the detailed and interpolated tracks is shown in Fig. 4.6. We use the results presented in this section to explore the impact of stellar evolution parameters on the evolution of massive stars.

We also compare said outcomes to those obtained using SSE for $Z = 0.00142$. For SSE the maximum mass of the detailed tracks used for calculating the fitting formulae was about 50 $M_\odot$. Stars above this mass are calculated by extrapolating the fitting formulae from less massive stars. Moreover, detailed tracks of Pols et al. (1998) do not include wind mass loss. Consequently, mass-loss in SSE is modelled by removing the mass from the stellar envelope. We have used the mass-loss rates of Belczynski et al. (2010) in the SSE tracks presented here.

4.6.1 Impact on remnant mass

Massive stars are the progenitors of compact objects: neutron stars and black holes whose mergers result in the emission of gravitational waves observable by LIGO/Virgo (Abbott et al., 2016). Therefore, the ability to accurately predict stellar remnant masses is crucial. The remnant masses can be calculated from the total mass and the core properties of the stars using prescriptions such as those in Fryer et al. (2012).

For tracks interpolated with METISSE using MESA and BEC models, we calculate the mass of stellar remnants in the manner outlined in Section A.2. We have followed Belczynski et al. (2008) for calculating the mass of remnants (same as StarTrack prescription in Fryer et al., 2012). For stars with final CO core mass less than 5 $M_\odot$, the prescription yields a remnant mass based on the iron-nickel (FeNi) core mass of the star while for stars with CO cores more massive than 7.6 $M_\odot$, it is assumed that the whole star collapses to form a black hole. In between the two regimes, partial fallback from the star is assumed and the mass of the remnant follows a linear fit between the FeNi core mass and the total mass of the star. The FeNi core mass itself is calculated from the CO core mass. To account for mass lost due to neutrino cooling of stellar cores before the supernova explosion,

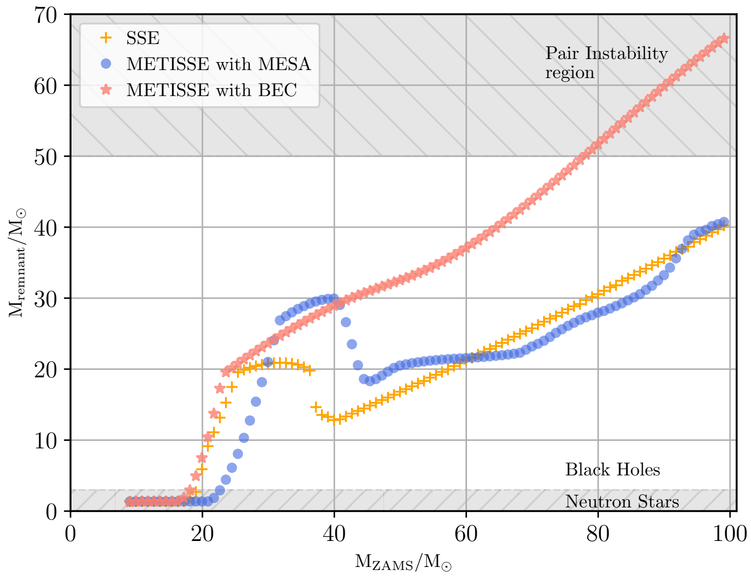

Figure 4.7 The mass of stellar remnants versus the mass of their progenitors, as predicted by SSE (yellow crosses), METISSE with MESA (blue circles) and METISSE with BEC (red stars). The grey area above $50\,M_{\odot}$ shows the region where stars may encounter pair instability. See section 4.6.1 for details.

the baryonic mass of the remnant obtained above is converted to its gravitational mass (following Equations 3 and 4 of Belczynski et al., 2008). This simple model assumes no mass gap (Özel et al., 2010; Farr et al., 2011) between neutron stars and black holes.

Following Belczynski et al. (2008) we suppose the maximum neutron star mass to be $3\,M_{\odot}$ in this work, although the maximum observed is $2.14\,M_{\odot}$ (Cromartie et al., 2020). The relationship between core mass and remnant mass may not follow this simple relation; recent works have suggested that in some mass ranges, certain stars may form neutron stars while others form black holes (e.g. Sukhbold & Woosley, 2014; Ertl et al., 2016; Sukhbold & Adams, 2020).

In Fig. 4.7, we plot the results in terms of remnant mass obtained using SSE, METISSE with MESA models and METISSE with BEC models against ZAMS mass of their progenitors. For the BEC models, stars with initial masses greater than $80\,M_{\odot}$ have final core masses greater than $50\,M_{\odot}$. Stars with core masses from about 50 to $130\,M_{\odot}$ are expected to encounter the well-known pair instability condition during their post-He-burning evolution (typically during O-burning), leading to enhanced mass loss or total destruction of the star (Fowler & Hoyle, 1964; Fraley, 1968; Woosley, 2017; Stevenson et al., 2019). Currently, we do not take into account the effect of pair instability or pulsational pair instability when predicting remnant masses in METISSE but, for reference, the region where pair instability becomes relevant is highlighted in the figure.

We find that there is a striking variation in remnant mass predicted by SSE and both the MESA and BEC models in METISSE. For stars with ZAMS mass between 9 and $18\,\mathrm{M}_\odot$, the three sets of tracks agree well. For stars with ZAMS masses between 19 and $30\,\mathrm{M}_\odot$, there is a linear increase in the remnant mass owing to partial fall-back of matter on to the collapsing core during the supernova explosion. For MESA tracks the rise in remnant mass is slower than the other two sets of tracks and peaks at around a $40\,\mathrm{M}_\odot$ ZAMS mass while for SSE the local maximum occurs around $30\,\mathrm{M}_\odot$. BEC tracks do not show any such decline and the difference in the remnant mass between MESA and BEC becomes pronounced (about $20\,\mathrm{M}_\odot$) for stars with a ZAMS mass more than $40\,\mathrm{M}_\odot$.

The mass of the remnant is clearly influenced by the choice of stellar models and the different choices of stellar parameters adopted therein. We discuss these differences, their origins and their impact on the remnant masses in Section 4.7.

4.6.2 Impact on radius evolution

Most stars expand as they evolve, becoming giants. This is especially important for stellar evolution in binary systems because the expanding star can fill its Roche lobe and initiate a phase of mass transfer in the system. Hence, accurately predicting the extent of radial expansion for a star is necessary to determine the evolution of binary systems.

In Fig. 4.8, we plot the maximum radii of stars uniformly distributed in mass between 9 and $100\,\mathrm{M}_\odot$ calculated with MESA and BEC models in METISSE and with SSE. Similar to Fig. 4.7, there is disparity between the results obtained with the three sets of tracks. For SSE and BEC the maximum radial expansion achieved by the stars increases with initial mass (aside from a slight decrease for SSE near $15\,\mathrm{M}_\odot$). For MESA tracks however, the trend changes considerably beyond $40\,\mathrm{M}_\odot$: the maximum radius decreases until $55\,\mathrm{M}_\odot$ reaching a minimum of about $100\,\mathrm{R}_\odot$ before slowly increasing for more massive stars.

The lower radii predicted by the various models impact the outcome of close binary interaction. The number of interacting binaries with orbital separations that lie within

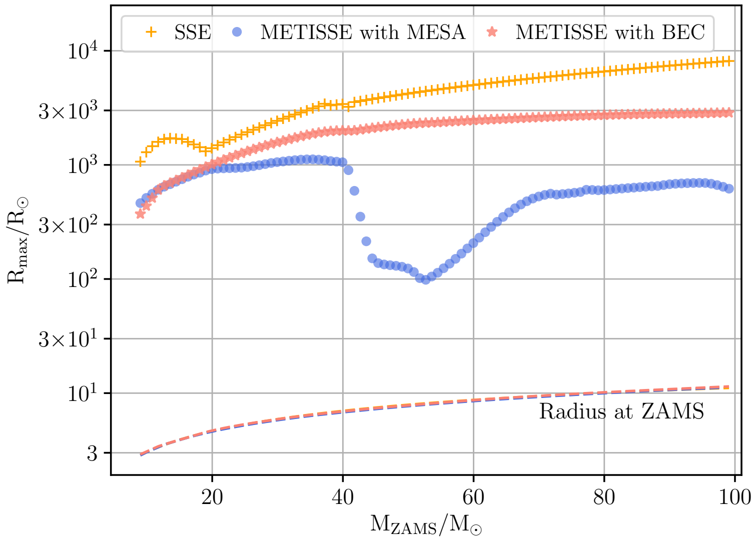

Figure 4.8 Maximum radii obtained by stars as a function of their ZAMS mass, symbols are the same as in Fig. 4.7. The dashed lines (indistinguishable here) represent the ZAMS radius for each of the three sets.

the range between the minimum radius (R_{min}) and the maximum radius (R_{max}) of the star can be given by

$$N = \int_{R_{\rm min}}^{R_{\rm max}} \frac{dN}{da} da\,. \tag{4.2}$$

Assuming a distribution of binary orbital separations a that is flat in $\log a$ (Öpik, 1924; Abt, 1983), $dN/da \propto 1/a$, for Equation 4.2 we can write

$$N \propto \int_{R_{\rm min}}^{R_{\rm max}} \frac{1}{a} da = [\ln a]_{R_{\rm min}}^{R_{\rm max}} = \ln R_{\rm max} - \ln R_{\rm min}\,. \tag{4.3}$$

Therefore, the ratio between the number of interacting binaries predicted by for example MESA to SSE can be given as

$$\frac{N^{\rm SSE}}{N^{\rm MESA}} = \frac{\ln R_{\rm max}^{\rm SSE} - \ln R_{\rm min}^{\rm SSE}}{\ln R_{\rm max}^{\rm MESA} - \ln R_{\rm min}^{\rm MESA}}\,. \tag{4.4}$$

We applied Equation 4.4 to each stellar track in the three sets. On average, SSE predicts 1.6 times more interacting binaries than METISSE with MESA. Doing a similar exercise using the BEC tracks, we find that SSE predicts 1.3 times more interacting binaries than METISSE with BEC. Both numbers are comparable to differences in uncertainties in the initial conditions of binaries (de Mink & Belczynski, 2015; Klencki et al., 2018). The difference can be larger for the most massive stars. E.g. for a 60 $M_\odot$ star, SSE predicts 2.3 times more interacting binaries than MESA, and 1.4 times more than BEC. However, to account for the fact that massive stars are less common in nature, we weight the above average by an initial mass function with a power law index of $\alpha = -2.3$ for masses above 1 $M_\odot$ (Salpeter, 1955; Kroupa, 2001). For this more realistic population of binaries, SSE still predicts 1.25 times more interacting binaries than MESA and 1.18 times more interacting binaries than BEC. We further discuss the origin of these differences Section 4.7.

4.6.3 Impact on main-sequence lifetime

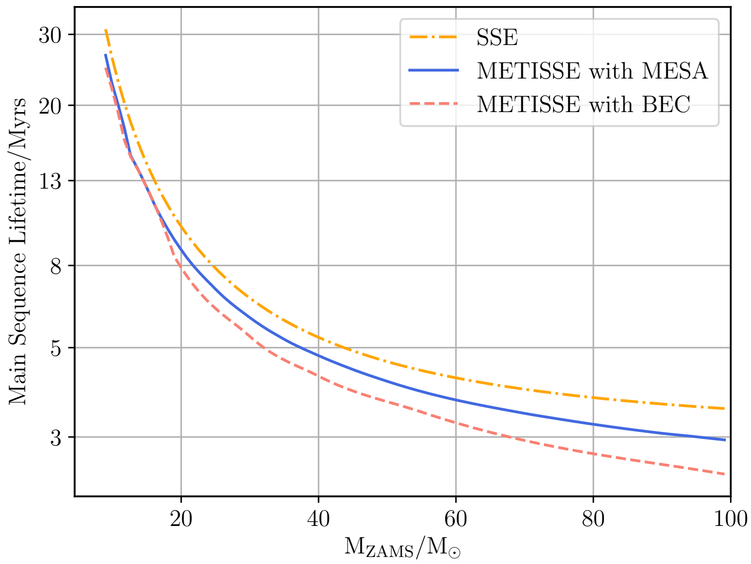

Figure 4.9 Main-sequence lifetime of stars as a function of their ZAMS mass, as predicted by SSE (dashed dotted line), METISSE with MESA tracks (solid line) and METISSE with BEC (dashed line).

Young massive star clusters are instrumental in the study of stellar dynamics and the stellar mass function (Portegies Zwart, McMillan, & Gieles, 2010). A key method for determining the age of star clusters is to use the main-sequence turnoff age which requires estimation of the main-sequence lifetime of stars (Pols et al., 1998; Kalirai & Richer, 2010). The MS lifetime can differ between models owing to the difference in the treatment of mixing processes inside the star. Processes like convection and overshooting can help replenish H supply in the core, prolonging the time spent in the MS phase. Mixing parameters are often calibrated using values from a solar model and might not be applicable to massive stars (Joyce & Chaboyer, 2018). Differences in the MS lifetimes of massive stars, as predicted by different sets of tracks, can be useful to explain phenomena such as extended main-sequence turnoffs and the age spread observed in young massive star clusters (Johnson et al., 2001; Li et al., 2017).

In Fig. 4.9, we plot the time spent on the MS by stars of mass 9 to 100 $\mathrm{M}_{\odot}$ as predicted by SSE, METISSE with MESA and METISSE with BEC. The difference in predicted lifetimes varies from about 0.5 Myr for a 40 $\mathrm{M}_{\odot}$ star to about 4 Myr for a 9 $\mathrm{M}_{\odot}$, between each set. This corresponds to roughly 10 to 20 per cent of the total time spent in the MS phase. In Section 4.7.3, we discuss the effect on the MS lifetimes arising from differences between the treatment of convection and the choice of the overshooting parameters adopted in the input stellar models.

4.7 Understanding the differences between input stellar models

As METISSE relies on having an input set of detailed models to provide information about the interpolated track, the difference in the properties of massive stars obtained with MESA and BEC models in METISSE pointed out in Section 4.6 can be attributed to the input parameters employed while computing the detailed stellar models.

In this section we discuss the role of three major contributors (i) modelling of radiation dominated envelopes of massive stars, (ii) mass-loss rates and (iii) convection and overshooting parameters. Although other factors such as rotation, chemical composition and surface boundary conditions can also have an impact on the structure and evolution of massive stars, the discussion of these requires dedicated future studies.

4.7.1 Massive stellar envelopes and the role of the Eddington luminosity

The Eddington limit for a spherically symmetric star in hydrostatic equilibrium is defined as the maximum outward radiative motion of stellar material that can be balanced by the inwards acting gravitational force (Eddington, 1926; Owocki, Gayley, & Shaviv, 2004).

For a star containing mass $m(r)$ inside radius r and radiative opacity $\kappa(r)$, the expression for the Eddington luminosity is given by

$$L_{\mathrm{Edd}}(r) = \frac{4\pi c G m(r)}{\kappa(r)}\,. \tag{4.5}$$

Hence a critical limit, known as the Eddington factor can be defined (following Langer, 1997) as

$$\Gamma = \frac{L(r)}{L_{\mathrm{Edd}}(r)} = \frac{\kappa(r)}{4\pi c G}\frac{L(r)}{m(r)}\,. \tag{4.6}$$

For massive stars, the luminosity inside the stellar envelope can exceed the Eddington limit ($\Gamma > 1$) due to elemental opacity peaks (Iglesias, Rogers, & Wilson, 1992; Cantiello, Langer, Brott, de Koter, Shore, Vink, Voegler, Lennon, & Yoon, 2009), e.g, towards the end of the main sequence. Moreover, the outer envelopes of massive stars are dominated by radiation pressure and the convective transport of energy given by standard Mixing Length Theory (MLT; see Section 4.7.3) becomes inefficient. As shown by Joss, Salpeter, & Ostriker (1973), $\Gamma > 1$ combined with inefficient convection can lead to pressure and density inversion inside the stars, $dp/dr > 0$ and $d\rho/dr > 0$. This means that density and gas pressure increases outwards for massive stars with super-Eddington luminosity in their outer envelopes and can cause numerical difficulty in modelling stars with 1D stellar evolution codes (Paxton et al., 2013). To push the evolution of a star beyond this point, 1D stellar evolution codes adopt different approximations.

In the BEC stellar models, density and pressure inversion inside the stellar envelope causes the hydrostatic expansion of the outermost layers of the star (envelope inflation, Sanyal et al., 2015, 2017). The stellar models develop an extended, tenuous envelope in response to temperature and density inversions until the Eddington limit is no longer exceeded. The star becomes a supergiant[1] even while burning hydrogen in the core which affects its structure and evolution. The small time-steps required to resolve the inflated envelope of a star on the hydrodynamical time-scale pose a numerical difficulty for the post-main-sequence evolution (Sanyal et al., 2015). The BEC track with initial mass of $100\,\mathrm{M}_\odot$ here has been post-processed in the framework of the BoOST project to include

[1]As pointed out by Szécsi et al. (2015), core-hydrogen burning cool supergiants are different from the usual red supergiants which expand in response to H-shell burning.

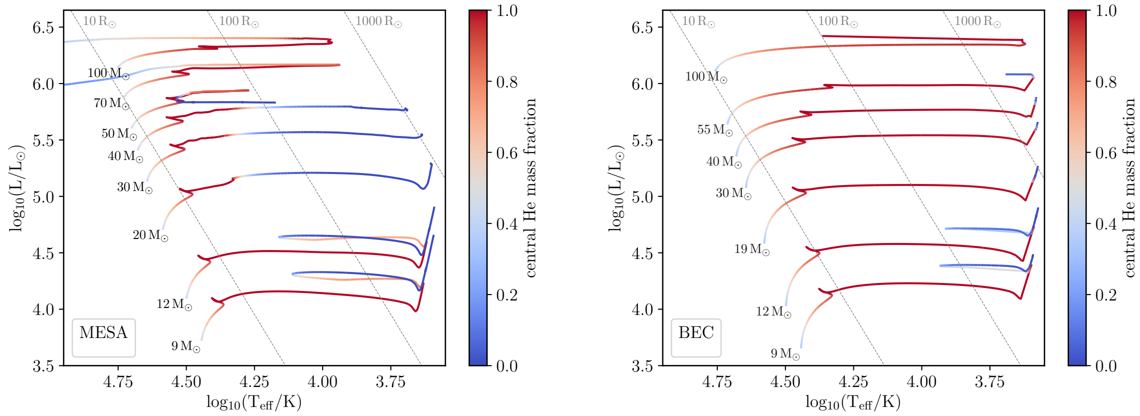

Figure 4.10 HR diagrams showing stellar tracks evolved using MESA (left) and BEC (right) and coloured according to their central helium mass fraction. For clarity, only nine (out of the 25 computed in this work) MESA tracks are shown here. The differences in the tracks are due to different physical inputs, as discussed in Section 4.7.

a smooth approximation of the core helium burning phase (see Szécsi et al., 2020, for details).

In MESA, the density and pressure inversion can be mitigated through a formalism known as MLT++. For each model, MESA calculates (cf. equation 38 of Paxton et al., 2013):

$$\lambda_{\text{max}} \equiv \max\left(\frac{L_{\text{rad}}}{L_{\text{Edd}}}\right) \quad \text{and} \quad \beta_{\text{min}} \equiv \min\left(\frac{P_{\text{gas}}}{P}\right). \tag{4.7}$$

Based on these parameters, MESA can artificially decrease the superadiabaticity (the difference between the isothermal and adiabatic temperature gradients) when stars approach their Eddington limits. Adopting the MLT++ formalism helps with the convergence of the models. However it can modify the radius and luminosity of the star and hence affect the mass-loss rates (Paxton et al., 2013). MESA models in this work make use of the MLT++ formalism. Radiative pressure at the surface of the star is also enhanced to help with convergence of the model.

To investigate the effect of Eddington limit proximity on the stellar models, we plot the detailed stellar tracks from MESA and BEC in Fig. 4.10. Each track is coloured based on the He fraction in the centre of the star to show the location of the star during core He burning. The figure shows that stars evolved with MESA burn helium at higher temperatures and smaller radii compared to BEC where stars burn He at lower temperatures

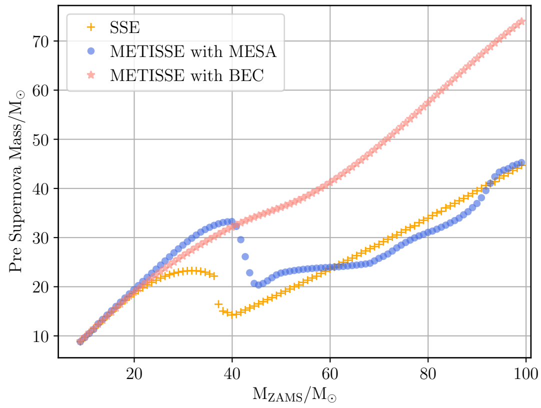

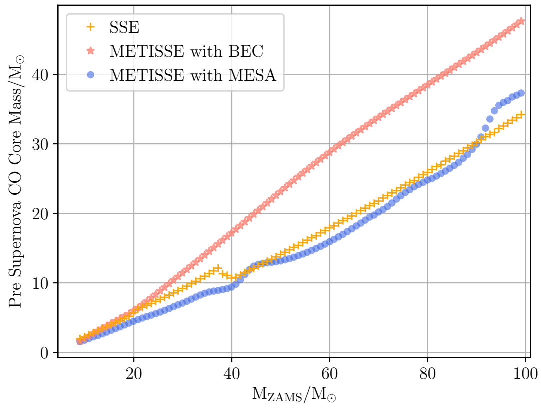

Figure 4.11 Pre-supernova mass *(left)* and final CO core mass *(right)* of stars as a function of their ZAMS mass, symbols are the same as in Fig. 4.7.

and larger radii.

With MESA, a $50\,M_\odot$ star approaches the Eddington limit at the end of the main sequence. The proximity to the Eddington limit causes the star to experience high mass-loss rates which expose the hotter inner layers and the star moves bluewards in the HR diagram. The onset of H-shell burning causes the star to expand, lowering the surface temperature, making it lose even more mass. Therefore, local minima for both remnant masses and maximum radii are encountered for the tracks interpolated from MESA models in this region (i.e. about 45 to $55\,M_\odot$ stars in Fig. 4.7 and Fig. 4.8). Stars more massive than $60\,M_\odot$ lose their envelope in MESA and become naked He star before they can finish burning He.

In Fig. 4.11 we plot the total mass and the core mass of stars (before supernova explosion) with respect to their initial mass as given by SSE, METISSE with MESA models and METISSE with BEC models. The total masses for MESA and BEC tracks show only a small variation until $40\,M_\odot$. Beyond $40\,M_\odot$, stars evolved with MESA start experiencing increased wind mass-loss rates owing to their proximity to the Eddington limit and hence end up with a lower mass. Stars evolved with BEC in the 40 to $100\,M_\odot$ range undergo envelope inflation as they encounter the Eddington limit inside the envelope. They experience owing due to the cool supergiant phase (see details in Section 4.7.2). None of the stars in the BEC models used here lose their envelope completely. Hence their remnant masses and maximal radii increase almost linearly in this region and are higher than those of MESA tracks.

The extrapolation of stellar models in the BEC and the MLT++ method of MESA are numerical solutions employed to push forward the evolution of massive stars when they encounter the Eddington limit. A more accurate treatment of the super-Eddington limit in 1D stellar evolution codes is not available. In fact, recent 3D simulations show that the 1D stellar evolution codes might not be modelling these envelopes accurately at all (Jiang et al., 2015, 2018). Note that METISSE provides enough flexibility that, if new stellar models with an updated treatment of Eddington limit proximity are published in the future, it will be straightforward to use them with METISSE.

4.7.2 Mass loss schemes

Depending on the mass, the chemical composition and the evolutionary phase of a star, mass loss through stellar winds can have a considerable effect on the evolution of stars. For massive stars, wind mass loss and its role in stellar evolution is particularly important (see e.g. Smith, 2014; Renzo et al., 2017).

Proximity to the Eddington limit on the stellar surface can also lead to departure from hydrostatic equilibrium and possible turbulence and mass outflows that exhibit as enhanced stellar winds (Humphreys & Davidson, 1994; Owocki et al., 2004). Although very massive stars (in the form of luminous blue variables) have been observed to undergo such high wind mass loss episodes, the presence of super-Eddington winds and their exact contribution is unconfirmed and remains a debated topic in the literature (Langer, 1997; Smith, 2017).

The MESA models used here are computed with mass-loss rates from Vink et al. (2001) for $T_{\rm eff} > 10\,000\,$K and de Jager, Nieuwenhuijzen, & van der Hucht (1988) for $T_{\rm eff} < 10\,000\,$K. In addition, they include a contribution to mass loss by super-Eddington winds. We find that the super-Eddington mass-loss rate calculated in the default MESA can be extremely high (about $10^{-2}\,{\rm M_\odot\,yr^{-1}}$). Hence we scale down the super-Eddington wind mass loss by a factor of 10 and only apply it whenever the surface luminosity exceeds 1.1 times the mean Eddington luminosity (mass-weighted average of $L_{\rm Edd}$, see Equation 4.5, from the surface up to the region with optical depth of 100). Additionally, the maximum mass-loss rate we allow is capped to $1.4 \times 10^{-4}\,{\rm M_\odot\,yr^{-1}}$ following Belczynski et al. (2010).

The BEC tracks also include mass-loss rates of Vink et al. (2001) for $T_{\rm eff} > 22\,000$ K. Below this, the mass-loss rate of Nieuwenhuijzen & de Jager (1990) is applied whenever it exceeds the rate of Vink et al. (2001). Although an enhancement of the mass loss due to rotation is an option in BEC as per Yoon & Langer (2005), the models here are slowly rotating (at 100 km s^{-1}) and thus the rotational enhancement of mass loss (which becomes important when the star rotates close to the Keplerian critical rotational rate) does not contribute significantly.

To examine the effect of the above schemes on the results obtained in Section 4.6 we plot the total mass of stars during different evolutionary phases in Fig. 4.12. We find that for both MESA and BEC, most of the mass loss happens towards the end of the core hydrogen burning (MS) and core helium burning (cHeB) phases. Towards the end of the main sequence, when BEC models become H-burning cool supergiants, the major contribution to mass loss comes from the supergiant mass-loss rates of Nieuwenhuijzen & de Jager (1990). Stars evolved with MESA, on the other hand, either experience mass loss according to Vink et al. (2001) or through super Eddington winds, depending on whether their surface luminosity exceeds the Eddington limit by 10 per cent.

As shown in Fig. 4.10, MESA models at $20\,M_\odot$ and above burn helium at different effective temperatures to those from the Bonn code, and therefore experience a different kind of mass-loss treatment. The massive stars in the BEC tracks experience mass-loss rates of Nieuwenhuijzen & de Jager (1990) during core helium burning due to their low effective temperatures but now at high luminosity. Hence, they lose more mass during this phase than towards the end of the main sequence. The MESA tracks up to $40\,M_\odot$ demonstrate moderate mass loss during cHeB because the models continue their slow transition from Vink et al. (2001) to de Jager et al. (1988) mass-loss rates. More massive stars with MESA, those experiencing super-Eddington winds, can lose their envelopes completely and become naked helium stars when this major mass-loss episode kicks in during cHeB. The remainder of the evolution of such stars is performed with fitting formulae for helium star models from SSE and the mass-loss scheme of Hamann et al. (1995) is applied (see Section 4.3.2 for details). We find that MESA stars do not spend much time in this phase and, as shown in Fig. 4.12, hardly lose any mass.

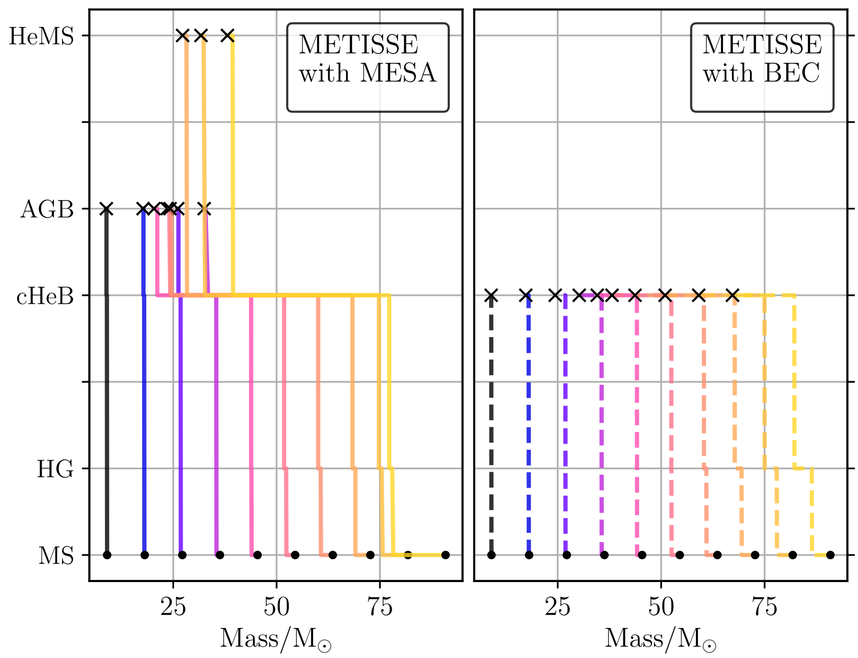

Figure 4.12 Mass of the star at different evolutionary phases calculated by METISSE with MESA (left panel, solid lines) tracks and BEC tracks (right panel, dashed lines). For each star, the dot represents the initial mass and the cross represents the pre-supernova mass. For explanation see Section 4.7.2

For SSE tracks, mass-loss rates have been calculated by Belczynski et al. (2010). Stars above $38\,\mathrm{M}_\odot$ experience mass loss at $1.5 \times 10^{-4}\,\mathrm{M}_\odot\,\mathrm{yr}^{-1}$ whenever the surface luminosity (L) exceeds $10^5\,\mathrm{L}_\odot$ and radius (R) satisfies $10^{-5}RL^{0.5} > 1.0\,\mathrm{R}_\odot\,\mathrm{L}_\odot{}^{0.5}$ (see equation 8 of Belczynski et al., 2010), and end up with lower remnant masses, similar to models evolved with MESA with METISSE.

Chemical composition also plays a key role in determining mass-loss rates. Stars with higher metal content have higher opacities and therefore have higher mass-loss rates (Vink et al., 2001; Puls et al., 2015). Following Vink et al. (2001), a metallicity dependence of $\mathrm{Z}^{0.86}$ is included into the treatment of mass loss in all models. The stellar models here have approximately the same Z, that is, nearly one tenth of solar as per Asplund et al. (2009b). The initial metallicity of the MESA models is $Z = 0.00142$ with element ratios scaled down from solar composition. BEC models are computed with $Z = 0.00105$ and have chemical composition scaled by a factor of 2 down from that of the Small Magellanic Cloud (SMC). While differences in the abundances of individual metal elements also influence the opacity and energy transport rates, the main contributors to the winds of massive stars are iron-like elements (Puls, Springmann, & Lennon, 2000). As shown in fig. 1 of Szécsi et al. (2015), except for carbon and nitrogen, SMC abundances are proportional to those of Solar and the contribution of these two elements to line driving (and thus to mass loss) is relatively minor.

4.7.3 Convection and overshooting

Massive stars have convective cores owing to a steep temperature gradient in the interior. These cores can overshoot beyond convective boundaries into non-convective regions due to finite particle velocities and cause enhanced mixing of elements inside stars (Böhm, 1963; Shaviv & Salpeter, 1973; Maeder, 1975). Thus the location of convective boundaries is important to determine the evolution of massive stellar cores and the lifetimes of different evolutionary phases of a star (Langer, 2012).

Convection and overshooting are complex 3D processes, although in 1D stellar evolution codes they are treated using the mixing length theory (MLT; Böhm-Vitense, 1958) or some modified version of it. Convection is modelled in terms of the mixing length parameter $\alpha_{\rm MLT}$ over a region determined by the Ledoux or Schwarzchild criteria (Kippenhahn & Weigert, 1990). Overshooting can be modelled with the step overshoot prescription where the convective boundary is simply extended by a fraction of the pressure scale height, given by the parameter $\delta_{\rm ov}$ (Böhm, 1963; Stothers & Chin, 1975).

The MESA models in this work use convection parameters calibrated to the Sun and a modified version of MLT by Henyey, Vardya, & Bodenheimer (1965) with $\alpha_{\rm MLT} = 1.82$ (Choi et al., 2016). Convective-overshoot is assumed to vanish exponentially outside the convective region with $\delta_{\rm ov} = 0.016$ (Magic et al., 2010; Choi et al., 2016). This is roughly equivalent to $\delta_{\rm ov} = 0.2$ in the step overshooting model.

On the other hand, BEC models have used standard MLT (Böhm-Vitense, 1958) with $\alpha_{\rm MLT} = 1.5$ and step overshoot with $\delta_{\rm ov} = 0.335$ (Langer, 1991; Brott et al., 2011a). The overshoot values have been calibrated to massive stars observed with the VLT-FLAMES survey (Hunter et al., 2008). Both the MESA and BEC models have the Ledoux criterion to determine convective boundaries.

Stars evolved with MESA have larger convective efficiency owing to the greater $\alpha_{\rm MLT}$

which decays exponentially outside the fiducial convective region while the larger $\delta_{\rm ov}$ in the BEC models means a more extended region for convection. However, other factors such as the adopted nuclear reaction rates and opacities in BEC lead to shorter MS lifetimes compared to MESA models (Fig. 4.9).

In SSE, the formulae for determining main-sequence lifetimes were calculated with models of Pols et al. (1998), where the authors adopted standard MLT with $\alpha_{\rm MLT} = 2.0$ while overshooting was modelled through a modification of the Schwarzchild criterion. Their overshooting coefficient ($\delta_{\rm ov} = 0.12$) approximates to $\delta_{\rm ov} \sim 0.4$ in the step overshooting prescription for the most massive stars ($\sim 50\,{\rm M}_\odot$) in the set. Due to the high value of the overshooting parameter, combined with the efficient mixing length parameter in the Pols et al. (1998) tracks, SSE predicts even longer MS lifetimes for stars compared to the MESA and BEC models (Fig. 4.9).

Mixing processes are not very well constrained for massive stars (Schootemeijer et al., 2019b). In particular, the convection and overshooting parameters are sensitive to quantities like opacities (Stothers & Chin, 1991) and the Solar abundance scale (Magic et al., 2010). Processes such as semiconvection (Langer, Fricke, & Sugimoto, 1983) and rotational mixing (Heger et al., 2000) also contribute significantly to the evolution of such stars. There are ongoing efforts to improve constraints on the mixing parameters with 3D hydrodynamic simulations (Trampedach et al., 2014, Magic, Weiss, & Asplund, 2015) and asteroseismic measurements (Noels et al., 2010). METISSE can be useful in the future to study the effects of varying different mixing parameters and comparing the outcome to observed populations of massive stars. This is a major advantage over an SSE style code in that any piece of physics in the stellar models can be changed without having to find a whole new set of fitting formulae.

4.8 Caveats and future work

Interpolation has the advantage of being fast, robust and able to utilize different sets of stellar evolution models with ease. As with any other method, it has some limitations as well. We discuss some of these in this section and how METISSE aims to address them.

4.8.1 Quality and completeness of input stellar tracks

Results produced by METISSE are a direct reflection of the quality of the input stellar models. Fine details in the input models can be reproduced but so can the flaws. For the calculation of stellar tracks up to their respective remnant phases, input models should at least be evolved until the formation of a CO core, because the CO core mass is needed to calculate remnant properties (Belczynski et al., 2008; Fryer et al., 2012). To avoid propagation of inaccuracies of the stellar models in the results obtained, input tracks need to be checked thoroughly for flaws and incompleteness.

The set of input stellar models should also be dense, particularly near mass cutoffs, to ensure accuracy of the interpolation. If some tracks are incomplete due to convergence issues, METISSE can attempt to calculate the missing phase as described in Section A.3. However, it fails if many tracks are incomplete over a small mass range or if the set of input models is too sparse.

4.8.2 Mass and metallicity limits

Currently in METISSE stellar tracks can only be interpolated for the same metallicity as the input models. Although interpolation between tracks of different metallicity could be implemented, the interpolated track might not be a good approximation of a detailed track of the same mass and metallicity unless these two metallicities are sufficiently close. Even then, tracks for interpolation will have to be carefully selected because the occurrence of evolutionary features in a track also depends on the metallicity.

Interpolation in METISSE is also bounded between the highest and lowest mass track present in the set of input models. Extrapolation can lead to spurious results if the tracks used for the extrapolation are sparsely distributed. Hence, we do not extrapolate beyond the maximum mass track of the input set in METISSE. However, we do extrapolate a new track from higher masses if an input mass falls between a critical mass (cf. Section A.1) and the initial mass of the next track. Because the density of stellar tracks where these mass cut-offs occur is usually high, the tracks obtained are a suitable approximation to the evolution of such stars. We are currently working on a new version of METISSE to further limit the reliance on extrapolation near mass cutoffs.

4.8.3 Information about stellar structure

Stars in binary systems can transfer mass on to each other if they expand beyond their Roche-lobe radii. If the mass transfer is significant, it can affect the structure and the evolution of the member stars. It can, for example, affect the structure of the core and the burning shells (Renzo et al., 2017) which can be crucial to determine the type of remnant formed by the star. Therefore, details of the stellar interior are needed to accurately compute properties of stars in response to mass transfer in a binary system.

Creation and storage of large sets of stellar evolution models and the use of them in conjunction with detailed codes for binaries as done by the Binary Population and Spectral Synthesis (BPASS; Eldridge & Stanway, 2016; Eldridge et al., 2017) project and the Brussels code (De Donder & Vanbeveren, 2004) is another way to account for the stellar structure in response to mass transfer in binaries. However, it requires expertise to maintain and run such models.

We intend to apply METISSE in binary population studies in the future. While METISSE cannot compute changes to the internal structure of a star in response to mass transfer, it can easily interpolate between any stellar structure parameters provided by the detailed models, thus extending more widely than the main parameters of total mass, core mass, luminosity and radius. Examples include the mass of the convective envelope (important for mass transfer), the moment of inertia (important for tidal evolution, c.f. de Mink et al., 2013) and the envelope binding energy (important for common envelope evolution, c.f. Loveridge, van der Sluys, & Kalogera, 2011; Xu & Li, 2010).

4.9 Conclusions

We have presented our new code METISSE and its capabilities as a standalone synthetic stellar evolution code. METISSE can simulate stars from the ZAMS to the end of the full range of stellar remnant phases, including naked helium star phases. We find that METISSE better reproduces stellar tracks than the SSE fitting formulae with the same input data. METISSE is similar in performance to SSE with the added advantage that it can be easily used with different sets of stellar evolution tracks.

Massive stars are the progenitors of compact objects, neutron stars and black holes, whose merging result in the emission of gravitational waves observable by LIGO/Virgo (Abbott et al., 2016). We have used METISSE to demonstrate that uncertainties in modelling the evolution of massive stars, such as their radiation dominated envelopes, can have a remarkable influence on their evolution. Such uncertainties can impact the radial expansion of stars and the properties of stellar remnants, which can subsequently change the interactions in binary and star cluster environments. Therefore, the ability to accurately predict stellar remnant masses is crucial when attempting to account for present day observations of compact object populations.

Surveys dedicated to the study of massive stars (Evans et al., 2011; Kaper et al., 2011; van Gelder et al., 2020) have advanced our understanding of these stars. In the coming years, instruments such as the James Webb Space Telescope (JWST: Gardner, 2003), the Giant Magellan Telescope (GMT: McCarthy & Bernstein, 2014), the Large Synoptic Survey Telescope (LSST: LSST Science Collaboration et al., 2009) and the Laser Interferometer Space Antenna (LISA: Amaro-Seoane et al., 2017) will further boost our knowledge of stars and stellar systems. As the data from newer observations becomes available, and the stellar structure and evolution codes become better at modelling stellar phenomena, both in 1D and 3D, we will be able to include the updated stellar models in our population synthesis codes through METISSE.

Since METISSE has been written in the same variable and file structure as SSE, it will be easy to include it in population synthesis codes as an alternative to SSE (Hurley et al., 2000). In the future we plan to publicly release METISSE as well as integrate it with the binary population synthesis codes BSE (Hurley, Tout, & Pols, 2002) and COMPAS (Stevenson et al., 2017; Vigna-Gómez et al., 2018) and the star cluster modelling code NBODY6 (Aarseth, 2003). Using METISSE will not only help us to include up to date treatments of stellar evolution in population synthesis codes but will also enable us to study the role of different stellar evolution parameters on the evolution of stellar systems and make predictions to pave the way for the new missions.

Acknowledgements

We thank Carolyn Doherty, Ilya Mandel, Alejandro Vigna-Gómez, Coen Neijssel, Jan Eldridge, Simon Campbell, Alex Kemp and Isobel-Romero Shaw for useful comments and suggestions. We also thank Aaron Dotter for making ISO open source. We are also grateful to the referee, Chris Tout, for helpful comments. DSz has been supported by the Alexander von Humboldt Foundation. PA, JH and SS acknowledge the support by the Australian Research Council Centre of Excellence for Gravitational Wave Discovery (OzGrav), through project number CE170100004. This work made use of the OzSTAR high performance computer at Swinburne University of Technology. OzSTAR is funded by Swinburne University of Technology and the National Collaborative Research Infrastructure Strategy (NCRIS).

5

The role of stellar evolution in mass transferring binaries and gravitational wave progenitors

"What is better than a star.. a binary star"

—Anonymous

5.1 Introduction

Stellar binaries play an important role in the evolution of the universe, opening up evolutionary pathways that would otherwise remain inaccessible through the evolution of single stars (see e.g., Eldridge, 2020). For massive stars, the role of binary evolution is even more crucial (Sana et al., 2012; de Mink et al., 2013) as massive binaries lead to the formation of X-ray binaries (Verbunt, 1993), gamma-ray bursts (Woosley & Heger, 2006), kilo-novae (Abbott et al., 2017a) and gravitational waves (Abbott et al., 2016), amongst many other astrophysical marvels. Recent studies even indicate the role of stellar triples in determining high-mass stellar evolution (Moe & Di Stefano, 2017).

With the recent release of the second LIGO-VIRGO gravitational wave (GW) catalogue (Abbott et al., 2021a), we now have 50 GW signals from the merger of binary systems of neutron stars and black holes, the end states of massive stars. The parameters measured from GW signals, such as the spins and masses of the binary components, helps us determine the evolution of massive stars and their interaction with their neighbours (e.g., Stevenson et al., 2015, 2017).

With the numbers of GW detections expected to increase significantly in the future (Abbott et al., 2018b), gravitational-wave astronomy is leading the way in shedding light onto the lives of massive stars. It is, therefore, a great time to incorporate the latest models of massive stars in our population synthesis codes and determine the impact of binarity on their evolution of stellar populations.

Population synthesis codes serve as the tool to calculate key properties and interactions between stellar populations in galaxies and star clusters. However, keeping such codes up-to-date with the latest results of stellar evolution studies is an arduous task as many population synthesis codes rely on fitting formulae to approximate single star evolution. These formulae are fast and robust but are not adaptable to changes in the stellar tracks.

Recently, the method of interpolating between stellar tracks has gained popularity as it provides the flexibility of switching between the sets of stellar tracks. Codes like SEVN (Spera et al., 2015) and COMBINE (Kruckow et al., 2018) make use of this method to compute single star properties for binary evolution. This helps study the effect of varying input physics on stellar tracks and hence on population synthesis models.

However, uncertainty in massive stellar evolution is not limited to the physical inputs but also depends on numerical techniques employed by different stellar evolution codes for evolving such stars. As shown in Chapter 3, these numerical methods can have a non-trivial impact on the evolution of massive stars. It is, therefore, crucial to compare not just the tracks computed with different physical inputs but also the tracks that are evolved with different codes.

Large uncertainties in the evolution of massive stars, both physical and numerical, also keeps us from an understanding of massive close binary systems (Dorn-Wallenstein & Levesque, 2020; Belczynski et al., 2021). To address this problem, we have developed MEthod of Interpolation for Single Star Evolution (METISSE; Agrawal et al., 2020) as an alternative to the Single Star Evolution (SSE; Hurley et al., 2000) fitting formulae in population synthesis codes. METISSE interpolates between sets of pre-computed stellar tracks to approximate evolution parameters for a population of stars. However, unlike other codes, METISSE can readily make use of stellar models computed with different stellar evolution codes. This allows us to test the predictions of stellar models computed using different codes on the evolution of stellar populations.

In this work, we update METISSE to include the implications of additional mass changes, such as mass loss through stellar winds, or mass loss/gain through mass transfer, that is not present in the underlying detailed stellar evolution tracks used as input. We combine this updated version of METISSE with the Binary Stellar Evolution (BSE; Hurley et al., 2002) code. This study lays the groundwork needed to combine our most up-to-date understanding of massive stars with population synthesis codes to constrain the formation of GW progenitors in stellar multiples and star clusters. We briefly summarise the capabilities and method of METISSE as a single stellar evolution code in Section 5.2. We describe our implementation of extra mass loss in METISSE in Section 5.3. In Section 5.4 we test the validity of the implementation by comparing the stellar tracks interpolated by METISSE with additional mass loss to the results from SSE and from the 1D stellar evolution code Modules for Experiments in Stellar Astrophysics (MESA; Paxton et al., 2019). In Section 5.5 we briefly review the physics of mass transfer in binary systems. We present preliminary results using METISSE in BSE and compare the results from using SSE in BSE in Section 5.6. We present conclusions and discuss potential future work in Section 5.7.

5.2 METISSE as single star evolution code

METISSE is a synthetic stellar evolution code that can quickly compute the evolution of many stars by interpolating between a finite set of models computed with 1D stellar evolution codes (also known as detailed stellar evolution codes). METISSE has been designed to serve as an alternative to the SSE fitting formulae in population synthesis codes such as BSE and NBODY6 (Aarseth, 2003). However it can also be used as a stand-alone code, for example, for population synthesis of single stars, or to test input stellar tracks. Further capabilities of METISSE are described in Agrawal et al. (2020).

The SSE package consists of several subroutines (sub-program units in Fortran), where each subroutine has a particular role. These subroutines are called by an overarching subroutine called EVOLV1 for calculating the evolution of a single star. For computing the evolution of a binary star, the subroutines in Table 5.1 are called twice by a similar overlying subprogram EVOLV2 to compute parameters of two stars at every time-step of

NAME	FUNCTION IN SSE	FUNCTION IN METISSE
ZCNSTS	Set all the constants of the formulae which depend on metallicity	Read detailed models of given metallicity and find mass cutoffs
STAR	Derive the parameters that divide the various evolution stages	Interpolate between detailed models to get a track of given mass
HRDIAG	Decide which evolution stage the star is currently at, and calculate the appropriate luminosity, radius and core mass	Interpolate within the new track to determine stellar parameters at given age
MLWIND	Derive the mass loss as a function of evolution stage	Same as SSE
DELTAT	Calculate the time-steps depending on the stage of evolution	Same as SSE

Table 5.1 Major subroutines in the SSE and METISSE packages and their functionality in each.

the evolution and calculate relevant binary evolution parameters. An exception to this is the subroutine ZCNSTS which needs to be called separately at the beginning of the program for calculations dependent on the metallicity.

METISSE is structured to contain similar subroutines to SSE with the same functionality. Major SSE subroutines, their functions and their equivalent in METISSE are listed in Table 5.1. These subroutines mimic the behaviour of the SSE subroutines from the outside, with the same name and input/output variables. They have been written in FORTRAN90/95 and make use of the modern Fortran architecture for efficiently storing and passing large arrays of data required for interpolation.

5.3 Implementing mass transfer in METISSE

The total mass of a star can change due to mass loss through stellar winds or due to mass transfer during interaction with a binary companion. Depending on the evolutionary phase, both mass loss and gain can have a substantial impact on the structure and the evolution of the star. Hence, it is important to incorporate the effects of mass change in the stellar tracks.

The stellar models from Pols et al. (1998) that were used in calculating the SSE fitting formulae did not include mass loss. Any kind of mass loss or gain in SSE is added on top of the existing formulae and stellar parameters are modified to reflect the change in mass. A change of stellar parameters in response to any kind of mass change is dealt with by making use of the current mass of the star M_t and the *'effective'* initial mass of the star M_0 (which can be distinct from the zero-age main-sequence – ZAMS – mass of the star). Parameters such as luminosity, timescales and core mass are calculated depending on M_0 while the radius is calculated using M_t. On the main sequence, it is assumed that M_0 is equal to M_t and in response to any mass changes M_0 is adjusted to account for the corresponding change to the main-sequence lifetime.

In METISSE, if wind mass loss is already incorporated in the input stellar models computed with a detailed code, one can simply interpolate between them to achieve the same effect. It is, in fact, more accurate compared to fitting formulae as the changes to stellar structure due to mass loss are better modelled in detailed codes and hence carried over by METISSE. However, we still have to take into account the impact of wind mass loss and subsequent changes in stellar parameters for input tracks computed without any mass loss and mass changes resulting from interaction with a binary companion. Therefore, we have improved METISSE to take into account changes in the evolutionary track of the star due to such mass changes.

Before explaining the implementation of mass loss, we briefly summarize the usual interpolation process in METISSE. For use in METISSE, input tracks must be divided into equivalent evolutionary phases (Prather, 1976; Bergbusch & VandenBerg, 2001). These phases are readily identifiable by the evolutionary features such as the central hydrogen mass fraction, with examples being the main-sequence (MS) phase or the Hertzsprung Gap (HG) phase. Each evolutionary phase is further sub-divided into an equally spaced set of points called Equivalent Evolutionary Points (EEPs), fixed in number across all masses. For a given initial mass, $\mathrm{M_{ini}}$, an evolutionary track is calculated by interpolating between the corresponding EEPs of the neighbouring mass tracks. The type of interpolation performed is either linear or monotonic piece-wise cubic interpolation (Steffen, 1990), depending on the number of tracks available in the neighbourhood of $\mathrm{M_{ini}}$. The resulting track is a collection of EEPs, containing stellar parameters at each EEP age. METISSE further interpolates within the mass-interpolated track, between the EEPs enveloping the given age, to calculate stellar parameters at any instant.

In the absence of any extra mass loss, mass interpolation only happens once for a star of the given initial mass. However, in the event of a mass change due to either mass loss or gain, a new mass interpolated track is calculated following the procedure described below.

- For a mass change dm at a time t in a star's life, the first step is to locate the nearest EEP to t, say EEP_i. Since evolutionary parameters of the input stellar tracks and track corresponding to the current mass of the star are only stored at the EEPs, the mass change is applied to the total mass of the star at EEP_i to get M_{new}.
- Next, we search all input tracks to find the two tracks whose mass at EEP_i envelops M_{new} and linearly interpolate between their initial masses to get the initial mass (M'_{ini}) of the star whose mass at EEP_i will be M_{new}.
- Finally we interpolate the track for the new initial mass (M'_{ini}).

The above procedure is repeated for every time-step whenever $dm > 10^{-8}\,\mathrm{M}_\odot$, before proceeding with the age interpolation to determine the stellar parameters for the age at that step. For input tracks computed without any mass loss, the new initial mass, M'_{ini} and M_{new} in METISSE are the same as the effective initial mass, M_0 and M_t of SSE. To account for the effect of mass loss on different stellar parameters, we currently apply similar assumptions in METISSE as in SSE, i.e., stellar parameters are designated to be dependent on either the track corresponding to the current mass M_t or the track corresponding to the effective initial mass of the star M_0.

On the main sequence, the stellar parameters are highly sensitive to the total mass of the star, therefore all parameters of the star beyond time t are calculated using the new track. However, the lower mass star (assuming mass loss) at the same age would have burned less hydrogen. Therefore, we follow SSE, and age the star to conserve the main-sequence time and therefore the fraction of hydrogen burned. The new age t_{new} is calculated using the main-sequence time for the old track (t_{MS}) and the newly interpolated track (t'_{MS}) (cf. Hurley et al., 2000) as follows,

$$t' = \frac{t'_{\mathrm{MS}}}{t_{\mathrm{MS}}} t. \tag{5.1}$$

During the post-main-sequence evolution of the star, the core evolution is assumed to be unaffected by the changes to the total mass. Thus, core mass and luminosity are calculated using the track corresponding to the total mass of the star at the end of the main-sequence. Radius on the other hand is calculated using the new track corresponding to the current total mass of the star. However, the time in the new track is modified to conserve the age of star at EEP$_i$ (t_i) and the duration of the current phase ($t_{\rm phase}$),

$$t_{\rm new} = t_i + \frac{t_{\rm phase}}{t'_{\rm phase}}(t' - t'_i), \tag{5.2}$$

where primes denotes quantities after the mass loss. This allows surface parameters to change according to the new total mass of the star while effectively conserving the core properties.

For massive stars ($M_{\rm ini} > 10\,{\rm M}_\odot$), mass loss due to stellar winds can be quite high ($\sim 10^{-4}\,{\rm M}_\odot{\rm yr}^{-1}$) and the star can lose its envelope before nuclear burning is completed. Depending on its mass and the evolutionary stage, the star can either become a helium white dwarf or naked helium star. We currently revert to using SSE formulae for further evolution of naked helium stars.

5.4 Testing the validity of implementation

In this section, we test the validity of the mass-loss implementation in METISSE described in Section 5.3. To calculate mass-loss rates across different evolutionary phases, we follow the algorithm described by Belczynski et al. (2010), which is the latest mass loss algorithm available in SSE. We apply these mass-loss rates consistently across all models we consider in this paper, including in METISSE to stellar tracks without mass loss (both those from Pols et al., 1998 and those from MESA), in SSE (which is also based on Pols et al. (1998) models without mass loss) and in MESA for computing detailed models with mass loss. Below we briefly describe the different components of the mass-loss scheme.

If the surface luminosity (L) of the star exceeds $10^5\,{\rm L}_\odot$ and radius (R) satisfies $10^{-5} R L^{0.5} > 1.0\,{\rm R}_\odot\,{\rm L}_\odot{}^{0.5}$, a fixed mass loss of $1.5 \times 10^{-4}\,{\rm M}_\odot\,{\rm yr}^{-1}$ is applied (see equation 8 of Belczynski et al., 2010), to account for Luminous Blue Variable (LBV) behaviour of the stars. For stars whose effective surface temperature, $T_{\rm eff}$, is in the range of 12500 K and 50000K, mass-loss rates from Vink et al. (2000, 2001) are used with the iron bi-stability jump temperature at 25000K. For stars more luminous than $4000\,{\rm L}_\odot$, the mass-loss rate from

Nieuwenhuijzen & de Jager (1990) is applied with a metallicity correction factor of 0.5 from Kudritzki et al. (1989).

Where none of the above conditions are met, i.e., for low mass stars, wind mass-loss rates from Kudritzki & Reimers (1978) are used on the giant branch (GB) and from Vassiliadis & Wood (1993) on the asymptotic giant branch (AGB), including the thermally-pulsating AGB (TPAGB). For naked helium stars, and for stars with small hydrogen-rich fractional envelope mass (μ; see equation 97 of Hurley et al., 2000) the wind prescription from Hamann & Koesterke (1998) is used (reduced by a factor $1-\mu$ in the latter case) with a metallicity scaling factor of $Z^{0.86}$ from Vink & de Koter (2005).

We use $Z = 2 \times 10^{-2}$ as reference solar metallicity in calculating the mass-loss rates as they have originally been scaled from this value. Everywhere else we adopt $Z = 1.42 \times 10^{-2}$ from Asplund et al. (2009a) as our solar reference. For Pols et al. (1998) models, the closest available metallicity is $Z = 10^{-2}$, so we use this value while comparing results from METISSE and SSE.

Fig 5.1 shows the evolutionary tracks, computed with and without mass loss with METISSE using Pols et al. (1998) models at metallicity $Z = 10^{-2}$. The effect of mass loss is visible on the stars more massive than $10\,\mathrm{M}_\odot$ in the Hertzsprung–Russell (HR) diagram. Tracks with mass loss are less luminous than tracks without mass loss. For the $40\,\mathrm{M}_\odot$ track, the inclusion of mass loss leads to a completely different final state, i.e., a naked helium star when mass loss is included, compared to a red supergiant when not including any mass loss. At the end of its life, the $40\,\mathrm{M}_\odot$ star without any mass loss forms a $36\,\mathrm{M}_\odot$ black hole while the same star with mass loss forms just an $11.3\,\mathrm{M}_\odot$ black hole. This simple comparison highlights the impact of mass loss in stellar evolution, especially for massive stars.

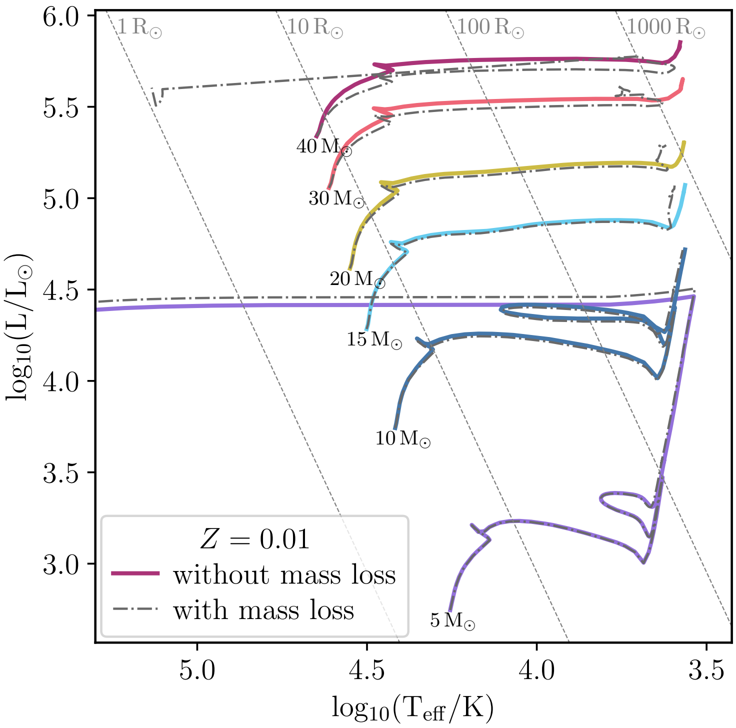

Figure 5.1 Hertzsprung–Russell (HR) diagram showing tracks interpolated by METISSE using detailed tracks from Pols et al. (1998) for metallicity, $Z = 10^{-2}$. Solid lines represent tracks without any mass loss while dashed lines represent the tracks including wind mass loss as described in Section 5.4.

5.4.1 Comparing tracks with mass loss for METISSE and SSE

In this section, we compare the stellar tracks given by the fitting formulae of SSE with the tracks interpolated by METISSE with mass loss using the Pols et al. (1998) models in the mass range 0.5–50 $M_\odot$ at $Z = 10^{-2}$ metallicity. We exclude stars less massive than 10 $M_\odot$ in our comparison here, as wind mass-loss rates are too small for them to cause any visible difference.

5.4.1.1 Differences in the HR diagram

Figure 5.2 shows the comparison between the evolutionary tracks computed by METISSE and SSE. Inspection of the figure reveals that the tracks agree reasonably well during the main-sequence but start diverging during post-main-sequence evolution. The maximum difference occurs for stars more massive than 10 $M_\odot$ towards the end of core helium

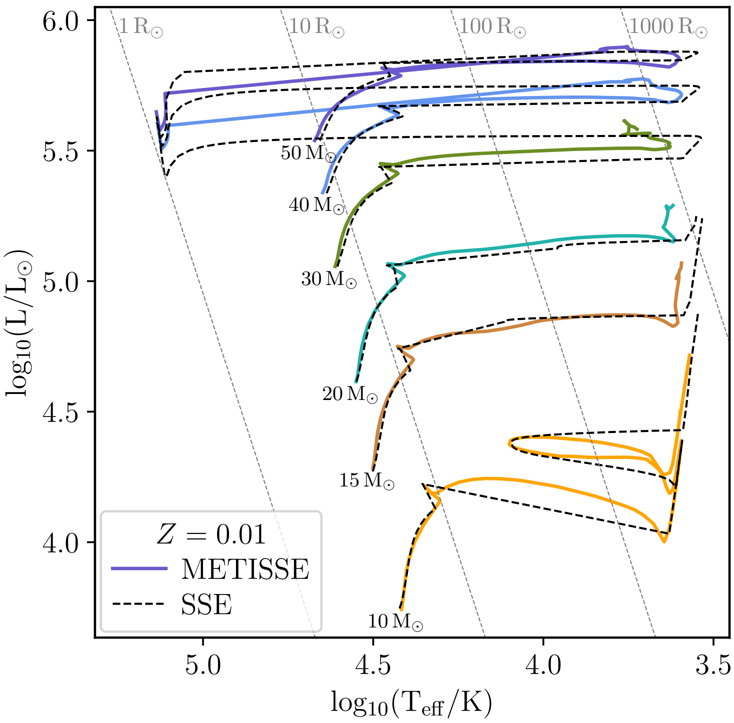

Figure 5.2 HR diagram comparing stellar tracks with mass loss as computed by SSE and METISSE using Pols et al. (1998) models for $Z = 10^{-2}$. For both sets wind mass-loss rates from Belczynski et al. (2010) were used in computing the tracks.

burning, where METISSE systematically predicts lower T_{eff} than SSE.

As shown in Agrawal et al. (2020), METISSE is better at reproducing input stellar tracks than the fitting formulae from SSE. The discrepancy between the methods is the main source of variation in the $10\,\mathrm{M}_\odot$ track in Figure 5.2. However, for more massive stars, the differences towards the end of the core helium burning phase are arising from technical details relating to how mass loss is implemented. To further understand the origin of these differences, we compare the radial evolution of the stars as predicted by METISSE and SSE in Figure 5.3.

SSE predicts a monotonic increase in radii during core helium burning for stars more massive than $10\,\mathrm{M}_\odot$, unless they lose their envelope and become naked helium stars. METISSE, on the other hand, predicts comparatively lower radii for the same phase of evolution. A substantial effect of the lower radii predicted by METISSE for post-main-sequence evolution is on the $30\,\mathrm{M}_\odot$ star. While SSE predicts that the $30\,\mathrm{M}_\odot$ star will

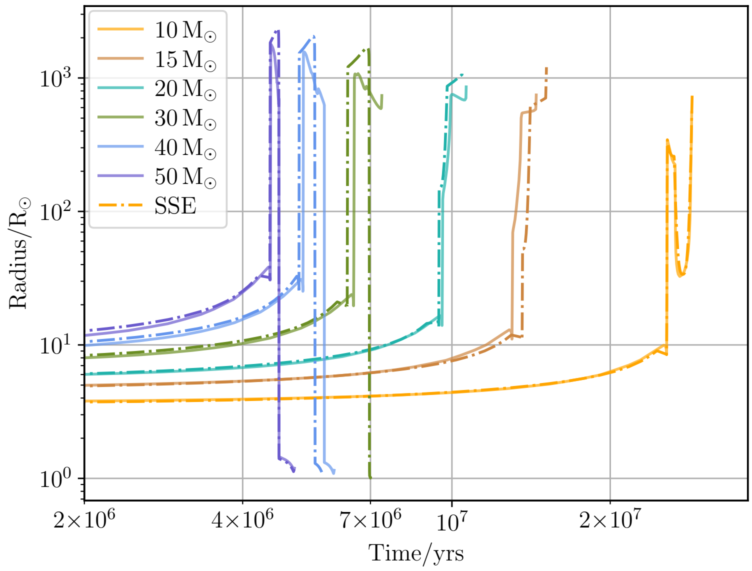

Figure 5.3 Radius versus time for stellar tracks computed with mass loss using METISSE (solid lines) with Pols et al. (1998) models and using SSE (dashed-dotted lines) for $Z = 10^{-2}$. For stars more massive than $15\,\mathrm{M}_\odot$, the radial evolution agrees for most of the evolution except beyond core helium burning.

become a naked helium star, METISSE predicts the formation of a red supergiant at the end of core helium burning. We further explore implications of this difference in radius in the next few subsections.

5.4.1.2 Differences in evolutionary timescales

In Figure 5.4, we compare the difference in the evolutionary timescale for each phase as predicted by METISSE and SSE. Overall, the timescales computed by METISSE are in good agreement with SSE. For 10 and $50\,\mathrm{M}_\odot$ stars the difference is $\lesssim$0.1 Myr, while for the $30\,\mathrm{M}_\odot$ star it is $\lesssim$0.4 Myr. The maximum difference in timescale, 0.6 Myr, occurs for a $15\,\mathrm{M}_\odot$ star. This is due to the proximity of the effective initial mass of the star to one of the critical masses at $16\,\mathrm{M}_\odot$. The critical masses in METISSE serve as the lower limits above which certain physical properties start to appear for stellar tracks and interpolation between these can lead to physically incorrect tracks (cf. Agrawal et al., 2020). Therefore, at each step of mass loss, the intermediate tracks during the evolution of $15\,\mathrm{M}_\odot$ stars in METISSE have been extrapolated from $16\,\mathrm{M}_\odot$ and $20\,\mathrm{M}_\odot$ models, leading to the slight

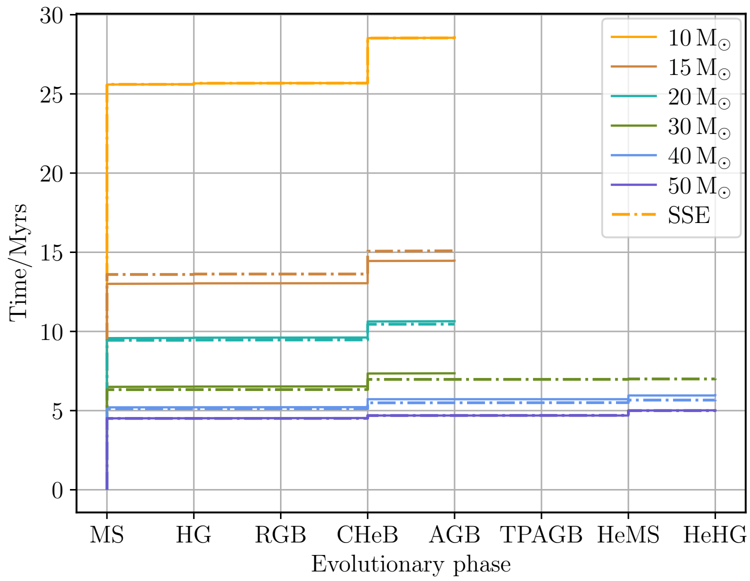

Figure 5.4 Time spent by stars in the different evolutionary phases as predicted by METISSE (solid lines) and SSE (dashed-dotted lines). Acronyms on the x-axis represent the following phases: MS: Main Sequence, HG: Hertzsprung Gap, RGB: Red Giant Branch, CHeB: core helium burning, AGB: Asymptotic Giant Branch, TPAGB: Thermally-Pulsating AGB, HeMS: helium Main Sequence, HeHG: helium Hertzsprung Gap.

deviation from a $15\,\mathrm{M}_{\odot}$ star computed with SSE.

5.4.1.3 Differences in the evolution of total mass with time

In Figure 5.5, we show the total mass of the star with time as computed by METISSE and SSE. The evolution of total mass for the $10\,\mathrm{M}_{\odot}$ and $50\,\mathrm{M}_{\odot}$ stars matches very well between the codes. For other stars, the decrease of mass with time is quite similar for most of their evolution. Differences appear only in the last $\sim$1 Myr, where SSE predicts a steeper decrease in mass compared to METISSE for 20, 30 and $40\,\mathrm{M}_{\odot}$ stars. To better understand the origin of these differences, we plot the total mass of the star as a function of its zero-age main-sequence mass at the end of different evolutionary phases for both SSE and METISSE in Figure 5.6. We find that the total mass of the stars agrees well until core helium burning begins (at the end of the HG) but starts to differ thereafter. By the end of nuclear burning (before the star becomes a remnant), the maximum difference predictions can be up to $1.5\,\mathrm{M}_{\odot}$, and happens for 25 and $30\,\mathrm{M}_{\odot}$ stars. The variations in mass are

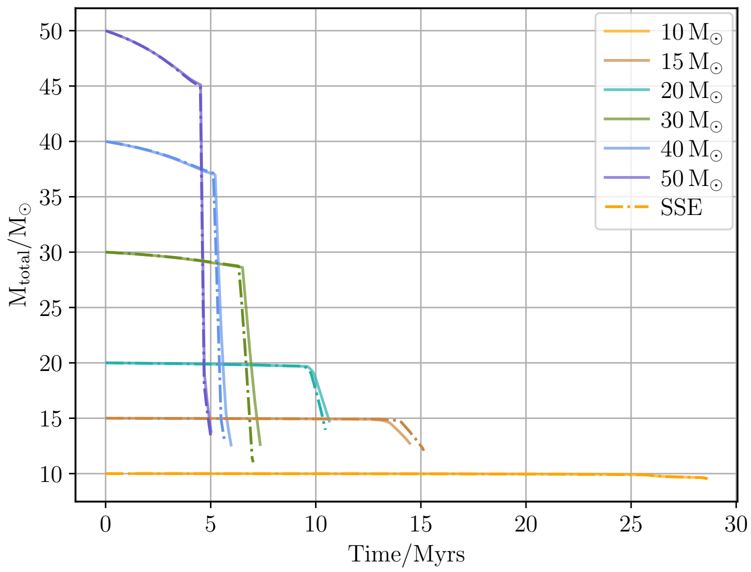

Figure 5.5 Evolution of total mass with time for stars computed with mass loss by METISSE (solid lines) and SSE (dashed-dotted lines). During the late evolution of the 20–40 $M_\odot$ stars, METISSE predicts a shallower decrease in mass compared to SSE. This agrees with the behaviour of stellar tracks in the HRD in Figure 5.2.

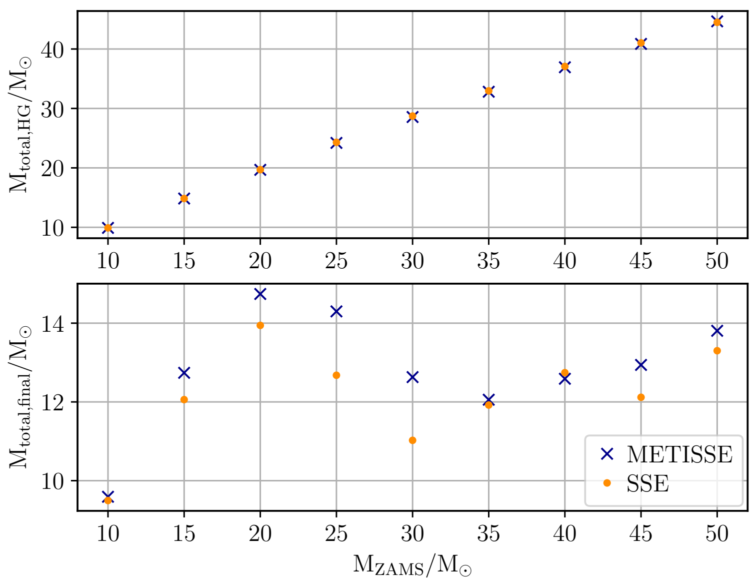

Figure 5.6 Total mass of the star as a function of its Zero-Age Main-Sequence (ZAMS) mass as predicted by SSE (orange dots) and METISSE (blue crosses). The top panel represents the total mass at the end of the HG (when core helium burning begins) while the bottom panel shows the values at the end of the nuclear burning life of the star (before the star becomes a remnant).

similar to the variations in the stellar tracks in the HR diagram during core helium burning. Since mass-loss rates depend on the surface properties of the star, these differences can be attributed to the differences in the tracks in the HR diagram, particularly radius.

5.4.1.4 Differences in the evolution of core mass with phase

As a star loses its envelope owing to stellar winds, the role of the core becomes increasingly important in determining stellar properties, especially the final fate of the star. There are several ways for determining the core boundaries in the detailed models based on properties such as chemical composition and sound speed (compressibility). Usually, the core is defined as the region interior to the boundary depleted in the element(s) undergoing nuclear fusion in the core and rich in the nuclear product(s). Core boundaries are not fixed but can increase e.g., as shell burning adds processed material, or even decrease e.g., as convection, dredge-ups and other mixing events dilute the outer layers of the core with the unprocessed material from the envelope.

In Figure 5.7 we show the core mass of the star with evolutionary phase for stellar tracks computed by METISSE and SSE. Following the SSE convention, the core mass here represents the mass of the helium-rich core for phases up to the AGB and the mass of the carbon-oxygen core for phases beyond the AGB (including naked helium star phases). Similar to Figure 5.6, we plot the core mass of the star as a function of its zero-age main-sequence mass for SSE and METISSE at the end of the HG (when core helium burning begins) and at the end of nuclear burning life (before the star becomes a remnant) in Figure 5.8.

From Figure 5.7, we see that the core masses at the end of each evolutionary phase for stars up to $20\,\mathrm{M}_{\odot}$ show a good agreement between METISSE and SSE, with the maximum difference being $0.2\,\mathrm{M}_{\odot}$ for a $15\,\mathrm{M}_{\odot}$ star at the end of the HG. Moreover, METISSE is better able to reflect the variation in core mass with time (due to mixing, shell burning etc.) compared to SSE where the fitting formulae are designed to only register the increase in core mass.

For stars with initial masses of $40\,\mathrm{M}_{\odot}$ and above, where both SSE and METISSE predict the formation of a naked helium star, there can be a difference of up to $1.4\,\mathrm{M}_{\odot}$ in the core masses (helium core) during the HG between the two codes. However, these differences reduce to ∼0.6 $M_\odot$ (carbon-oxygen core) in the end as the star becomes a naked helium star and both codes switch to using fitting formulae for naked helium stars.

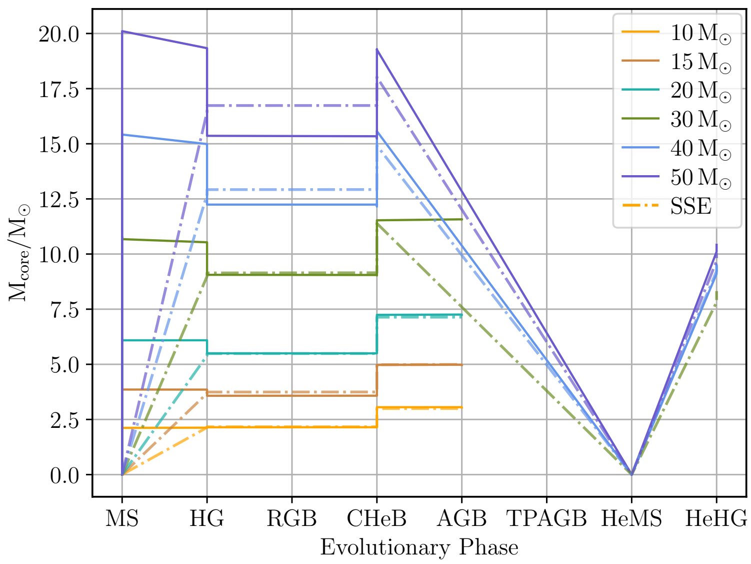

Figure 5.7 Evolution of core mass with phase as predicted by SSE (dashed-dotted) and METISSE (solid lines). Here the core mass represents the mass of the helium core up until the AGB and the mass of carbon-oxygen core thereafter.

For the 30 $M_\odot$ star, the difference in the core mass prediction at the end of HG is less than 0.1 $M_\odot$. However, lower radii predicted by METISSE during core helium burning causes a shallower decrease in mass. Therefore, despite having similar envelope mass (19.50 $M_\odot$) compared to SSE (19.56 $M_\odot$) at the beginning of core helium burning, the 30 $M_\odot$ star in METISSE is able to retain its envelope and end its life as a red supergiant. The difference in the evolutionary paths for the 30 $M_\odot$ star beyond core helium burning shows up as a difference of about 3 $M_\odot$ in the core mass at the end of nuclear burning. It is important to highlight that this difference is between the helium core mass in METISSE and the carbon-oxygen core mass in SSE. The difference between the respective carbon-oxygen core masses is only 0.2 $M_\odot$.

In a nutshell, METISSE can closely reproduce the results from SSE with the exception of a few cases. The majority of the differences between METISSE and SSE occur for high-mass stars (defined as the stars that ignite helium on the HG and do not undergo the RGB phase) in late phases of the evolution (core helium burning and beyond). The origin

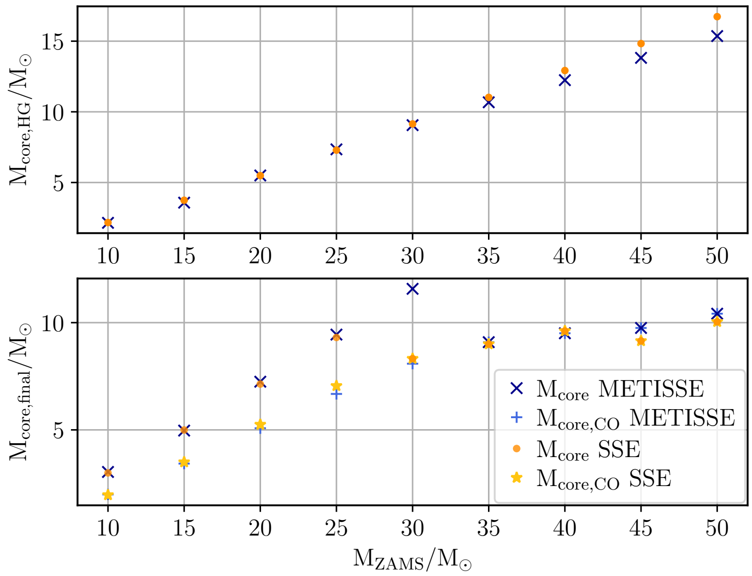

Figure 5.8 Core mass of the star as a function of its ZAMS mass as predicted by SSE (orange dots) and METISSE (dark blue crosses). The top panel represents the core masses at the end of the HG and the bottom panel shows the values at the end of the nuclear burning life of the star. For all stars with M_{ZAMS} up to $25\,M_\odot$, and the $30\,M_\odot$ star with METISSE, that end their lives on the giant branch, the core mass represents the mass of the helium core. Therefore, the masses of the carbon-oxygen core from SSE and METISSE are explicitly plotted with yellow stars and blue pluses respectively. For stars that lose their envelope during the evolution to become naked helium stars, the core mass represents the mass of the carbon-oxygen core only.

of these differences can be traced back to the variation in the radial evolution of the star during core helium burning, as predicted by METISSE and SSE (Figure 5.3). During core helium burning, SSE uses a relative age of the star $\tau = (t - t_{HeI})/t_{He}$ (cf. Hurley et al., 2000), and fitting formulae for radii of the star with the new total mass M_t to compute the current radius of the star following the mass loss. Thus the formulae depend only on the initial and final radius of the star during core helium burning and are independent of the variations that may be present in-between. Moreover for high-mass stars in SSE, the radius calculation transitions to using the fitting formulae for the AGB phase even before the end of core helium burning (see Section 5.3 of Hurley et al., 2000).

In METISSE, the radius of the star after any instance of mass loss is calculated from the new mass interpolated track. It depends both on the radial expansion properties of the new track during core helium burning, and how the age is mapped between the EEPs in the old and the new track, for each time step. However, as the high-mass stars in METISSE expand to become giants, they encounter high mass-loss rates and the age mapping given by equation 5.2 is possibly unable to reflect the required change in age, leading to the predictions of a smaller radii. Investigating the reason for these differences, and improving METISSE to account for the behaviour of stellar radius will be an essential next step.

5.4.2 Comparing METISSE with detailed models with mass loss from MESA

Any method of rapid population synthesis should be able to mimic the results of the detailed evolution as closely as possible. The method for accounting for mass changes in stellar tracks in METISSE shows good agreement with the results of SSE. However, the ideal scenario will be to be able to reproduce results from detailed evolution computed including mass loss. Therefore, in this section, we test the validity of our method using models from MESA both with and without mass loss.

For this purpose, we have computed two sets of models with MESA for stars in the mass range of 8–55 $\mathrm{M}_\odot$ at metallicity $Z = 1.42 \times 10^{-2}$, using the same physical inputs as discussed in Chapter 3 except for the mass-loss rates. The first set of models with MESA have been computed without any mass loss. The models have been converted into EEP-format using the ISO program (Dotter, 2016) to be used as a input in METISSE. Mass-loss through winds has then been subsequently added using the method described in Section 5.3. The second set of models has been computed using the mass-loss rates from Belczynski et al. (2010), by modifying the subprogram unit `run_star_extras` in MESA to match the implementation in METISSE.

In the left panel of Figure 5.9 we show the evolutionary tracks computed with and without mass loss with MESA for metallicity $Z = 1.42 \times 10^{-2}$. Differences in both radius and luminosity are easily visible in the tracks more massive than 20 $\mathrm{M}_\odot$, most notably the change in the position of the main-sequence-hook. The effect of mass loss becomes more pronounced in tracks with higher initial masses.

The right panel of Figure 5.9 shows the comparison between the stellar models computed by MESA with mass loss (labelled as MESA) and the stellar tracks computed by adding mass loss in METISSE using stellar models without mass loss from MESA (labelled

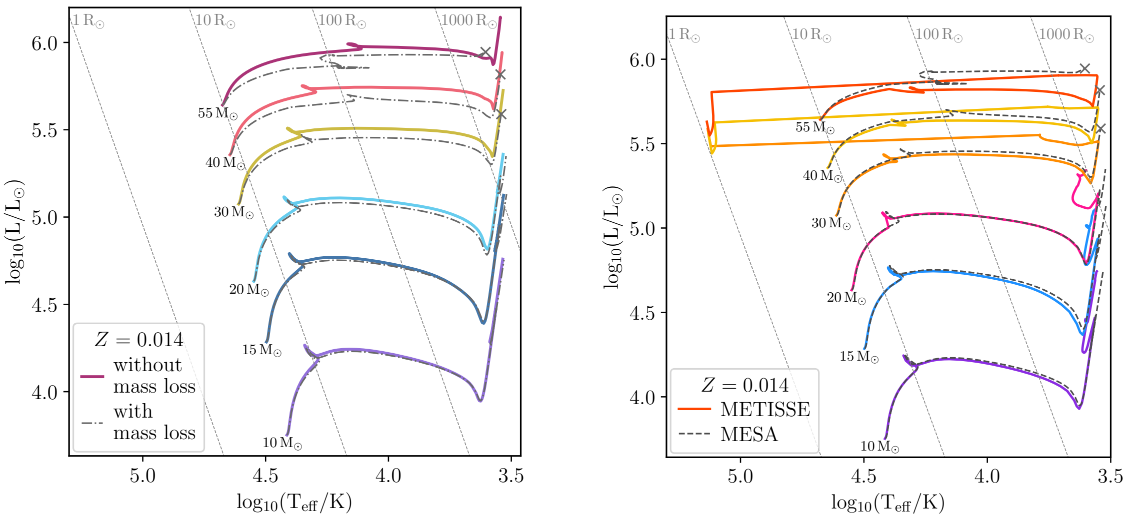

Figure 5.9 The left panel shows the evolutionary tracks computed with mass loss (dashed lines) and without mass loss (solid lines) with MESA for metallicity $Z = 1.42 \times 10^{-2}$. For the same metallicity, the right panel presents the comparison between stellar tracks interpolated by METISSE (solid lines) using stellar models without mass loss from MESA (adding mass loss on top) with the detailed models computed with MESA itself (dashed lines), computed using the same mass-loss rates as in METISSE. Due to numerical instabilities, the tracks computed with mass loss in MESA are incomplete for $20\,\mathrm{M}_\odot$ and above.

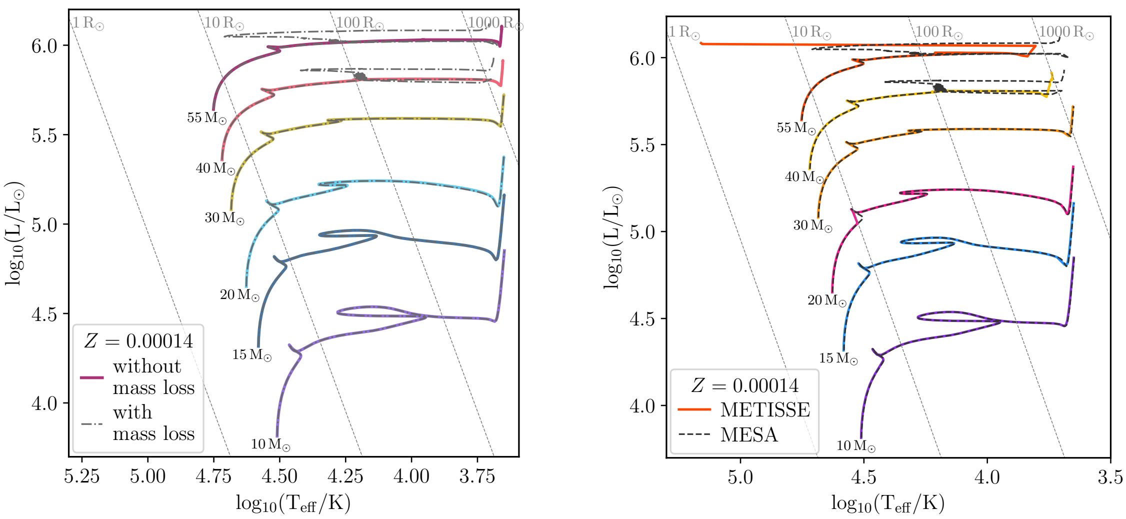

Figure 5.10 Same as Figure 5.9 for metallicity $Z = 1.42 \times 10^{-4}$. All the tracks computed with MESA are complete here and agree well with METISSE up to $30\,\mathrm{M}_\odot$. See Section 5.4.2 for details.

as METISSE). Up to $20\,\mathrm{M}_\odot$, the tracks agree well during the main-sequence and the HG phases of evolution. The differences between the interpolated and the detailed tracks increase with the mass-loss rates, and the two sets of tracks show significant deviation during the core helium burning phase.

For stars more massive than $20\,\mathrm{M}_\odot$, the interpolated tracks exhibit a different behaviour compared to the detailed tracks even on the main-sequence. Not only are there differences in the predictions of stellar radii but the luminosities of stars also differ. Similar to the detailed tracks in the left panel, tracks computed with METISSE in the right panel predict a change in the position of MS-hook, when mass loss in added in stars above $20\,\mathrm{M}_\odot$. Although, the degree of change is different and the hook feature does not coincide between the two sets of tracks.

For $Z = 1.42 \times 10^{-2}$, detailed models with mass loss computed with MESA fail to evolve during the core helium burning phase and hence are rendered incomplete for stars with initial masses greater than $20\,\mathrm{M}_\odot$. This happens due to the presence of numerical instabilities described in Chapter 3. We therefore, switch to a metallicity 100 times smaller than solar value for a better coverage of the mass range.

Similar to Figure 5.9, the left panel in Figure 5.10 represents the evolutionary tracks computed with and without mass loss with MESA for metallicity $Z = 1.42 \times 10^{-4}$ while the right panel shows the stellar tracks computed by adding mass loss in METISSE using stellar models without mass loss from MESA and the stellar models computed by MESA with Belczynski et al. (2010) mass loss. At this metallicity, the mass-loss rates are usually small (10^{-6}–$10^{-8}\,\mathrm{M}_\odot\,\mathrm{yr}^{-1}$), except when stars become LBVs and the mass-loss rate jumps to $\sim 10^{-4}\,\mathrm{M}_\odot\,\mathrm{yr}^{-1}$. For stars up to $30\,\mathrm{M}_\odot$, wind mass loss is not strong ($\lesssim 10^{-8}\,\mathrm{M}_\odot\,\mathrm{yr}^{-1}$), and the tracks computed with METISSE agree well with MESA. Above $30\,\mathrm{M}_\odot$, the tracks only agree until the HG. For a $55\,\mathrm{M}_\odot$ star, MESA predicts that the star will burn core helium as a supergiant while METISSE predicts that it will lose all its envelope during core helium burning and will become a naked helium star instead.

This is further elaborated in Figure 5.11, where we plot the evolution of core mass and total mass with time for a $55\,\mathrm{M}_\odot$ star, as predicted by METISSE and MESA. For most of the star's evolution METISSE and MESA predict similar behaviour. At around 3.9 Myr the star starts experiencing high mass-loss rates due to LBV winds. In METISSE, this continues until the star becomes a naked helium star at about 4.1 Myr. In MESA, however, mass-loss rates drop at about 4.1 Myr as the star evolves towards lower radii and away from experiencing LBV winds. The evolution of mass with time almost flattens out, with about a $4.5\,\mathrm{M}_\odot$ envelope remaining. Figure 5.12 shows the predictions of mass-loss rate and stellar radii with time by METISSE and MESA for the last $\propto$1 Myr of evolution. As the mass-loss rates ramp up due to LBV winds, the radius evolution in METISSE starts differing from MESA. The difference in stellar radius further increases the difference in the mass-loss rates, and finally leads to different evolutionary outcomes.

Aside from the reasons mentioned in Section 5.4.1.4, another possible reason for this discrepancy in radius is that METISSE is interpolating between the models which are in complete hydrostatic and thermal equilibrium. As we add mass loss, it interpolates between lower mass models to get stellar radii, still in equilibrium. However, the removal

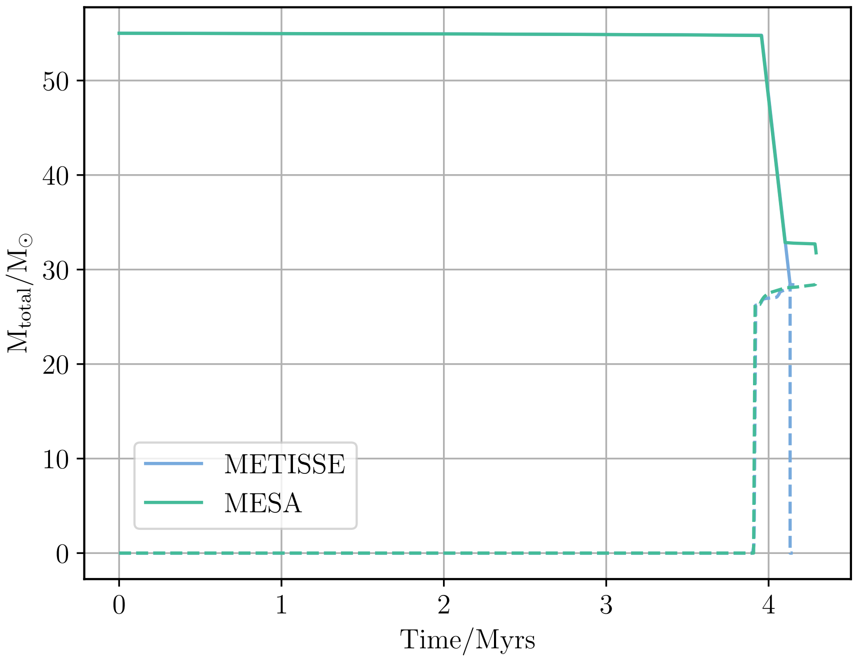

Figure 5.11 Evolution of stellar mass with time for a $55\,\mathrm{M}_\odot$ star at $Z = 1.42 \times 10^{-4}$, as predicted by METISSE (shown in blue) and MESA (shown in green). The solid lines represent the total mass of the star while the dashed lines represent the core mass of the star. At high mass-loss rates, the predictions from METISSE start to differ from MESA. While MESA predicts the end of the star's life as a red supergiant star with an $\sim$$4\,\mathrm{M}_\odot$ envelope, METISSE predicts the formation of a naked helium star at the end of 4.13 Myr.

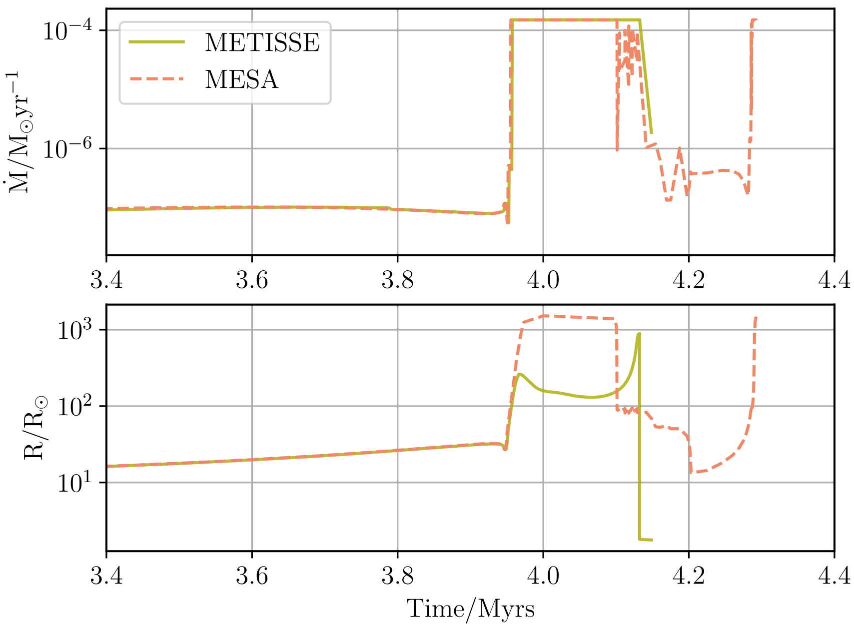

Figure 5.12 Zooming in on the last 1 Myr of the life of a 55 $M_{\odot}$ star evolved using METISSE (solid line) and MESA (dashed line) for $Z = 1.42 \times 10^{-4}$. The top panel shows the mass-loss rates with time while the bottom panel shows the evolution of stellar radius with time. At about 3.9 Myr, as mass-loss rates spike up due to LBV mass loss, METISSE predicts different radial evolution compared to MESA.

of the outer layers of a star through mass loss disturbs both hydrostatic and thermal equilibrium in the star. Depending on the structure of the envelope, whether it is convective or radiative, the star either expands or contracts to restore equilibrium. If the mass-loss rates are low, fewer layers are removed from the star and its structure remains almost unaltered. However, at high mass-loss rates, more mass layers are removed from the star, therefore the degree of adjustment of the stellar radius to restore the equilibrium is also high. A detailed code like MESA can encapsulate such details and therefore predicts a different evolutionary path for a star with a high-mass-loss rate.

The SSE assumption of calculating luminosity using the effective initial mass of the star does not hold true for high-metallicity massive stars in METISSE, when stellar models without mass loss from MESA are used as input (Figure 5.9). In future, the assumptions on how the stellar parameters respond to mass changes in METISSE will be improved to make METISSE mimic detailed evolution as closely as possible.

5.5 Mass transfer in binary systems

Two stars gravitationally bound to each other and orbiting a common centre of mass are said to form a binary system. Binary stars can interact with each other in a myriad of ways and studying their evolution is an active field of research. In this section we provide a brief overview of mass transfer and its role in binary evolution.

In the co-rotating reference frame of the binary there exists equipotential surfaces around each star known as 'Roche lobes'. They meet at the inner Lagrangian point (L_1), one of five Lagrangian points where the gravitational force exerted by the both stars is balanced by the centrifugal force. The two Roche lobes can be considered to be almost spherical, each with an effective radius known as the 'Roche lobe radius'. The Roche lobe radius is defined as the radius of the sphere containing the same volume as the Roche lobe, and is a function of the mass ratio of the stars and the orbital separation between them (Eggleton, 1983).

Most binary systems begin life with each star sufficiently distant that each star's radius is well below its corresponding Roche lobe radius (Abt, 1983; Duchêne & Kraus, 2013). Even in this detached state, stars can still interact through tides, gravitational radiation, magnetic braking, and through the accretion of stellar winds (Tout et al., 1997; Hurley et al., 2002). As the stars expand to become giants and supergiants, their radii can change by several orders of magnitude. If one of the stars in the binary system (the donor) expands beyond its Roche lobe radius, its outer layers become dominated by the gravitational influence of the second star (the accretor). Material flows through L_1, and depending on its energy and momentum, can be accreted by the companion star. The binary is now in a semi-detached state and is said to be undergoing mass transfer through Roche-lobe overflow. A third possibility is that the accretor may fill its own Roche lobe (due to its own stellar evolution or in response to mass transfer on it) and stars form a contact binary system.

Following Kippenhahn & Weigert (1967), mass transfer in an interacting binary system can be classified as one of three cases based on the evolutionary state of the donor star when it first fills its Roche lobe.

1. Case A: if the donor is undergoing core hydrogen burning on the main-sequence,

2. Case B: if the donor has finished core hydrogen burning and is undergoing hydrogen-shell burning (HG, RGB, CHeB).

3. Case C: if the donor has finished core helium burning (AGB).

Binary interactions can change the mass, angular momentum and the surface composition of the individual stars as well as the properties of the binary system, such as the orbital separation between the stars. If the total mass and the total angular momentum of the system is conserved then the mass transfer is described as conservative. In the opposite scenario, both mass and the angular momentum can be lost from the system and the mass transfer is non-conservative. In general, Case A and Case B mass transfers tend to be conservative while Case C mass transfer and wind-accretion are typically non-conservative (Schneider et al., 2015).

It is also useful to classify mass transfer according to its stability. The stability of mass transfer depends primarily on the response of the donor stellar radius and Roche lobe radius to mass transfer (see, e.g., Soberman et al., 1997). Of critical importance is the response of the donor's envelope to mass loss (Webbink, 1985; Ge et al., 2015). If the donor star has a radiative envelope, it will contract in response to the mass loss. Although if the star is on the main-sequence, its nuclear evolution will again lead to an increase in radius. Alternatively, angular momentum losses can lead to a reduction in the Roche lobe radii of the stars. In the equilibrium scenario, the donor star stays large enough to just fill its Roche lobe and transfer mass to the companion. The mass transfer is stable and proceeds on the nuclear timescale of the donor star.

For HG stars with radiative envelopes, radial contraction of the donor due to mass transfer can be outpaced by the radial expansion due to stellar evolution. This leads to increasing mass transfer rates limited by the thermal time scale of the donor i.e., the time needed to restore the thermal equilibrium of the star. In this case, mass transfer is unstable and proceeds on the thermal timescale of the donor.

If the donor star has a deep convective envelope, its radius increases in response to mass loss, and may quickly lead to a run away situation. The mass-transfer is unstable and can have significant consequences on the evolution of the binary. For example, if the expansion of the donor occurs beyond the outer Lagrangian point of the system, or the donor transfers more mass than the accretor can accrete (which is limited by its thermal timescale), then the outer layers of the star form a common envelope around the binary (Paczynski, 1976; Iben & Livio, 1993). As the cores spiral inside the common envelope, their orbital energy is slowly transferred to the envelope, causing subsequent decay of the orbit and may ultimately lead to the ejection of the envelope. If the orbital decay does not lead to stellar merger before the envelope is ejected, it can leave behind two tightly orbiting cores (Ivanova et al., 2013).

Common envelope evolution is a proposed channel for the formation of close binary systems that can lead to phenomena such as Type Ia supernovae, X-ray binaries, and compact binary coalescence. In general, episodes of most mass transfer tend to reduce the orbital separation of stellar binaries. However, a binary system can also widen in response to certain mass transfer episodes e.g., when mass transfer occurs conservatively from a lower mass star to a more massive companion. Such a situation can arise, for example, in Algol systems (Plavec, 1968; Paczyński, 1971). In these systems, an initially more massive donor loses enough mass during its evolution through mass transfer to become less massive than its less evolved companion.

Finally, if a star is massive enough, it will end its life in a supernova, leaving behind a compact object (a neutron star or a black hole) or, in the case of a pair instability supernova, leaving no remnant. Compact objects are thought to receive kicks when they are born (Hansen & Phinney, 1997; Hobbs et al., 2005). A combination of mass loss during the supernova explosion and the natal kick received by the newly formed neutron star or black hole may significantly widen or even disrupt the binary (Blaauw, 1961; Janka & Mueller, 1994).

5.6 METISSE in BSE

METISSE provides us with the ability to test the impact of stellar evolution on the progenitors of GWs. However, we also require a binary evolution mechanism to predict the evolution of compact binary systems whose mergers give rise to GWs. To achieve this, we implemented METISSE in the binary evolution code BSE (Hurley et al., 2002). BSE is a popular binary population synthesis code that can rapidly compute the evolution of stars in binary system, along with providing algorithms to model the necessary binary physics. BSE relies on the subroutines and the fitting formulae from SSE to compute single stellar evolution properties. The resulting algorithm is computationally cheap, fast and robust and many other binary evolution codes such as STARTRACK (Belczynski et al., 2002, 2008), binary_c (Izzard et al., 2004; Claeys et al., 2014), COMPAS (Stevenson et al., 2017; Vigna-Gómez et al., 2018), MOBSE (Giacobbo et al., 2018) and COSMIC (Breivik et al., 2020) are based on BSE.

A binary system in BSE is characterized by its metallicity, the mass of the primary (initially more massive) star, the mass of the secondary (initially less massive) star, the orbital period (or orbital separation), and the eccentricity of the orbit. The Roche lobe radius for each star is given by the fitting formula from Eggleton (1983). The evolution of the binary is classified in to two parts depending on if either of the stars are filling their Roche lobe or not. The first part is for detached binary systems where neither of the stars have filled their Roche lobes, and they interact (if at all) solely through wind accretion and tidal interactions. Interaction of detached binaries through tides is treated using parametrized formulae from Hut (1981), Zahn (1977) and Campbell (1984), while wind-accretion from a companion star is estimated via the Bondi-Hoyle mechanism (Bondi & Hoyle, 1944). The second part of the evolution is where one or both stars fill their Roche lobes. The stability of mass transfer through Roche-lobe overflow is determined using stability parameters from Webbink (1985), while the treatment of Roche-lobe overflow closely follows Tout et al. (1997). If the binary reaches the state of common envelope, the outcome of the common envelope evolution is determined by comparing the total binding energy of the envelope and the orbital energy of the cores (Paczynski, 1976). The efficiency of energy transfer from the orbit to the common envelope is determined through the parameter α (Webbink, 1984) whereas the binding energy of the envelope depends on the structure parameter λ (de Kool, 1990), both of which are treated as free parameters in BSE due to large uncertainties in their values.

Angular momentum losses through gravitational radiation and magnetic braking are estimated using the weak-field approximation of general relativity (Landau & Lifshitz, 1975) and parameterizations from Rappaport et al. (1983) and Skumanich (1972) respectively. If either of the stars undergoes a supernova explosion, a kick velocity is taken randomly from a Maxwellian distribution following Hansen & Phinney (1997) with dispersion or root mean-square velocity of 190 km sec^{-1}, to calculate the loss in angular momentum from the system. We refer readers to Hurley et al. (2002) for further details on binary evolution with BSE.

5.6.1 Comparing binary evolution for METISSE and SSE

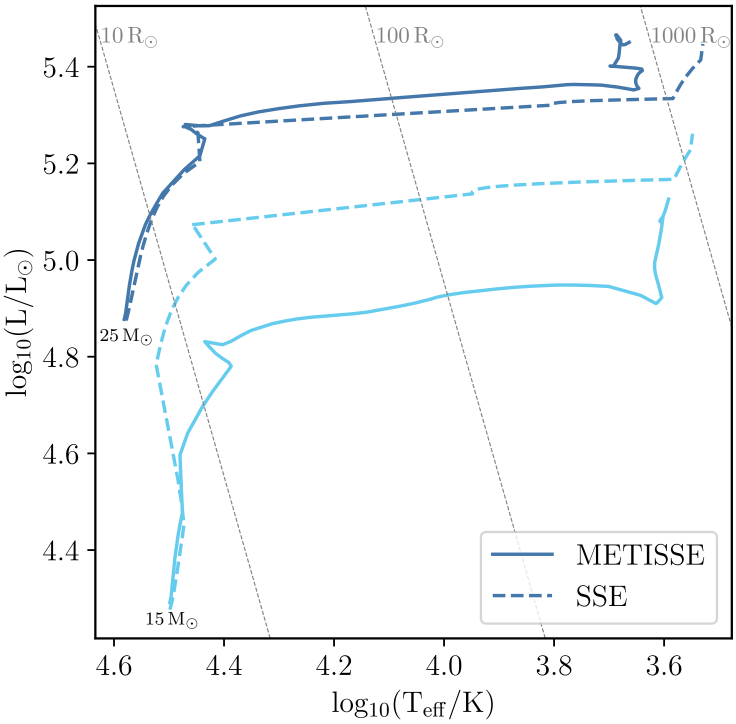

Figure 5.13 HR diagram showing the evolutionary tracks for a 25 M$_\odot$ and 15 M$_\odot$ binary system of stars with initial orbital period of 1800 days and $Z = 10^{-2}$. Solid lines represent the evolution of the binary as predicted by using METISSE in BSE with Pols et al. (1998) models while dashed lines represent the predictions from using SSE in BSE. See Section 5.6.1 for details of the evolution and mass transfer.

In this section, we test the implementation of METISSE in BSE using Pols et al. (1998) models by comparing with results obtained using SSE in BSE. In particular, to demonstrate the impact of uncertainties in massive stellar evolution on the formation of gravitational-wave sources, we choose to investigate massive, wide binaries similar to the progenitors proposed for double neutron star (Vigna-Gómez et al., 2018; Chattopadhyay et al., 2020) and neutron star-black hole binaries (Chattopadhyay et al., 2021; Broekgaarden et al., 2021). As an example, we study the evolution of a massive binary system of stars with initial masses $25\,\mathrm{M}_{\odot}$ and $15\,\mathrm{M}_{\odot}$ at a metallicity $Z = 10^{-2}$ in a circular orbit (eccentricity $e = 0$) with an initial orbital period of 1800 days. Mass loss due to stellar winds is given by Belczynski et al. (2010) and remnant masses are calculated from Belczynski et al. (2008) (also 'StarTrack prescription' in Fryer et al., 2012). The maximum neutron star mass is assumed to be $3\,\mathrm{M}_{\odot}$. For a fair comparison between SSE and METISSE, we nullify the kick velocity imparted to remnants during supernova explosions by setting the dispersion factor for the Maxwellian distribution of velocity to zero. The full set of input parameters used for both SSE and METISSE are listed in Table 5.2.

Figure 5.13 shows the HR diagram with the evolutionary tracks for each star, as predicted by BSE with METISSE and with SSE. The evolution of the binary system by each method is summarized in Figure 5.14 while a comparison between the different evolutionary parameters of the binary is presented in Figure 5.15.

The left panel of Figure 5.14 depicts the evolution of the binary computed using BSE with SSE. The system starts with both stars on the main sequence with an orbital separation of $2128\,\mathrm{R}_{\odot}$. The large separation allows the binary to evolve as a detached system, interacting primarily through wind accretion and tides. Some of the mass lost by the $25\,\mathrm{M}_{\odot}$ primary through stellar winds is accreted non-conservatively by the $15\,\mathrm{M}_{\odot}$ secondary. The mass loss through stellar winds increases the orbital separation of the binary to $2193\,\mathrm{R}_{\odot}$. As the primary evolves, it expands and eventually fills its Roche lobe during the core helium burning phase at 7.57 Myr, while the secondary is still burning hydrogen on the main-sequence (Figure 5.15). Roche-lobe overflow ensues and mass is transferred from the now $23.59\,\mathrm{M}_{\odot}$ primary onto the $15.01\,\mathrm{M}_{\odot}$ secondary. This mass transfer initially decreases the orbital separation as mass is transferred conservatively from the more massive primary to the less massive secondary. The mass ratio reverses at the orbital separation of $2183\,\mathrm{R}_{\odot}$, and further mass transfer only widens the binary. Mass transfer continues as the primary evolves through the giant phases and stops at an orbital separation of $2573\,\mathrm{R}_{\odot}$, when the primary undergoes a supernova explosion at 8.26 Myr. The primary, with a pre-supernova mass of $11.84\,\mathrm{M}_{\odot}$ and a carbon-oxygen core mass of $7.1\,\mathrm{M}_{\odot}$, forms a $9\,\mathrm{M}_{\odot}$ black hole (BH). The secondary, on the other hand, has become a blue straggler star with a total mass of $20.15\,\mathrm{M}_{\odot}$. The evolution of the secondary continues while the

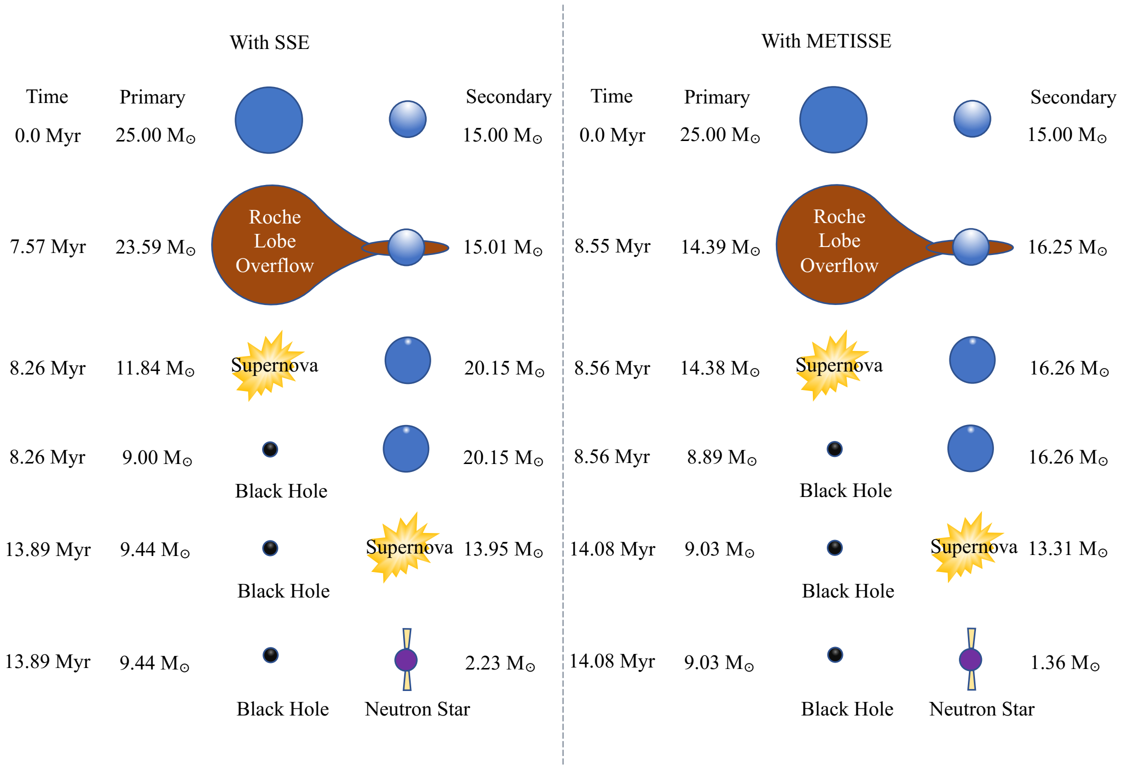

Figure 5.14 Evolution summary of a binary system consisting of a $25\,M_\odot$ and a $15\,M_\odot$ star in a circular orbit with an initial orbital period of 1800 days. The left panel shows the evolution of the binary as predicted by using BSE with SSE while the right panel shows the evolutionary prediction from BSE with METISSE. Both SSE and METISSE predict similar evolutionary pathways for the binary system. However, depending on when the Roche-lobe overflow is initiated from the primary, the final properties of the system can be different, such as the mass of the neutron star formed by the secondary.

companion BH grows through wind accretion to a final mass of $9.44\,M_\odot$. The secondary evolves to become a $13.95\,M_\odot$ giant with a $5.38\,M_\odot$ carbon-oxygen core before exploding in a supernova at 13.89 Myr to form a $2.23\,M_\odot$ neutron star. By construction, no natal kick is imparted to the newly formed neutron star, although the large amount of mass lost during the supernova explosion disrupts the binary and the system becomes unbound.

METISSE initially predicts a similar evolutionary path for the binary, as shown in the right panel of Figure 5.14 but the evolution diverges from SSE during core helium burning. The primary evolves from a $25\,M_\odot$ main-sequence star to a $14.39\,M_\odot$ giant as the $15\,M_\odot$ secondary accretes material from the wind of the primary to become a $16.25\,M_\odot$ star.

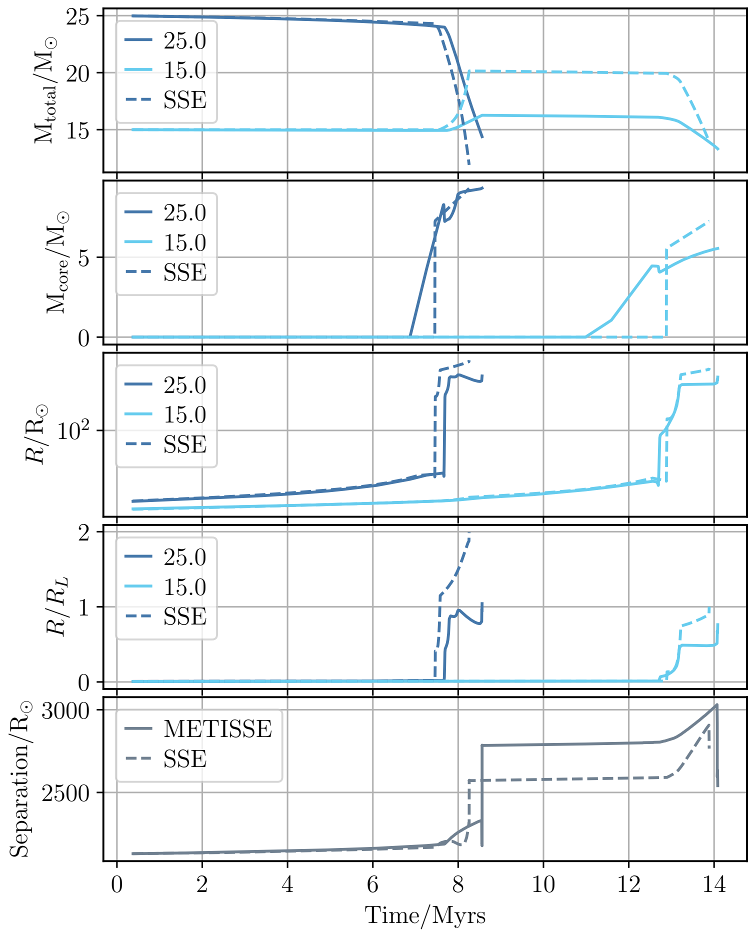

Figure 5.15 Evolution of various evolutionary parameters of the binary system as predicted by METISSE in BSE using Pols et al. (1998) models (solid lines) and SSE in BSE (dashed lines). The dark blue colour represents evolutionary parameters for the 25 $M_\odot$ primary while the light blue colour shows the same for the 15 $M_\odot$ secondary. Due to differences in the radial evolution of the primary between SSE and METISSE, SSE predicts that the primary fills its Roche lobe during core helium burning and is able to transfer more mass to the secondary compared to METISSE. METISSE predicts that Roche-lobe overflow occurs only in the final 10^4 years of the primary's evolution, long after the primary has finished burning helium in the core.

However, compared to SSE, METISSE predicts a smaller radius for the 25 $M_\odot$ star during core helium burning (Figure 5.15). Thus the primary does not fill its Roche lobe until after the end of core-helium burning. Mass transfer from the primary to the secondary through Roche-lobe overflow starts at 8.56 Myr but is short-lived as the primary explodes only 10^4 yrs later in a supernova to become a 8.89 $M_\odot$ BH. During this brief period of Roche-lobe overflow, mass transfer from the less massive primary to the more massive secondary increases the orbital separation from 2180 $R_\odot$ to 2785 $R_\odot$, despite the secondary accreting just 4×10^{-3} $M_\odot$. The secondary evolves to become a giant star losing mass through winds, some of which is accreted by the companion BH which grows to 9.03 $M_\odot$. The secondary ends its life in a supernova with a pre-supernova mass of 13.31 $M_\odot$, and a core mass of 3.85 $M_\odot$ to form a 1.36 $M_\odot$ neutron star. Similar to SSE, the system loses more than 10 $M_\odot$ mass during the supernova, which is enough to disrupt the binary.

Discrepancies in the evolution of the binary system evolved using METISSE and SSE are primarily caused by differences in the implementation of mass-transfer. During core helium burning, wind mass-loss rates for the 25 $M_\odot$ primary can be of the order of 10^{-5} $M_\odot\,yr^{-1}$, and the current implementation of mass transfer in METISSE seemingly under-predicts the stellar radii at high mass-loss rates, as discussed in Section 5.4.1. The most notable impact of this discrepancy for the binary we consider is in determining when Roche-lobe overflow is initiated, and therefore the amount of mass and angular momentum transferred between the stars. SSE predicts that the Roche-lobe overflow is initiated earlier in the primary's life, during the core helium burning phase. However, METISSE predicts that Roche-lobe overflow does not start until much later, after the primary has finished core helium burning and lost a significant portion of its envelope ($\gtrsim$10 $M_\odot$) through stellar winds.

However, another unrelated discrepancy can be seen between the METISSE and SSE predictions of the BH mass when the primary undergoes supernova. SSE, despite predicting a lower pre-supernova mass for the primary, predicts the formation of a more massive BH compared to METISSE. This discrepancy is a result of carbon-oxygen core mass predicted by each code. METISSE relies on the underlying input tracks to provide information about the carbon-oxygen core mass, and therefore can better capture its evolution. SSE, on the other hand, uses a simplified method where the carbon-oxygen core mass grows until a critical value is reached (see Section 5.2 of Agrawal et al., 2020, for details), resulting in a higher carbon-oxygen core mass than METISSE.

To summarize, the successful implementation of METISSE in BSE paves way for binary population synthesis studies. Once the differences in radius predictions between METISSE and SSE with extra mass loss are resolved, it will be trivial to incorporate them in BSE.

Parameter	Value
Primary Mass ($M_\odot$)	25
Secondary Mass ($M_\odot$)	15
Metallicity	0.01
Maximum evolution time (Myr)	12000
Orbital period (days)	1800
Eccentricity	0.0
Reimers mass loss scaling factor	0.5
Binary wind enhancement	0.0
Helium star mass loss factor	1.0
Common-envelope efficiency parameter	3.0
Binding energy factor for common envelope	0.5
Tides	On
White dwarf cooling scheme	Hurley & Shara (2003)
Velocity kick at BH formation	Off
Remnant mass scheme	Belczynski et al. (2008)
Maximum NS mass ($M_\odot$)	3.0
Random number seed for kick	29769
Dispersion in the Maxwellian for the supernova kick speed ($\mathrm{km\,sec^{-1}}$)	0.0
Wind velocity factor	0.125
Wind accretion efficiency factor	1.0
Bondi-Hoyle wind accretion factor	1.5
Fraction of accreted matter retained in nova eruption	0.001
Eddington limit factor	10.0
Gamma angular momentum loss	-1.0

Table 5.2 Input parameters for BSE used in testing the implementation of METISSE and comparing the output with SSE. See Hurley et al. (2002) for an explanation of each input quantity.

5.7 Conclusion and future work

We updated our interpolation based rapid stellar evolution code METISSE to include the impact of mass changes due to stellar winds and binary interaction. While METISSE already had the capability to interpolate between detailed models that included wind mass loss, it now has the capability to add extra mass loss, enabling its use for modelling mass transfer in binary systems.

We tested the implementation of mass transfer by comparing tracks interpolated with METISSE using stellar models from Pols et al. (1998), adding mass loss on top, with the tracks computed using the SSE (Hurley et al., 2000) fitting formulae. We find that

METISSE is able to closely replicate the results from SSE for low mass-loss rates. For high mass-loss rates, we find a mismatch in the behaviour of the stellar radius, leading to different amounts of mass loss, which in turn can lead to different evolutionary behaviour. We find similar results when comparing METISSE with detailed tracks computed by MESA using the same mass-loss rates.

We demonstrated that METISSE works in the binary evolution code BSE (Hurley et al., 2002), and compared the results with BSE using SSE. The evolution of the binary agrees well until differences in the radial evolution during core helium burning between SSE and METISSE become dominant.

While this radius discrepancy is concerning, and is one of the most pressing topics for future work with METISSE, the similarity in other evolutionary parameters in both cases is extremely promising. With some modifications, METISSE will be ready for use in the rapid binary evolution codes such as BSE to evaluate the effect of differing stellar evolution on binary evolution outcomes. It can then be incorporated in similar codes such as COMPAS (Stevenson et al., 2017; Vigna-Gómez et al., 2018), COSMIC (Breivik et al., 2020) and *N*BODY6 (Aarseth, 2003) and used to perform populations synthesis calculations for GW progenitors, along with many other studies.

The use of interpolation within METISSE offers great flexibility regarding input stellar models as one can easily use models generated with different stellar evolution codes and different input parameters. Similar to other interpolation based codes such as SEVN and COMBINE, it uses the approach of switching to tracks of different mass in the presence of mass transfer, although the method of finding the new track varies between the codes. Moreover, while SSE uses fitting formulae for the stellar parameters that are explicitly required in binary evolution, such as the core radius and envelope binding energy, other interpolation-based codes require them as input data for interpolation. METISSE can combine these options freely. Whenever the extra parameters required for binary evolution are present in the input tracks, METISSE interpolates between them. Otherwise, it can switch to using fitting formulae from SSE. This approach allows METISSE to be very robust, an important requirement for population synthesis purposes.

Moreover, the modular structure of METISSE and its SSE-like subprogram units (cf. Section 5.2) for interfacing makes it easier to make modifications in METISSE without affecting the working of the overlying population synthesis codes. This is useful not just for implementing changes related to the current issues with mass transfer but also for improving METISSE in future. An example of potential future work with METISSE includes the use of detailed helium star models for stars that lose their hydrogen envelope during nuclear burning (see Agrawal et al., 2020 for details).

In future, we will also revisit the assumptions underpinning mass transfer in METISSE to better mimic the detailed evolution of binary systems. For example, the current implementation of extra mass transfer mechanisms in METISSE uses similar assumptions as in SSE. Under these assumptions, the structure of the core is assumed to be unaffected by the mass transfer. However, recent studies (Renzo et al., 2017; Laplace et al., 2021) indicate that not only does mass transfer affect the core structure, the pre-supernova structure of the core is different for massive single and binary stripped stars. Differences in the internal structure of the star also have important consequences for the binding energy of the envelope, which determines the outcome of common envelope evolution. Thus, there are a plethora of possibilities with METISSE, and its future looks bright.

Acknowledgements

The authors acknowledge support from the Australian Research Council Centre of Excellence for Gravitational Wave Discovery (Oz- Grav), through project number CE170100004. This work made use of the OzSTAR high performance computer at Swinburne University of Technology. OzSTAR is funded by Swinburne University of Technology and the National Collaborative Research Infrastructure Strategy (NCRIS).

6 Conclusion

"You are allowed to be both a masterpiece and a work in progress simultaneously"

—Sophia Bush

The evolution of massive stars is the basis of several astrophysical investigations, from predicting gravitational-wave event rates to studying star-formation and stellar populations in clusters. However, uncertainties in their evolution present a significant challenge while accounting for their behaviour in stellar population studies. This hurdle is further exacerbated by the way stellar evolution is handled by the population synthesis codes – codes used for modelling the evolution of large systems of stars and the various interactions between them. Therefore, in this thesis we have explored the current state of modelling the evolution of massive stars and, to apply this knowledge in simulating stellar populations, we have developed an alternative approach for modelling stellar evolution in population synthesis codes. In conclusion the three main outcomes of this thesis can be listed as follows:

- Uncertainties in the evolution of massive stars, physical as well numerical, can significantly impact their evolutionary outcomes.
- METISSE offers a computationally cheap, fast, robust approach to test predictions of different models of massive stars in population synthesis simulations.
- With some modifications, METISSE can be used to explore the impact of these uncertainties in binary stellar systems.

6.1 Summary

In Chapter 2, we examined the differences in the models of massive stars with initial mass between 9–200 $M_\odot$ at near-solar composition, computed using various one-dimensional (1D) stellar evolution codes. We compared five sets of stellar models, namely, models from the PAdova and TRieste Stellar Evolution Code (PARSEC; Chen et al., 2015), MESA Isochrones and Stellar Tracks (MIST; Choi et al., 2016) from the Modules for Experiments in Stellar Astrophysics (MESA; Paxton et al., 2011), models (Ekström et al., 2012) from the Geneva code (Eggenberger et al., 2008), models from the Binary Population and Spectral Synthesis (BPASS; Eldridge et al., 2017), and the Bonn Optimized Stellar Tracks (BoOST; Szécsi et al., 2020) from the Bonn Code.

The different sets of stellar models have been computed using various physical inputs such as the chemical composition, mass-loss rates, and internal mixing properties. Additionally, the computation of these models also employed various methods to overcome the numerical instabilities that arise due to the presence of density inversions in the outer layers of massive stars. These density inversions result from the combination of inefficient convection in the low-density envelopes of massive stars and the excess of radiative luminosity to the Eddington luminosity (the maximum luminosity required to balance gravitational pressure in stars). At solar metallicity, such conditions are easily achievable in the envelopes of stars more massive than 40 $M_\odot$.

We find that predictions for the maximum radial expansion of a star can differ between ∼100–2 000 $R_\odot$, while the mass of the stellar remnant can vary up to 20 $M_\odot$ between various sets of models. We also find that stars with initial masses 40 $M_\odot$ and more, show a larger difference in evolutionary properties compared to lower mass stars, signifying the contribution of the methods used in treating the aforementioned numerical instabilities.

The differences in the stellar models are important, as these evolutionary models are extensively used to explain the observations of stellar populations such as the gravitational-wave event rate predictions. Moreover, comparing stellar models with observations is helpful in determining the evolution of massive stars themselves. Hence, it is necessary to untangle the impact of uncertainties arising due to numerical methods in 1D codes from that due to physical processes in massive stars.

We have quantified the impact of these methods on the evolutionary properties of massive stars in Chapter 3. Using the stellar evolution code MESA with commonly used input parameters for massive stellar models, we computed the evolution of stars in the initial mass range of 10–110 $M_\odot$ at one tenth of solar metallicity. We find that the presence of density inversions in the stellar models with initial mass greater than or equal to 30 $M_\odot$, leads to prohibitively small time-steps. Consequently these models fail to reach the end of core helium burning in a reasonable amount of time. We then recomputed these models using the same physical inputs but three different numerical methods to treat the numerical instability. The three methods: using a larger mixing length to increase the efficiency of the mixing process, using higher mass-loss rates to remove the outer layers of the star where numerical instabilities occur, and suppressing density inversions by limiting the temperature gradient, are general forms of the methods used by different 1D codes to evolve massive stars beyond numerical instabilities.

Even when using the minimum enhancements needed to overcome numerical instabilities, we find that the differences between the methods can be non-trivial: the maximum radial expansion achieved by stars can again vary by up to 2 000 $R_\odot$ while the remnant mass of the stars can vary by up to 14 $M_\odot$ between the sets.

We further try to analyze which of these methods can better mimic the behaviour of massive stars in nature, by computing the time spent by stars beyond the Humphreys-Davidson (HD) limit for each set of stellar models. The HD limit defines a region of the Hertzsprung-Russell diagram where very few massive stars have been observed to date. We find that the models computed with extra mass loss spend the least time in this region ($\lesssim 10^5$ yrs) compared to the models computed with other methods. This suggests they are probably closest to the observations (or lack of observations) of massive stars. However, other evolutionary properties predicted by this set of models such as the mass of stellar remnants or the maximum stellar radii, present significant challenges in explaining other observations of massive stars such as the masses of black holes inferred through GW observations.

Since convection is a three-dimensional process, there are ongoing efforts to model the behaviour of density inversions in massive stars using multi-dimensional codes (Jiang et al., 2015, 2017, e.g.,) and develop alternative theories for modelling convection in massive stars

(Arnett et al., 2018; Schultz et al., 2020). Thus the problem of density inversion in stars and the associated numerical instabilities in 1D stellar evolution codes, might be resolved in the near future. Until then, it is important to be aware of these uncertainties, both physical and numerical, while accounting for the behaviour of massive stars in stellar populations studies. The results of populations synthesis should be tested using different models of massive stars.

However, as discussed in Chapter 4, the dependence of most population synthesis codes on the fitting formulae for modelling single star properties prevents us from achieving this goal. These fitting formulae have been a popular choice for population synthesis due to their speed, robustness and ease of use. However, defining these formulae for different set of tracks is a non-trivial task (Church et al., 2009).

To address this problem, we have developed the Method of Interpolation for Single Star Evolution (METISSE; Agrawal et al., 2020) as an alternative to the Single Star Evolution (SSE; Hurley et al., 2000) fitting formulae. It uses interpolation between sets of pre-computed 1D stellar models to approximate the evolution of stellar parameters for a population of stars. It is as fast as SSE and can better reproduce stellar tracks computed using the STARS code compared to SSE. Importantly, the biggest advantage of using METISSE is the capability to easily switch between different sets of input stellar models, computed with different physical inputs and even with different 1D evolution codes.

METISSE is therefore well suited for systematic studies dedicated to probing the impact of massive stellar evolution on the properties of stellar populations. We demonstrated this by comparing stellar models computed with MESA and the Bonn code as input in METISSE. We find that for stars in the mass range 9–100 $\mathrm{M}_{\odot}$ at one tenth of solar metallicity, the predictions of remnant masses can vary by up to 20 $\mathrm{M}_{\odot}$, while the maximum radial expansion achieved by a star can differ by up to 2 000 $\mathrm{R}_{\odot}$ for the two sets of stellar models. These results are similar to those obtained in Chapter 3, thus validating the usefulness of METISSE in exploring uncertainties in massive stellar evolution. These differences can significantly impact the interactions between stars in binary and star cluster environments, and can have vital implications while accounting for present day observations of compact object populations.

Since massive stars are commonly found in binaries, and most of them can exchange mass with their companion (Sana et al., 2012; Moe & Di Stefano, 2017), it is important to be able to account for the effects of mass changes in the stellar models. In Chapter 5, we have updated METISSE to include the implications of additional mass changes, including mass loss through stellar winds and mass transfer in a binary system, that are not already present in the underlying detailed stellar evolution models used as input. To do this, we have used similar assumptions that were used to add the impact of mass changes in SSE.

Using stellar models from Pols et al. (1998) and adding mass loss on top, we find that METISSE can closely replicate the tracks obtained through SSE fitting formulae at low mass-loss rates. However, for high mass-loss rates, we find a discrepancy in the evolutionary parameters between METISSE and SSE. We trace the origin of this discrepancy to be the variation in the radius predictions by METISSE and SSE. We further test our assumptions for mass-transfer in METISSE using detailed tracks computed without mass loss in MESA as input. We find METISSE exhibits a similar discrepancy in stellar radius with detailed tracks computed by MESA using the same mass-loss rates.

To address this discrepancy, we will be modifying our assumptions for modelling mass changes in METISSE in the future. For now, we have used METISSE to study the impact of differences in the radial expansion on a massive, wide binary system of stars. Such systems are similar to the progenitors proposed for double neutron star (Vigna-Gómez et al., 2018; Chattopadhyay et al., 2020) and neutron star-black hole binaries (Chattopadhyay et al., 2021; Broekgaarden et al., 2021). For this purpose, we integrated METISSE in the binary stellar evolution code, BSE (Hurley et al., 2002). Using METISSE in BSE with Pols et al. (1998) models as input, we compared the evolution of a binary with initial masses $25\,\mathrm{M}_{\odot}$ and $15\,\mathrm{M}_{\odot}$ using SSE in BSE, at a metallicity $Z = 10^{-2}$ in a circular orbit with an initial orbital period of 1800 days. Both SSE and METISSE predict similar evolutionary pathways for the binary system and even the same end state: a disrupted system of a black hole and a neutron star. However, due to differences in the radial evolution of the $25\,\mathrm{M}_{\odot}$ primary between SSE and METISSE, SSE predicts that the primary fills its Roche lobe during core helium burning and is able to transfer more mass to the secondary compared to METISSE, whereas METISSE predicts that Roche-lobe overflow occurs only in the final 10^4 years of the primary's evolution, long after the primary has finished burning helium in the core, leading to less mass transfer and hence the formation of a less massive neutron star compared to SSE.

We have thus demonstrated how differences in the predictions of stellar parameters can impact the interaction of a star with its companion. As shown in Chapters 2–4, the differences in radius prediction between models of massive stars can be greater than $1\,000\,\mathrm{R}_{\odot}$, which in turn can have significant consequences on predicting the evolution of massive binaries.

6.2 Future prospects

In this thesis we have developed a framework for exploring the contribution of massive stars in populations synthesis studies. This framework can be applied to study a variety of astrophysical problems such as the phenomenon of multiple stellar populations in globular clusters and the origin of gravitational waves that have been described in the Introduction (Chapter 1). We list three of several possible future avenues for research following up on the work presented in this thesis.

1. Multiple studies have shown that rotation and magnetic fields in massive stars can have a substantial effect on their evolution by modifying the mass-loss rates and surface abundances (Maeder & Meynet, 2010; Walder et al., 2012; Keszthelyi et al., 2019). These magnetic fields can also have a significant effect on the sub-surface convection regions and numerical instabilities in massive stars (Jiang et al., 2018). Recently, they have been invoked to explain properties of compact stellar remnants including the formation of massive black holes detected in gravitational wave observations (Petit et al., 2017; Groh et al., 2020).

   Thus one avenue of future research will be to investigate the role of rotation and magnetic fields in modifying the properties of massive stars. The goal will be to develop comprehensive grids of stellar models using MESA accounting for the effect of rotation and magnetic fields. This will involve testing the existing methods of modelling rotation and magnetic fields in MESA, and implementing new methods based on the latest simulations (e.g., Takahashi & Langer, 2021).

   These updated stellar models will have applications in many fields, including supernova studies and the study of massive binaries to predict the properties of compact binary mergers leading to gravitational wave emission. Moreover, METISSE provides enough flexibility that when new stellar models are ready in the future, it will be straightforward to use them in the population synthesis codes.

2. We plan on continuing to develop the binary mass transfer capabilities of METISSE. Binary mass transfer can result in dramatic differences in not only the surface properties but also the structure of the star. For example, it can affect the structure of the core and the burning shells (Renzo et al., 2017; Laplace et al., 2021). This in turn can have important consequences for determining the outcome of evolutionary processes such as supernovae or common envelope evolution.

   Moreover, improvements in modelling capabilities have seen a rise in the studies dedicated to exploring the connection between the surface features of stars with their structural properties (Farrell et al., 2021a). Results from these studies can once again be incorporated in METISSE to improve modelling of the change in structure with mass transfer processes in binaries.

   Thus we will be revisiting the assumptions underpinning mass transfer in METISSE to better mimic the detailed evolution of binary systems. METISSE has been carefully designed to allow easy integration of updates such as these without affecting the working of the overlying population synthesis code. This will also be extremely useful for extending other capabilities of METISSE such as those outlined in Chapter 4.

3. Despite its advantages, using interpolation to compute stellar parameters is still an approximate method. With the advent of modern computing facilities, codes similar to METISSE that rely on this method for population synthesis purposes have become increasingly popular. While all of them work on the same underlying principle – interpolating between a table of stellar parameters at each point in the simulation – the details of the interpolation scheme and the method for sampling within the tracks used by each code can be quite different. This can lead to disparities in the evolutionary properties predicted by each code. Thus, a detailed comparison of METISSE with other state of the art interpolation based codes such as SEVN (Spera, Mapelli, & Bressan, 2015; Spera & Mapelli, 2017) and ComBinE (Kruckow et al., 2018) will be an important part of future work. This comparison will assist in

the identification and, where possible, mitigation of any systematic biases inherent to METISSE.

4. Different population synthesis codes focus on different aspects of stellar populations but stellar evolution is inherently basic to all of them. It is therefore important to determine and characterise the uncertainties resulting from the evolution of single stars.

   We plan to integrate METISSE with a range of population synthesis codes and test the predictions of different stellar models for populations of stars. This will include binary population synthesis codes such as COMPAS (Stevenson et al., 2017; Vigna-Gómez et al., 2018; Riley et al., 2021), COSMIC (Breivik et al., 2020), as well as globular cluster modelling codes such as NBODY6 (Aarseth, 2003).

   The integration of METISSE with binary population synthesis codes will allow a range of up-to-date stellar evolution models to be used, providing better theoretical constraints on uncertain parameters in binary evolution such as mass transfer, common envelope evolution and compact binary mergers. The integration of METISSE with N-body codes, on the other hand, will bring entirely new capabilities to these studies, including the ability to self-consistently vary stellar mass-loss rates and mixing parameters. It will allow us to probe how uncertainties in stellar evolution can impact stars in dynamical systems.

   Upcoming observing runs with the current gravitational wave detectors aLIGO and VIRGO, accompanied by the recent addition of KAGRA (Abbott et al., 2018b; Kagra Collaboration et al., 2019), are expected to significantly increase the number of future gravitational wave detections. The use of METISSE with different population synthesis codes will enable us to constrain the formation channels of compact isolated binaries versus those in globular clusters as progenitors of gravitational waves. Its flexibility should be particularly useful in explaining exotic gravitational wave events such as the detection of black holes in the pair instability mass gap (GW190521; Abbott et al., 2020).

   Finally, METISSE allows for the easy calculation of various additional stellar parameters including the surface abundances of stars. With some effort, we can apply this information to approximate changes in the surface abundances of the stars while using METISSE to model the evolution of binaries (similar to, e.g., Izzard et al., 2004). This will be useful in tracing the evolution of different elements in stellar populations, and aid the study of the origin of multiple stellar populations in different star clusters. Understanding how these populations could have formed can have far-reaching consequences. It can shed light on the formation and the early evolution of globular clusters and their role in the evolution of the galaxies.

Bibliography

Aarseth, S. J. 2003, Gravitational N-Body Simulations: Tools and Algorithms, Cambridge Monographs on Mathematical Physics (Cambridge University Press)

Aarseth, S. J., Tout, C. A., & Mardling, R. A. 2008, Lecture Notes in Physics, Vol. 760, The Cambridge N-Body Lectures (Springer Netherlands)

Aasi, J., Abadie, J., Abbott, B. P., et al. 2015, Classical and Quantum Gravity, 32, 115012

Abbott, B. P., Abbott, R., Abbott, T. D., et al. 2016, Phys. Rev. Lett., 116, 061102

Abbott, B. P., Abbott, R., Abbott, T. D., et al. 2017a, ApJ, 848, L13

Abbott, B. P., Abbott, R., Abbott, T. D., et al. 2017b, Physical Review Letters, 119, 161101

Abbott, B. P., Abbott, R., Abbott, T. D., et al. 2017c, ApJ, 848, L12

Abbott, B. P., Abbott, R., Abbott, T. D., et al. 2018a, Phys. Rev. Lett., 121, 161101

Abbott, B. P., Abbott, R., Abbott, T. D., et al. 2018b, Living Reviews in Relativity, 21, 3

Abbott, B. P., Abbott, R., Abbott, T. D., et al. 2019, Phys. Rev. X, 9, 031040

Abbott, R., Abbott, T. D., Abraham, S., et al. 2020, Phys. Rev. Lett., 125, 101102

Abbott, R., Abbott, T. D., Abraham, S., et al. 2020, ApJ, 900, L13

Abbott, R., Abbott, T. D., Abraham, S., et al. 2021a, Physical Review X, 11, 021053

Abbott, R., Abbott, T. D., Abraham, S., et al. 2021b, ApJ, 915, L5

Abt, H. A. 1983, ARA&A, 21, 343

Acernese, F., Agathos, M., Agatsuma, K., et al. 2015, Classical and Quantum Gravity, 32, 024001

Agrawal, P., Hurley, J., Stevenson, S., Szécsi, D., & Flynn, C. 2020, MNRAS, 497, 4549

Aguilera-Dena, D. R., Langer, N., Moriya, T. J., & Schootemeijer, A. 2018, ApJ, 858, 115

Ahumada, J. A., & Lapasset, E. 2007, A&A, 463, 789

Alastuey, A., & Jancovici, B. 1978, ApJ, 226, 1034

Alongi, M., Bertelli, G., Bressan, A., et al. 1993, A&AS, 97, 851

Amaro-Seoane, P., Audley, H., Babak, S., et al. 2017, ArXiv e-prints

Anagnostou, O., Trenti, M., & Melatos, A. 2020, arXiv e-prints, arXiv:2010.06161

Antonini, F., & Gieles, M. 2020, Phys. Rev. D, 102, 123016

Antonini, F., & Rasio, F. A. 2016, ApJ, 831, 187

Arca Sedda, M. 2020, ApJ, 891, 47

Arnett, W. D., Hirschi, R., Campbell, S. W., et al. 2018, arXiv e-prints, arXiv:1810.04659

Arnett, W. D., Meakin, C., Hirschi, R., et al. 2019, ApJ, 882, 18

Asplund, M., Amarsi, A. M., & Grevesse, N. 2021, arXiv e-prints, arXiv:2105.01661

Asplund, M., Grevesse, N., & Sauval, A. J. 2005, in Astronomical Society of the Pacific Conference Series, Vol. 336, Cosmic Abundances as Records of Stellar Evolution and Nucleosynthesis, ed. T. G. Barnes, III & F. N. Bash, 25

Asplund, M., Grevesse, N., Sauval, A. J., & Scott, P. 2009a, ARA&A, 47, 481

Asplund, M., Grevesse, N., Sauval, A. J., & Scott, P. 2009b, ARA&A, 47, 481

Banerjee, S. 2017, MNRAS, 467, 524

Barrett, J. W., Gaebel, S. M., Neijssel, C. J., et al. 2018, MNRAS, 477, 4685

Bastian, N., Lamers, H. J. G. L. M., de Mink, S. E., et al. 2013, MNRAS, 436, 2398

Bastian, N., & Lardo, C. 2018, ARA&A, 56, 83

Basu, S. 2009, in Astronomical Society of the Pacific Conference Series, Vol. 416, Solar-Stellar Dynamos as Revealed by Helio- and Asteroseismology: GONG 2008/SOHO 21, ed. M. Dikpati, T. Arentoft, I. González Hernández, C. Lindsey, & F. Hill, 193

Beasor, E. R., Davies, B., Smith, N., et al. 2020, MNRAS, 492, 5994

Belczynski, K. 2020, ApJ, 905, L15

Belczynski, K., Bulik, T., Fryer, C. L., et al. 2010, ApJ, 714, 1217

Belczynski, K., Kalogera, V., & Bulik, T. 2002, ApJ, 572, 407

Belczynski, K., Kalogera, V., Rasio, F. A., et al. 2008, ApJS, 174, 223

Belczynski, K., Romagnolo, A., Olejak, A., et al. 2021, arXiv e-prints, arXiv:2108.10885

Bellazzini, M., Bragaglia, A., Carretta, E., et al. 2012, A&A, 538, A18

Bergbusch, P. A., & VandenBerg, D. A. 2001, ApJ, 556, 322

Bestenlehner, J. M., Gräfener, G., Vink, J. S., et al. 2014, A&A, 570, A38

Blaauw, A. 1961, Bull. Astron. Inst. Netherlands, 15, 265

Bloecker, T. 1995, A&A, 297, 727

Böhm, K.-H. 1963, ApJ, 138, 297

Bohm, K. H., & Cassinelli, J. 1971, A&A, 12, 21

Böhm-Vitense, E. 1958, ZAp, 46, 108

Bondi, H., & Hoyle, F. 1944, MNRAS, 104, 273

Bouffanais, Y., Mapelli, M., Santoliquido, F., et al. 2021, MNRAS

Bowman, D. M. 2020, Frontiers in Astronomy and Space Sciences, 7, 70

Bragaglia, A., Gratton, R. G., Carretta, E., et al. 2012, A&A, 548, A122

Bragaglia, A., Carretta, E., Gratton, R. G., et al. 2010, ApJ, 720, L41

Breivik, K., Coughlin, S., Zevin, M., et al. 2020, ApJ, 898, 71

Bressan, A., Marigo, P., Girardi, L., et al. 2012, MNRAS, 427, 127

Bressan, A. G., Chiosi, C., & Bertelli, G. 1981, A&A, 102, 25

Broekgaarden, F. S., Berger, E., Neijssel, C. J., et al. 2021, arXiv e-prints, arXiv:2103.02608

Brott, I., de Mink, S. E., Cantiello, M., et al. 2011a, A&A, 530, A115

Brott, I., Evans, C. J., Hunter, I., et al. 2011b, A&A, 530, A116

Caffau, E., Ludwig, H. G., Steffen, M., Freytag, B., & Bonifacio, P. 2011, Sol. Phys., 268, 255

Campbell, C. G. 1984, MNRAS, 207, 433

Cannon, R. D., Croke, B. F. W., Bell, R. A., Hesser, J. E., & Stathakis, R. A. 1998, MNRAS, 298, 601

Cantiello, M., Langer, N., Brott, I., et al. 2009, A&A, 499, 279

Carretta, E., Bragaglia, A., Gratton, R., & Lucatello, S. 2009, A&A, 505, 139

Carretta, E., Bragaglia, A., Gratton, R. G., et al. 2010, A&A, 520, A95

Castro, N., Oey, M. S., Fossati, L., & Langer, N. 2018, ApJ, 868, 57

Chattopadhyay, D., Stevenson, S., Hurley, J. R., Bailes, M., & Broekgaarden, F. 2021, Mon. Not. Roy. Astron. Soc., 504, 3682

Chattopadhyay, D., Stevenson, S., Hurley, J. R., Rossi, L. J., & Flynn, C. 2020, Mon. Not. Roy. Astron. Soc., 494, 1587

Chen, Y., Bressan, A., Girardi, L., et al. 2015, MNRAS, 452, 1068

Chernoff, D. F., & Weinberg, M. D. 1990, ApJ, 351, 121

Choi, J., Dotter, A., Conroy, C., et al. 2016, ApJ, 823, 102

Christensen-Dalsgaard, J. 2008, Ap&SS, 316, 113

Church, R. P., Tout, C. A., & Hurley, J. R. 2009, Publ. Astron. Soc. Australia, 26, 92

Claeys, J., Pols, O., Izzard, R., Vink, J., & Verbunt, F. 2014, Astronomy & Astrophysics, 563, A83

Conti, P. S. 1975, Memoires of the Societe Royale des Sciences de Liege, 9, 193

Costa, G., Bressan, A., Mapelli, M., et al. 2021, MNRAS, 501, 4514

Costa, G., Girardi, L., Bressan, A., et al. 2019, MNRAS, 485, 4641

Cox, J., & Giuli, R. 1968, Principles of Stellar Structure: Physical principles, Principles of Stellar Structure (Gordon and Breach)

Cromartie, H. T., Fonseca, E., Ransom, S. M., et al. 2020, Nature Astronomy, 4, 72

Crowther, P. 2012, Astronomy and Geophysics, 53, 4.30

Crowther, P. A. 2000, A&A, 356, 191

Cunha, K., Hubeny, I., & Lanz, T. 2006, ApJ, 647, L143

Cyburt, R. H., Amthor, A. M., Ferguson, R., et al. 2010, ApJS, 189, 240

Dalessandro, E., Lapenna, E., Mucciarelli, A., et al. 2016, ApJ, 829, 77

Dall'Amico, M., Mapelli, M., Niccolò Di Carlo, U., et al. 2021, arXiv e-prints, arXiv:2105.12757

D'Antona, F., Vesperini, E., D'Ercole, A., et al. 2016, MNRAS, 458, 2122

Davies, B., Crowther, P. A., & Beasor, E. R. 2018, MNRAS, 478, 3138

Davies, B., Kudritzki, R.-P., Plez, B., et al. 2013, ApJ, 767, 3

de Bruijne, J. H. J. 2012, Ap&SS, 341, 31

De Donder, E., & Vanbeveren, D. 2004, New Astron. Rev., 48, 861

de Jager, C., Nieuwenhuijzen, H., & van der Hucht, K. A. 1988, A&AS, 72, 259

de Kool, M. 1990, ApJ, 358, 189

de Mink, S. E., & Belczynski, K. 2015, ApJ, 814, 58

de Mink, S. E., Cantiello, M., Langer, N., et al. 2009a, A&A, 497, 243 de Mink, S. E., Langer, N., Izzard, R. G., Sana, H., & de Koter, A. 2013, ApJ, 764, 166

de Mink, S. E., Pols, O. R., Langer, N., & Izzard, R. G. 2009b, A&A, 507, L1

de Mink, S. E., Sana, H., Langer, N., Izzard, R. G., & Schneider, F. R. N. 2014, ApJ, 782, 7

Decressin, T., Charbonnel, C., & Meynet, G. 2007a, A&A, 475, 859

Decressin, T., Mathis, S., Palacios, A., et al. 2009, A&A, 495, 271

Decressin, T., Meynet, G., Charbonnel, C., Prantzos, N., & Ekström, S. 2007b, A&A, 464, 1029

Degl'Innocenti, S., Prada Moroni, P. G., Marconi, M., & Ruoppo, A. 2008, Ap&SS, 316, 25

Denisenkov, P. A., & Denisenkova, S. N. 1990, Soviet Astronomy Letters, 16, 275

Denissenkov, P. A., & Hartwick, F. D. A. 2014, MNRAS, 437, L21

D'Ercole, A., Vesperini, E., D'Antona, F., McMillan, S. L. W., & Recchi, S. 2008, MNRAS, 391, 825

Dorn-Wallenstein, T. Z., & Levesque, E. M. 2020, ApJ, 896, 164

Dotter, A. 2016, ApJS, 222, 8

Drukier, G. A. 1993, MNRAS, 265, 773

Duchêne, G., & Kraus, A. 2013, ARA&A, 51, 269

Dull, J. D., Cohn, H. N., Lugger, P. M., et al. 1997, ApJ, 481, 267

Eddington, A. S. 1926, The Internal Constitution of the Stars, Cambridge Science Classics (Cambridge University Press)

Eggenberger, P., Meynet, G., Maeder, A., et al. 2008, Ap&SS, 316, 43

Eggleton, P. P. 1971, MNRAS, 151, 351

Eggleton, P. P. 1973, MNRAS, 163, 279

Eggleton, P. P. 1983, ApJ, 268, 368

Eggleton, P. P. 1996, in IAU Symposium, Vol. 174, Dynamical Evolution of Star Clusters: Confrontation of Theory and Observations, ed. P. Hut & J. Makino, 213

Eggleton, P. P., Fitchett, M. J., & Tout, C. A. 1989, ApJ, 347, 998

Einstein, A. 1916, Sitzungsberichte der Königlich Preußischen Akademie der Wissenschaften (Berlin, 688

Ekström, S., Meynet, G., Georgy, C., et al. 2020, in Stars and their Variability Observed from Space, ed. C. Neiner, W. W. Weiss, D. Baade, R. E. Griffin, C. C. Lovekin, & A. F. J. Moffat, 223–228

Ekström, S., Georgy, C., Eggenberger, P., et al. 2012, A&A, 537, A146

Eldridge, J. J. 2020, Astronomy and Geophysics, 61, 2.24

Eldridge, J. J., & Stanway, E. R. 2016, MNRAS, 462, 3302

Eldridge, J. J., & Stanway, E. R. 2020, arXiv e-prints, arXiv:2005.11883

Eldridge, J. J., Stanway, E. R., Xiao, L., et al. 2017, Publications of the Astronomical Society of Australia, 34, e058

Eldridge, J. J., & Tout, C. A. 2004, MNRAS, 353, 87

Érgma, É. 1971, Soviet Ast., 15, 51

Ertl, T., Janka, H. T., Woosley, S. E., Sukhbold, T., & Ugliano, M. 2016, Astrophys. J., 818, 124

Evans, C. J., Smartt, S. J., Lee, J. K., et al. 2005, A&A, 437, 467

Evans, C. J., Taylor, W. D., Hénault-Brunet, V., et al. 2011, A&A, 530, A108

Eyer, L., Rimoldini, L., Rohrbasser, L., et al. 2019, arXiv e-prints, arXiv:1912.07659

Farmer, R., Fields, C. E., Petermann, I., et al. 2016, ApJS, 227, 22

Farmer, R., Renzo, M., de Mink, S. E., Fishbach, M., & Justham, S. 2020, ApJ, 902, L36

Farmer, R., Renzo, M., de Mink, S. E., Marchant, P., & Justham, S. 2019, ApJ, 887, 53

Farr, W. M., Sravan, N., Cantrell, A., et al. 2011, ApJ, 741, 103

Farrell, E., Groh, J., Meynet, G., & Eldridge, J. 2021a, arXiv e-prints, arXiv:2109.02488

Farrell, E., Groh, J. H., Hirschi, R., et al. 2021b, MNRAS, 502, L40

Fields, C. E., Timmes, F. X., Farmer, R., et al. 2018, ApJS, 234, 19

Fowler, W. A., & Hoyle, F. 1964, ApJS, 9, 201

Fraley, G. S. 1968, Ap&SS, 2, 96

Fryer, C. L., Belczynski, K., Wiktorowicz, G., et al. 2012, ApJ, 749, 91

Gallegos-Garcia, M., Berry, C. P. L., Marchant, P., & Kalogera, V. 2021, arXiv e-prints, arXiv:2107.05702

Gardner, J. P. 2003, in IAU Joint Discussion, Vol. 25, IAU Joint Discussion, E10

Gatto, A., Walch, S., Naab, T., et al. 2017, MNRAS, 466, 1903

Ge, H., Webbink, R. F., Chen, X., & Han, Z. 2015, ApJ, 812, 40

Giacobbo, N., & Mapelli, M. 2018, MNRAS, 480, 2011

Giacobbo, N., Mapelli, M., & Spera, M. 2018, MNRAS, 474, 2959

Giersz, M., & Heggie, D. C. 2003, MNRAS, 339, 486

Gilkis, A., Shenar, T., Ramachandran, V., et al. 2021, MNRAS, 503, 1884

Glebbeek, E., Gaburov, E., de Mink, S. E., Pols, O. R., & Portegies Zwart, S. F. 2009, A&A, 497, 255

Glebbeek, E., Pols, O. R., & Hurley, J. R. 2008, A&A, 488, 1007

Götberg, Y., de Mink, S. E., McQuinn, M., et al. 2020, A&A, 634, A134

Graboske, H. C., Dewitt, H. E., Grossman, A. S., & Cooper, M. S. 1973, ApJ, 181, 457

Gräfener, G. 2021, A&A, 647, A13

Gräfener, G., & Hamann, W. R. 2008, A&A, 482, 945

Gräfener, G., Owocki, S. P., & Vink, J. S. 2012, A&A, 538, A40

Grassitelli, L., Fossati, L., Langer, N., et al. 2016, A&A, 593, A14

Gratton, R., Bragaglia, A., Carretta, E., et al. 2019, A&A Rev., 27, 8

Gratton, R. G., Carretta, E., & Bragaglia, A. 2012, A&A Rev., 20, 50

Grevesse, N., & Noels, A. 1993, in Origin and Evolution of the Elements, ed. N. Prantzos, E. Vangioni-Flam, & M. Casse, 15–25

Grevesse, N., Noels, A., & Sauval, A. J. 1996, in Astronomical Society of the Pacific Conference Series, Vol. 99, Cosmic Abundances, ed. S. S. Holt & G. Sonneborn, 117

Grevesse, N., & Sauval, A. J. 1998, Space Sci. Rev., 85, 161

Groh, J. H., Farrell, E. J., Meynet, G., et al. 2020, ApJ, 900, 98

Halley, E. 1715, Philosophical Transactions of the Royal Society of London Series I, 29, 390

Hamann, W. R., & Koesterke, L. 1998, A&A, 335, 1003

Hamann, W. R., Koesterke, L., & Wessolowski, U. 1995, A&A, 299, 151

Hansen, B. M. S., & Phinney, E. S. 1997, MNRAS, 291, 569

Harpaz, A. 1984, MNRAS, 210, 633

Harris, C. R., Millman, K. J., van der Walt, S. J., et al. 2020, Nature, 585, 357

Heger, A., Langer, N., & Woosley, S. E. 2000, ApJ, 528, 368

Heger, A., Woosley, S. E., Rauscher, T., Hoffman, R. D., & Boyes, M. M. 2002, New Astron. Rev., 46, 463

Heger, A., Woosley, S. E., & Spruit, H. C. 2005, ApJ, 626, 350

Heggie, D., & Hut, P. 2003, The Gravitational Million-Body Problem: A Multidisciplinary Approach to Star Cluster Dynamics (Cambridge University Press)

Henyey, L., Vardya, M. S., & Bodenheimer, P. 1965, ApJ, 142, 841

Herwig, F. 2000, A&A, 360, 952

Higgins, E. R., & Vink, J. S. 2020, Astron. Astrophys., 635, A175

Hobbs, G., Lorimer, D. R., Lyne, A. G., & Kramer, M. 2005, MNRAS, 360, 974

Humphreys, R. M., & Davidson, K. 1979, ApJ, 232, 409

Humphreys, R. M., & Davidson, K. 1994, PASP, 106, 1025

Hunter, I., Lennon, D. J., Dufton, P. L., et al. 2008, A&A, 479, 541

Hunter, J. D. 2007, Computing in Science and Engineering, 9, 90

Hurley, J. R., Pols, O. R., & Tout, C. A. 2000, MNRAS, 315, 543

Hurley, J. R., & Shara, M. M. 2003, ApJ, 589, 179

Hurley, J. R., Sippel, A. C., Tout, C. A., & Aarseth, S. J. 2016, Publ. Astron. Soc. Australia, 33, e036

Hurley, J. R., Tout, C. A., Aarseth, S. J., & Pols, O. R. 2001, MNRAS, 323, 630

Hurley, J. R., Tout, C. A., & Pols, O. R. 2002, MNRAS, 329, 897

Hut, P. 1981, A&A, 99, 126

Hut, P., Shara, M. M., Aarseth, S. J., et al. 2003, New Astron., 8, 337

Iben, Icko, J., & Livio, M. 1993, PASP, 105, 1373

Iglesias, C. A., & Rogers, F. J. 1993, ApJ, 412, 752

Iglesias, C. A., & Rogers, F. J. 1996, ApJ, 464, 943

Iglesias, C. A., Rogers, F. J., & Wilson, B. G. 1992, ApJ, 397, 717

Inayoshi, K., Hirai, R., Kinugawa, T., & Hotokezaka, K. 2017, MNRAS, 468, 5020

Ishii, M., Ueno, M., & Kato, M. 1999, PASJ, 51, 417

Itoh, N., Totsuji, H., Ichimaru, S., & Dewitt, H. E. 1979, ApJ, 234, 1079

Ivanova, N., Justham, S., Chen, X., et al. 2013, A&A Rev., 21, 59

Izzard, R. G., Tout, C. A., Karakas, A. I., & Pols, O. R. 2004, Monthly Notices of the Royal Astronomical Society, 350, 407

Janka, H. T., & Mueller, E. 1994, A&A, 290, 496

Jiang, D., Han, Z., & Li, L. 2014, ApJ, 789, 88

Jiang, Y.-F., Cantiello, M., Bildsten, L., Quataert, E., & Blaes, O. 2015, ApJ, 813, 74

Jiang, Y.-F., Cantiello, M., Bildsten, L., Quataert, E., & Blaes, O. 2017, ApJ, 843, 68

Jiang, Y.-F., Cantiello, M., Bildsten, L., et al. 2018, Nature, 561, 498

Johnson, H. L., & Sandage, A. R. 1955, ApJ, 121, 616

Johnson, R. A., Beaulieu, S. F., Gilmore, G. F., et al. 2001, MNRAS, 324, 367

Johnston, C. 2021, arXiv e-prints, arXiv:2107.09075

Jones, S., Hirschi, R., Pignatari, M., et al. 2015, MNRAS, 447, 3115

Joss, P. C., Salpeter, E. E., & Ostriker, J. P. 1973, ApJ, 181, 429

Joyce, M., & Chaboyer, B. 2018, ApJ, 856, 10

Kagra Collaboration, Akutsu, T., Ando, M., et al. 2019, Nature Astronomy, 3, 35

Kaiser, E. A., Hirschi, R., Arnett, W. D., et al. 2020, MNRAS, 496, 1967

Kalirai, J. S., & Richer, H. B. 2010, Philosophical Transactions of the Royal Society of London Series A, 368, 755

Kaper, L., Ellerbroek, L. E., Ochsendorf, B. B., & Caballero Pouroutidou, R. N. 2011, Astronomische Nachrichten, 332, 232

Karakas, A. I., & Lattanzio, J. C. 2014, Publ. Astron. Soc. Australia, 31, e030

Kasen, D., Metzger, B., Barnes, J., Quataert, E., & Ramirez-Ruiz, E. 2017, Nature, 551, 80

Kassis, M., Chan, D., Kwok, S., et al. 2018, in Society of Photo-Optical Instrumentation Engineers (SPIE) Conference Series, Vol. 10702, Proc. SPIE, 1070207

Kemp, A. J., Karakas, A. I., Casey, A. R., et al. 2021, MNRAS, 504, 6117

Kennicutt, R. C., & Evans, N. J. 2012, ARA&A, 50, 531

Keszthelyi, Z., Meynet, G., Georgy, C., et al. 2019, MNRAS, 485, 5843

Kimball, C., Talbot, C., Berry, C. P. L., et al. 2021, ApJ, 915, L35

Kimpson, T. O., Spera, M., Mapelli, M., & Ziosi, B. M. 2016, MNRAS, 463, 2443

Kippenhahn, R., Ruschenplatt, G., & Thomas, H. C. 1980, A&A, 91, 175

Kippenhahn, R., & Thomas, H. C. 1970, in IAU Colloq. 4: Stellar Rotation, ed. A. Slettebak, 20

Kippenhahn, R., & Weigert, A. 1967, ZAp, 65, 251

Kippenhahn, R., & Weigert, A. 1990, Stellar Structure and Evolution (Springer)

Kippenhahn, R., Weigert, A., & Weiss, A. 2012, Stellar Structure and Evolution (Springer)

Kirsten, F., Marcote, B., Nimmo, K., et al. 2021, arXiv e-prints, arXiv:2105.11445

Klencki, J., Moe, M., Gladysz, W., et al. 2018, A&A, 619, A77

Klencki, J., Nelemans, G., Istrate, A. G., & Pols, O. 2020, A&A, 638, A55

Kozai, Y. 1962, AJ, 67, 591

Kraft, R. P. 1964, ApJ, 139, 457

Kremer, K., Piro, A. L., & Li, D. 2021, ApJ, 917, L11

Kroupa, P. 2001, Mon. Not. Roy. Astron. Soc., 322, 231

Kruckow, M. U., Tauris, T. M., Langer, N., Kramer, M., & Izzard, R. G. 2018, MNRAS, 481, 1908

Kudritzki, R. P., Pauldrach, A., Puls, J., & Abbott, D. C. 1989, A&A, 219, 205

Kudritzki, R. P., & Reimers, D. 1978, A&A, 70, 227

Kupka, F. 2009, Turbulent Convection and Numerical Simulations in Solar and Stellar Astrophysics, Vol. 756 (Springer Berlin Heidelberg), 49

Kurucz, R. L. 1979, ApJS, 40, 1

Lamers, H., & Cassinelli, J. 1999, Introduction to Stellar Winds (Cambridge University Press)

Lamers, H. J. G. L. M. 2008, in Astronomical Society of the Pacific Conference Series, Vol. 388, Mass Loss from Stars and the Evolution of Stellar Clusters, ed. A. de Koter, L. J. Smith, & L. B. F. M. Waters, 443

Lamers, H. J. G. L. M., & Fitzpatrick, E. L. 1988, ApJ, 324, 279

Lamers, H. J. G. L. M., & Levesque, E. M. 2017, Understanding Stellar Evolution, 2514-3433 (IOP Publishing)

Landau, L. D., & Lifshitz, E. M. 1975, The classical theory of fields (Oxford: Pergamon Press)

Langer, G. E., Hoffman, R., & Sneden, C. 1993, PASP, 105, 301

Langer, N. 1991, A&A, 252, 669

Langer, N. 1997, in Astronomical Society of the Pacific Conference Series, Vol. 120, Luminous Blue Variables: Massive Stars in Transition, ed. A. Nota & H. Lamers, 83

Langer, N. 2012, ARA&A, 50, 107

Langer, N., El Eid, M. F., & Fricke, K. J. 1985, A&A, 145, 179

Langer, N., Fricke, K. J., & Sugimoto, D. 1983, A&A, 126, 207

Laplace, E., Götberg, Y., de Mink, S. E., Justham, S., & Farmer, R. 2020, A&A, 637, A6

Laplace, E., Justham, S., Renzo, M., et al. 2021, arXiv e-prints, arXiv:2102.05036

Lardo, C., Bellazzini, M., Pancino, E., et al. 2011, A&A, 525, A114

Lau, H. H. B., Gil-Pons, P., Doherty, C., & Lattanzio, J. 2012, A&A, 542, A1

Ledoux, P. 1947, ApJ, 105, 305

Levesque, E. M. 2017, Astrophysics of Red Supergiants, 2514-3433 (IOP Publishing)

Li, C., de Grijs, R., Deng, L., & Milone, A. P. 2017, ApJ, 844, 119

Lidov, M. L. 1962, Planet. Space Sci., 9, 719

Liu, B., & Lai, D. 2021, MNRAS, 502, 2049

Loveridge, A. J., van der Sluys, M. V., & Kalogera, V. 2011, ApJ, 743, 49

LSST Science Collaboration, Abell, P. A., Allison, J., et al. 2009, arXiv e-prints, arXiv:0912.0201

Mackey, A. D. 2008, in The Cambridge N-Body Lectures, ed. S. J. Aarseth, C. A. Tout, & R. A. Mardling, Vol. 760 (Springer Netherlands), 347

Maeder, A. 1975, A&A, 40, 303

Maeder, A. 1987, A&A, 173, 247

Maeder, A. 1992, in Instabilities in Evolved Super- and Hypergiants, ed. C. de Jager & H. Nieuwenhuijzen, 138

Maeder, A. 2009, Physics, Formation and Evolution of Rotating Stars (Springer Berlin Heidelberg)

Maeder, A., & Meynet, G. 2005, A&A, 440, 1041

Maeder, A., & Meynet, G. 2010, New Astron. Rev., 54, 32

Magic, Z., Serenelli, A., Weiss, A., & Chaboyer, B. 2010, ApJ, 718, 1378

Magic, Z., Weiss, A., & Asplund, M. 2015, A&A, 573, A89

Mandel, I., & de Mink, S. E. 2016, MNRAS, 458, 2634

Mapelli, M. 2016, MNRAS, 459, 3432

Mapelli, M., Spera, M., Montanari, E., et al. 2020, ApJ, 888, 76

Mapelli, M., Dall'Amico, M., Bouffanais, Y., et al. 2021, MNRAS, 505, 339

Marchant, P., Langer, N., Podsiadlowski, P., Tauris, T. M., & Moriya, T. J. 2016, A&A, 588, A50

Marcolini, A., Gibson, B. K., Karakas, A. I., & Sánchez-Blázquez, P. 2009, MNRAS, 395, 719

Marino, A. F., Milone, A. P., Karakas, A. I., et al. 2015, MNRAS, 450, 815

Martins, F., & Palacios, A. 2013, A&A, 560, A16

Mastrobuono-Battisti, A., & Perets, H. B. 2021, MNRAS, 505, 2548

Matthews, L. D. 2019, PASP, 131, 016001

Maund, J. R., Crowther, P. A., Janka, H.-T., & Langer, N. 2017, Philosophical Transactions of the Royal Society of London Series A, 375, 20170025

McCarthy, P., & Bernstein, R. A. 2014, in Thirty Meter Telescope Science Forum, 61

McKenzie, M., & Bekki, K. 2021, MNRAS, 507, 834

Messier, C. 1774, Catalogue des Nébuleuses et des Amas d'Étoiles que l'on découvre parmi les Étoiles fixes sur l'horizon de Paris; observées á l'Observatoire de la Marine, avec differens instruments (Catalog of nebulas and star clusters, that one discovers among the fixed stars on the horizon of Paris; observed at the Naval Observatory, with various instruments), https://www.biodiversitylibrary.org/bibliography/4004

Mészáros, P., Fox, D. B., Hanna, C., & Murase, K. 2019, Nature Reviews Physics, 1, 585

Meylan, G., & Heggie, D. C. 1997, A&A Rev., 8, 1

Meynet, G., & Maeder, A. 1997, A&A, 321, 465

Mihalas, D. 1969, ApJ, 156, L155

Mihalas, D. 1978, Stellar atmospheres (W. H. Freeman)

Miller-Jones, J. C. A., Bahramian, A., Orosz, J. A., et al. 2021, Science, 371, 1046

Milone, A. P. 2020, Proceedings of the International Astronomical Union, 351, 251

Milone, A. P., Marino, A. F., Bedin, L. R., et al. 2017, MNRAS, 469, 800

Misra, D., Fragos, T., Tauris, T. M., Zapartas, E., & Aguilera-Dena, D. R. 2020, A&A, 642, A174

Moe, M., & Di Stefano, R. 2017, ApJS, 230, 15

Moorwood, A. 2009, Astrophysics and Space Science Proceedings, 9

Mucciarelli, A., Origlia, L., Ferraro, F. R., & Pancino, E. 2009, ApJ, 695, L134

Nabi, J.-U., Shehzadi, R., & Majid, M. 2019, New Astron., 71, 12

Neijssel, C. J., Vinciguerra, S., Vigna-Gómez, A., et al. 2021, ApJ, 908, 118

Neijssel, C. J., Vigna-Gómez, A., Stevenson, S., et al. 2019, MNRAS, 490, 3740

Nieuwenhuijzen, H., & de Jager, C. 1990, A&A, 231, 134

Nishida, M., & Schindler, A. M. 1967, PASJ, 19, 606

Noels, A., Montalban, J., Miglio, A., Godart, M., & Ventura, P. 2010, Ap&SS, 328, 227

Norris, J. 1987, ApJ, 313, L65

Nugis, T., & Lamers, H. J. G. L. M. 2000, A&A, 360, 227

O'Connor, E., & Ott, C. D. 2011, ApJ, 730, 70

Öpik, E. 1924, Publications of the Tartu Astrofizica Observatory, 25, 1

Osborn, W. 1971, The Observatory, 91, 223

Owocki, S. P. 2015, Instabilities in the Envelopes and Winds of Very Massive Stars, Vol. 412 (Springer International Publishing), 113

Owocki, S. P., Gayley, K. G., & Shaviv, N. J. 2004, ApJ, 616, 525

Özel, F., Psaltis, D., Narayan, R., & McClintock, J. E. 2010, ApJ, 725, 1918

Paczyński, B. 1971, ARA&A, 9, 183

Paczynski, B. 1976, in IAU Symposium, Vol. 73, Structure and Evolution of Close Binary Systems, ed. P. Eggleton, S. Mitton, & J. Whelan, 75

pandas development team, T. 2020, pandas-dev/pandas: Pandas

Paresce, F. 1991, in Evolutionary Phenomena in the Universe, ed. P. Giannone, F. Melchiorri, & F. Occhionero, 371

Paxton, B. 2004, PASP, 116, 699

Paxton, B., Bildsten, L., Dotter, A., et al. 2011, ApJS, 192, 3

Paxton, B., Cantiello, M., Arras, P., et al. 2013, ApJS, 208, 4

Paxton, B., Marchant, P., Schwab, J., et al. 2015, ApJS, 220, 15

Paxton, B., Schwab, J., Bauer, E. B., et al. 2018, ApJS, 234, 34

Paxton, B., Smolec, R., Schwab, J., et al. 2019, ApJS, 243, 10

Pedersen, M. G., Chowdhury, S., Johnston, C., et al. 2019, ApJ, 872, L9

Pelupessy, F. I., van Elteren, A., de Vries, N., et al. 2013, A&A, 557, A84

Petit, V., Keszthelyi, Z., MacInnis, R., et al. 2017, MNRAS, 466, 1052

Petrovic, J., Langer, N., Yoon, S.-C., & Heger, A. 2005, A&A, 435, 247

Petrovic, J., Pols, O., & Langer, N. 2006, A&A, 450, 219

Phinney, E. S., & Kulkarni, S. R. 1994, ARA&A, 32, 591

Piotto, G., De Angeli, F., King, I. R., et al. 2004, ApJ, 604, L109

Piotto, G., Bedin, L. R., Anderson, J., et al. 2007, ApJ, 661, L53

Plavec, M. 1968, Advances in Astronomy and Astrophysics, 6, 201

Poelarends, A. J. T., Herwig, F., Langer, N., & Heger, A. 2008, ApJ, 675, 614

Pols, O. R., & Dewi, J. D. M. 2002, Publ. Astron. Soc. Australia, 19, 233

Pols, O. R., Schröder, K.-P., Hurley, J. R., Tout, C. A., & Eggleton, P. P. 1998, MNRAS, 298, 525

Portegies Zwart, S., McMillan, S. L. W., van Elteren, E., Pelupessy, I., & de Vries, N. 2013, Computer Physics Communications, 184, 456

Portegies Zwart, S., McMillan, S., Harfst, S., et al. 2009, New Astron., 14, 369

Portegies Zwart, S. F., McMillan, S. L. W., & Gieles, M. 2010, ARA&A, 48, 431

Portegies Zwart, S. F., & Verbunt, F. 1996, A&A, 309, 179

Prantzos, N., & Charbonnel, C. 2006, A&A, 458, 135

Prantzos, N., Charbonnel, C., & Iliadis, C. 2007, A&A, 470, 179

Prather, M. J. 1976, PhD thesis, Yale University., New Haven, CT.

Puls, J., Markova, N., & Scuderi, S. 2008, in Astronomical Society of the Pacific Conference Series, Vol. 388, Mass Loss from Stars and the Evolution of Stellar Clusters, ed. A. de Koter, L. J. Smith, & L. B. F. M. Waters, 101

Puls, J., Springmann, U., & Lennon, M. 2000, A&AS, 141, 23

Puls, J., Sundqvist, J. O., & Markova, N. 2015, Proceedings of the International Astronomical Union, 307, 25

Raithel, C. A., Sukhbold, T., & Özel, F. 2018, ApJ, 856, 35

Ramírez-Agudelo, O. H., Simón-Díaz, S., Sana, H., et al. 2013, A&A, 560, A29

Ransom, S. M. 2008, in IAU Symposium, Vol. 246, Dynamical Evolution of Dense Stellar Systems, ed. E. Vesperini, M. Giersz, & A. Sills, 291–300

Rappaport, S., Verbunt, F., & Joss, P. C. 1983, ApJ, 275, 713

Reimers, D. 1975, Memoires of the Societe Royale des Sciences de Liege, 8, 369

Renzini, A. 1987, A&A, 188, 49

Renzo, M., Farmer, R. J., Justham, S., et al. 2020, MNRAS, 493, 4333

Renzo, M., Ott, C. D., Shore, S. N., & de Mink, S. E. 2017, A&A, 603, A118

Ricci, F. 2019, in European Physical Journal Web of Conferences, Vol. 209, European Physical Journal Web of Conferences, 01045

Riley, J., Mandel, I., Marchant, P., et al. 2021, MNRAS, 505, 663

Rodriguez, C. L., Chatterjee, S., & Rasio, F. A. 2016, Phys. Rev. D, 93, 084029

Rodriguez, C. L., Weatherford, N. C., Coughlin, S. C., et al. 2021, arXiv e-prints, arXiv:2106.02643

Ruiter, A. J., Belczynski, K., Sim, S. A., Seitenzahl, I. R., & Kwiatkowski, D. 2014, MNRAS, 440, L101

Sabhahit, G. N., Vink, J. S., Higgins, E. R., & Sander, A. A. C. 2021, arXiv e-prints, arXiv:2107.02183

Saio, H., Baker, N. H., & Gautschy, A. 1998, MNRAS, 294, 622

Saio, H., Georgy, C., & Meynet, G. 2013, in Astronomical Society of the Pacific Conference Series, Vol. 479, Progress in Physics of the Sun and Stars: A New Era in Helio- and Asteroseismology, ed. H. Shibahashi & A. E. Lynas-Gray, 47

Salpeter, E. E. 1955, ApJ, 121, 161

Sana, H., de Mink, S. E., de Koter, A., et al. 2012, Science, 337, 444

Sandage, A. R. 1953, AJ, 58, 61

Sander, A. A. C., & Vink, J. S. 2020, MNRAS, 499, 873

Santoliquido, F., Mapelli, M., Giacobbo, N., Bouffanais, Y., & Artale, M. C. 2021, MNRAS, 502, 4877

Sanyal, D., Grassitelli, L., Langer, N., & Bestenlehner, J. M. 2015, A&A, 580, A20

Sanyal, D., Langer, N., Szécsi, D., -C Yoon, S., & Grassitelli, L. 2017, A&A, 597, A71

Sarkisyan, A., Sholukhova, O., Fabrika, S., et al. 2020, MNRAS, 497, 687

Schaller, G., Schaerer, D., Meynet, G., & Maeder, A. 1992, A&AS, 96, 269

Schilling, G. 1998, Science, 280, 1520

Schneider, F. R. N., Izzard, R. G., Langer, N., & de Mink, S. E. 2015, ApJ, 805, 20

Schneider, F. R. N., Langer, N., de Koter, A., et al. 2014, A&A, 570, A66

Schootemeijer, A., Langer, N., Grin, N. J., & Wang, C. 2019a, A&A, 625, A132

—. 2019b, A&A, 625, A132

Schultz, W. C., Bildsten, L., & Jiang, Y.-F. 2020, ApJ, 902, 67

Schwarzschild, M. 1958, Structure and evolution of the stars. (Princeton University Press)

Shaviv, G., & Salpeter, E. E. 1973, ApJ, 184, 191

Shenar, T., Gilkis, A., Vink, J. S., Sana, H., & Sander, A. A. C. 2020, A&A, 634, A79

Siess, L., Izzard, R. G., Davis, P. J., & Deschamps, R. 2013, A&A, 550, A100

Simón-Díaz, S., Godart, M., Castro, N., et al. 2017, A&A, 597, A22

Simón-Díaz, S., & Herrero, A. 2014, A&A, 562, A135

Simón-Díaz, S., Negueruela, I., Maíz Apellániz, J., et al. 2015, in Highlights of Spanish Astrophysics VIII, 576–581

Simpson, E., Hills, R. E., Hoffman, W., et al. 1970, ApJ, 159, 895

Skumanich, A. 1972, ApJ, 171, 565

Smith, N. 2014, ARA&A, 52, 487

Smith, N. 2017, Philosophical Transactions of the Royal Society of London Series A, 375, 20160268

Smith, N., & Tombleson, R. 2015, MNRAS, 447, 598

Smith, N., Vink, J. S., & de Koter, A. 2004, ApJ, 615, 475

Smolec, R., & Moskalik, P. 2008, Acta Astron., 58, 193

Sneden, C., Kraft, R. P., Prosser, C. F., & Langer, G. E. 1992, AJ, 104, 2121

Soberman, G. E., Phinney, E. S., & van den Heuvel, E. P. J. 1997, A&A, 327, 620

Spera, M., & Mapelli, M. 2017, MNRAS, 470, 4739

Spera, M., Mapelli, M., & Bressan, A. 2015, MNRAS, 451, 4086

Spera, M., Mapelli, M., Giacobbo, N., et al. 2019, MNRAS, 485, 889

Spitzer, L. 1978, Physical processes in the interstellar medium (John Wiley & Sons, New York)

Spruit, H. C. 2002, A&A, 381, 923

Stancliffe, R. J. 2006, MNRAS, 370, 1817

Stancliffe, R. J., Tout, C. A., & Pols, O. R. 2004, MNRAS, 352, 984

Stanway, E. R., Eldridge, J. J., & Becker, G. D. 2016, MNRAS, 456, 485

Steffen, M. 1990, A&A, 239, 443

Stevance, H. F., Eldridge, J. J., & Stanway, E. 2020, Journal of Open Source Software, 5, 1987

Stevenson, S., Berry, C. P. L., & Mandel, I. 2017, Mon. Not. Roy. Astron. Soc., 471, 2801

Stevenson, S., Ohme, F., & Fairhurst, S. 2015, Astrophys. J., 810, 58

Stevenson, S., Sampson, M., Powell, J., et al. 2019, ApJ, 882, 121

Stevenson, S., Vigna-Gómez, A., Mandel, I., et al. 2017, Nature Communications, 8, 14906

Stockman, H. S. 1994, in Astrophysics and Space Science Library, Vol. 187, Frontiers of Space and Ground-Based Astronomy, ed. W. Wamsteker, M. S. Longair, & Y. Kondo, 87

Stothers, R., & Chin, C. W. 1975, ApJ, 198, 407

Stothers, R., & Chin, C. W. 1979, ApJ, 233, 267

Stothers, R. B., & Chin, C.-W. 1991, ApJ, 381, L67

Stothers, R. B., & Chin, C.-W. 1993, ApJ, 408, L85

Strömgren, B. 1939, ApJ, 89, 526

Sukhbold, T., & Adams, S. 2020, MNRAS, 492, 2578

Sukhbold, T., & Woosley, S. 2014, Astrophys. J., 783, 10

Szecsi, D. 2017, in XII Multifrequency Behaviour of High Energy Cosmic Sources Workshop (MULTIF2017), 65

Szécsi, D., Langer, N., Yoon, S.-C., et al. 2015, A&A, 581, A15

Szécsi, D., Mackey, J., & Langer, N. 2018, A&A, 612, A55

Szécsi, D., & Wünsch, R. 2019, ApJ, Vol. 871, nr. 1

Szécsi, D., Wünsch, R., Agrawal, P., & Langer, N. 2020, arXiv e-prints, arXiv:2004.08203

Takahashi, K., & Langer, N. 2021, A&A, 646, A19

Tanikawa, A., Yoshida, T., Kinugawa, T., Takahashi, K., & Umeda, H. 2019, arXiv e-prints, arXiv:1906.06641

Terlevich, E. 1987, MNRAS, 224, 193

The LIGO Scientific Collaboration, & the Virgo Collaboration. 2020, arXiv e-prints, arXiv:2004.08342

The LIGO Scientific Collaboration, the Virgo Collaboration, Abbott, B. P., et al. 2018, arXiv e-prints, arXiv:1811.00364

Toonen, S., & Nelemans, G. 2013, A&A, 557, A87

Tout, C. A., Aarseth, S. J., Pols, O. R., & Eggleton, P. P. 1997, MNRAS, 291, 732

Tout, C. A., Pols, O. R., Eggleton, P. P., & Han, Z. 1996, MNRAS, 281, 257

Townsend, R. H. D., Goldstein, J., & Zweibel, E. G. 2018, MNRAS, 475, 879

Townsend, R. H. D., & Teitler, S. A. 2013, MNRAS, 435, 3406

Trampedach, R., Stein, R. F., Christensen-Dalsgaard, J., Nordlund, Å., & Asplund, M. 2014, MNRAS, 445, 4366

Tutukov, A., & Yungelson, L. 1996, MNRAS, 280, 1035

Vallenari, A. 2014, in EAS Publications Series, Vol. 67-68, EAS Publications Series, 155–158

van den Heuvel, E. P. J., Portegies Zwart, S. F., & de Mink, S. E. 2017, MNRAS, 471, 4256

van Gelder, M. L., Kaper, L., Japelj, J., et al. 2020, arXiv e-prints, arXiv:2002.02690

van Loon, J. T., Cioni, M. R. L., Zijlstra, A. A., & Loup, C. 2005, A&A, 438, 273

van Rensbergen, W., de Greve, J. P., Mennekens, N., Jansen, K., & de Loore, C. 2011, A&A, 528, A16

Vassiliadis, E., & Wood, P. R. 1993, ApJ, 413, 641

Verbunt, F. 1993, ARA&A, 31, 93

Verbunt, F., van den Heuvel, E. P. J., van Paradijs, J., & Rappaport, S. A. 1987, Nature, 329, 312

Vesperini, E., Hong, J., Giersz, M., & Hypki, A. 2021, MNRAS, 502, 4290

Vesperini, E., McMillan, S. L. W., D'Antona, F., & D'Ercole, A. 2013, MNRAS, 429, 1913

Vigna-Gómez, A., Neijssel, C. J., Stevenson, S., et al. 2018, MNRAS, 481, 4009

Villanova, S., Geisler, D., Carraro, G., Moni Bidin, C., & Muñoz, C. 2013, ApJ, 778, 186

Vink, J. S. 2011, Ap&SS, 336, 163

Vink, J. S., & de Koter, A. 2005, A&A, 442, 587

Vink, J. S., de Koter, A., & Lamers, H. J. G. L. M. 2000, A&A, 362, 295

Vink, J. S., de Koter, A., & Lamers, H. J. G. L. M. 2001, A&A, 369, 574

Vink, J. S., Higgins, E. R., Sander, A. A. C., & Sabhahit, G. N. 2021, MNRAS, 504, 146

Vink, J. S., & Sander, A. A. C. 2021, MNRAS, 504, 2051

Wade, G. A., Grunhut, J., Alecian, E., et al. 2014, in Magnetic Fields throughout Stellar Evolution, Vol. 302, Magnetic Fields throughout Stellar Evolution, ed. P. Petit, M. Jardine, & H. C. Spruit, 265–269

Walder, R., Folini, D., & Meynet, G. 2012, Space Sci. Rev., 166, 145

Wang, L., Kroupa, P., Takahashi, K., & Jerabkova, T. 2020, MNRAS, 491, 440

Weaver, R., McCray, R., Castor, J., Shapiro, P., & Moore, R. 1977, ApJ, 218, 377

Weaver, T. A., Zimmerman, G. B., & Woosley, S. E. 1978, ApJ, 225, 1021

Webbink, R. F. 1984, ApJ, 277, 355

Webbink, R. F. 1985, Stellar evolution and binaries, Cambridge Astrophysics Series (Cambridge University Press), 39

Weinberger, R., Springel, V., & Pakmor, R. 2020, ApJS, 248, 32

Wielen, R. 1968, Bull. Astron. (Ser. 3) 127-13, 3, 127

Wielen, R. 1970, Celestial Mechanics, 2, 353

Wilkes, B. J. 2019, Astronomy and Geophysics, 60, 6.19

Williams, D., & IceCube Collaboration. 2020, Nuclear Instruments and Methods in Physics Research A, 952, 161650

Wong, K. W. K., Breivik, K., Kremer, K., & Callister, T. 2021, Phys. Rev. D, 103, 083021

Woosley, S. E. 2017, Astrophys. J., 836, 244

Woosley, S. E. 2019, ApJ, 878, 49

Woosley, S. E., & Heger, A. 2006, ApJ, 637, 914

Woosley, S. E., Heger, A., & Weaver, T. A. 2002, Reviews of Modern Physics, 74, 1015

Xu, X.-J., & Li, X.-D. 2010, ApJ, 716, 114

Yoon, S. C., & Langer, N. 2005, A&A, 435, 967

Yoon, S.-C., Langer, N., & Norman, C. 2006, A&A, 460, 199

Yoon, S. C., Woosley, S. E., & Langer, N. 2010, ApJ, 725, 940

Zahn, J. P. 1977, A&A, 500, 121

Zevin, M., Pankow, C., Rodriguez, C. L., et al. 2017, ApJ, 846, 82

Zevin, M., Bavera, S. S., Berry, C. P. L., et al. 2021, ApJ, 910, 152

A

Extra details on the METISSE methodology

A.1 Z-parameters and mass cutoffs

Searching within the set of stellar tracks to find neighbouring mass tracks for interpolation may seem straight forward but there is a catch to it. The tracks of neighbouring masses are usually similar in properties but certain features occur only in a range of masses and not in others. Interpolation between these can result in incorrect tracks.

Hence, we define five critical masses similar to those defined by Pols et al. (1998). These critical masses or Z-parameters are fixed for a given metallicity, and serve as the lower limits above which certain physical properties start to appear for stellar tracks. They are

- $M_{\rm hook}$ – Mass above which the hook feature starts to appear on the MS,
- $M_{\rm HeF}$ – Mass above which He ignition occurs non-degenerately in the core,
- $M_{\rm FGB}$ – Mass above which He ignition occurs on the HG,
- $M_{\rm up}$ – Mass above which off-centre C/O ignition can occur non-degenerately in the core and
- $M_{\rm ec}$ – Mass above which a star avoids electron captures on neon and proceeds to form an iron core.

Some Z-parameters correspond to the behaviour of core properties and are useful to determine the type of remnant a star will become. The locations at which these critical masses occur in the set are stored as an array of mass cutoffs. For any input mass, only tracks whose initial masses are located within the mass cutoffs are used for the interpolation in mass. If the input mass falls between a critical mass and the initial mass of the next track then its track is extrapolated from the higher mass tracks.

Use of these critical masses not only helps avoid interpolation between dissimilar tracks but also narrows down the range to search for the nearest mass track, thus saving computation time. Z-parameters and mass cutoffs are automatically located by METISSE for any input set of stellar models. If the automatic location method fails to provide a correct value, then METISSE has the option of using Z-parameters supplied by the user.

A.2 Stellar remnants

In METISSE, when the star reaches the end of its nuclear burning life either after the AGB or by satisfying equation 4.1, it becomes a remnant. The type of remnant formed depends on whether or not the core of the star is able to ignite carbon, and if the ignition leads to the formation of an iron core, which can gravitationally collapse in a supernova. Hence, in METISSE we utilize the corresponding critical mass cutoffs $M_{\rm up}$ and $M_{\rm ec}$ (as defined above in Sec. A.1) in the decision-making.

The type and mass of the remnant formed by a star can then be determined by comparison of the He core mass of the star at the base of the AGB ($M_{\rm c,BAGB}$) to the core masses at $M_{\rm up}$ ($M_{\rm up,core}$) and $M_{\rm ec}$ ($M_{\rm ec,core}$) as described below while other properties (e.g., luminosity and radius) are calculated with SSE formulae (see section 6.2 of Hurley et al., 2000). The outcomes are as follows,

1. **White Dwarf:** if the final CO mass of the star is less than the Chandrasekhar mass ($M_{\rm ch}$), it can either become a carbon-oxygen white dwarf (CO-WD) if $M_{\rm c,BAGB} < M_{\rm up,core}$ or an oxygen-neon white dwarf (ONe-WD) if $M_{\rm c,BAGB} \geq M_{\rm up,core}$. The mass of the white dwarf is taken to be the same as the final CO core mass of the star.

2. **Neutron Star or Black Hole:** if the final CO core mass of a star exceeds $M_{\rm ch}$, it is assumed to explode in a supernova. If $M_{\rm c,BAGB} < M_{\rm up,core}$, then the carbon ignites under degenerate conditions and the star leaves behind no remnant. On the other hand, if $M_{\rm c,BAGB} \geq M_{\rm ec,core}$ the star undergoes core-collapse to form either a

neutron star or black hole. The type and mass of the resulting compact remnant can be calculated from one of the following prescriptions: (a) Belczynski, Kalogera, & Bulik (2002) (b) Eldridge & Tout (2004) (c) Belczynski et al. (2008). In between the two limits the star is assumed to explode as an electron-capture supernova and form a neutron star of $1.26\,M_\odot$.

A.3 Calculation of missing phases

With the EEP based format, one can define a limit on the number of data points depending on how many phases a particular track has. This can be different for stars that undergo C burning to become a neutron star or a black hole to that of stars that form a white dwarf. Due to numerical and convergence issues there can be incomplete tracks present in the input set of models. In such cases, even when a single track used for interpolation has insufficient data points, the interpolated track is also rendered incomplete.

Hence, in METISSE we check if, after interpolation, the track has a certain minimum required number of points. By default, this minimum is the TPAGB for low-mass stars and end of C burning for high-mass stars. Both limits can be changed by the user for different sets of stellar models. If the track is incomplete, METISSE searches in the input set (within mass cutoffs) for complete tracks closest to the input mass and interpolates the remaining track from there. The method works only if there are at least two complete tracks within the mass cutoff and there are no large mass gaps in the input set.

B

Extra details on the METISSE methodology - Part II

B.1 Criteria for identifying critical masses

The critical masses described in Section A.1 are identified using the following scheme in METISSE.

1. $M_{\rm hook}$:

   For tracks with initial masses up to $3\,\mathrm{M}_{\odot}$, $M_{\rm hook}$ is the lowest initial mass of the track where the maximum of the central temperature between the IAMS (Intermediate age main sequence, defined as the point where the central hydrogen mass fraction drops to 0.3) and TAMS EEPs is greater than the central temperature at the TAMS EEP i.e.,

   $T_{\rm c,max} > T_{\rm c,TAMS}$.

2. $M_{\rm HeF}$:

   For tracks with initial masses up to $3\,\mathrm{M}_{\odot}$, where $M_{\rm HeF}$ is found, the minimum temperature for core helium burning is about 100 million Kelvin. In stars that undergo the helium flash, a slight expansion of the core following the flash causes the central temperature to decrease a little before increasing again with stable helium burning.

Thus, we identify $M_{\rm HeF}$ as the initial mass of the least massive track whose central temperature from the cHeI EEP to the TAcHeB EEP exceeds 25 million Kelvin at all times, or,

$log_{10}(T_{\rm c,min}) > 7.4$.

3. $M_{\rm FGB}$:

   $M_{\rm FGB}$ is found in tracks with initial masses less than $20\,{\rm M}_\odot$ and can be easily identified by checking if the effective temperate at the cHeI EEP is greater than 6300 K, or

   $log_{10}(T_{\rm eff,cHeI}) > 3.8$

4. $M_{\rm up}$:

   $M_{\rm up}$ is the lowest initial mass of tracks where the absolute fractional change in the central carbon-oxygen mass fraction exceeds 0.01 at the end of the AGB (TPAGB EEP), or

   $\Delta(M_{\rm carbon} + M_{\rm oxygen})/(M_{\rm carbon} + M_{\rm oxygen}) > 0.01$

5. $M_{\rm ec}$:

   The criteria for determining $M_{\rm ec}$ in METISSE is the same as the criteria for determining high-mass stars in Dotter (2016). It is the lowest mass track where either of the following conditions are satisfied:

   (a) If the maximum of the central carbon mass fraction exceeds 0.4 during the star's lifetime but depletes to 0.05 by the end of it, i.e.,

   $M_{\rm carbon,max} > 0.4$ and, $M_{\rm carbon,end} < 0.05$

   (b) If central temperatures can exceed 300 million Kelvin,

   $log_{10}(T_{\rm c,max}) > 8.5$.

(c) If the initial mass of the star is more than $10\,\mathrm{M}_{\odot}$,

$M_i \geq 10\,\mathrm{M}_{\odot}$.

B.2 Details of Interpolation

To compute the parameters of a star with initial mass M_i and metallicity Z_i, at time t_i, the following procedure is adopted in METISSE:

1. The input set of tracks for metallicity Z_i is divided into smaller subsets based on the different mass cutoffs (cf. Section A.1). The first step is to find the neighboring mass tracks for interpolation within these subsets. This is done by identifying the lowest critical mass cutoff $M_{cut}(j)$ greater than M_i.

2. Next we find the track with initial mass M_{min} closest to M_i, using a linear search method within the subset of tracks with initial masses $\leq M_{cut}(j)$ and $> M_{cut}(j-1)$. If the difference between M_{min} and M_i is less than a certain tolerance defined by the user (default is 10^{-4}), then the new track is assigned the same parameters as that of M_{min} and interpolation is not needed.

   If M_i is less than the initial mass of the second lowest mass track in the subset, or greater than the initial mass of the second most massive track, then the new track is generated using linear interpolation. If M_i is less than the initial mass of the lowest mass track in the subset then it is linearly extrapolated from the higher mass tracks.

   In all other cases, there are four tracks whose initial masses immediately envelop M_i. If $M_{min} > M_i$, these tracks correspond to the input tracks with initial masses $M_{min-2}, M_{min-1}, M_{min}, M_{min+1}$. Otherwise, they correspond to the initial masses $M_{min-1}, M_{min}, M_{min+1}, M_{min+2}$. The new track is then generated using monotonic interpolation with a piece-wise cubic function (Steffen, 1990).

3. The new track contains a set of stellar parameters obtained through interpolation in mass between corresponding EEP points in the neighbouring mass tracks. While METISSE can interpolate in any user-defined set of columns, it compulsorily requires certain columns as they are used for computing other evolutionary properties of the star. These columns are: the age, the total mass of the star, the mass of the helium

core, the mass of the carbon-oxygen core, the logarithm of the total luminosity and the logarithm of the stellar radius. The logarithm of the effective temperature is obtained using the black body formula at each time-step. After interpolation stellar phases are assigned as described in Section 4.3.2.

4. To compute the stellar parameters at t_i, a second interpolation occurs within the mass-interpolated track, using a similar procedure as above. Using a linear search method, we search for the EEP point corresponding to age t_k closest to t_i, within the subset of ages constrained by the key EEPs relevant for the current evolutionary phase of the star. For continuity, here both EEPs are included in the subset, excluding the need for extrapolation. Once neighbouring EEP points are identified, stellar parameters at t_i are obtained by linearly interpolating between t_k and t_{k+1} (if $t_k < t_i$) or t_{k-1} and t_k (if $t_k \geq t_i$).

C

Details of MLT++

In MLT++, MESA makes convection efficient by reducing superadiabaticity in the stellar envelope. In the regions where superadiabaticity is greater than threshold `gradT_excess_f1`, it decreases $\nabla_{\rm T}$ to make it closer to $\nabla_{\rm ad}$. The fraction of decrease is determined by the parameter `gradT_excess_alpha` or α and is calculated based on the value of (cf. equation 38 of Paxton et al., 2013):

$$\lambda_{\rm max} \equiv \max\left(\frac{L_{\rm rad}}{L_{\rm Edd}}\right) \quad \text{and} \quad \beta_{\rm min} \equiv \min\left(\frac{P_{\rm gas}}{P}\right), \tag{C.1}$$

For each stellar model, MESA computes α by comparing $\lambda_{\rm max}$ with the thresholds λ_1 and λ_2 and $\beta_{\rm min}$ with β_1 and β_2 using the following conditions.

If $\lambda_{\rm max} \geq \lambda_1$ then,

$$\alpha = \begin{cases} 1 & \beta_{\rm min} \leq \beta_1 \\ \dfrac{\beta_1 + d\beta - \beta_{\rm min}}{d\beta} & \beta_1 < \beta_{\rm min} < \beta_1 + d\beta \\ 0 & \text{otherwise} \end{cases} \cdot \tag{C.2}$$

If $\lambda_{\text{max}} \geq \lambda_2$ then,

$$\alpha = \begin{cases} 1 & \beta_{\text{min}} \leq \beta_{\text{limit}} \\ \dfrac{\beta_{\text{limit}} + d\beta - \beta_{\text{min}}}{d\beta} & \beta_{\text{min}} < \beta_{\text{limit}} + d\beta \\ 0 & \beta_{\text{min}} \geq \beta_{\text{limit}} + d\beta \end{cases}. \tag{C.3}$$

If $\lambda_{\text{max}} > \lambda_2 - d\lambda$ then,

$$\alpha = \begin{cases} 1 & \beta_{\text{min}} \leq \beta_2 \\ \dfrac{\lambda_{\text{max}} + d\lambda - \lambda_2}{d\lambda} & \beta_2 < \beta_{\text{min}} < \beta_2 + d\beta \\ 0 & \text{otherwise} \end{cases}. \tag{C.4}$$

The net fraction of decrease is determined by a combination of alpha and user defined `gradT_excess_f2` or f_2 using the following equation,

$$\alpha_{\text{net}} = f_2 + (1 - f_2)(1 - \alpha). \tag{C.5}$$

The excess fraction is then subtracted from ∇_{T}, to give reduced $\nabla_{\text{T,new}}$ as,

$$\nabla_{\text{T,new}} = \alpha_{\text{net}} \times \nabla_{\text{T}} + (1 - \alpha_{\text{net}}) \times \nabla_{\text{ad}}. \tag{C.6}$$

The default values for the different thresholds in the Equations C.2–C.4 are: $\lambda_1 = 1.0$ and $\lambda_2 = 0.5$, $\beta_1 = 0.35$ and $\beta_2 = 0.25$, $d\lambda = 0.1$ and $d\beta = 0.1$. `gradT_excess_f1` defaults to 10^{-4} while the default value of `gradT_excess_f2` or f_2 is 10^{-3}. These values can be redefined by the user.

Equations C.2–C.4 yield a value of α between 0 and 1. The maximum fraction of ∇_{T} used in calculating $\nabla_{\text{T,new}}$ is limited to f_2 (when $\alpha = 1$), with smaller f_2 implying larger contribution of ∇_{ad} in the equation C.6 and therefore larger reduction in superadiabaticity.

We tested our models with for different values of f_2, λ_1 and β_1. The HR diagram for 110 $\text{M}_\odot$ stellar model, calculated with the four different combinations of parameters in MLT++ is shown in Figure C.1. We find that using a small reduction in superadiabaticity with f_2=10^{-1} and setting $\lambda_1 = 0.6$ and $\beta_1 = 0.05$ helps the stellar models reach completion timely and without any numerical inaccuracies or difficulty.

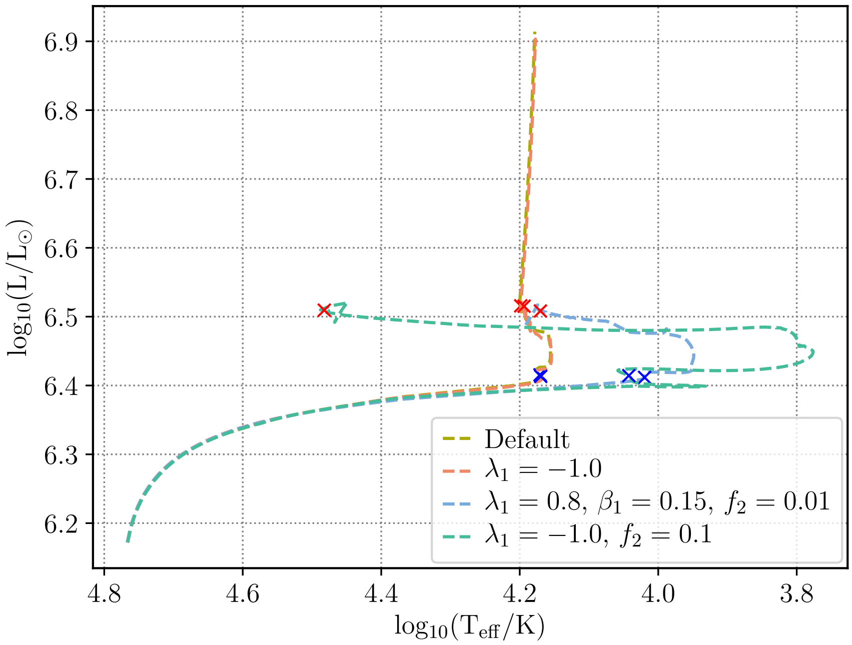

Figure C.1 Evolutionary tracks of a 110 $M_\odot$ star evolved with four different MLT++ parameter combinations. Apart from the changes indicated in the figure legend, default values for all other MLT++ parameters have been used. A negative value of λ_1 implies that the maximum reduction in superadiabaticity is applied throughout the track. The tracks corresponding to the default values of MLT++ and to $\lambda_1 = -1.0$ are indistinguishable here and predict unrealistic luminosities.